Anorexia's roots in genes and the brain p. 124

Histone modification and cocaine addiction pp. 134 & 197

An anthropoid primate from South America pp. 136 & 194

Science

$15
10 APRIL 2020
sciencemag.org

AAAS

EXOTIC STATISTICS

Anyons show their true colors in a tiny collider pp. 131 & 173

WE WRITE THE FUTURE OF DIGITAL PCR

Introducing the fastest track to discovery

Bio-Rad has set the standard for digital PCR since 2011. This year, we raise the standard — fully automated multiplexed digital PCR. The new QX ONE Droplet Digital PCR (ddPCR) System integrates partitioning, amplification, and four-color detection into a single high-throughput experience that delivers superior precision, sensitivity, and absolute quantification.

Take an interactive first look at bio-rad.com/info/QXONE

BIO-RAD

BIO-RAD, DDPCR, DROPLET DIGITAL PCR, and QX ONE are trademarks of Bio-Rad Laboratories, Inc. in certain jurisdictions.

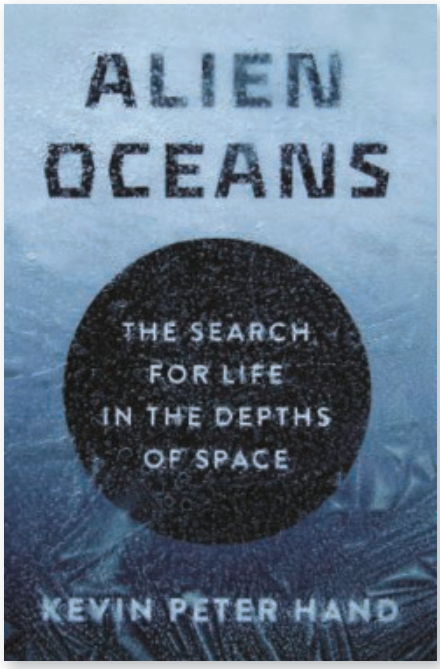

"A beautiful portrayal of the science behind our search for life in alien oceans, and the connection to our precious ocean here on Earth."
—James Cameron

Cloth $27.95

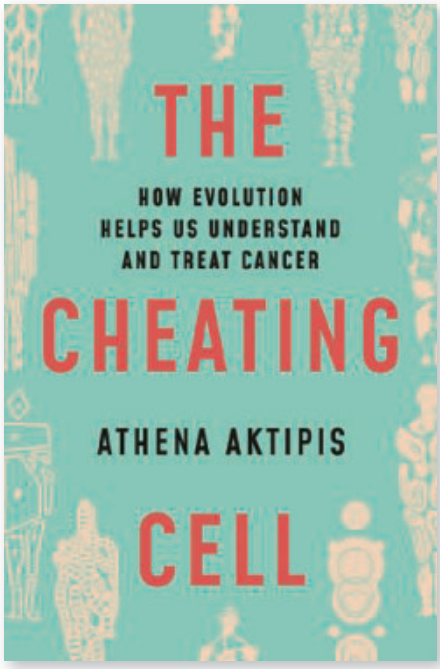

"This wise, erudite, and engaging book will change how we think about cancer and life itself."
—Daniel E. Lieberman, author of *The Story of the Human Body*

Cloth $24.95

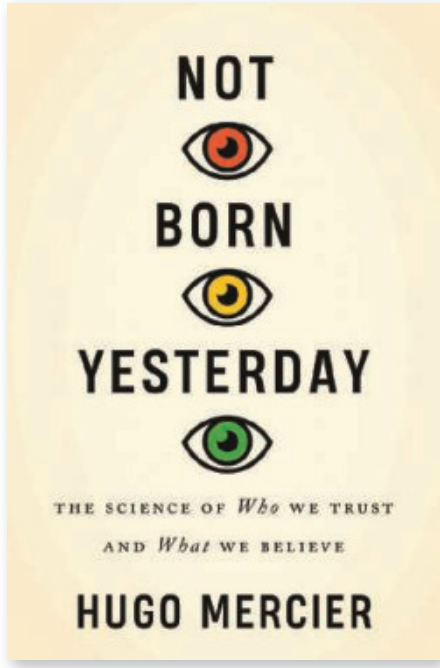

"A bracing book that might make you less gullible about gullibility."
—Barbara Kiser, *Nature*

Cloth $29.95

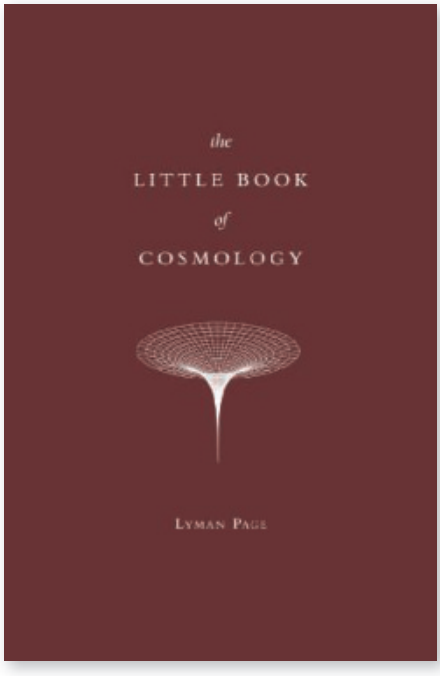

"Readers will find no better introduction to our modern view of cosmology."
—Avi Loeb, Harvard University

Cloth $19.95

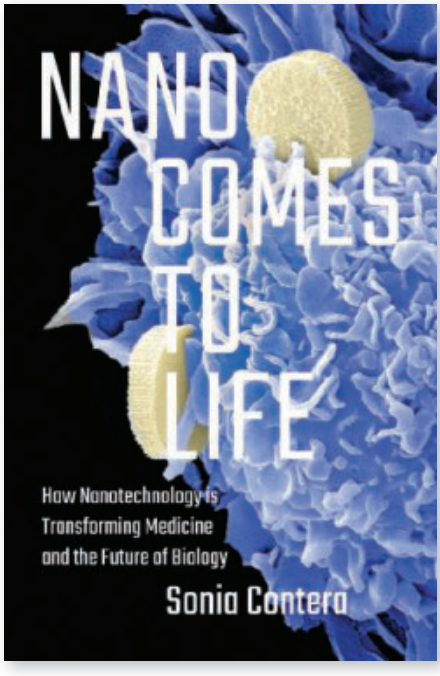

"This book is a must-read for anyone interested in research at the interface between nanotechnology and biology."
—Eric Mazur, Harvard University

Cloth $24.95

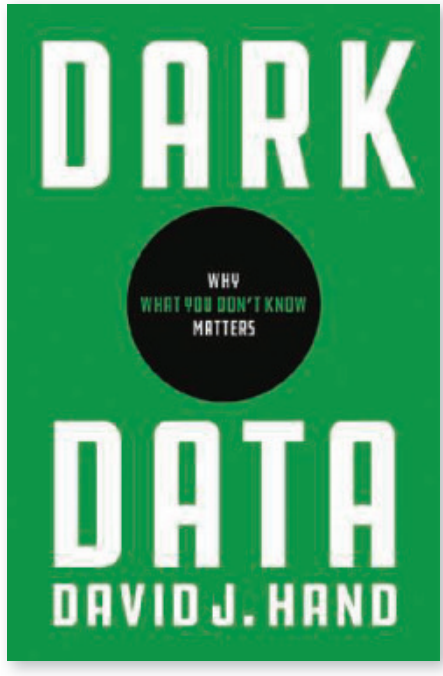

"It is hard to think of anyone having anything at all to do with data-driven decisions who couldn't benefit from reading this book."
—Arno Siebes, Universiteit Utrecht

Cloth $29.95

PRINCETON UNIVERSITY PRESS

MOLECULAR DEVICES

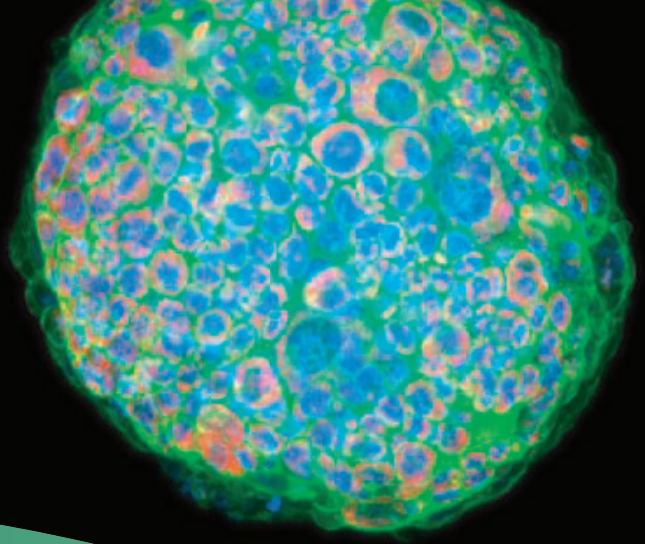

CAPTURE the micro moments that matter

NEW Water Immersion Objectives

Gain the sensitivity to capture more phenotypic data at greater depths. Our high-content imagers and team are here to help your lab simplify imaging and analysis of complex, 3D assay workflows and fast-track discoveries.

Learn more at
moleculardevices.com/water

For Research Use Only. Not for use in diagnostic procedures.
© 2020 Molecular Devices, LLC. All Rights Reserved. The trademarks mentioned herein are the property of Molecular Devices, LLC or their respective owners.

CONTENTS

10 APRIL 2020 • VOLUME 368 • ISSUE 6487

ILLUSTRATION: ILARIA URBINATI

NEWS

IN BRIEF

114 News at a glance

IN DEPTH

116 Pandemic brings mass vaccinations to a halt
Polio, measles, other diseases set to surge as COVID-19 forces suspension of campaigns *By L. Roberts*

117 Tested by HIV and TB, South Africa confronts new pandemic
Infrastructure and tactics developed for existing epidemics could aid the coronavirus fight *By L. Nordling*

118 Can prophylactic drugs keep fragile health systems running?
A raft of trials will test whether chloroquine and other treatments can protect health workers from COVID-19 *By K. Kupferschmidt*

119 NAS letter suggests 'normal breathing' can expel coronavirus
But some experts are skeptical that small respiratory particles transmit infectious virus
By R. F. Service

120 European Union gets in the venture capital game
Flush with cash, new EU innovation agency buys shares in disruptive technology startups *By N. Wallace*

121 United States aims to curb vaccination injury payouts
Proposal would make it harder to get compensated for shoulder injuries after misplaced injections *By M. Wadman*

122 Help for a wheat fungal disease comes from a surprising source
Resistance gene found in wild grass originated in a fungus *By E. Stokstad*

FEATURES

124 Rethinking anorexia
Challenging long-standing theories about the eating disorder, new research suggests biology is a powerful driver *By J. Couzin-Frankel*
PODCAST

INSIGHTS

PERSPECTIVES

128 Tree diversity reduced to the bare essentials
Tropical forest dynamics can be explained by merely two functional trait axes *By H. Bugmann*
REPORT p. 165

129 The "iron will" of the gut
A gut-derived hormone controls iron concentrations, microbiota composition, and mucosal healing *By M. Rescigno*
REPORT p. 186

131 The smallest particle collider
A new experiment finds direct evidence for anyons in a semiconductor heterostructure
By D. E. Feldman
REPORT p. 173

132 Autoimmunity provoked by foreign antigens
In celiac disease, exogenous gluten drives T cell–B cell interactions that cause autoimmunity *By R. Iversen and L. M. Sollid*

134 Epigenetic tinkering with neurotransmitters
Some neurotransmitters modify chromatin and modulate gene expression
By J.-A. Girault
REPORT p. 197

135 Spin pumping gathers speed
Coherent spin pumping from an antiferromagnet into a metal occurs at ~400 gigahertz *By A. Hoffmann*
RESEARCH ARTICLE p. 160

136 Rafting on a wide and wild ocean
During the Oligocene, now-extinct monkeys crossed the treacherous ocean from Africa to South America *By M. Godinot*
REPORT p. 194

NEW ENGLAND BioLabs® Inc.

be INSPIRED
drive DISCOVERY
stay GENUINE

Flexible Precision.

NEBNext Direct® Custom Ready Panels for NGS target enrichment

Employing the unique NEBNext Direct hybridization-based enrichment method, NEBNext Direct Custom Ready Panels allow rapid customization of targeted gene panels for Illumina® sequencing. Select from a list of genes for which baits have been carefully designed and optimized to give complete coverage of the full coding regions. High quality panels can be designed by you and rapidly delivered, from any combination of genes. NEBNext Direct Custom Ready Panels provide the content you want with the performance you need.

- Choose from a single gene to hundreds of genes
- Experience unmatched specificity and coverage uniformity
- Eliminate synthesis and optimization steps for faster turnaround
- Improve sensitivity with our Unique Molecule Index (UMI)
- Generate results in one day with our automation-friendly workflow

For more information visit

NEBNextDirect.com

NEBNext Direct Custom Ready Panels demonstrate optimum performance across a wide range of panel sizes

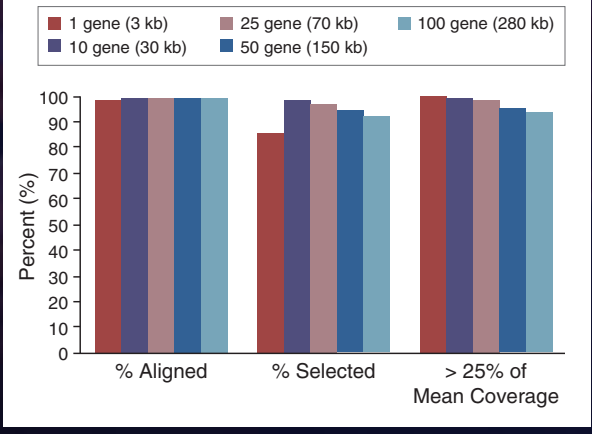

Key target enrichment metrics demonstrate consistent performance across a range of panel sizes. 100 ng of DNA was tested against panels of 1, 10, 25, 50 and 100 genes, and sequenced using Illumina® paired-end 150 bp sequencing. Larger panels included all genes present in smaller panels.

For research use only; not intended for diagnostic use.
One or more of these products are covered by patents, trademarks and/or copyrights owned or controlled by New England Biolabs, Inc.
For more information, please email us at gbd@neb.com.
The use of these products may require you to obtain additional third party intellectual property rights for certain applications.
ILLUMINA® is a registered trademark of Illumina, Inc.
© Copyright 2018, New England Biolabs, Inc.; all rights reserved.

POLICY FORUM

138 Embrace experimentation in biosecurity governance
We must rethink and test assumptions about relationships among biological research, security, and society *By S. W. Evans* et al.

BOOKS *ET AL.*

142 Adaptation in the Anthropocene
Through actions big and small, intentional and unintentional, we are reshaping life on Earth *By M. Schilthuizen*

143 Considering nonhuman culture
Animals have much to teach us about communication, mate preference, and social hierarchy *By M. E. Hannibal*

LETTERS

145 Protecting older adults during social distancing
By A. Jawaid

145 Aggregated mobility data could help fight COVID-19
By C. O. Buckee et al.

146 Disinfection threatens aquatic ecosystems
By H. Zhang et al.

147 Technical Comment abstracts

147 Errata

RESEARCH

IN BRIEF

149 From *Science* and other journals

REVIEW

152 Cancer
Metabolic reprogramming and cancer progression *B. Faubert* et al.
REVIEW SUMMARY; FOR FULL TEXT: DX.DOI.ORG/10.1126/SCIENCE.AAW5473

RESEARCH ARTICLES

153 Molecular biology
Transcription polymerase–catalyzed emergence of novel RNA replicons *N. Jain* et al.
RESEARCH ARTICLE SUMMARY; FOR FULL TEXT: DX.DOI.ORG/10.1126/SCIENCE.AAY0688

154 Neuroscience
Widespread receptor-driven modulation in peripheral olfactory coding *L. Xu* et al.
RESEARCH ARTICLE SUMMARY; FOR FULL TEXT: DX.DOI.ORG/10.1126/SCIENCE.AAZ5390

155 Solar cells
Efficient, stable silicon tandem cells enabled by anion-engineered wide-bandgap perovskites *D. Kim* et al.

160 Spintronics
Subterahertz spin pumping from an insulating antiferromagnet *P. Vaidya* et al.
PERSPECTIVE p. 135

REPORTS

165 Tropical forests
Demographic trade-offs predict tropical forest dynamics *N. Rüger* et al.
PERSPECTIVE p. 128

169 Brown dwarfs
A measurement of the wind speed on a brown dwarf *K. N. Allers* et al.

173 Mesoscopic physics
Fractional statistics in anyon collisions *H. Bartolomei* et al.
PERSPECTIVE p. 131

177 Device technology
Ratcheting quasi-ballistic electrons in silicon geometric diodes at room temperature *J. P. Custer Jr.* et al.

181 Developmental biology
Intravital imaging of mouse embryos *Q. Huang* et al.

186 Immunology
Dendritic cell–derived hepcidin sequesters iron from the microbiota to promote mucosal healing *N. J. Bessman* et al.
PERSPECTIVE p. 129

190 Quantum gases
Bose polarons near quantum criticality *Z. Z. Yan* et al.

194 Paleontology
A parapithecid stem anthropoid of African origin in the Paleogene of South America *E. R. Seiffert* et al.
PERSPECTIVE p. 136

197 Neuroscience
Dopaminylation of histone H3 in ventral tegmental area regulates cocaine seeking *A. E. Lepack* et al.
PERSPECTIVE p. 134

DEPARTMENTS

111 Editorial
G20 leaders must answer to COVID-19
By Caroline Atkinson

113 Editorial
Arab women in science
By Sumaya bint El Hassan

206 Working Life
Finding community during a pandemic
By Arpit Sharma

ON THE COVER

Artist's impression of an anyon collider implemented in a two-dimensional conductor. When colliding on the beamsplitter (at center), fermions (gray) always exit in two different outputs whereas bosons (yellow) always bunch together in the same output. Anyons (orange) display an intermediate behavior, revealing that their fractional statistics interpolate between those of bosons and fermions. See pages 131 and 173.
*Illustration: C. Bickel/*Science

Science Staff 108
New Products 202
Science Careers 203

SCIENCE (ISSN 0036-8075) is published weekly on Friday, except last week in December, by the American Association for the Advancement of Science, 1200 New York Avenue, NW, Washington, DC 20005. Periodicals mail postage (publication No. 484460) paid at Washington, DC, and additional mailing offices. Copyright © 2020 by the American Association for the Advancement of Science. The title SCIENCE is a registered trademark of the AAAS. Domestic individual membership, including subscription (12 months): $165 ($74 allocated to subscription). Domestic institutional subscription (51 issues): $2148; Foreign postage extra: Air assist delivery: $98. First class, airmail, student, and emeritus rates on request. Canadian rates with GST available upon request, GST #125488122. Publications Mail Agreement Number 1069624. **Printed in the U.S.A.**
Change of address: Allow 4 weeks, giving old and new addresses and 8-digit account number. **Postmaster:** Send change of address to AAAS, P.O. Box 96178, Washington, DC 20090–6178. **Single-copy sales:** $15 each plus shipping and handling available from backissues.sciencemag.org; bulk rate on request. **Authorization to reproduce** material for internal or personal use under circumstances not falling within the fair use provisions of the Copyright Act can be obtained through the Copyright Clearance Center (CCC), www.copyright.com. The identification code for *Science* is 0036-8075. *Science* is indexed in the *Reader's Guide to Periodical Literature* and in several specialized indexes.

PHOTO: DEAN HUTTON/BLOOMBERG/GETTY IMAGES

Science AAAS

Editor-in-Chief Holden Thorp, hthorp@aaas.org

Executive Editor Monica M. Bradford

Editors, Research Valda Vinson, Jake S. Yeston **Editor, Insights** Lisa D. Chong

DEPUTY EDITORS Julia Fahrenkamp-Uppenbrink (UK), Stella M. Hurtley (UK), Phillip D. Szuromi, Sacha Vignieri **SR. EDITORIAL FELLOW** Andrew M. Sugden (UK) **SR. EDITORS** Gemma Alderton (UK), Caroline Ash (UK), Brent Grocholski, Pamela J. Hines, Paula A. Kiberstis, Marc S. Lavine (Canada), Steve Mao, Ian S. Osborne (UK), Beverly A. Purnell, L. Bryan Ray, H. Jesse Smith, Keith T. Smith (UK), Jelena Stajic, Peter Stern (UK), Valerie B. Thompson, Brad Wible, Laura M. Zahn **ASSOCIATE EDITORS** Michael A. Funk, Priscilla N. Kelly, Tage S. Rai, Seth Thomas Scanlon (UK), Yury V. Suleymanov **LETTERS EDITOR** Jennifer Sills **LEAD CONTENT PRODUCTION EDITORS** Harry Jach, Lauren Kmec **CONTENT PRODUCTION EDITORS** Amelia Beyna, Jeffrey E. Cook, Chris Filiatreau, Julia Katris, Nida Masiulis, Suzanne M. White **SR. EDITORIAL COORDINATORS** Carolyn Kyle, Beverly Shields **EDITORIAL COORDINATORS** Aneera Dobbins, Joi S. Granger, Jeffrey Hearn, Lisa Johnson, Maryrose Madrid, Ope Martins, Shannon McMahon, Jerry Richardson, Hilary Stewart (UK), Alana Warnke, Alice Whaley (UK), Anita Wynn **PUBLICATIONS ASSISTANTS** Jeremy Dow, Alexander Kief, Ronmel Navas, Brian White **EXECUTIVE ASSISTANT** Jessica Slater **ASI DIRECTOR, OPERATIONS** Janet Clements (UK) **ASI SR. OFFICE ADMINISTRATOR** Jessica Waldock (UK)

News Editor Tim Appenzeller

NEWS MANAGING EDITOR John Travis **INTERNATIONAL EDITOR** Martin Enserink **DEPUTY NEWS EDITORS** Elizabeth Culotta, Lila Guterman, David Grimm, Eric Hand (Europe), David Malakoff **SR. CORRESPONDENTS** Daniel Clery (UK), Jon Cohen, Jeffrey Mervis, Elizabeth Pennisi **ASSOCIATE EDITORS** Jeffrey Brainard, Catherine Matacic **NEWS REPORTERS** Adrian Cho, Jennifer Couzin-Frankel, Jocelyn Kaiser, Kelly Servick, Robert F. Service, Erik Stokstad, Paul Voosen, Meredith Wadman **INTERNS** Eva Frederick, Rodrigo Perez Ortega **CONTRIBUTING CORRESPONDENTS** Warren Cornwall, Ann Gibbons, Mara Hvistendahl, Sam Kean, Eli Kintisch, Kai Kupferschmidt (Berlin), Andrew Lawler, Mitch Leslie, Eliot Marshall, Virginia Morell, Dennis Normile (Shanghai), Elisabeth Pain (Careers), Charles Piller, Michael Price, Tania Rabesandratana (Barcelona), Emily Underwood, Gretchen Vogel (Berlin), Lizzie Wade (Mexico City) **CAREERS** Donisha Adams, Rachel Bernstein (Editor), Katie Langin (Acting Editor) **COPY EDITORS** Julia Cole (Senior Copy Editor), Cyra Master (Copy Chief) **ADMINISTRATIVE SUPPORT** Meagan Weiland

Creative Director Beth Rakouskas

DESIGN MANAGING EDITOR Marcy Atarod **GRAPHICS MANAGING EDITOR** Alberto Cuadra **PHOTOGRAPHY MANAGING EDITOR** William Douthitt **WEB CONTENT STRATEGY MANAGER** Kara Estelle-Powers **SENIOR DESIGNER** Chrystal Smith **DESIGNER** Christina Aycock **GRAPHICS EDITOR** Nirja Desai **INTERACTIVE GRAPHICS EDITOR** Xing Liu **SENIOR SCIENTIFIC ILLUSTRATORS** Valerie Altounian, Chris Bickel **SCIENTIFIC ILLUSTRATOR** Alice Kitterman **SENIOR GRAPHICS SPECIALISTS** Holly Bishop, Nathalie Cary **SENIOR PHOTO EDITOR** Emily Petersen **PHOTO EDITOR** Kaitlyn Dolan

Chief Executive Officer and Executive Publisher Sudip Parikh

Publisher, Science Family of Journals Bill Moran

DIRECTOR, BUSINESS SYSTEMS AND FINANCIAL ANALYSIS Randy Yi **DIRECTOR, BUSINESS OPERATIONS & ANALYSIS** Eric Knott **DIRECTOR OF ANALYTICS** Enrique Gonzales **MANAGER, BUSINESS OPERATIONS** Jessica Tierney **SENIOR BUSINESS ANALYST** Cory Lipman, Meron Kebede **FINANCIAL ANALYST** Alexander Lee **ADVERTISING SYSTEM ADMINISTRATOR** Tina Burks **SENIOR SALES COORDINATOR** Shirley Young **DIGITAL/PRINT STRATEGY MANAGER** Jason Hillman **QUALITY TECHNICAL MANAGER** Marcus Spiegler **ASSISTANT MANAGER DIGITAL/PRINT** Rebecca Doshi **SENIOR CONTENT SPECIALISTS** Steve Forrester, Jacob Hedrick, Antoinette Hodal, Lori Murphy **DIGITAL PRODUCTION MANAGER** Lisa Stanford **CONTENT SPECIALIST** Kimberley Oster **ADVERTISING PRODUCTION OPERATIONS MANAGER** Deborah Tompkins **DESIGNER, CUSTOM PUBLISHING** Jeremy Huntsinger **SR. TRAFFIC ASSOCIATE** Christine Hall **SPECIAL PROJECTS ASSOCIATE** Sarah Dhere

ASSOCIATE DIRECTOR, BUSINESS DEVELOPMENT Justin Sawyers **GLOBAL MARKETING MANAGER** Allison Pritchard **DIGITAL MARKETING MANAGER** Aimee Aponte **JOURNALS MARKETING MANAGER** Shawana Arnold **MARKETING ASSOCIATES** Tori Velasquez, Mike Romano, Ashley Hylton **DIGITAL MARKETING SPECIALIST** Asleigh Rojanavongse **SENIOR DESIGNER** Kim Huynh

DIRECTOR AND SENIOR EDITOR, CUSTOM PUBLISHING Sean Sanders **ASSISTANT EDITOR, CUSTOM PUBLISHING** Jackie Oberst

DIRECTOR, PRODUCT & PUBLISHING DEVELOPMENT Chris Reid **DIRECTOR, BUSINESS STRATEGY AND PORTFOLIO MANAGEMENT** Sarah Whalen **ASSOCIATE DIRECTOR, PRODUCT MANAGMENT** Kris Bishop **SR. PRODUCT ASSOCIATE** Robert Koepke **DIGITAL PRODUCT STRATEGIST** Michael Hardesty **SPJ ASSOCIATE** Samantha Bruno Fuller

DIRECTOR, INSTITUTIONAL LICENSING Iquo Edim **ASSOCIATE DIRECTOR, RESEARCH & DEVELOPMENT** Elisabeth Leonard **MARKETING MANAGER** Kess Knight **SENIOR INSTITUTIONAL LICENSING MANAGER** Ryan Rexroth **INSTITUTIONAL LICENSING MANAGER** Marco Castellan **MANAGER, AGENT RELATIONS & CUSTOMER SUCCESS** Judy Lillibridge **SENIOR OPERATIONS ANALYST** Lana Guz **FULFILLMENT COORDINATOR** Melody Stringer **SALES COORDINATOR** Josh Haverlock

DIRECTOR, GLOBAL SALES Tracy Holmes **US EAST COAST AND MID WEST SALES** Stephanie O'Connor **US WEST COAST SALES** Lynne Stickrod **US SALES MANAGER, SCIENCE CAREERS** Claudia Paulsen-Young **US SALES REP, SCIENCE CAREERS** Tracy Anderson **ASSOCIATE DIRECTOR, ROW** Roger Goncalves **SALES REP, ROW** Sarah Lelarge **SALES ADMIN ASSISTANT, ROW** Bryony Cousins **DIRECTOR OF GLOBAL COLLABORATION AND ACADEMIC PUBLISHING RELATIONS, ASIA** Xiaoying Chu **ASSOCIATE DIRECTOR, INTERNATIONAL COLLABORATION** Grace Yao **SALES MANAGER** Danny Zhao **MARKETING MANAGER** Kilo Lan **ASCA CORPORATION, JAPAN** Kaoru Sasaki (Tokyo), Miyuki Tani (Osaka) **COLLABORATION/CUSTOM PUBLICATIONS/JAPAN** Adarsh Sandhu

DIRECTOR, COPYRIGHT, LICENSING AND SPECIAL PROJECTS Emilie David **RIGHTS AND LICENSING COORDINATOR** Jessica Adams **RIGHTS AND PERMISSIONS ASSOCIATE** Elizabeth Sandler **CONTRACTS AND LICENSING ASSOCIATE** Lili Catlett

---

MAIN HEADQUARTERS
Science/AAAS
1200 New York Ave. NW
Washington, DC 20005

SCIENCE INTERNATIONAL
Clarendon House
Clarendon Road
Cambridge, CB2 8FH, UK

SCIENCE CHINA
Room 1004, Culture Square
No. 59 Zhongguancun St.
Haidian District, Beijing, 100872

SCIENCE JAPAN
ASCA Corporation
Sibaura TY Bldg. 4F, 1-14-5
Shibaura Minato-ku
Tokyo, 108-0073 Japan

EDITORIAL
science_editors@aaas.org

NEWS
science_news@aaas.org

INFORMATION FOR AUTHORS
sciencemag.org/authors/science-information-authors

REPRINTS AND PERMISSIONS
sciencemag.org/help/reprints-and-permissions

MEDIA CONTACTS
scipak@aaas.org

MULTIMEDIA CONTACTS
SciencePodcast@aaas.org
ScienceVideo@aaas.org

INSTITUTIONAL SALES AND SITE LICENSES
sciencemag.org/librarian

PRODUCT ADVERTISING & CUSTOM PUBLISHING
advertising.sciencemag.org/products-services
science_advertising@aaas.org

CLASSIFIED ADVERTISING
advertising.sciencemag.org/science-careers
advertise@sciencecareers.org

JOB POSTING CUSTOMER SERVICE
employers.sciencecareers.org
support@sciencecareers.org

MEMBERSHIP AND INDIVIDUAL SUBSCRIPTIONS
sciencemag.org/subscriptions

MEMBER BENEFITS
aaas.org/membercentral

AAAS BOARD OF DIRECTORS
CHAIR Steven Chu
PRESIDENT Claire M. Fraser
PRESIDENT-ELECT Susan G. Amara
TREASURER Carolyn N. Ainslie
CHIEF EXECUTIVE OFFICER Sudip Parikh
BOARD Cynthia M. Beall, Rosina M. Bierbaum, Ann Bostrom, Stephen P.A. Fodor, S. James Gates, Jr., Laura H. Greene, Kaye Husbands Fealing, Maria M. Klawe, Robert B. Millard, Alondra Nelson, William D. Provine

Science serves as a forum for discussion of important issues related to the advancement of science by publishing material on which a consensus has been reached as well as including the presentation of minority or conflicting points of view. Accordingly, all articles published in *Science*—including editorials, news and comment, and book reviews—are signed and reflect the individual views of the authors and not official points of view adopted by AAAS or the institutions with which the authors are affiliated.

BOARD OF REVIEWING EDITORS (Statistics board members indicated with **(S)**)

Adriano Aguzzi, *U. Hospital Zürich*
Takuzo Aida, *U. of Tokyo*
Leslie Aiello, *Wenner-Gren Foundation*
Judith Allen, *U. of Manchester*
Sebastian Amigorena, *Institut Curie*
James Analytis, *U. of California, Berkeley*
Paola Arlotta, *Harvard U.*
Johan Auwerx, *EPFL*
David Awschalom, *U. of Chicago*
Clare Baker, *U. of Cambridge*
Nenad Ban, *ETH Zürich*
Franz Bauer, *Pontificia Universidad Católica de Chile*
Ray H. Baughman, *U. of Texas at Dallas*
Peter Bearman, *Columbia U.*
Carlo Beenakker, *Leiden U.*
Yasmine Belkaid, *NIAID, NIH*
Philip Benfey, *Duke U.*
Gabriele Bergers, *VIB*
Bradley Bernstein, *Mass. General Hospital*
Alessandra Biffi, *Harvard Med. School*
Peer Bork, *EMBL*
Chris Bowler, *École Normale Supérieure*
Ian Boyd, *U. of St. Andrews*
Emily Brodsky, *U. of California, Santa Cruz*
Ron Brookmeyer, *U. of California, Los Angeles* **(S)**
Christian Büchel, *UKE Hamburg*
Dennis Burton, *Scripps Research*
Carter Tribley Butts, *U. of California, Irvine*
György Buzsáki, *New York U. School of Med.*
Blanche Capel, *Duke U.*
Annmarie Carlton, *U. of California, Irvine*
Nick Chater, *U. of Warwick*
Zhijian Chen, *UT Southwestern Med. Ctr.*
Ib Chorkendorff, *Denmark TU*
James J. Collins, *MIT*
Robert Cook-Deegan, *Arizona State U.*
Alan Cowman, *Walter & Eliza Hall Inst.*
Carolyn Coyne, *U. of Pittsburgh*
Roberta Croce, *VU Amsterdam*
Jeff L. Dangl, *U. of North Carolina*
Tom Daniel, *U. of Washington*
Chiara Daraio, *Caltech*
Nicolas Dauphas, *U. of Chicago*
Frans de Waal, *Emory U.*
Claude Desplan, *New York U.*
Sandra Díaz, *Universidad Nacional de Córdoba*
Ulrike Diebold, *TU Wien*
Hong Ding, *Inst. of Physics, CAS*
Jennifer Dionne, *Stanford U.*
Dennis Discher, *U. of Penn.*
Gerald Dorn, *Washington U. in St. Louis*
Jennifer A. Doudna, *U. of California, Berkeley*
Bruce Dunn, *U. of California, Los Angeles*
William Dunphy, *Caltech*
Christopher Dye, *U. of Oxford*
Todd Ehlers, *U. of Tübingen*
Jennifer Elisseeff, *Johns Hopkins U.*
Tim Elston, *U. of North Carolina*
Andrea Encalada, *U. San Francisco de Quito*
Nader Engheta, *U. of Penn.*
Karen Ersche, *U. of Cambridge*
Barry Everitt, *U. of Cambridge*
Vanessa Ezenwa, *U. of Georgia*
Michael Feuer, *The George Washington U.*
Toren Finkel, *U. of Pittsburgh Med. Ctr.*
Gwenn Flowers, *Simon Fraser U.*
Peter Fratzl, *Max Planck Inst. Potsdam*
Elaine Fuchs, *Rockefeller U.*
Eileen Furlong, *EMBL*
Jay Gallagher, *U. of Wisconsin*
Daniel Geschwind, *U. of California, Los Angeles*
Karl-Heinz Glassmeier, *TU Braunschweig*
Ramon Gonzalez, *U. of South Florida*
Elizabeth Grove, *U. of Chicago*
Nicolas Gruber, *ETH Zürich*
Hua Guo, *U. of New Mexico*
Kip Guy, *U. of Kentucky College of Pharmacy*
Taekjip Ha, *Johns Hopkins U.*
Christian Haass, *Ludwig Maximilians U.*
Sharon Hammes-Schiffer, *Yale U.*
Wolf-Dietrich Hardt, *ETH Zürich*
Louise Harra, *U. College London*
Jian He, *Clemson U.*
Carl-Philipp Heisenberg, *IST Austria*
Ykä Helariutta, *U. of Cambridge*
Janet G. Hering, *Eawag*
Hans Hilgenkamp, *U. of Twente*
Kai-Uwe Hinrichs, *U. of Bremen*
Lora Hooper, *UT Southwestern Med. Ctr.*
Fred Hughson, *Princeton U.*
Randall Hulet, *Rice U.*
Auke Ijspeert, *EPFL*
Akiko Iwasaki, *Yale U.*
Stephen Jackson, *USGS and U. of Arizona*
Kai Johnsson, *EPFL*
Peter Jonas, *IST Austria*
Matt Kaeberlein, *U. of Washington*
William Kaelin Jr., *Dana-Farber Cancer Inst.*
Daniel Kammen, *U. of California, Berkeley*
V. Narry Kim, *Seoul Nat. U.*
Robert Kingston, *Harvard Med. School*
Nancy Knowlton, *Smithsonian Institution*
Etienne Koechlin, *École Normale Supérieure*
Alexander L. Kolodkin, *Johns Hopkins U.*
Julija Krupic, *U. of Cambridge*
Thomas Langer, *Max Planck Inst. Cologne*
Mitchell A. Lazar, *U. of Penn.*
Ottoline Leyser, *U. of Cambridge*
Wendell Lim, *U. of California, San Francisco*
Jianguo Liu, *Michigan State U.*
Luis Liz-Marzán, *CIC biomaGUNE*
Jonathan Losos, *Washington U. in St. Louis*
Ke Lu, *Chinese Acad. of Sciences*
Christian Lüscher, *U. of Geneva*
Jean Lynch-Stieglitz, *Georgia Inst. of Tech.*
Fabienne Mackay, *U. of Melbourne*
Anne Magurran, *U. of St. Andrews*
Oscar Marín, *King's College London*
Charles Marshall, *U. of California, Berkeley*
Christopher Marx, *U. of Idaho*
Geraldine Masson, *CNRS*
C. Robertson McClung, *Dartmouth College*
Rodrigo Medellín, *U. Nacional Autónoma de México*
Graham Medley, *London School of Hygiene & Tropical Med.*
Jane Memmott, *U. of Bristol*
Baoxia Mi, *U. of California, Berkeley*
Edward Miguel, *U. of California, Berkeley*
Tom Misteli, *NCI, NIH*
Yasushi Miyashita, *U. of Tokyo*
Alison Motsinger-Reif, *NIEHS, NIH* **(S)**
Daniel Nettle, *Newcastle U.*
Daniel Neumark, *U. of California, Berkeley*
Beatriz Noheda, *U. of Groningen*
Helga Nowotny, *Vienna Science, Research & Tech. Fund*
Rachel O'Reilly, *U. of Birmingham*
Harry Orr, *U. of Minnesota*
Pilar Ossorio, *U. of Wisconsin*
Andrew Oswald, *U. of Warwick*
Isabella Pagano, *Istituto Nazionale di Astrofisica*
Margaret Palmer, *U. of Maryland*
Elizabeth Levy Paluck, *Princeton U.*
Jane Parker, *Max Planck Inst. Cologne*
Giovanni Parmigiani, *Dana-Farber Cancer Inst.* **(S)**
Samuel Pfaff, *Salk Inst. for Biological Studies*
Julie Pfeiffer, *UT Southwestern Med. Ctr.*
Matthieu Piel, *Institut Curie*
Kathrin Plath, *U. of California, Los Angeles*
Martin Plenio, *Ulm U.*
Katherine Pollard, *U. of California, San Francisco*
Elvira Poloczanska, *Alfred-Wegener-Inst.*
Julia Pongratz, *Ludwig Maximilians U.*
Philippe Poulin, *CNRS*
Jonathan Pritchard, *Stanford U.*
Félix A. Rey, *Institut Pasteur*
Trevor Robbins, *U. of Cambridge*
Joeri Rogelj, *Imperial College London*
Amy Rosenzweig, *Northwestern U.*
Mike Ryan, *U. of Texas at Austin*
Mitinori Saitou, *Kyoto U.*
Shimon Sakaguchi, *Osaka U.*
Miquel Salmeron, *Lawrence Berkeley Nat. Lab*
Nitin Samarth, *Penn. State U.*
Jürgen Sandkühler, *Med. U. of Vienna*
Alexander Schier, *Harvard U.*
Wolfram Schlenker, *Columbia U.*
Susannah Scott, *U. of California, Santa Barbara*
Rebecca Sear, *London School of Hygiene & Tropical Med.*
Vladimir Shalaev, *Purdue U.*
Jie Shan, *Cornell U.*
Beth Shapiro, *U. of California, Santa Cruz*
Jay Shendure, *U. of Washington*
Steve Sherwood, *U. of New South Wales*
Brian Shoichet, *U. of California, San Francisco*
Robert Siliciano, *Johns Hopkins U. School of Med.*
Lucia Sivilotti, *U. College London*
Alison Smith, *John Innes Centre*
Richard Smith, *U. of North Carolina* **(S)**
Mark Smyth, *QIMR Berghofer*
Pam Soltis, *U. of Florida*
John Speakman, *U. of Aberdeen*
Tara Spires-Jones, *U. of Edinburgh*
Allan C. Spradling, *Carnegie Institution for Science*
V. S. Subrahmanian, *Dartmouth College*
Ira Tabas, *Columbia U.*
Sarah Teichmann, *Wellcome Sanger Inst.*
Rocio Titiunik, *Princeton U.*
Shubha Tole, *Tata Inst. of Fundamental Research*
Wim van der Putten, *Netherlands Inst. of Ecology*
Reinhilde Veugelers, *KU Leuven*
Bert Vogelstein, *Johns Hopkins U.*
Kathleen Vohs, *U. of Minnesota*
David Wallach, *Weizmann Inst. of Science*
Jane-Ling Wang, *U. of California, Davis* **(S)**
David Waxman, *Fudan U.*
Jonathan Weissman, *U. of California, San Francisco*
Chris Wikle, *U. of Missouri* **(S)**
Terrie Williams, *U. of California, Santa Cruz*
Ian A. Wilson, *Scripps Research* **(S)**
Yu Xie, *Princeton U.*
Jan Zaanen, *Leiden U.*
Kenneth Zaret, *U. of Penn. School of Med.*
Jonathan Zehr, *U. of California, Santa Cruz*
Xiaowei Zhuang, *Harvard U.*
Maria Zuber, *MIT*

CORNING

WE GET YOU

Every day. Every step of the way.

As a laboratory scientist, you never stop thinking about where your research is headed, or if there's a better way to get there. At Corning, we get it. That's why we offer you a comprehensive portfolio of vessels, advanced surfaces, and cell culture media, and work with you one-on-one to help you make the most of Corning products – from start-up to scale-up.

Our products deliver consistency, reliability, and reproducibility so you can achieve your research goals faster, at every stage of the journey. Learn more at **www.corning.com/cellculture**

VESSELS | SURFACES | MEDIA

NEVER STOP

SUPPORTING LIFE SCIENCE RESEARCH

Uncovering the mechanisms of human disease requires years of dedication and access to the right tools. That's why we'll never stop encouraging therapeutic innovation by developing and supplying critical equipment and materials for researchers and academics. Our tissue-specific human cell products, cell culture media and unique laboratory reagents are designed to support life science research. By accelerating the availability of new treatments and diagnostics, we are helping to make the world a healthier place.

FUJIFILM
Value from Innovation

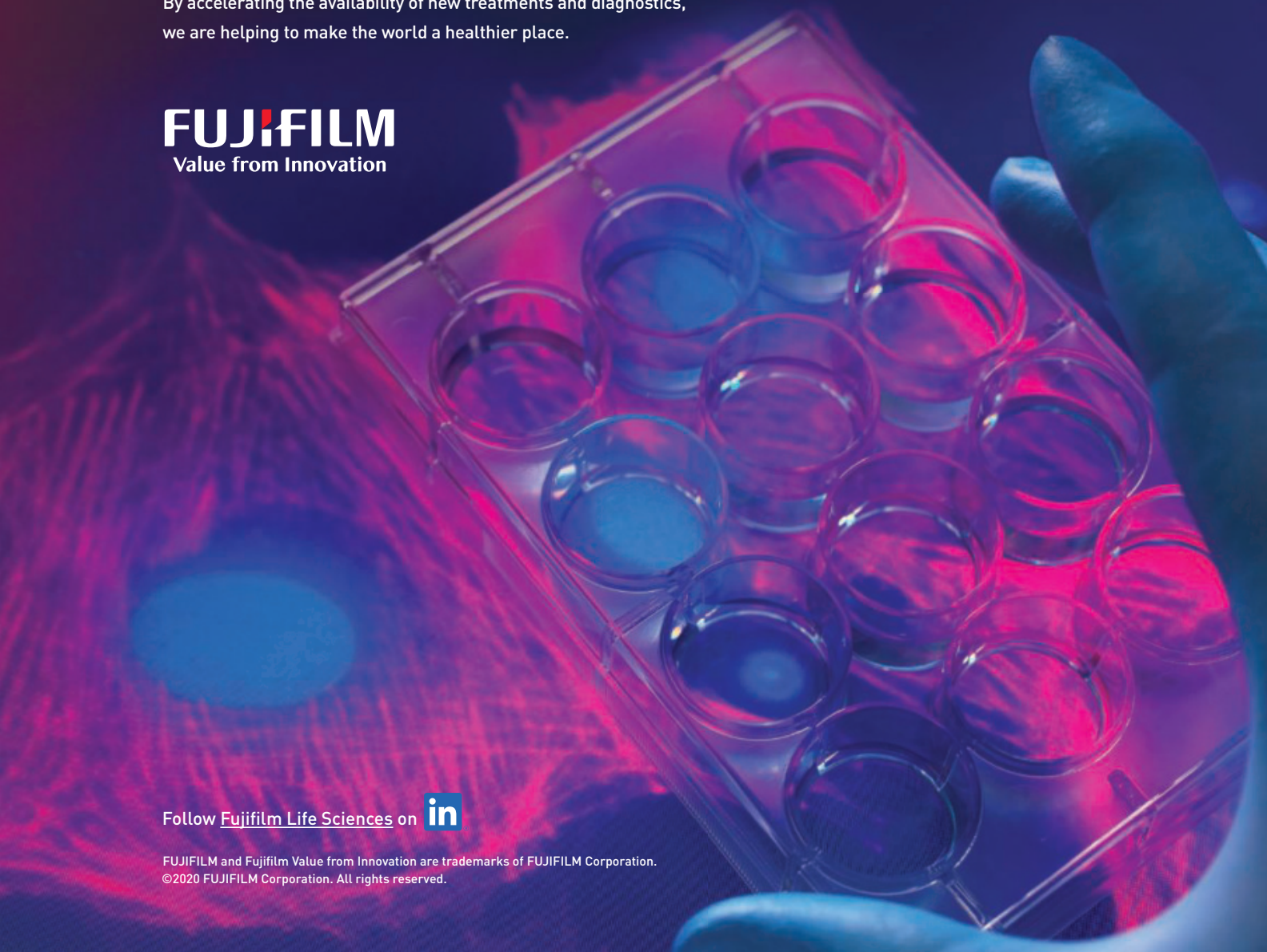

Follow Fujifilm Life Sciences on in

FUJIFILM and Fujifilm Value from Innovation are trademarks of FUJIFILM Corporation.
©2020 FUJIFILM Corporation. All rights reserved.

EDITORIAL

G20 leaders must answer to COVID-19

Caroline Atkinson is a senior adviser at the Rock Creek Group, Washington, DC, and is the former U.S. Deputy National Security Advisor. caroline.atkinson@therockcreekgroup.com

Last week, the United Nations declared the coronavirus disease 2019 (COVID-19) pandemic to be the greatest test the world has faced since World War II. Every day brings news of more infections and deaths, together with rising economic hardship as businesses close and jobs are lost. A global health crisis is now triggering a global economic crisis. On 26 March, the G20 nations, representing the world's 20 largest economies, declared their intention to unite in response to the emergency. What should be their next steps?

As COVID-19 has swept across the world, governments have reacted piecemeal and in starkly different ways. In China, after a dangerous period of denial, the government enacted drastic measures to stop disease spread. In South Korea, Taiwan, Singapore, and Hong Kong, governments swiftly implemented mass testing, contact tracing, and firm guidelines. By contrast, in Europe and the United States, most leaders were slow to react. Rampant spread of COVID-19 across these continents is now illuminating how serious this threat is to life and livelihoods.

> "Hoping that this crisis can be solved... by national governments acting alone is a dangerous illusion."

The scientific community has been quick to collaborate across borders to try to understand the virus and develop ways to combat it. Now governments must come together and coordinate broader global action to address the pandemic, to reinforce the impact of economic and financial measures being taken at a national level, and to plot the way forward out of this crisis and beyond to forestall the next one.

Luckily, the G20 is a mechanism for major countries to coordinate, even though governments' initial impulses were to turn sharply inward. Its informal network of policy-makers, who advise government leaders and prepare for top-level summits, has broad reach across their governments. The direct link between these advisers and G20 leaders can drive cooperation and secure swift agreement when a meeting looms. As such an adviser to U.S. President Obama, I witnessed that directly.

G20 leaders—whose nations account for more than 80% of the world economy—have met annually since the global financial crisis of 2008. Their actions in response to that crisis—enacting coordinated budget stimulus, easing monetary policy, and providing emergency funding for countries in trouble—were credited with stabilizing the global financial system and pulling the world back from a depression. Since then, G20 agreements have not been as dramatic or sweeping. However, political push from G20 leaders has been important to resolve differences on multiple global issues, from trade, to cybersecurity, to health (during the Ebola outbreak in 2014), to climate. Indeed, ahead of the 2015 Paris Agreement, these leaders signed key provisions that underpinned successful consensus for strengthening global response to climate change. Faced with a clear global crisis as we are today, the G20 network is there to be activated.

As of now, the next G20 discussion is scheduled for November in Saudi Arabia. The world cannot wait that long. G20 leaders should act on five key issues immediately. These include deeper scientific and medical cooperation across borders to ensure that emerging disease solutions are rapidly shared and scaled. Also key is financing for vaccine and drug development and distribution. This is vital and costs little (about $9.4 billion) relative to the huge budget outlays already being committed to in national economic rescue plans.

The G20 must also support emergency and longer-term funding through international channels for poorer countries with limited resources to respond to COVID-19. This can only happen at sufficient scale if governments of the major countries agree. Most importantly, G20 leaders should push ahead with further economic and financial measures to combat the sharp contraction in the global economy that is now occurring and financially support an eventual economic recovery and return-to-work strategy.

And to prepare for the next pandemic, as we collectively failed to do for COVID-19 (despite warnings from Ebola), nations will need to improve national and global health systems and create incentives so that drug and vaccine markets work in new ways.

Enormous uncertainty about the path of this new coronavirus—and thus of the global economy—complicates policy-making. But global leaders must rise to the occasion. Hoping that this crisis can be solved for the long-term by national governments acting alone is a dangerous illusion.

–Caroline Atkinson

10.1126/science.abc1025

PHOTO: 2016 ROUSE PHOTOGRAPHY GROUP LLC

ScienceTranslationalMedicine.org

PUT HUMAN HEALTH AT THE HEART OF YOUR RESEARCH

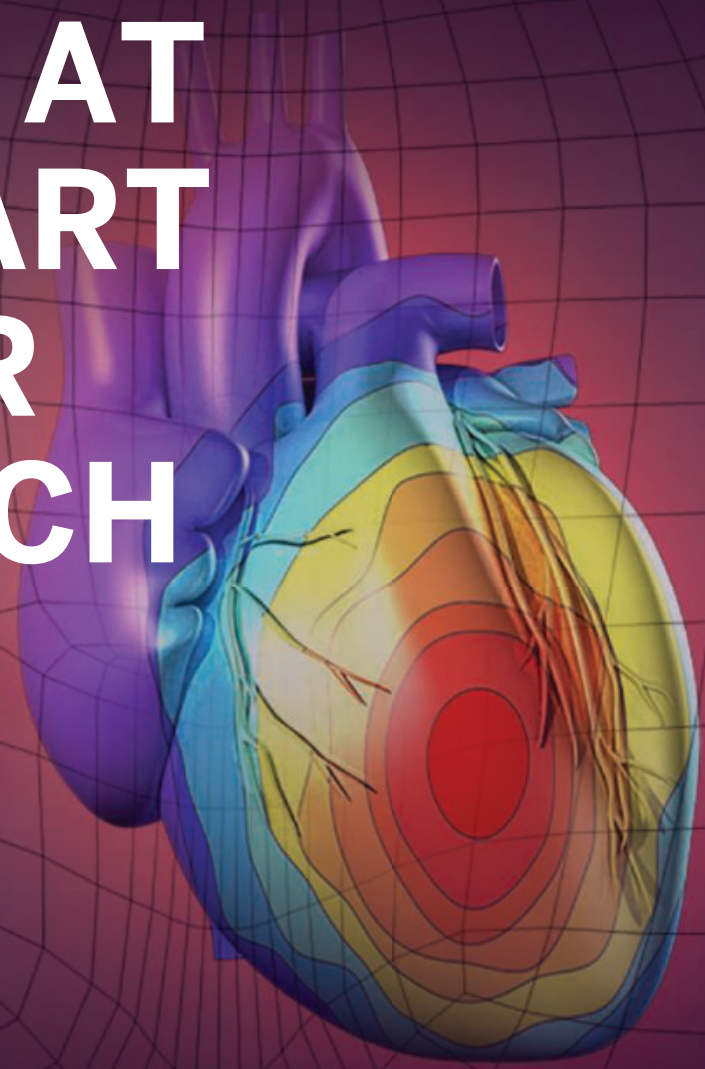

Submit your research:
cts.ScienceMag.org

Science Translational Medicine
AAAS

Twitter: @ScienceTM
Facebook: @ScienceTranslationalMedicine

EDITORIAL

Arab women in science

It's a common trope that Arab women lack equality of opportunity and freedom to engage with the world. The received wisdom is that they are prevented from pursuing an education and a career by religious and/or cultural restrictions. But the truth is more nuanced. Religion and culture are not the strongest determinants of Arab nations' approaches to women's education—systems and resources are. Choosing to see religion or ethnicity over economics and prosperity is both careless and damaging.

There is no religious bar to education for women in my faith, Islam. Indeed, according to religious doctrine, the acquisition of knowledge is binding on all Muslims, regardless of gender. A peppering of female role models, stretching back to the earliest days of Islam, supports this assertion and gives women today a pedigree to be proud of. For example, in 859 CE, Fatima al-Fihri founded the University of al-Qarawiyyin in Morocco, today the oldest continuously operating university in the world. Of course, highlighting this heritage of education must not disguise the cultural impact of patriarchy in some societies that are predominantly Muslim, but it is a way to put that in its proper place—that is, patriarchy is neither unique to the Arab world nor intrinsic to its predominant religious tradition. Arab women have more opportunities to pursue an education and career in Malaysia, Qatar, Kuwait, and Bahrain but fare much worse in Afghanistan, Yemen, Sudan, and Chad. Why? The differences have little to do with a common religion and more to do with economic development and national prosperity.

For Jordan, there is an interesting story to be found in the middle of those extremes. In a 2019 report by the Organization for Economic Cooperation and Development, Jordan was one of three countries where women felt more comfortable with mathematics than men. The reality of Jordan's university output is also surprising. According to the most recent data available (2016), almost half (47%) of undergraduates in science, technology, engineering, and mathematics (STEM) fields were women. In the same year, 56% of M.Sc. degrees and 61% of Ph.D. degrees in STEM fields were awarded to women. Unfortunately, many of these women graduates now face an environment that provides a strong university education but little opportunity to forge a career path close to home.

The challenge is not persuading Arab societies, and the families that define them, to open STEM education to their daughters. The issues arise further downstream. Jordan's pipeline of scientific female talent flows most strongly at its beginning. Like many other nations, research-strong or not, the cracks begin appearing quickly as this talent flows through. Today, just 19% of Ph.D. researchers in Jordan are women.

This is partly because the deep social cohesion within Arab societies places a greater onus on women to juggle their careers while playing an integral role in family development. This challenge is not specific to Arab women but to most women in science. We, in Jordan, must ensure that opportunities are available closer to home for women scientists to flourish. Jordan spends only 0.3% of its gross domestic product on research and development, which translates into a failure to create meaningful career pathways for women—or anyone—with a STEM education. This has left Jordan as a consumer, rather than a producer, of new knowledge.

> "Arab women in science are educated and ambitious."

Jordan cannot create opportunities without the honest engagement of global actors. Research-strong nations are well-placed to leverage our research-weak systems and to profit from talent mobility. For Arab nations, like Jordan, the result is a drain of STEM talent, including women. This situation is not going to change overnight. If we truly want to help Arab women scientists to thrive, then both Arab governments and the global science community must invest in improving career prospects in Arab countries.

The global science community needs to be mindful of the real challenges facing Arab women in science—those that are universal to women in science and those that are distinctly related to an absent science infrastructure—and not to be sidelined by the tropes that veil the truth. Arab women in science are educated and ambitious. Let's give them opportunities at home so that they can help build a better future for all.

–Sumaya bint El Hassan

PHOTO: JUBEHA STUDIOS

Sumaya bint El Hassan
Her Royal Highness (HRH) Princess Sumaya bint El Hassan is president of the Royal Scientific Society in Amman, Jordan. HRH is the founder of the Reticular Foundry, which provides research opportunities to emerging scholars in Jordan. president.office@rss.jo

10.1126/science.abc0631

> “It will be a few billion dollars we’ll waste. It is worth it.”
>
> **Billionaire Bill Gates,** on *The Daily Show*, about his foundation’s plan to build seven factories to make leading COVID-19 vaccine candidates, then abandon any factory whose vaccine proves ineffective.

IN BRIEF

Edited by **Jeffrey Brainard**

DISPATCHES FROM THE PANDEMIC

Study probes antibody prevalence

IMMUNOLOGY | To understand how many people have been infected with the new coronavirus, the World Health Organization expects to launch this month a coordinated study to test blood samples for the presence of antibodies to the microbe. The program, Solidarity II, will involve more than half a dozen countries. Knowing the true number of cases, including mild ones, will help pin down the prevalence and mortality rates of COVID-19 in different age groups, which could help policymakers decide how long school closures and other shutdowns should last. Compared with assays that directly detect the COVID-19 virus, antibody tests can give a better indication of the virus’ true spread because they show past infections that left people with antibodies that might protect against future infection. Initial results from Solidarity II could be available within a few months. Smaller antibody surveys launched last week by groups in California, Germany, and elsewhere could yield preliminary results even sooner.

◀ Tiger tests positive for virus

ANIMAL SCIENCE | Nadia, a 4-year-old Malayan tiger (left) at the Bronx Zoo, has tested positive for the COVID-19 virus, the U.S. Department of Agriculture (USDA) announced this week. The report is the first case of a tiger being infected by the virus, and the first known infection of any animal in the United States. Several other lions and tigers at the zoo showed symptoms of respiratory illness, but none was tested. The big cats may have been exposed to a zoo employee infected with the virus. “At this time, there is no evidence to suggest that any animals, including pets or livestock, can spread COVID-19 infection to people,” USDA reported.

Coronavirus studies fell off

PUBLISHING | The number of published research articles about the COVID-19 virus has exploded. During outbreaks of two other diseases caused by human coronaviruses—severe acute respiratory syndrome starting in 2002 and Middle East respiratory syndrome in 2012—relevant articles also rose, but they dwindled quickly afterward, according to a preprint study posted in March by researchers at Ben-Gurion University of the Negev. Less than 0.5% of all studies in virology published over the past 20 years focused on coronaviruses, compared with 8.1% on HIV, they also noted. A separate preprint study by a team at the University of Southampton found a similar rise and abrupt fall in funding for coronavirus research.

Virus-hunting project extended

ZOONOTIC DISEASE | After being criticized for winding down a program designed to provide early warning of pathogens that have jumped from animals to humans, such

PHOTO: © WCS

as the new coronavirus, the U.S. government last week gave the effort a 6-month stay of execution. The PREDICT Project, an alliance of research institutions led by the University of California, Davis, will continue to help labs in Africa, Asia, and the Middle East test people for the COVID-19 virus and investigate what animal species it came from. The Agency for International Development had funded the program for 10 years before deciding in 2019 to renew its contract only through March, saying other programs would effectively continue its work. But some public health experts say the program remains needed to confront a growing risk of animal-to-human transmission of disease.

U.N. postpones climate talks

POLICY | Citing the COVID-19 pandemic, the United Nations last week delayed a key annual climate summit, scheduled for November in Glasgow, U.K., until next year. The talks were to be the most high-profile effort in climate diplomacy since 2015, with countries expected to strengthen their pledges to cut carbon emissions. The pandemic would have made it difficult to hold the talks as planned, the United Nations and the U.K. government said; the planned conference venue, for example, is being used as a field hospital. The delay will allow countries to gauge the climate implications of economic stimulus measures taken to counteract the pandemic's effects.

FEATURED INTERVIEW

What it takes to track cases

Many governments and news organizations are closely following an online dashboard from Johns Hopkins University that provides regular updates on the coronavirus pandemic's grimly rising toll. The COVID-19 Coronavirus Global Cases tracker was created by civil and systems engineering professor Lauren Gardner and her graduate student Ensheng Dong. Gardner previously created spatial models of measles and Zika virus epidemics.

"We've been doing this full on since January. We dropped everything else in the lab," Gardner says. "It's probably going to be this way for at least another couple months. And we'll track the outbreak for, I'm sure, a year. It'll keep going and bouncing around all over the world. ... It's exhausting. I think all public health people working in this space feel the same."

A full interview is available at https://scim.ag/LGardner.

SCIENCEMAG.ORG/TAGS/CORONAVIRUS
Read *Science*'s online coverage of the pandemic.

PHOTO: JURGEN FREUND/MINDEN PICTURES

GLOBAL WARMING

Great Barrier Reef bleached again

A 2017 image shows the impact of a bleaching event.

Recent surveys reveal the Great Barrier Reef has suffered the second most severe coral bleaching ever recorded there, driven by record ocean temperatures in February. It's the third "mass bleaching event" to hit the reef in just 5 years, say scientists at James Cook University. The overall severity of bleaching in 2016 was worse, but the damage done in recent summer months covered a wider area, including relatively cooler areas to the south, they report this week in a news release. Observers conducted aerial surveys of 1036 reef locations in March. They found that 25% were severely affected, with more than 60% of each location's corals bleached; an additional third of sites had more modest levels of bleaching. The scientists will next monitor how many of the bleached corals die this year. In 2016, more than half the severely bleached coral in the reef's northern section died.

Science adviser adds NSF hat

LEADERSHIP | Kelvin Droegemeier took on a second job last week, adding acting director of the U.S. National Science Foundation (NSF) to his duties as head of the White House Office of Science and Technology Policy. The NSF post is vacant because France Córdova completed her 6-year term on 31 March and the U.S. Senate has yet to confirm Sethuraman Panchanathan, who in December 2019 was nominated to become the agency's 15th director.

NIH dropping more reviewers

RESEARCH INTEGRITY | More than 120 scientists who have failed to disclose foreign ties or breached confidentiality have been removed as peer reviewers by the U.S. National Institutes of Health (NIH). A new report by the Office of Inspector General at NIH's parent body, the Department of Health and Human Services, notes that 77 reviewers found to have breached confidentiality have been put on a "Do Not Use" list as of November 2019. NIH removed another 47 after it found "potentially substantiated" evidence that they had failed to disclose affiliations with foreign institutions. And in December 2019, NIH said 55 scientists facing allegations of sexual harassment had been given the boot. The report notes that two-thirds of the scientists who failed to disclose foreign ties remain as reviewers and says NIH "can do more" to guard against "undue foreign influences." In all, the agency enlists about 27,000 reviewers annually.

Marine microbes given new DNA

MARINE BIOLOGY | Biologists took a big step this week toward understanding some of the ocean's most important ecosystem engineers and harnessing them to benefit humans. An international consortium has come up with ways to genetically modify 13 marine protists, some of which help produce the oxygen we breathe and become the food that fuels the ocean's food web. The team devised ways to grow these understudied species of plankton in the lab and insert foreign DNA, employing enzymes not usually used in genetic engineering. The new techniques, reported in this week's issue of *Nature Methods*, may enable biotechnologists to track down genes that can help make antibiotics or reveal the evolutionary history of protists.

Door-to-door campaigns against polio, such as this one in Kenya in 2018, could help spread COVID-19.

PHOTO: YASUYOSHI CHIBA/AFP/GETTY IMAGES

GLOBAL HEALTH

Pandemic brings mass vaccinations to a halt

Polio, measles, other diseases set to surge as COVID-19 forces suspension of campaigns

By **Leslie Roberts**

"A devil's choice." That's how Seth Berkley, head of GAVI, the Vaccine Alliance, describes the dilemma facing global health organizations in the past few weeks. They could either continue to support mass vaccination campaigns in poor countries but risk that they would inadvertently help spread COVID-19—or recommend their suspension, inevitably triggering an upsurge of many other infectious diseases.

In the end, they chose the latter, and mass vaccination campaigns against a host of diseases are now grinding to a halt in many countries. For many children, these campaigns are the only chance to get vaccines. Some 13.5 million have already missed out on vaccinations for polio, measles, human papillomavirus, yellow fever, cholera, and meningitis since the suspensions began, Berkley says. "I tell you those numbers will be much larger than what we see today." The fallout may last long after the pandemic subsides. And in the case of polio, the pause imperils the success of a 3-decade eradication campaign that was already in trouble.

The suspensions began on 24 March, when leaders of the Global Polio Eradication Initiative (GPEI) called on countries to postpone all polio vaccination campaigns until the second half of the year. The huge campaigns—door-to-door efforts that reach 400 million to 450 million annually—are the mainstay of the eradication program. Yet, "We had no choice," says Michel Zaffran of the World Health Organization (WHO), who heads GPEI. The vaccination drives would put both communities and frontline health workers at risk of infection with the coronavirus, he says. But he concedes more children will be paralyzed in countries where polio is still circulating, and the virus will likely spread to countries that are now polio-free.

Science's COVID-19 coverage is supported by the Pulitzer Center.

The polio eradication effort is already reeling from setbacks in Afghanistan and Pakistan, where the wild virus is surging, and in Africa, where outbreaks caused by the live polio vaccine itself are spiraling out of control (*Science*, 3 January, p. 14). "Everyone was uncomfortable" with suspending campaigns, Zaffran says. But in the end, the only real tension among GPEI leaders was whether to call for a firm halt not only to preventive campaigns, but also to the targeted campaigns in response to the vaccine-derived outbreaks in Africa. Ultimately, "The guidance came from a very high level to pause everything," says Rebecca Martin of the U.S. Centers for Disease Control and Prevention (CDC). (GPEI's Polio Oversight Board is composed of the heads of all the partner agencies, including WHO Director-General Tedros Adhanom Ghebreyesus.) The program will reassess the decision every 2 weeks.

On 26 March, WHO's Strategic Advisory Group of Experts on Immunization (SAGE) issued a broader call, recommending that countries stop mass vaccination campaigns against all vaccine-preventable diseases. "Any mass campaigns would go against the idea of social distancing," says Alejandro Cravioto of the National Autonomous University of Mexico's Faculty of Medicine, who chairs SAGE.

Twenty-three countries have already suspended their measles campaigns, and as a result, 78 million children will miss out on the vaccine, says Robb Linkins, a measles expert in CDC's Global Immunization Division. Sixteen other countries are still deciding. Linkins foresees "tragic" consequences. In poor countries, the virus can kill 3% to 6% of those it infects, WHO says, with malnourished children especially at risk. Measles infected an estimated 10 million and killed

140,000 in 2018, the last year for which numbers are complete. And because measles is incredibly contagious, case numbers could quickly surge following the suspensions.

Unlike the polio initiative, SAGE stopped short of recommending that countries halt campaigns to quell ongoing outbreaks, but it said they should carefully weigh the risk of an immediate response against that of a delayed one. For now, measles campaigns are continuing in the Democratic Republic of the Congo, where the world's biggest outbreak has so far killed an estimated 6500 children—far more than the recent Ebola outbreak in that country—and sickened more than 340,000.

WHO, GAVI, and other health organizations stress that routine immunization of individual children at clinics must continue as much as possible during the pandemic. But health systems in many countries were already stretched thin, and protective gear is often lacking. Berkley fears severe disruptions of routine immunization if health workers are diverted to COVID-19 or become sick or die, or if parents are afraid to bring their children to a clinic. Vaccines may run out as well. Some countries are already experiencing shortages as flights are grounded and borders close, Berkley says.

Other essential health services will also be disrupted, says Augustin Augier, executive director of the Alliance for International Medical Action. Every year, ALIMA trains about 500,000 African mothers to diagnose acute, potentially fatal malnutrition in their children; those programs have been suspended. The knock-on consequences of the pandemic "will be much stronger and more lethal for the world's most vulnerable populations," Augier says.

Across all these programs, the goal is to come back hard and fast to regain lost ground once the pandemic is over. In the meantime, WHO says, countries should continue surveillance for vaccine-preventable diseases to figure out where pathogens are circulating and which children are most at risk. But that, too, is a challenge amid the fear and disruption from COVID-19.

Berkley sees some hope in the experience in West Africa after the 2014–15 Ebola outbreak. "There was an unprecedented flow of finance and good will," he says. "We did campaigns once Ebola was over and strengthened routine immunization. We not only recovered coverage levels, but exceeded them." But that epidemic was largely confined to three countries with a combined population of fewer than 25 million people. This time, the entire world is affected. ■

Leslie Roberts is a science writer in Washington, D.C.

COVID-19

Tested by HIV and TB, South Africa confronts new pandemic

Infrastructure and tactics developed for existing epidemics could aid the coronavirus fight

By **Linda Nordling**

As the COVID-19 pandemic sweeps into South Africa, the decades the country has spent fighting the world's worst combined epidemic of tuberculosis (TB) and HIV could give it an advantage. But those infections could also worsen the pandemic's impact.

South Africa had 1686 confirmed COVID-19 infections at press time, the highest number on the continent—and that is almost certainly an undercount. At the same time, one in five people aged 15 to 49 is HIV positive and two to three people die every hour from TB. South African scientists hope the resources and health networks built to fight those diseases will help them battle the new pandemic. "The COVID-19 response draws on the same skills as TB and HIV," says Gavin Churchyard, director of the Aurum Institute, a Johannesburg-based research and health care nonprofit.

> **"Just having this technical capacity does not guarantee that we will contain this new epidemic."**
> **Gavin Churchyard**, Aurum Institute

Infection control measures are similar for COVID-19 and TB, he points out, because both seem to spread through exhaled droplets. That means health care workers are familiar with the protective gear they need to treat suspected COVID-19 patients. And South Africa's government is repurposing the aggressive "find, treat, and prevent" strategy that's key to its HIV response, Churchyard says. It began to send mobile COVID-19 testing clinics into densely populated areas this week to identify cases and contacts.

His own institute has "massively slowed down" its regular research on TB and HIV and mobilized its 3000-strong staff to help national COVID-19 testing and contact tracking efforts. Aurum's researchers also plan to study treatments and vaccines and will monitor how well South Africa's COVID-19 response is working, Churchyard says.

The African Health Research Institute (AHRI) in Durban, South Africa, which normally focuses on HIV and TB, has redeployed its entire infrastructure and staff to fight the pandemic. It has made its mobile clinics, community workers, and labs available for coronavirus testing, and its researchers will help run a trial to see whether the malaria drug chloroquine can protect health care workers (see story, p. 118). Funders—which include the Wellcome Trust and the Howard Hughes Medical Institute—have been "astonishingly flexible," says AHRI Director Willem Hanekom.

COVID-19 is just beginning to take a toll across Africa. Many countries face the question of whether existing illnesses will worsen the impacts. In South Africa, two national surveillance sites, one run by AHRI, will screen 40,000 households in areas with high rates of TB and HIV. Researchers hope to learn whether HIV-positive people have impaired immunity to the new virus, and how lung damage from TB might influence disease outcome.

A Cape Town, South Africa, laboratory run by the Desmond Tutu HIV Foundation is also joining the effort. The lab studies how TB is transmitted by putting patients in phone booth–size rooms and sampling their exhaled air for microorganisms. It plans to see whether the same technique can detect the new coronavirus, which could yield a way to diagnose asymptomatic COVID-19 cases, says foundation leader Robin Wood.

Churchyard thinks South Africa is in for a rough ride. Despite the millions spent fighting TB and HIV, the toll from both remains among the world's highest. "Just having this technical capacity does not guarantee that we will contain this new epidemic," he says.

For him, the disease has already hit home. Last week, Aurum senior researcher Gita Ramjee became one of the first people in South Africa to die from COVID-19. That was a heavy blow, Churchyard says, but it galvanized him and his colleagues. "Gita was a fighter. She would want us to be out there doing what we can." ■

Linda Nordling is a journalist in Cape Town, South Africa.

Doctors see patients at a New Delhi hospital on 18 March. India recommends hydroxychloroquine for health care workers at risk of COVID-19.

PHOTO: SANCHIT KHANNA/*HINDUSTAN TIMES*/GETTY IMAGES

COVID-19

Can prophylactic drugs keep fragile health systems running?

A raft of trials will test whether chloroquine and other treatments can protect health workers from COVID-19

QQ group:1067583220

By **Kai Kupferschmidt**

When malaria researcher Nicholas White saw coronavirus infections picking up around the world 2 months ago, he immediately thought of the impact they could have on poorer countries. "In fragile health care systems, if you start knocking out a few nurses and doctors, the whole thing can collapse," says White, who is based at Mahidol University in Bangkok. "So we realized that the priority would be to protect them."

White and his colleagues at the Mahidol Oxford Tropical Medicine Research Unit wondered whether widely available drugs could help. They have designed a trial in which 40,000 doctors and nurses in Asia, Africa, and Europe will prophylactically receive chloroquine or hydroxychloroquine, two old drugs against malaria. White hopes the trial will start this month, but its launch has been "incredibly difficult because of bureaucratic processes," he says.

The international study is one of several in preparation or underway that seek to use drugs for what is called pre-exposure prophylaxis (PrEP), a strategy already widely used against HIV. The Bill & Melinda Gates Foundation is funding plans for another huge study that will test the same two drugs in Africa, North America, and Europe. Separate studies of the same drugs are planned or underway in the United States, Australia, Canada, Spain, and Mexico. Researchers are also considering other potential preventives, including nitazoxanide, a drug used to treat parasitic infections, and the antibody-laden serum from people who have recovered from an infection.

"If there was a drug that could prevent infections and that health care workers could take, that would be an enormous public health benefit," says Jeremy Farrar, head of the Wellcome Trust, which is funding White's effort.

PrEP studies of the malaria drugs could also be the best way to settle the heated debate—inflamed by U.S. President Donald Trump's advocacy—over whether they are a promising treatment for COVID-19, says virologist Matthew Frieman of the University of Maryland School of Medicine. The weak and equivocal studies so far were mainly done in seriously ill patients. "To show an effect you really have to treat early," Frieman says. "I don't know any drug that works better late in infection." Giving a drug before exposure is as early as it gets.

White adds that chloroquine and hydroxychloroquine are good choices to test because they are widely available—a major consideration given the huge number of people who might be eligible for any drug that proves its worth. "The attraction … is that they are potentially readily deployable and we know an awful lot about them."

In White's proposed trial, health care workers in Asia will be randomized to take chloroquine or a placebo for 3 months, while hydroxychloroquine will be used in Africa and Europe. Participants have to take their temperature twice a day and report it, along with any symptoms, through an app or a website. The researchers will compare the number of symptomatic and asymptomatic infections in both groups, as well as the severity and duration of illness in those who become infected.

Meanwhile, a trial of a related approach called postexposure prophylaxis (PEP) started in Barcelona, Spain, in mid-March. The idea behind that study, born before Spain's COVID-19 epidemic exploded, is that a short course of a drug might prevent disease or lessen its impact in health care workers, nursing home residents, and household contacts of COVID-19 patients who have already been exposed to the virus. "We said, we need something stronger than nonpharmacological interventions like isolation and quarantine," says Oriol Mitjà of the Germans Trias I Pujol University Hospital, who leads the study.

In the Spanish trial, people with symptoms who test positive for COVID-19 are treated with the HIV combination drug darunavir/cobicistat plus hydroxychloroquine. Anyone known to have spent more than 15 minutes with them in the previous 5 days is treated with hydroxychloroquine for 4 days. Patients in a control group and their contacts receive no drug—there was no time to prepare an appropriate placebo, Mitjà says.

The researchers plan to compare how many new symptomatic infections occur in the two groups after 14 days. More than

1000 contacts have been included already; a first result from that subset should be available around 15 April, Mitjà says. Similar studies are underway in Minnesota, Washington, and New York.

Experience with HIV has shown that PrEP and PEP can work to reduce infections. But before large-scale studies in HIV began, scientists had an "amazing amount of data" from a monkey model and epidemiology studies suggesting the strategies would work, says Steven Deeks, an HIV researcher at the University of California, San Francisco (UCSF). "I'm not sure any of that applies to what's happening now."

Potential side effects of chloroquine and hydroxychloroquine, including heart arrhythmia, are another concern. "The risks that might be acceptable in someone with disease may be much less acceptable when you are treating someone who doesn't have it," says Annie Luetkemeyer, an infectious disease physician at UCSF. "And you're very unlikely to be monitoring them in the same way."

Some countries aren't waiting for the new trials. India, for instance, has already recommended hydroxychloroquine for health care workers caring for suspected or confirmed COVID-19 cases as well as patients' household contacts. Many scientists say such measures are premature. "The idea that it is better than nothing is not true," White says. "It could be worse than nothing."

That's not just because of the potential side effects. People who think they are protected may also become less cautious and run a greater risk of infection. And broad use of the drugs will make them harder to obtain for other conditions. In addition to curing malaria, chloroquine and hydroxychloroquine are mainstays for patients with lupus and rheumatoid arthritis, Luetkemeyer says. "We better be really sure that these drugs are working before we start impacting that drug supply."

Even if chloroquine works, it is unlikely to confer 100% protection—and a low level of protection may not make the risk of side effects worthwhile. "If you were a health care worker and I said, 'Here's a medicine which you have to take every day and it reduces your risk of getting COVID-19 by 20%,' would you take it?" White asks. Below that, people probably wouldn't bother, he says.

White hopes for a quick answer, but he is still navigating the "myriad rules, regulations, and sequential hurdles that govern the conduct of clinical trials." No one is acting with ill intent, he adds, but he thinks the emergency warrants faster action. "Is it really ethical to take 3 weeks to review an application for a medicine that has been available for 70 years?" ■

COVID-19

NAS letter suggests 'normal breathing' can expel coronavirus

But some experts are skeptical that small respiratory particles transmit infectious virus

By **Robert F. Service**

On 31 March, University of California, San Diego, atmospheric chemist Kimberly Prather set off an online debate by saying people should stop surfing during the coronavirus outbreak. Her reasoning: Viruses can travel long distances if carried by wind. "I ignited a bomb," Prather says, as commenters pushed back, pointing to official assurances that the novel coronavirus is transmitted only short distances in respiratory droplets from a sneeze or cough.

The surfing controversy just adds to the fog surrounding how the novel coronavirus is transmitted. When people cough and sneeze, the droplets they expel fall to the ground within 1 or 2 meters. The fallen droplets deposit virus on surfaces, where people can pick it up and infect themselves by touching their faces. But if the coronavirus can be suspended in an ultrafine mist of particles smaller than 5 micrometers—known as aerosols—people could potentially spread infection when they exhale. And aerosol particles are so light that they can float like dust for hours in air.

8 meters
The distance a single sneeze can propel aerosol particles

The National Academy of Sciences (NAS) weighed in last week, suggesting it's likely the novel coronavirus can spread this way. A 1 April letter to Kelvin Droegemeier, head of the White House Office of Science and Technology Policy, noted that current studies are inconclusive. But, it added, "The results of available studies are consistent with aerosolization of virus from normal breathing."

The debate was kicked off by a finding published 17 March in *The New England Journal of Medicine* that the new coronavirus, SARS-CoV-2, can float in mechanically generated aerosols for up to 3 hours and remain infectious. People readily shed such particles, and an analysis published 26 March in *JAMA* reported that a single sneeze can propel them up to 8 meters. "From the physics it's very clear the emissions go beyond [2 meters]," says the paper's author, Lydia Bourouiba, a physicist at the Massachusetts Institute of Technology.

The NAS letter also pointed to a preprint posted on medRxiv on 26 March by Joshua Santarpia and colleagues at the University of Nebraska Medical Center that found widespread evidence of viral RNA in rooms of patients being treated for COVID-19. Viral RNA turned up on hard-to-reach surfaces and in air samples more than 2 meters from the patients. Another preprint posted 10 March on bioRxiv found the coronavirus can be resuspended in the air when health care workers remove their personal protective equipment, clean the floors, and move through infected areas. Considering all the data, "The presence of viral RNA in air droplets and aerosols indicates the possibility of viral transmissions via these routes," the NAS letter concluded.

"This added airborne pathway helps explain why [the virus] is spreading so fast," Prather says.

To others, the question is far from settled. A 27 March scientific brief from the World Health Organization states that aerosol transmission "may be possible in specific circumstances and settings that generate aerosols," such as when severely ill patients are intubated. However, the brief adds, an analysis of more than 75,000 coronavirus cases in China revealed no cases of airborne transmission. As for studies such as Santarpia's, it notes that detection of viral RNA doesn't necessarily mean infectious virus persists.

Meanwhile, some researchers are considering another possible transmission route: feces. According to the Centers for Disease Control and Prevention, no cases of fecal transmission have been documented even though the novel coronavirus has been detected in the feces of some patients. CDC says the risk "is expected to be low based on data from previous outbreaks of related coronaviruses, such as severe acute respiratory syndrome and Middle East respiratory syndrome." ■

With reporting by Jocelyn Kaiser.

SCIENCE FUNDING

European Union gets in the venture capital game

Flush with cash, new EU innovation agency buys shares in disruptive technology startups

By **Nicholas Wallace**

The EpiShuttle, a hospital gurney enclosed in a bubble of plastic and studded with sealed access ports, keeps contagious patients isolated while on the move—eliminating the need to disinfect ambulances and helicopters after each run. EpiGuard, the Norwegian startup behind it, is racing to satisfy the hundreds of orders that have been placed amid the coronavirus pandemic, says founder Fridtjof Heyerdahl, a doctor who began to develop the equipment after the 2014 Ebola epidemic in West Africa.

The company owes its growth to the European Innovation Council (EIC), a little-known but ambitious EU agency that aims to do for startups and spinoffs what the grantmaking European Research Council does for basic research. Without EIC support, "our organization would have been so tiny, we wouldn't have been able to ramp up," Heyerdahl says. Last year, EpiGuard won a €2.5 million grant from EIC. Now, EIC is offering the company a more radical form of government support. On 13 March, Heyerdahl was invited to apply for an EIC equity investment, which could give EpiGuard up to €15 million—and the European Union a stake in the company.

A new European agency has funded Norwegian startup EpiGuard, which makes gurneys that isolate patients.

EpiGuard was one of the beneficiaries of EIC's 3-year pilot program. But in January 2021, EIC is set to become a major part of Horizon Europe, the European Union's proposed €94 billion R&D program for 2021–27. The European Commission wants €10.5 billion of that to go to EIC; national governments will settle on the final numbers in the coming months.

Frustrated by Europe's lack of home-grown tech giants, Commission officials hope EIC will help small tech firms grow in Europe, instead of being lured away to Silicon Valley. "The aim here is to close the big gap that exists between Europe and the United States," says Mark Ferguson, Ireland's chief scientist and EIC board chair. But one challenge will be backing risky but promising startups without becoming "the financiers of last resort for all the failing companies that aren't going to do very well," says Christopher Tucci, a professor of technology management at the Swiss Federal Institute of Technology, Lausanne, who advised the Commission while it drafted Horizon Europe.

A lack of venture capital (VC) has slowed tech growth in Europe. According to the Commission, in 2016 venture capitalists invested just €6.5 billion in European startups, compared with €39.4 billion in the United States. VC funds in Europe are also barely one-third the size of U.S. funds. That limits their ability to help small companies scale up past the so-called "valley of death," says EIC board member Kerstin Bock, whose Berlin-based consultancy, Openers, gives advice to startups. "When it comes to the growth stage, scaling companies, there might not be that many [investors] that are risk takers," she says.

EIC is meant to remedy the problem through a combination of grants, high-risk equity investments, and one-off cash prizes for competitions. (The EIC pilot is now offering €10 million for the winning design of a cheap method to launch small satellites into orbit, and €5 million for cheap batteries for electric vehicles.) It offers two main award types: the Pathfinder, which provides grants up to €4 million for early-stage tech development, and the Accelerator, which offers grants up to €2.5 million and equity investments of up to €15 million for companies trying to scale.

It is also forgoing a standard requirement of most EU research grants: that applicants form consortia, which forces them to share findings with other participants. Danaë Delbeke, CEO of Belgian firm Indigo, was pleased that she could apply for EIC money as a small company acting alone, in stealth mode. "We are in a very, very competitive field," says Delbeke, who spun out Indigo from photonics research at Ghent University and the Interuniversity Microelectronics Centre. The firm won an Accelerator grant to develop a subcutaneous sensor to simultaneously monitor glucose, ketones, and lactase in diabetic patients.

Bock says EIC will help companies that need more time and money to get market ready, such as medical device and biotechnology companies, which have to satisfy complex regulations and certifications. It will also target firms developing "disruptive" technologies, and is hiring program managers who can identify them—experts in fields like artificial intelligence, clean energy, and nanometrology.

Georg Licht, an economist at the Leibniz Centre for European Economic Research, says picking disruptive technologies early isn't easy. Once it's clear a technology is disruptive, it's already too late for public investment, because "if they can be sure, then it's clear also to the private sector."

EIC's most radical idea may be equity investment, something the Commission, which runs EIC, has never done before (although since 2014 it has acted as guarantor for some investments made by the independent European Investment Bank). EIC in-

PHOTO: EPIGUARD

vestments aren't meant to make money for the European Union, and for legal reasons the shares will be owned by a separate investment vehicle. Any returns will go there first, but a Commission spokesperson says the long-term plan is for the money to come back to the EU budget. If some EIC bets pay off and it finds the next Google, the profits could help reduce the dues that EU member states must pay.

EIC guidelines say the goal is "investment impact," not maximizing returns, and Tucci says it won't be a sign of failure if EIC loses money on some turkeys. "There'll be lots of failures, there's going to be moderate successes, and if there's one really big success, that's going to create lots of jobs," Tucci says. Another goal is to stimulate the European VC market, Ferguson says. EIC won't buy shares unless there are co-investors; if none can be found, EIC will offer a loan, to be turned into shares when private capital shows up.

One company with pending EIC equity investment is Hiber, a Dutch satellite startup. It aims to provide cheap, low-bandwidth internet access to low-power sensors used by agriculture and industry in remote places. The sensors could, for example, monitor moisture in beehives or fields, broadcasting small data packets every hour or so.

Coen Janssen, Hiber's CEO, says EIC financing is a "perfect fit," because his company needs to invest a huge amount of capital in satellites and ground stations before it can profit from subscriptions to its service. "Satellites are not cheap," he says. "It's a risky game that we're playing." To launch its first two satellites, Janssen says Hiber raised €15 million: €10 million from the private sector, plus grants of €3 million from the European Space Agency and €2 million from the Dutch government. EIC will invest up to €15 million in Hiber alongside a grant of up to €2.5 million, but the exact amount isn't yet public.

Not everyone is convinced that EIC's experiment will work. "There is a history with such organizations that they tend to lose their policy role and drift into the game of making money," says Charles Edquist, a specialist in innovation policy at Lund University. "That's competing with private investments." And Tucci cautions that critics may portray each failed investment as a policy failure.

If EIC succeeds, it may not be around forever, Ferguson says. He wants to build a European VC market for new technologies, not to imitate one with public money. "In my dream," Ferguson says, "we will put ourselves out of business." ■

Nicholas Wallace is a journalist in Brussels.

GRAPHIC: V. ALTOUNIAN/*SCIENCE*

U.S. POLICY

United States aims to curb vaccination injury payouts

Proposal would make it harder to get compensated for shoulder injuries after misplaced injections

By **Meredith Wadman**

The Trump administration is quietly considering reversing a rule that made it much easier for people who sustain serious shoulder injuries from improperly administered vaccines to win cash compensation from the federal government. Some physicians support the proposal, but vaccine injury lawyers and the vaccine injured are pushing back, saying the administration is ignoring science that has established a causal link between misplaced injections and shoulder inflammation. Both sides say that if their position does not prevail, more people could resist receiving life-saving vaccines—including vaccines that might one day beat back the novel coronavirus pandemic.

In a draft proposal it circulated in February to outside advisers, the Department of Health and Human Services (HHS) argues there is "nearly uniform agreement in the scientific community" that shoulder injuries result from the improper administration of vaccines and not from the vaccines themselves. HHS also says the injury claims, which have surged since compensation rules were eased in 2017, could squeeze the finances of the $4 billion National Vaccine Injury Compensation Program, created by Congress in 1986 to protect vaccine-makers from lawsuits.

Under the program, which is funded by a tax on many vaccines, any person who believes they have been injured by any vaccine on a government-approved list can file a petition with the U.S. Court of Federal Claims. HHS medical experts then recommend whether the government should pay the claim or fight it. Under the change, made by former President Barack Obama's administration, petitioners no longer have to prove an injection caused their shoulder injury. They simply need to document a previously healthy shoulder, the administration of a vaccine in that arm, and the onset within 48 hours of shoulder pain that persisted for at least 6 months. (Petitioners are also not required to prove causation for a list of other vaccine-related injuries, such as life-threatening allergic reactions.)

After the change, claims for shoulder injury shot up; they accounted for 54% of 2520 vaccine injury petitions in 2018 and 2019. Shoulder injury payouts averaged $31 million annually in those years.

That surge has alarmed HHS and others, who say it threatens to bog down what is supposed to be a speedy compensation system. To ease the congestion, HHS wants to remove inflamed shoulders from the list of injuries for which petitioners don't have to prove causation. It says such claims should be handled by lawsuits filed in civil courts rather than by the compensation program.

"What you're seeing is a complication that's not related to the vaccine itself," said H. Cody Meissner, chair of HHS's Advisory Commission on Childhood Vaccines (ACCV), at a 6 March meeting that became polarized over the proposal. The real culprit, he and others argue, is not the vaccine, but faulty injection technique (see graphic, left), in which the needle penetrates the shoulder joint rather than the upper arm muscle. Gillian Woollett, senior research scientist with the consultancy Avalere Health, believes the change could motivate vaccine admin-

Best shot

The United States wants to reduce claims for vaccination-related shoulder injuries, which can be avoided with proper technique.

Patient and vaccinator both seated
Lowers risk of aiming from above

Aim for middle of triangle.
Avoiding upper third ensures delicate structures are not touched.

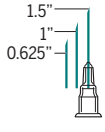

Use appropriate needle length.
Different builds have various thicknesses of subcutaneous fat.

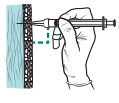

Insert at 90° angle with dartlike motion.
Higher likelihood of reaching muscle depth

Lift arm slightly out to side.
Bursa will slide underneath the acromion for protection.

istrators, including pharmacy chains, to improve training of vaccinators. "This is a critically important program—and people should be administering vaccines properly. You shouldn't have to trade off between the benefit of the vaccine and the worry of misadministration."

Critics of the proposal say it is flawed. HHS "represents the scientific literature in a misleading way," says Uma Srikumaran, a shoulder surgeon at Johns Hopkins University's School of Medicine. Studies show a misplaced needle alone doesn't necessarily cause shoulder injury and that the vaccine material itself is needed to trigger inflammation, he wrote in a recent open letter to HHS Secretary Alex Azar. He noted that physicians regularly inject shoulder joints with other substances, such as the anesthetic lidocaine, without causing an inflammatory reaction.

Some lawyers, meanwhile, reject HHS's suggestion that shoulder injury claims be resolved in civil court. The federal law that established the program was designed to forestall such lawsuits, they observe, and does not exclude injuries associated with administration. And Srikumaran warns that if shoulder cases are moved to civil courts, health care providers will need to buy expensive malpractice insurance to protect against liability. "This could unnecessarily drive up the costs of delivering vaccines and reduce the number of people willing to administer them," he wrote to Azar.

The critics also question whether HHS has been adequately transparent. In the past, ACCV has spent months reviewing changes to the compensation program in public. This time, HHS sent the panel a draft, marked "confidential," 3 weeks before its 6 March meeting and initially asked the panel not to discuss the draft publicly before giving permission. Now, the panel must submit its comments by 21 May, but it won't have another public session until early June. "I have a huge concern about why none of this is being discussed publicly," says Karen Kain, an ACCV member whose daughter died as the result of a different kind of vaccine injury. (HHS will have to submit any final proposal for public comment.)

Both camps worry about how the outcome of the debate will affect public perceptions of vaccination. HHS argues that people opposed to vaccination have used the shoulder payouts to bolster unfounded claims. Speaking for himself and not ACCV, Meissner concurs. "The antivaccine folks say, 'Oh, look how dangerous vaccines are because this fund pays out hundreds of millions of dollars every year,'" he says. Foes of the change, meanwhile, fear it will only give those uncertain about the benefits of vaccines yet another reason to reject them. ■

PLANT DISEASES

Help for a wheat fungal disease comes from a surprising source

Resistance gene found in wild grass originated in a fungus

By **Erik Stokstad**

Wheat scab hits farmers with a double punch. The fungal disease, also known as Fusarium head blight, shrivels grain and can significantly dent harvests of wheat and barley. Worse, the toxins released by the fungus *Fusarium graminearum*, a growing problem in the breadbaskets of Europe, North America, and China, remain in grain intended for food. Above legal limits, they can harm people and animals. Grain from infected plants must be discarded in many countries, although some allow blending with uninfected grain.

Fungicides are no panacea, in part because the pathogen infects during wet weather, when the chemicals wash away. But researchers have now found a protective gene in a wild relative called wheatgrass. Called *Fhb7*, it encodes a toxin-destroying enzyme, the team reports online in *Science* this week. "The gene could have a very large impact in breeding for *Fusarium* resistance in wheat," says James Anderson, a wheat breeder at the University of Minnesota, Twin Cities.

The fungus *Fusarium graminearum* makes toxins that harm wheat kernels.

PHOTO: WANG *ET AL.*/*SCIENCE*

The gene originated in a benign fungus that lives inside wild grasses, then somehow slipped into the wheatgrass genome. Such symbiotic fungi can help their plant hosts defend against a destructive invader. The study authors suggest fungal DNA could yield other potential resistance genes for plants.

The best resistance so far to *F. graminearum* comes from an heirloom variety of Chinese wheat. Breeders have for decades transferred a chromosome segment from it containing a resistance gene, dubbed *Fhb1*, into other cereals. But the gene's identity and mechanism remain disputed and the segment provides only modest protection. About 2 decades ago, geneticist Lingrang Kong, then a postdoc at Purdue University, and colleagues found another source of wheat scab resistance farther afield, in the wheatgrass *Thinopyrum elongatum*.

Over the years, they narrowed down the gene's chromosomal location, and in the new research, Kong, now at Shandong Agricultural University, and many colleagues finished the job. They sequenced the wheatgrass—yielding genetic markers—then made multiple crosses of the plant to home in on candidate genes. By silencing the genes individually, they found one, *Fhb7*, required for resistance. Then, the team showed it codes for an enzyme, glutathione S-transferase, and demonstrated that it degrades several fungal toxins, called trichothecenes, that cause wheat scab symptoms.

"This is a great paper, describing an enormous amount of work," says molecular biologist Gerhard Adam of the University of Natural Resources and Life Sciences, Vienna. The gene, Adam adds, is likely to be broadly effective against many other trichothecenes.

The team had assumed *Fhb7* arose in plants, but they found a 97% match with a gene in *Epichloë aotearoae*, a fungus that protect its grass hosts from pathogens. Bacteria often transfer DNA to plant genomes, but there aren't many examples of fungi doing so. "I thought it was an artifact" initially, says co-author Hongwei Wang of Shandong Agricultural University.

Encouragingly, field tests showed that adding *Fhb7* to wheat had no adverse impacts on grain yield. Kong says the team hopes to release a commercial variety within 1 year, although it's unclear how resistance provided by *Fhb7* compares to that offered by *Fhb1*. A bigger question is whether the new gene will increase the resistance of strains with *Fhb1*. So far, Kong says, they found "only a little improvement."

But the hope is to identify other, similar genes and "stack" them to toughen up wheat and barley, Anderson says. "There's going to be a rush now to find other genes in the genome of wheat and related species that may do the same thing." ■

eppendorf & Science

PRIZE FOR NEURO BIOLOGY

2019 Winner
Lauren Orefice, Ph.D.

For research on the causes and potential therapies for autism spectrum disorders

Now It's Your Turn!

Application Deadline
June 15, 2020

Eppendorf & Science Prize for Neurobiology
The annual Eppendorf & Science Prize for Neurobiology is an annual international prize which honors young scientists for their outstanding contributions to neurobiological research based on methods of molecular and cell biology. The winner and finalists are selected by a committee of independent scientists, chaired by *Science's* Senior Editor, Dr. Peter Stern. If you are 35 years of age or younger and doing great research, now is the time to apply for this prize.

As the Grand Prize Winner, you could be next to receive
> Prize money of US$25,000
> Publication of your work in *Science*
> Full support to attend the Prize Ceremony held in conjunction with the Annual Meeting of the Society for Neuroscience in the USA
> 10-year AAAS membership and online subscription to *Science*
> Complimentary products worth US$1,000 from Eppendorf
> An invitation to visit Eppendorf in Hamburg, Germany

It's easy to apply! Write a 1,000-word essay and tell the world about your work. Learn more at:

www.eppendorf.com/prize

eppendorf Science AAAS

AAAS® and Science® are registered trademarks of the American Association for the Advancement of Science, USA. Eppendorf® and the Eppendorf Brand Design are registered trademarks of Eppendorf AG, Germany. All rights reserved, including graphics and images. Copyright © 2020 by Eppendorf AG. Kurstin Roe Photography.

RETHINKING ANOREXIA

Challenging long-standing theories about the eating disorder, new research suggests biology is a powerful driver

By **Jennifer Couzin-Frankel**

ILLUSTRATION: ILARIA URBINATI

In college in the 1990s, Alix Timko wondered why she and her friends didn't have eating disorders. "We were all in our late teens, early 20s, all vaguely dissatisfied with how we looked," says Timko, now a psychologist at Children's Hospital of Philadelphia. Her crowd of friends matched the profile she had seen in TV dramas—overachievers who exercised regularly and whose eating was erratic, hours of fasting followed by "a huge pizza."

"My friends and I should have had eating disorders," she says. "And we didn't."

It was an early clue that her understanding of eating disorders was off the mark, especially for the direst diagnosis of all: anorexia nervosa. Anorexia is estimated to affect just under 1% of the U.S. population, with many more who may go undiagnosed. The illness manifests as self-starvation and weight loss so extreme that it can send the body into a state resembling hibernation. Although the disorder also affects boys and men, those who have it are most often female, and about 10% of those affected die. That's the highest mortality rate of any psychiatric condition after substance abuse, on par with that of childhood leukemia. With current treatments, about half of adolescents recover, and another 20% to 30% are helped.

As a young adult, Timko shared the prevailing view of the disease: that it develops when girls, motivated by a culture that worships thinness, exert extreme willpower to stop themselves from eating. Often, the idea went, the behavior arises in reaction to parents who are unloving, controlling, or worse. But when Timko began to treat teens with anorexia and their families, that narrative crumbled—and so did her certainties about who is at risk. Many of those young people "don't have body dissatisfaction, they weren't on a diet, it's not about control," she found. "Their mom and dad are fabulous and would move heaven and Earth to get them better."

Timko wasn't alone. Other researchers were also questioning psychological theories of anorexia that had reigned for generations. "Hunger is a basic drive," says Cynthia Bulik, a clinical psychologist who runs eating disorder centers at the University of North Carolina, Chapel Hill, and at the Karolinska Institute. The idea that patients use willpower to override hunger "never rang true," she says. "My patients have said for years that … when they starve, they feel better." She began to consider another possibility: What if their biology is driving them to eschew food?

Bulik and Timko are now part of a small band of researchers working to untangle the biology of anorexia. The more they look, the more they find to suggest the disease's biological roots run deep. For instance, genetic studies indicate it's about as heritable as obesity or depression. The circuitry of the brain's reward system behaves differently in unaffected volunteers than in people with anorexia and those who have recovered. And new treatments drawing on biology are being tested, including deep-brain stimulation and psychedelic drugs. Those experiments aim not only to improve the outlook for patients, but also to explore how closely the disease aligns with others across psychiatry, including obsessive-compulsive disorder (OCD) and addiction.

Scientists pursuing those new ideas face a challenge, in part because of money: For fiscal year 2019, anorexia got $11 million in funding from the National Institutes of Health (NIH), a figure that hasn't changed notably in many years and that researchers decry as shockingly low given the disease's burdens. By contrast, schizophrenia—which has a similar prevalence and also surges during adolescence—garnered $263 million. The dearth of funder interest, many say, springs from the view that anorexia's roots are cultural, along with shame and stigma still clouding the disease. But evidence is mounting that biology is at its core.

> **"A lot of patients will say, 'It was never about being thin for me, ever.'"**
>
> **Cynthia Bulik**,
> University of North Carolina, Chapel Hill

LORI ZELTSER PIVOTED to anorexia from studying obesity. A developmental neuroscientist at Columbia University, she studied the brains of developing mice, trying to identify feeding circuits that increase susceptibility to obesity in adulthood. Then about 10 years ago, Zeltser saw a notice for funding from the Klarman Family Foundation, formed by hedge fund manager Seth Klarman and his wife, Beth, now the foundation's president. The foundation wanted to stimulate basic research into eating disorders, and because of Zeltser's research on appetite, she submitted a proposal.

To get up to speed on anorexia, Zeltser turned to the literature. Researchers in Sweden and Minnesota had compared anorexia rates in identical and fraternal twins, a common approach to tease out heritability of complex traits and diseases. Those reports showed that 50% to 60% of the risk of developing anorexia was due to genes, implying DNA is a powerful driver. By contrast, family studies suggest the heritability of breast cancer is about 30%, and that of depression is roughly 40%. "I was shocked," Zeltser says.

Layered on the genetics work was a data point that caught Zeltser's attention. An antipsychotic drug, olanzapine, which causes profound weight gain as a side effect, had little to no effect on weight when tested in people with anorexia. Something in people's biology prevented olanzapine from causing weight gain, Zeltser believes. "That is not just [mental] control."

But a deep schism remains, with many practitioners concerned that biology is getting more attention than it deserves. "If I had to choose nature versus nurture in the development of anorexia and other eating disorders, I would choose nurture," says Margo Maine, a psychologist who has treated eating disorders for years. Eating disorders are primarily female, she says, in part because "gender is a cultural experience."

Psychotherapist Carolyn Costin, who recovered from anorexia in the late 1970s and established a network of private treatment centers around the United States, says biology plays a role but that cultural messages and psychological stressors are also important factors. She worries especially that the way biology research is described could discourage patients about their prospects for recovery. About 8 years ago, she says, "Clients started coming in, saying, 'It's genetic, why bother'" trying to get well?

Such comments agitate researchers like Bulik. The patients she treats, she says, are reassured, not distressed, to learn that the disorder is rooted in biology and that biology doesn't translate into destiny. Although she, Zeltser, and others agree that anorexia has environmental drivers, as most chronic conditions do, they object to the idea that environment leads the way. "Exposure to this ideal [of thinness] is ubiquitous, but everybody doesn't get anorexia nervosa," Bulik says. "None of the sociocultural literature has ever been able to explain why." She adds, "A lot of patients will say, 'It was never about being thin for me, ever.'"

"If you look at psychiatric syndromes over 200 years, anorexia hasn't changed at all," whereas our culture has, says James Lock, a child psychiatrist who heads the child and adolescent eating disorders program at Stanford University School of Medicine.

To begin digging into the biology of anorexia, Zeltser used a 2010 grant from the Klarman foundation to build a mouse model of the disease. Because feeding is easy to measure, she reasoned that anorexia's restrained feeding behavior is well-suited for animal modeling. Her goal was to study the

eating and starvation patterns of the mice and explore how genetics and the environment interact to trigger the disorder.

In a 2016 issue of *Translational Psychiatry*, Zeltser described mice with a variant in a gene that in people is linked to anorexia. On its own, the variant didn't noticeably affect mouse feeding behavior. To mimic the pullback from eating that often precedes a diagnosis, the researchers restricted the animals' caloric intake by 20% to 30%. Then they induced stress, another factor linked to anorexia, by housing the normally social animals alone. The result: "The mice stop eating," Zeltser says.

Zeltser is talking with clinical colleagues about comparing her rodents' behavior with videos of patients in a "feeding lab," where researchers observe how much people eat, which nutrients they choose, and which they avoid. If the behaviors seem parallel, the mice could help point the way to new treatments or even different environments that could better support eating.

But publishing her animal work has proved difficult. Zeltser is often asked, "How do you know if what you're finding is relevant to humans?" That's a common question of anyone doing mouse work, but Zeltser says the challenge here runs deeper. "This is not taken seriously as a disease" that has a biological basis, she says. Instead, it's dismissed as "extreme girl behavior and 'oh my God, they're crazy,'" pushback she finds immensely frustrating.

Accumulating genetic data could change that by making anorexia's biological roots harder to ignore. Some of the strongest evidence emerged last summer, when Bulik and others published in *Nature Genetics* the largest genetics study on the disease, with roughly $9 million in funding from the Klarman foundation and additional funds from NIH. By analyzing the genomes of nearly 17,000 people with anorexia and more than 55,000 people without, the researchers identified eight statistically significant genomic regions, along with other patterns of genetic associations that yielded important clues. Some of those associations tracked with results of studies of other psychiatric illnesses, including OCD and depression, which didn't surprise Bulik. What did were overlapping associations with DNA controlling body mass index (BMI), lipids, and other metabolic traits.

"We said, 'This doesn't look like any other psychiatric disorder,'" Bulik says. "It might be the inverse of obesity—these people might be genetically predisposed to low BMI." In the February 2019 issue of the *Journal of the American Academy of Child & Adolescent Psychiatry*, she and her team sifted through BMI records for young people later diagnosed with anorexia and other eating disorders. The BMIs of 243 people diagnosed with anorexia began to diverge from those of a control group before they started kindergarten.

Bulik is now launching the Eating Disorders Genetics Initiative, with more than $7 million from NIH, additional funding from Sweden and the United Kingdom, and potential infusions from other countries and individual donors. The initiative aims to include 100,000 people with anorexia nervosa, bulimia nervosa, and binge eating disorder. Although genetics is unlikely to offer quick solutions, Bulik hopes it can "shine the light in the direction you need to go" for effective therapies, including medications.

Lori Zeltser, a developmental neuroscientist at Columbia University, has developed a mouse model of anorexia nervosa.

PHOTO: CHRIS TAGGART

THE GENETIC FINDINGS might one day intersect with another line of research: studies of brain structures and signaling that are revealing tantalizing differences between people with and without anorexia. At Columbia, psychiatrist Joanna Steinglass wanted to understand how the brains of people with anorexia guide their food choices. In two studies, she and her colleagues recruited inpatients with eating disorders along with a control group. In people with anorexia, both during and after hospitalization, MRI scans showed the region of the brain associated with selecting foods was the dorsal striatum, which is key to forming habits. In people without an eating disorder, a different brain region guides choices. The work first appeared in 2015 in *Nature Neuroscience*, and the team presented more findings at a conference last year.

"They're using different circuits when they make decisions," Steinglass says. This jibes with her idea that as people repeatedly restrict eating, the behavior moves to a different brain region and becomes less amenable to change. That could help explain why many recovered patients relapse.

Another clue to how the brain might throw eating off track was reported last month in *The American Journal of Psychiatry*. Walter Kaye, a psychiatrist who directs the eating disorders program at the University of California (UC), San Diego, led a study looking at how the brains of people with anorexia behave when their bodies are hungry. Kaye, whose program treats about 70 patients per day, ran a study that included 48 women, 26 of whom had anorexia. Each was studied twice with brain imaging, once immediately after a meal and, on a separate visit, after fasting for 16 hours.

Kaye knew hunger activates brain circuits that in turn motivate eating, making food desirable. That relationship was clear during brain imaging of the control group volunteers: When they were offered sugar water after 16 hours of fasting, their reward and motivation circuits lit up. But in people with anorexia, those circuits were much less active after fasting. "They could identify being hungry," Kaye says, but their brains couldn't convert that into a desire to eat. The patients also experienced heightened anxiety and inhibition, along with diminished reward signaling in their brains. That effect may further impair their drive to eat. Kaye suggests people with anorexia "miscode food as risky rather than rewarding."

Psychiatrist Rebecca Park at the University of Oxford also suspects the disease hijacks the brain's reward system. Some of her patients experience "this sense of aberrant reward," almost a high from starvation, she says. Park's neuroscience research indicates aberrant brain responses to reward cues.

Are those brain differences a cause or a result of starvation? Studying people in remission eliminates the effects of malnutrition on the brain but can't definitively answer the question. It's likely that "starvation in adolescence is going to damage your brain," Park says. One way to begin to disentangle whether the brain differences predate the disease is to study people very early in its course. Steinglass is in the third year of a brain scanning study of reward

circuitry, which now includes 55 recently diagnosed teenagers and a control group of 25 others. The coronavirus pandemic has halted enrollment for now, but Steinglass hopes to have results in 2 to 3 years. Other researchers are working to understand how, and to what degree, the brain recovers once eating resumes.

THERE'S AN "OVERALL SENSE that we're joining the rest of the world" by finally applying scientific methods to anorexia nervosa, Steinglass says. The ultimate goal is new treatments, which are sorely needed.

The most studied and most effective strategy to date is called family-based treatment (FBT), which originated at the Maudsley Hospital in London. It was later refined by Lock and psychologist Daniel Le Grange, of UC San Francisco, who trained at Maudsley.

FBT asks parents to set aside many of their family's day-to-day activities—scaling back school, work, hobbies—to sit with their children, requiring them to eat. Faced with food as a form of medicine, and with their world having contracted, many young people do start to eat again despite the fear and anxiety it causes them. Researchers are working to understand how FBT is intertwined with the biology of the illness, but for about half who try FBT in adolescence—and perhaps 70% who try it early in the disease—the treatment is effective.

But many families aren't told about that therapeutic strategy, even though decades have passed since it first showed success in a randomized trial, in 1987. Practitioners may not be familiar with FBT, Timko says, they may believe the family played a role in anorexia's onset, or they may feel that adolescents must want to get better before starting FBT—a view she disputes.

Laura Collins Lyster-Mensh experienced the regimen up close after her daughter Olympia, then 14, stopped eating one day in 2002. Lyster-Mensh says a succession of therapists urged her and her husband to stand back and let Olympia eat when she was ready. Meanwhile, her weight continued to spiral downward. "We had been told she wouldn't recover, families were really at fault, to back off and let her do this on her own," Lyster-Mensh says. Then she learned about FBT from a newspaper article and raced to try it.

The first agonizing meals took hours, while Olympia mashed her food into a pulp or cried and raged at her parents. "I know families whose kids have jumped out of moving cars to avoid a sandwich," says Lyster-Mensh, echoing comments of many clinicians who describe patients' crushing fear of food. Olympia ultimately recovered, although not without challenges that included a relapse during college.

The young patients treated with FBT who do start to eat again do well on the one measure that predicts longer-term prognosis: early weight gain. In 2019, a study in the *European Eating Disorders Review* led by Le Grange confirmed earlier research showing that gaining about 2.3 kilograms in the first month of treatment is a predictor of health 1 year later. Girls with anorexia who boosted their calorie intake and gained weight experienced increases in estrogen levels (which plummet in starvation), reduced stress, and improved ability to navigate different situations, a psychological trait called flexibility.

Researchers are exploring ways to build on and improve FBT—or find new strategies to help patients in whom it has failed. Some clinical trials are testing whether certain talk therapies, such as cognitive behavioral therapy to help patients reframe their thinking, can help—for example, by reducing anxiety or other impediments to eating.

New biological models of anorexia hint at other kinds of interventions. An 18-person study at Johns Hopkins University is offering the psychedelic drug psilocybin to patients. Early data suggest it holds promise in helping smokers quit and combating alcoholism—and many researchers believe that in certain ways, anorexia shares some features with addiction. Park is leading a seven-person study of deep-brain stimulation in people with severe enduring anorexia, some of whom also have OCD.

"There's a certain neural network that's well characterized" in OCD, she says, and disrupting the signaling in that network with deep-brain stimulation can help those patients. Because OCD and anorexia have shared features and some genetic links, she's interested in whether disrupting the same neural network might also help people with the eating disorder.

Still, studies remain sparse, Lock says. With limited funding, there's little chance of attracting new scientists to a small field. "As researchers, you don't want to go to the pot that's empty," he says. "Why aren't we investing more?" It's especially frustrating because, Lock points out, many patients with anorexia successfully heal and enjoy a bright future. "What [other] illness in psychiatry can you say you cure?" he asks.

For families, regardless of whether a patient recovers, the shame can persist—and with it hesitation to speak up and lobby for funding. Lyster-Mensh is an exception. After her family's experience, she began to voice support for evidence-based treatment—first in a memoir, *Eating with Your Anorexic*, which she wrote under the name Laura Collins, and then through FEAST, a message board turned advocacy group.

"It's still a pretty small group," Lyster-Mensh says, of those willing to speak openly. "Most families are so burned out, crushed, guilty, that they don't want to come forward," she says. "There are still these myths out there—that these are chosen illnesses and parents somehow failed to prevent, or caused, or exacerbated the problem." Still, she hopes that as researchers doggedly track the disease's biological roots in genes and the brain, those enduring myths will fade. ■

Money woes

Many researchers lament that eating disorders, including anorexia nervosa, are underfunded given their prevalence. These numbers are drawn from 2017 data for the United States; the number of individuals affected is an estimate.

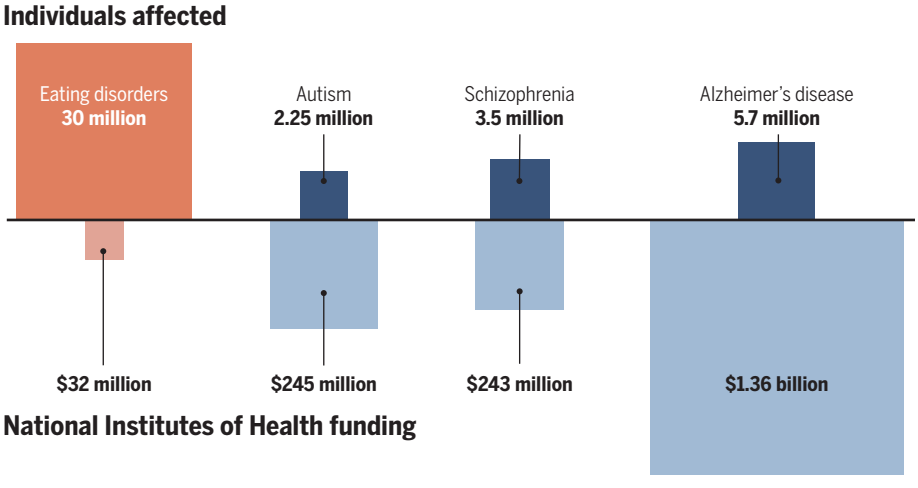

CREDITS: (GRAPHIC) X. LIU/*SCIENCE*; (DATA) BRYN AUSTIN/BOSTON CHILDREN'S HOSPITAL; NATIONAL INSTITUTES OF HEALTH

INSIGHTS

PERSPECTIVES

TROPICAL FORESTS

Tree diversity reduced to the bare essentials

Tropical forest dynamics can be explained by merely two functional trait axes

By **Harald Bugmann**

Forests are a key component of the global climate system, particularly regarding the fluxes of carbon and water (*1*). Tropical forests are hotspots in this context, and thus their future fate could have strong implications for livelihoods and feedbacks to the climate. These forests are also key targets for biodiversity conservation (*2*). Their species richness applies to multiple organism groups, including trees, often featuring several hundred tree species per hectare compared to perhaps a dozen or just a few for temperate and boreal forests, respectively. This high tree species diversity hinders attempts to project future forest properties in the tropics. On page 165 of this issue, Rüger *et al.* (*3*) present an innovative approach for handling this vast biodiversity by simply considering two trait axes and five tree functional types. Reducing species diversity with these parameters may allow reliable projections of future tropic forest responses to climate change.

Ongoing and expected anthropogenic changes of the climate, such as heat and drought, will trigger strong, albeit considerably lagged, responses of forests (*4*). Assessing these responses is important from both a global climate and a local livelihood perspective, as most human societies depend in multiple ways on ecosystem services provided by forests (*5*). They include goods (such as timber and fuel), ecological functions (such as carbon storage and providing habitat for wildlife), and social benefits (such as recreation). However, such assessments cannot be done for forest vegetation as an entity, because the tree species making up a forest will react individually (*6*). Hence, forests will not change as monolithic units, but climate change will induce nonlinear trajectories that begin with current complex forest stand (i.e., tree community) structures to unknown, sometimes new future stand structures that may feature a very different species composition (*7*).

Projecting these future trajectories of forest structure and function is thus an important task that is greatly complicated by the vast number of tree species in tropical forests. The concept of plant functional types (PFTs) is typically used to collapse the large set of species to a few manageable units. Yet, defining PFTs is typically done in a pragmatic manner, lacking a systematic approach (*8*). Rüger *et al.* used trait data for 282 tree species of the tropical moist forest at Barro Colorado Island (Panama) to demonstrate that forest dynamics can be

Forest Ecology, Department of Environmental Systems Science, ETH Zürich, 8092 Zürich, Switzerland. Email: harald.bugmann@env.ethz.ch

PHOTO: CYRIL RUOSO/MINDEN PICTURES

Tropical rainforests—such as this experimental plot at Barro Colorado Island (Panama)—often contain more than 200 and up to 650 tree species per hectare.

captured with a strongly reduced set of rigorously defined PFTs. The classical view of the traits that underlie forest succession—and thus changes in species composition—relates to the trade-off between growth and survival (i.e., at the extremes, the organisms either grow fast and die young, or they grow slowly and reach high longevity) (*9*). Rüger *et al.* complement this one-dimensional view with a second axis representing the stature-recruitment trade-off, which allows them to explain the existence (and often dominance) of long-lived pioneers that grow tall but do not invest much into recruitment, whereas at the other end of the gradient there are short-stature pioneers that invest heavily into recruitment and do not grow old.

In a carefully designed simulation experiment with an individual-based model of forest dynamics, Rüger *et al.* demonstrate that five functional groups of trees based on these two trade-off axes are sufficient to capture forest dynamics as well as when the entire set of 282 species is used. Their demonstration challenges earlier research on tropical forest tree diversity that has relied on the assumption that the fast-slow continuum alone governs most of tropical forest dynamics.

The finding of Rüger *et al.* is notable for several reasons. The approach allows for the prediction of key functional aspects of forests (including biomass and composition) on the basis of a small set of attributes of functional diversity, which is in stark contrast to the large taxonomic diversity. This does not mean that most tree species in tropical forests would be redundant and thus not important, because they have multiple other roles beyond carbon and water cycling, of course. Yet, the rigorous definition and testing of PFTs provide the basis for representing tropical forest dynamics much more accurately in dynamic global vegetation models (*10*) that are often integrated in Earth system models (*11*).

Also, previous approaches to using PFTs in climate impact research were often marred by the problem that PFT-based approaches worked well for the current climate but not under scenarios of climate change, thus greatly limiting the applied value of these concepts (*12*). It is quite pleasing to see that with the approach by Rüger *et al.*, this problem appears to be solved.

Ecology is getting closer to a theory-driven understanding of long-term forest dynamics ("succession"), an issue that has kept ecologists busy for more than a century (*13*). It is certainly true that the results of Rüger *et al.* for Barro Colorado Island need evaluation and corroboration in other tropical forests, but they are sound enough to serve at least as a general hypothesis for forests on other continents, and most likely beyond the tropical zone.

Rüger *et al.* also show that there is huge potential in combining the ever-larger data sets on species and ecological processes that are becoming available increasingly online (*14*), with rigorous statistical analyses and dynamic forest models. This could allow for robust projections of ecosystem dynamics at temporal and spatial scales that are accessible neither to experimentation nor direct observation. ■

REFERENCES AND NOTES

1. T. A. M. Pugh *et al.*, *Proc. Natl. Acad. Sci. U.S.A.* **116**, 4382 (2019).
2. J. A. LaManna *et al.*, *Science* **356**, 1389 (2017).
3. N. Rüger *et al.*, *Science* **368**, 165 (2020).
4. R. S. Snell, C. Elkin, S. Kotlarski, H. Bugmann, *Reg. Environ. Change* **18**, 2145 (2018).
5. A. S. Mori *et al.*, *J. Appl. Ecol.* **54**, 12 (2017).
6. M. B. Davis, in *Forest Succession: Concepts and Application*, D. C. West, H. H. Shugart, D. B. Botkin, Eds. (Springer, 1981), pp. 132–153.
7. M. Mina *et al.*, *J. Appl. Ecol.* **54**, 389 (2017).
8. F. I. Woodward, W. Cramer, *J. Veg. Sci.* **7**, 306 (1996).
9. C. Bigler, T. T. Veblen, *Oikos* **118**, 1130 (2009).
10. Y. Q. Luo *et al.*, *Biogeosciences* **9**, 3857 (2012).
11. P. Friedlingstein, *Philos. Trans. R. Soc. A Math. Phys. Eng. Sci.* **373**, 20140421 (2015).
12. H. Bugmann, *J. Veg. Science* **7**, 359 (1996).
13. J. Lienard *et al.*, *PLOS ONE* **10**, e0117138 (2015).
14. J. Kattge *et al.*, *Glob. Change Biol.* **26**, 119 (2020).

10.1126/science.abb7020

IMMUNOLOGY

The "iron will" of the gut

A gut-derived hormone controls iron concentrations, microbiota composition, and mucosal healing

By **Maria Rescigno**

The importance of trace elements in the mammalian diet, such as minerals, cannot be underestimated. For example, deficiency of iron results in anemia, accompanied by tiredness and fatigue due to the inability to carry oxygen to tissues. Conversely, iron excess is also dangerous, leading to liver disease, heart problems, and diabetes related to iron-mediated oxidative stress. Hence, iron metabolism is tightly controlled at both cellular and systemic levels (*1*). On page 186 of this issue, Bessman *et al.* (*2*) demonstrate an additional level of iron metabolism control that occurs in the gut and is mediated by the interplay between dendritic cells (antigen-presenting cells linking innate with adaptive immunity) and the microbiota through the hormone hepcidin in mice. This cross-talk is essential to allow recovery from intestinal inflammation.

Mammalian cells and most of the bacteria in the gut microbiota rely on iron for many cellular processes (*3*). Hence, they compete with each other for iron procurement. Under homeostatic conditions and with adequate intake of dietary iron, this is not harmful because iron is not generally excreted from the body, and only small amounts that are lost through bleeding, sweating, or urinary excretion have to be replaced through dietary sources (*1*). However, during intestinal inflammation and associated bleeding, the massive amount of iron that is lost in the intestinal lumen can have two major consequences: It can foster the growth of iron-dependent bacteria such as potentially pathogenic enterobacteria (*4*), and it deprives the host of this essential nutrient, which has to be reabsorbed from the intestinal lumen.

Iron metabolism is controlled within the cell by iron regulatory proteins that

Humanitas Clinical and Research Center (IRCCS), 20089 Rozzano, Milan, Italy, and Humanitas University, Department of Biomedical Sciences, 20090 Milan, Italy. Email: maria.rescigno@hunimed.eu

bind iron-responsive elements in DNA to regulate the expression of iron metabolism genes. It is controlled systemically by hepcidin, which induces the degradation of the iron exporter ferroportin and thereby limits extracellular efflux of iron (*3*). High hepcidin serum concentrations occur in inflammatory bowel disease (IBD) patients, particularly in those with Crohn's disease (*5*). This positively correlates with the amount of the intracellular iron storage protein ferritin and negatively correlates with hemoglobin concentrations in the blood, which suggests that high serum hepcidin is associated with chronic anemia. Bessman *et al.* show that mice lacking hepcidin are as susceptible to dextran sodium sulfate (DSS)–induced experimental colitis as wild-type animals, but upon removal of the inflammatory insult, they struggle to recover body weight and have reduced mucosal healing.

The authors found that ferroportin, the target of hepcidin, is expressed only by colonic epithelial cells (enterocytes), macrophages, and neutrophils. This suggested that DC-released hepcidin was not acting in an autocrine fashion. Indeed, elegant genetic manipulations demonstrated that macrophages and/or neutrophils were the target of hepcidin-mediated ferroportin degradation that is responsible for mucosal healing. This corroborates the idea of a division of labor between intestinal phagocytes (*7*). The finding that enterocyte ferroportin is not the target of hepcidin during mucosal healing suggests that either iron is not reabsorbed from the intestinal lumen, or iron is not stored within enterocytes but is quickly delivered to macrophages or neutrophils, which preserve it during inflammation owing to hepcidin released by DCs.

Hepcidin-driven wound healing in the gut

During intestinal inflammation, dendritic cells (DCs) release hepcidin, which induces the degradation of ferroportin in phagocytes and intracellular retention of iron. When hepcidin is deleted in DCs during inflammation, iron accumulates in the intestinal lumen, and *Bifidobacterium* species (which are important for barrier repair) are particularly reduced.

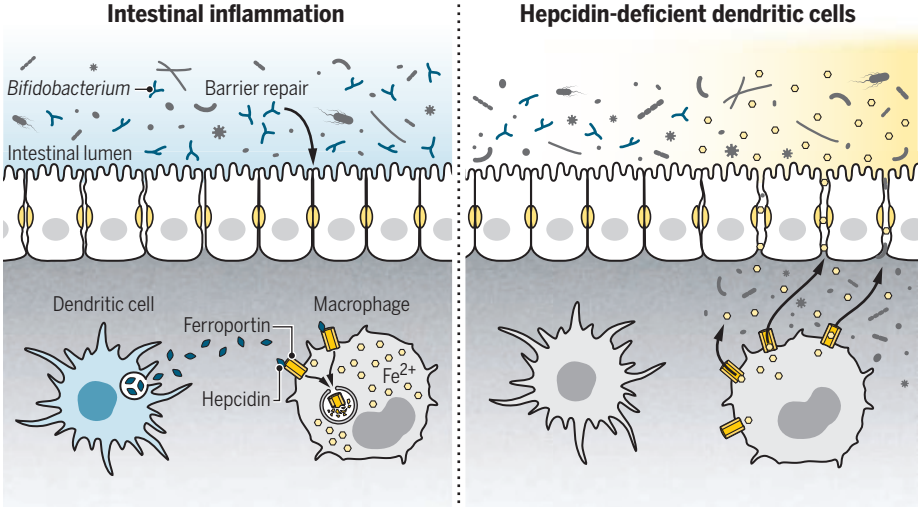

DCs release hepcidin, which induces the degradation of ferroportin, and iron is retained intracellularly.

In the absence of DC-derived hepcidin, iron is released extracellularly through ferroportin.

The major source of hepcidin is considered to be hepatocytes; however, Bessman *et al.* found that during intestinal inflammation, the major producers of hepcidin are dendritic cells (DCs) in the lamina propria of the gut in mice and IBD patients. A similar production of hepcidin upon parasite infection has been shown in fish skin (*6*), which suggests that local induction of hepcidin in response to microbial infection may be evolutionarily conserved. Deletion of hepcidin in DCs resulted in the inability to undergo mucosal healing upon DSS removal.

Not all gut bacteria require iron for their growth (*8*, *9*). Bessman *et al.* show that hepcidin deletion in DCs resulted in differences in microbiota composition, suggesting a role for hepcidin control of intestinal iron—and consequently of the microbiota—under homeostatic conditions. When this altered gut microbiota was transplanted into wild-type animals that were then treated with DSS, recovery and mucosal healing were reduced. This suggests that at least some of the effects observed in mice with hepcidin-deficient DCs were mediated by changes in microbiota composition. *Bifidobacterium* species, which protect the intestinal barrier, were reduced by hepcidin deletion in DCs; this finding suggests that luminal iron affected this genus (*4*). *Bifidobacterium* supplementation in mice with hepcidin-deficient DCs facilitated mucosal healing, presumably by controlling epithelial barrier permeability.

The study of Bessman *et al.* suggests that the intracellular storage of iron by macrophages or neutrophils is controlled by inflammation-induced DC-derived hepcidin, which blocks iron efflux from intracellular pools by degrading ferroportin (see the figure). In the absence of this control during intestinal inflammation, iron concentration rises in the lumen and alters the composition of the microbiota. Other possible events may occur concomitantly when iron accumulates in the intestinal lumen, such as loss of iron-reducing bacteria (which may limit iron absorption from the lumen) or an enrichment of iron-dependent pathogenic Enterobacteriaceae. The effect of increased luminal iron on mucosal healing may explain why oral administration of iron in anemic IBD patients is not preferred (*10*). It will be interesting to evaluate which other conditions might lead to increased iron concentration in the intestinal lumen and whether hepcidin deletion in DCs in a chronic inflammatory setting may affect systemic iron pools, which may resemble IBD-associated anemia. These findings provide a rationale for the beneficial effects of *Bifidobacterium* supplementation observed in IBD patients (*11*). Clinical trials to better understand the precise *Bifidobacterium* strain and/or iron sequestration, dosage, and time of intervention would advance the efficacy of this approach. ■

REFERENCES AND NOTES

1. A. U. Steinbicker, M. U. Muckenthaler, *Nutrients* **5**, 3034 (2013).
2. A. J. Bessman *et al.*, *Science* **368**, 186 (2020).
3. G. J. Anderson, D. M. Frazer, *Am. J. Clin. Nutr.* **106** (suppl. 6), 1559S (2017).
4. T. Jaeggi *et al.*, *Gut* **64**, 731 (2015).
5. R. J. Basseri *et al.*, *J. Crohn's Colitis* **7**, e286 (2013).
6. Y. Hu *et al.*, *Fish Shellfish Immunol.* **66**, 398 (2017).
7. E. Mazzini, L. Massimiliano, G. Penna, M. Rescigno, *Immunity* **40**, 248 (2014).
8. M. Elli *et al.*, *J. Appl. Microbiol.* **88**, 695 (2000).
9. K. Skrypnik, J. Suliburska, *J. Sci. Food Agric.* **98**, 2449 (2018).
10. C. J. Gargallo-Puyuelo, E. Alfambra, J. A. García-Erce, F. Gomollon, *Nutrients* **10**, E1959 (2018).
11. M. J. Saez-Lara, C. Gomez-Llorente, J. Plaza-Diaz, A. Gil, *BioMed Res. Int.* **2015**, 505878 (2015).

ACKNOWLEDGMENTS

The author is supported by grants from the Italian Association for Cancer Research (AIRC IG 17628) and the European Research Council (ERC, no. 615735—homeogut).

10.1126/science.abb2915

GRAPHIC: A. KITTERMAN/*SCIENCE*

PHYSICS

The smallest particle collider

A new experiment finds direct evidence for anyons in a semiconductor heterostructure

By **D. E. Feldman**

The standard model of particle physics classifies all elementary particles as fermions or bosons. Fermions, like electrons, avoid each other. Bosons, like photons, can bunch together. The classification rests on a fundamental spin-statistics theorem of quantum field theory and keeps these two types of particles distinct from each other. However, on page 173 of this issue, Bartolomei *et al*. (*1*) report an observation of particles that are neither bosons nor fermions.

The authors' notable experiment in no way disproves the standard model. Indeed, the standard model deals with particles in three-dimensional space at the highest accessible energies. The experiment deals with electric charges in two spatial dimensions at low temperatures. According to theory (*2*, *3*), this type of two-dimensional system in a high magnetic field can give rise to emergent anyon quasiparticles. Anyons have the distinctive feature that their charge can be less than the charge of an electron e (*3*), making them the smallest in terms of charge. The quantum statistics of anyons is an even more interesting property. Quantum statistics tells us what happens when identical particles exchange their positions or run in circles around each other. Although bosons and fermions behave quite differently when exchanged, they show no interesting behavior when one particle encircles another. This is because all particles return to where they started after a full circle. When one anyon encircles another, their long-range statistical interaction has a nontrivial effect (*2*, *3*).

Experimental observation of anyon statistics is a major challenge. The most natural approach is based on interferometry, which forces anyons to run around each other. Promising results arrived a decade ago (*4*), but theoretical interpretation of interferometry data has been difficult. Evidence for anyon statistics has unexpectedly come from thermal transport (*5*–*7*), which revealed non-Abelian anyons (*2*, *3*) that possess multiple locally indistinguishable quantum states. This property makes these anyons ideal building blocks for a topological quantum computer (*2*), which would require fewer qubits than conventional quantum computers that need error correction. Abelian anyons have no locally indistinguishable states. However, the thermal transport observations lacked the direct experimental evidence that Bartolomei *et al*. provide of Abelian anyon statistics.

The authors' experiment implements a theoretical proposal for an anyon collider (*8*). The device resembles an elementary-particle collider but is much smaller in size and operates at much lower energies. Bartolomei *et al*. built a GaAs/AlGaAs heterostructure that confines electrons in two dimensions. The heterostructure was placed in a strong perpendicular magnetic field. This field made the bulk of the heterostructure a fractional quantum Hall insulator that hosts anyons of charge $e/3$. Chiral conducting channels also formed along the edges of the heterostructure. These properties allowed the authors to explore a collision of two anyons propagating along the edges (*1*, *8*). This was accomplished by creating two dilute beams of anyons at two quantum point contacts (QPCs). Quantum tunneling in the form of charge-$e/3$ quasiparticles occurs when electric charge generated from two different sources reaches the QPCs. The tunneling particles reach a third QPC. This is when quantum statistics enters the game, as the two anyons approach the QPC from opposite sides (see the figure). If the particles were fermions instead, they would block each other from tunneling through the third QPC because identical fermions cannot reside in the same place. This means that any fluctuations in the fermion currents collected in the drains would be uncorrelated. If the particles were bosons, this would cause a correlation between the two drain currents as these particles bunch together. Abelian anyons are intermediate in their properties between fermions and bosons. Therefore, some correlation of the two drain currents is expected, although the specific details depend on the anyon statistics.

The authors' experiment shows excellent agreement with the theory (*8*) for charge-$e/3$ (also called Laughlin) anyons (*3*). The observations provide experimental support to long-predicted anyon statistics of quasiparticles in fractional quantum Hall liquids. They also bring with them a surprise. Calculations in Rosenow *et al*. (*8*) were based on the simplest model of edge channels (called the chiral Luttinger liquid model), which often fails to quantitatively describe experimental data (*3*). It is tempting to think that the observed signature of anyon statistics has a deep reason that goes beyond a particular model. Indeed, this happens with a related nonequilibrium fluctuation-dissipation theorem, which was first discovered in the simplest model but applies very generally (*9*).

Extending the experiment to other types of Abelian and non-Abelian anyons would be of great interest, as would be other probes of anyon statistics. Recent progress includes a new approach to interferometry (*10*) and the extension of the thermal conductance technique to graphene (*11*). Such advances may eventually contribute to the development of topological quantum computing. Anyons are also of interest for answering very basic questions about quantum matter. ■

Schematics of an anyon collider

The collider is a heterostructure that hosts a quantum Hall liquid (yellow) in a strong magnetic field. Electric charge from a source tunnels at the quantum point contact (QPC) as an anyon (dashed lines). Anyons colliding at QPC2 create current fluctuations measured at points D3 and D4 characteristic of anyon statistics.

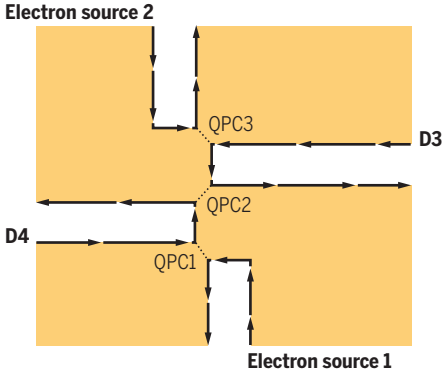

GRAPHIC: N. CARY/*SCIENCE*

Brown Theoretical Physics Center and Department of Physics, Brown University, Providence, RI 02912-1843, USA. Email: dmitri_feldman@brown.edu

REFERENCES AND NOTES

1. H. Bartolomei *et al.*, *Science* **368**, 173 (2020).
2. C. Nayak *et al.*, *Rev. Mod. Phys.* **80**, 1083 (2008).
3. M. Heiblum, D. E. Feldman, arXiv:1910.07046 [cond-mat.mes-hall] (2019).
4. R. L. Willett, L. N. Pfeiffer, K. W. West, *Proc. Natl. Acad. Sci. U.S.A.* **106**, 8853 (2009).
5. M. Banerjee *et al.*, *Nature* **545**, 75 (2017).
6. M. Banerjee *et al.*, *Nature* **559**, 205 (2018).
7. Y. Kasahara *et al.*, *Nature* **559**, 227 (2018).
8. B. Rosenow, I. P. Levkivskyi, B. I. Halperin, *Phys. Rev. Lett.* **116**, 156802 (2016).
9. C. Wang, D. E. Feldman, *Phys. Rev. Lett.* **110**, 030602 (2013).
10. J. Nakamura *et al.*, *Nat. Phys.* **15**, 563 (2019).
11. S. K. Srivastav *et al.*, *Sci. Adv.* **5**, eaaw5798 (2019).

ACKNOWLEDGMENTS

This work was supported by NSF grant DMR-1902356.

10.1126/science.abb3552

HYPOTHESIS

Autoimmunity provoked by foreign antigens

In celiac disease, exogenous gluten drives T cell–B cell interactions that cause autoimmunity

By **Rasmus Iversen**[1] and **Ludvig M. Sollid**[1,2]

Celiac disease (CeD) is a common gastrointestinal disorder that can be diagnosed at any age. The disease is associated with intake of cereal gluten proteins, and the diagnostic scheme initially relied on elimination-provocation diets, typical of food intolerances. This has changed. Currently, diagnosis in pediatric patients can be made solely on the basis of the presence of high serum concentrations of autoantibodies (antibodies that recognize "self" antigens) to transglutaminase 2 (TG2, also known as TGM2), a cytosolic enzyme with broad tissue expression. Accumulating evidence indicates that these autoantibodies are formed as a result of an adaptive immune response to gluten and that interactions between gluten-specific T cells and TG2-specific B cells are important for development of CeD.

No other human autoantibodies are better diagnostic markers for disease than TG2-specific antibodies. Without knowledge of disease dependence on dietary gluten, the presence of these autoantibodies would categorize CeD as an archetypical autoimmune disease rather than a food intolerance. Although autoimmune disorders are a collection of heterogeneous conditions, for which a single unifying mechanism is unlikely, some autoimmune diseases might share key pathogenic processes with CeD. Indeed, a provocative idea is that immune reactions to exogenous antigens can drive autoimmune diseases other than CeD (*1*).

Environmental factors such as viral or bacterial infections have often been associated with development of autoimmunity. Yet, CeD is the only autoimmune disease for which pathogenic T cell epitopes originating from an exogenous antigen (gluten) have been identified. CeD shows strong association to certain genetic variants (allotypes) of major histocompatibility complex (MHC) class II molecules that mediate antigen presentation to $CD4^+$ T cells. Hence, gluten-reactive $CD4^+$ T cells are considered key pathogenic players in CeD. These $CD4^+$ T cells reside in the gut lamina propria and release proinflammatory cytokines in response to gluten in the diet. As recently demonstrated in a mouse model of CeD, cytokines from $CD4^+$ T cells control the action of cytotoxic intraepithelial lymphocytes (*2*). The result is release of cytotoxic molecules that kill epithelial cells and thus cause the typical destruction of the small intestinal tissue structure that is seen in CeD.

The gluten epitopes that are recognized by the $CD4^+$ T cells uniformly contain negatively charged glutamate residues that are important for binding to the CeD-associated MHC class II molecules. The glutamate residues are introduced into gluten peptides through deamidation, a posttranslational modification that is catalyzed by TG2. The dual role of TG2 in CeD as the target of autoantibodies and responsible for creating T cell epitopes can be explained in the context of T cell–B cell collaboration. TG2-specific B cells can take up TG2-gluten complexes through B cell receptor (BCR)–mediated endocytosis. Deamidated gluten peptides may then be presented to $CD4^+$ T cells in a complex with MHC class II molecules on the surface of the B cells. The outcome is mutual activation of B cells and T cells, resulting in production of TG2-specific antibodies by the B cells and release of proinflammatory cytokines by the T cells (see the figure).

The generation of autoantibodies in CeD implies breaking of B cell self-tolerance to TG2. However, a recent study in genetically modified mice expressing a CeD patient–derived, TG2-specific BCR suggested that there is no active induction of B cell tolerance to TG2 under normal conditions (*3*). The reason for the lack of tolerance induction is probably that TG2 is a cytosolic enzyme and that TG2-reactive B cells are therefore not exposed to extracellular antigen during their development. Hence, TG2-reactive naïve B cells are most likely continuously present both in CeD and in healthy individuals. In CeD, such B cells receive activation signals from gluten-reactive effector T cells. We hypothesize that once efficient T cell–B cell collaboration has been established, autoimmunity and tissue damage could ensue, in CeD and likely also in other autoimmune diseases.

Although T cell–B cell interactions have been implicated in other autoimmune diseases, the well-characterized target epitopes in CeD offer distinct possibilities for studying pathogenic mechanisms. Hence, collaboration between TG2-specific B cells and gluten-specific T cells has been demonstrated both in vitro and in vivo (*3*). Gluten presentation by TG2-specific B cells was shown to depend on the TG2 epitope that is recgnized by the BCR (*4*). Thus, targeting of some TG2 epitopes allowed more efficient presentation of gluten on MHC class II than others, and antibody production against those epitopes correlated with the onset of clinical disease. Efficient T cell–B cell interactions therefore seem to be important for CeD development, and B cells are likely to be the main antigen-presenting cells (APCs) for pathogenic $CD4^+$ T cells in inductive lymphoid structures. In addition, B-lineage cells may be involved in antigen presentation in nonlymphoid tissues. Plasma cells were recently identified as the main cell type presenting an immunodominant gluten epitope in gut biopsies of CeD patients (*5*). Plasma cells are terminally differentiated B cells whose main function is to secrete antibodies. However, plasma cells secreting immunoglobulin A (IgA) and IgM antibodies also express cell-surface immunoglobulins (*6*), which serve as functional BCRs (*7*), allowing receptor-mediated uptake of cognate antigen. Although the ability of plasma cells to stimulate $CD4^+$ T cells has yet to be demonstrated, these observations suggest that they may act as APCs for tissue-resident $CD4^+$ effector T cells in CeD.

A role of B cells as the main APCs in CeD is supported by characteristics of gluten-reactive $CD4^+$ T cells in blood and gut biopsies of CeD patients. These cells were recently described to have a distinct phenotype with features resembling those of T follicular helper (T_{FH}) cells that are specialized for providing activation signals to B cells and that rely on B cell interactions for their differentiation (*8*). Thus, the $CD4^+$ T cells expressed high amounts of the cytokine interleukin-21 and C-X-C motif chemokine ligand 13 (CXCL13), which are important for activating and attracting B cells. But, they lacked expression of the chemokine receptor CXCR5, which is required for homing to B cell follicles. A similar expression profile was observed in $CD4^+$ T cells of patients with other autoimmune dieseases, including systemic lupus erythematosus (SLE) (*8*) and rheumatoid arthritis (*9*). The lack of CXCR5 expression suggests that inductive T cell–B cell interactions take place not in conventional germinal centers (GCs) in secondary lymphoid organs, but rather at

[1]KG Jebsen Coeliac Disease Research Centre, Department of Immunology and Institute of Clinical Medicine, University of Oslo, Oslo, Norway. [2]Department of Immunology, Oslo University Hospital, Oslo, Norway. Email: l.m.sollid@medisin.uio.no

extrafollicular sites such as the border between the T cell zone and the B cell follicle in lymph nodes or Peyer's patches of the gut. Extrafollicular activation of B cells in CeD is supported by the observation that TG2-specific antibodies rapidly disappear when patients start a gluten-free diet, indicating that GC-dependent long-lived plasma cells are not generated. Furthermore, these antibodies contain relatively few mutations, consistent with B cells being activated extrafollicularly rather than in GCs (*6*). Curiously, activated B cells in SLE patients were also found to lack CXCR5, consistent with a non–GC-dependent origin (*10*).

Similarities between CeD and other autoimmune diseases may not be restricted to immune cell phenotypes and interactions. Common mechanisms could also guide the targeting of antigens. Similar to the deamidation of gluten in CeD, posttranslational modifications of antigens have been implicated in other autoimmune diseases. Yet, it remains to be established whether T cells specific to modified (self)-peptides are controlling tissue destruction in patients or if posttranslational modifications are a side effect of autoimmune reactions. Posttranslational modifications can potentially create neoepitopes that the immune system perceives as foreign, thereby facilitating escape of autoreactive cells from tolerance. The underlying mechanisms of neoepitope formation and their potential role in autoimmunity are poorly understood. Environmental factors such as smoking and viral infections are candidate triggers that may induce inflammatory tissue alterations, accompanied by dysregulation of posttranslational modifications and formation of neoantigens that could lead to autoimmunity.

A prominent example of the connection between viral infections and autoimmunity is the association of Epstein-Barr virus (EBV) infection with development of multiple sclerosis (MS) (*11*)—a demyelinating autoimmune disease that affects the central nervous system. EBV persists in a latent state in memory B cells, which could serve as a permanent reservoir of viral antigens that can stimulate other immune cells. The disease is traditionally considered T cell mediated. Nevertheless, B cell depletion therapy with CD20-specific antibodies has a beneficial effect and limits relapses in MS, suggesting that B cells play an important role. If persistent viral antigens are important drivers of autoimmunity, a possible explanation for the clinical observations is that EBV-infected B cells are depleted by anti-CD20 therapy, thereby effectively removing the driving antigen (*12*). In this case, B cell depletion in MS would resemble the exclusion of gluten from the diet of CeD patients.

Path to celiac autoimmunity

Several of the steps involved in celiac disease (CeD) pathogenesis have also been implicated in other autoimmune diseases. In CeD, however, there is more knowledge about the target antigens and the basis for the association with major histocompatibility complex (MHC) class II allotypes than in other autoimmune diseases.

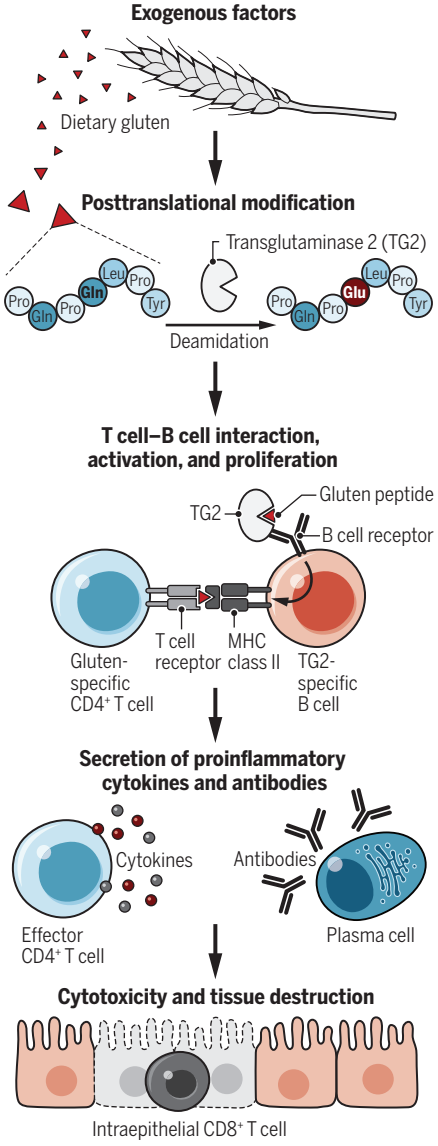

Although intriguing, it has not been proven experimentally that viral antigens can drive autoimmune disease. Thus, the exact role of EBV in MS remains unclear, and it is not established whether EBV-specific T cells are pathogenic or if EBV-infected B cells in the central nervous system give rise to inflammation. Antibody production is typically considered the main function of B cells. However, B cells can play additional roles in regulation of immune reactions through secretion of cytokines or antigen presentation. Indeed, because anti-CD20 therapy does not deplete plasma cells, the clinical benefits of the treatment in MS strongly suggest that B cells have pathogenic involvement independent of antibody production. Circulating B cells in MS patients were shown to stimulate autoreactive, potentially pathogenic T cells that home to the brain (*13*). In addition, ablation of MHC class II expression specifically on B cells in mice resulted in amelioration of symptoms in experimental autoimmune encephalomyelitis, the primary mouse model of MS (*14*). Similar findings were also obtained in a mouse model of SLE (*15*), suggesting that antigen presentation by B cells to CD4⁺ T cells plays a key role in development of destructive immune reactions, at least in some autoimmune diseases.

Dendritic cells are usually credited as the main APCs for T cells during an immune response. However, B cells are receiving increased attention as potent APCs in several autoimmune diseases. The main limitation to our understanding of pathogenic T cell–B cell interactions is the lack of well-defined target antigens in most autoimmune disorders. Characterization of T cell and B cell specificities will allow the study of disease-relevant immune cells that potentially can be targeted. Another major challenge is to understand why some people develop autoimmunity. Genetic predisposition is part of the answer, but environmental factors also play a role, possibly both by triggering and driving autoimmune reactions. Defining such factors is crucial for efficient treatment and prevention of autoimmune diseases. It is important to note that autoimmune disorders are a heterogeneous group of diseases with different manifestations and etiologies. Nevertheless, the mechanisms that are beginning to be unraveled in CeD could be relevant for other autoimmune conditions. ■

REFERENCES AND NOTES

1. L. M. Sollid, B. Jabri, *Nat. Rev. Immunol.* **13**, 294 (2013).
2. V. Abadie *et al.*, *Nature* **578**, 600 (2020).
3. M. F. du Pré *et al.*, *J. Exp. Med.* **217**, e20190860 (2020).
4. R. Iversen *et al.*, *Proc. Natl. Acad. Sci. U.S.A.* **116**, 15134 (2019).
5. L. S. Høydahl *et al.*, *Gastroenterology* **156**, 1428 (2019).
6. R. Di Niro *et al.*, *Nat. Med.* **18**, 441 (2012).
7. D. Pinto *et al.*, *Blood* **121**, 4110 (2013).
8. A. Christophersen *et al.*, *Nat. Med.* **25**, 734 (2019).
9. D. A. Rao *et al.*, *Nature* **542**, 110 (2017).
10. S. A. Jenks *et al.*, *Immunity* **49**, 725 (2018).
11. L. I. Levin, K. L. Munger, E. J. O'Reilly, K. I. Falk, A. Ascherio, *Ann. Neurol.* **67**, 824 (2010).
12. U. C. Meier *et al.*, *Clin. Exp. Immunol.* **167**, 1 (2012).
13. I. Jelcic *et al.*, *Cell* **175**, 85 (2018).
14. N. Molnarfi *et al.*, *J. Exp. Med.* **210**, 2921 (2013).
15. J. R. Giles *et al.*, *J. Immunol.* **195**, 2571 (2015).

ACKNOWLEDGMENTS

The authors are supported by the University of Oslo World-leading research program on human immunology (WL-IMMUNOLOGY) and by grants from the South-Eastern Norway Regional Health Authority (project 2016113), the European Commission (project ERC-2010-Ad-268541), and Stiftelsen KG Jebsen (SKGJ-MED-017).

10.1126/science.aay3037

GRAPHIC: KELLIE HOLOSKI/*SCIENCE*

NEUROSCIENCE

Epigenetic tinkering with neurotransmitters

Some neurotransmitters modify chromatin and modulate gene expression

By **Jean-Antoine Girault**

Dopamine is a monoamine neurotransmitter associated with movement and reward responses. The ventral tegmental area (VTA), a tiny midbrain region involved in motivation and addiction, and the neighboring substantia nigra contain most brain dopamine neurons. Dopamine neurons encode reward prediction errors (*1*, *2*), and dopamine conveys motivational value and promotes movement at multiple time scales (*3*). VTA dopamine neurons are part of the brain reward circuit. A central mechanism activated by addictive drugs and addictive behaviors, such as gambling, is to increase extracellular dopamine in the regions innervated by these neurons, such as the nucleus accumbens (*4*). It therefore comes as a surprise that dopamine is also an epigenetic mark. On page 197 of this issue, Lepack *et al.* (*5*) show that covalent attachment of dopamine (dopaminylation) to histone H3 glutamine 5 (H3Q5dop) plays a role in cocaine-induced transcriptional plasticity. Reducing dopaminylation prevented withdrawal-induced changes in gene expression and reduced cocaine-seeking behavior in rats.

The existence of protein modification by a monoamine neurotransmitter (monoaminylation) was initially shown to occur in platelets (*6*, *7*). When platelets are stimulated, serotonylation of fibrinogen and small guanosine triphosphatases (GTPases) facilitates platelet adhesion and blood clot formation. Several other intracellular and extracellular proteins are serotonylated during diverse biological responses, including cytoskeleton and spine remodeling, muscle contraction, insulin secretion, and serotonin transporter translocation (*8*). The transfer of serotonin to the side chain of a glutamine residue is catalyzed by tissue transglutaminase 2 (TGM2). This is a ubiquitous member of the transglutaminase family, present inside and outside of cells, and it is also a key antigen in celiac disease, which is a gluten-associated autoimmune disease (*9*, *10*). TGM2 cross-links proteins and covalently couples primary amines to a peptide-bound glutamine residue, a reaction called monoaminylation (*7*).

It was recently discovered that histone H3 glutamine 5 serotonylation (H3Q5ser) occurs in the brain and gut of diverse organisms that are capable of producing serotonin (*11*). This modification also occurs when the neighboring residue, lysine 4 (K4), is trimethylated (H3K4me3), a modification associated with transcriptional initiation (*12*). Serotonylation in vivo only occurs with concomitant trimethylation of the adjoining amino acid residue (*11*). During differentiation of serotonin neurons from human pluripotent stem cells, this dual modification (H3K4me3Q5ser) is enriched at active gene promoters and correlates with increased gene expression (*11*). This suggests that H3K4me3Q5ser is an epigenetic mark that is permissive for transcription during differentiation of serotonergic neurons. Indeed, doubly modified histone H3 enhances binding of the general transcription factor IID (TFIID) to H3K4me3 (*11*, *12*) (see the figure).

Lepack *et al.* found that histone H3 dopaminylation in VTA neurons results from TGM2 activity. In the postmortem VTA of cocaine users, H3Q5dop concentrations were decreased. In rats self-administering cocaine during 10 days with extended access to the drug, H3Q5dop initially decreased, as in the case of human users whose brains contained cocaine at the time of death. Yet in these rats, after a month of cocaine withdrawal, H3Q5dop was higher than in controls. Extended self-administration of cocaine was necessary for the H3Q5dop biphasic change to occur, because neither restricted self-administration nor passive administration of cocaine nor self-administration of food had any effect, suggesting a specific regulatory mechanism.

To test the function of H3Q5dop, Lepack *et al.* used viral overexpression of a histone H3 variant (H3.3) in which glutamine 5 was replaced by an alanine residue, preventing dopaminylation. In rats expressing mutated H3.3 in the VTA before the 30-day cocaine withdrawal, changes in gene expression were reduced, supporting a permissive epigenetic role of H3Q5dop. The firing rate of VTA dopamine neurons from these rats was decreased, and they released less dopamine in the nucleus accumbens. Prevention of H3Q5dop generation in the VTA also selectively decreased the drug-seeking behavior of rats trained to self-administer cocaine, without altering other behaviors. These results suggest that H3Q5dop plays a role in the transcriptional alterations that underlie neuronal and circuit adaptations leading to drug seeking. The downstream effects of H3Q5dop are unknown. They could be similar to those of serotonylation and facilitate transcription by enhancing H3K4me3 interactions with TFIID or other transcription factors. However, H3Q5dop and H3K4me3 were at least partly dissociated in vivo, and the chemical differences between the serotonyl and dopaminyl moieties may have differ-

Monoaminylation of histone H3

Serotonylated glutamine (Q) 5 in histone H3 during serotonergic neuron differentiation is catalyzed by transglutaminase 2 (TGM2) and associated with trimethylation of lysine 4 (K4me3). Serotonylation enhances general transcription factor IID (TFIID) binding to K4me3 and facilitates transcription. Dopaminylated Q5 in histone H3 is initially decreased during cocaine withdrawal and then increased. This facilitates withdrawal-induced gene expression alteration in ventral tegmental area (VTA) neurons and enhances dopaminergic neuron excitability and drug-seeking behavior in rats. A, alanine; R, arginine; T, threonine.

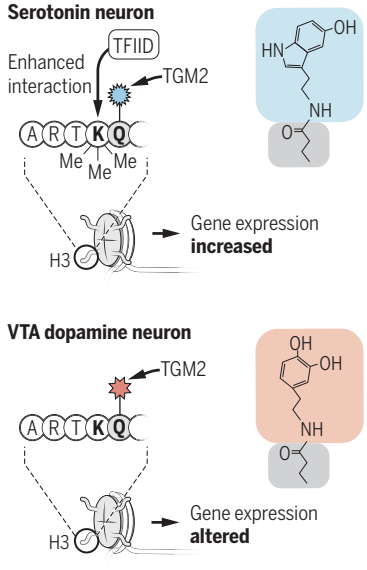

GRAPHIC: V. ALTOUNIAN/*SCIENCE*

Institut du Fer à Moulin, Inserm, Sorbonne Université, Faculty of Sciences and Engineering, UMR-S 1270, 75005 Paris, France. Email: jean-antoine.girault@inserm.fr

ent consequences for histone interactions.

The use of the same monoamine molecule as a neurotransmitter and a histone modification in the same cells illustrates that evolution proceeds by molecular tinkering, using available odds and ends to make innovations (*13*). These findings also raise exciting questions for future research. It is unclear what regulates serotonylation and dopaminylation and their removal from histone H3. Because TGM2 concentrations are regulated and its activity is calcium (Ca^{2+})–dependent (*9*, *10*), it will be important to examine the role of synaptic and neuronal activity. What is the role of substrate availability? It is unclear whether changes in intranuclear concentration of dopamine or serotonin matter. Cocaine increases extracellular concentrations of dopamine by blocking the dopamine transporter, but the subsequent changes in intracellular dopamine concentration in VTA neurons are not known. A decrease due to reuptake inhibition could hypothetically decrease dopaminylation after cocaine self-administration. However, it would be expected to also occur when rats received cocaine passively, suggesting the existence of more integrated regulation. It will also be interesting to examine the effects of antidepressant drugs on serotonylation. Is there a role of H3K5ser in the delayed clinical effects of these drugs that act by preventing serotonin reuptake or degradation? Additionally, the similarities and differences of dopaminylation and serotonylation on epigenetic regulation are important to understand. Future work will tell whether monoaminylation of H3Q5 is a curious and isolated epigenetic modification limited to a single histone residue in monoamine-rich cells or whether it is a more general mechanism. ■

REFERENCES AND NOTES

1. W. Schultz, P. Dayan, P. R. Montague, *Science* **275**, 1593 (1997).
2. W. Dabney *et al.*, *Nature* **577**, 671 (2020).
3. J. D. Berke, *Nat. Neurosci.* **21**, 787 (2018).
4. C. Lüscher, R. C. Malenka, *Neuron* **69**, 650 (2011).
5. A. E. Lepack *et al.*, *Science* **368**, 197 (2020).
6. R. Szasz, G. L. Dale, *Blood* **100**, 2827 (2002).
7. D. J. Walther *et al.*, *Cell* **115**, 851 (2003).
8. N. A. Muma, Z. Mi, *ACS Chem. Neurosci.* **6**, 961 (2015).
9. S. E. Iismaa *et al.*, *Physiol. Rev.* **89**, 991 (2009).
10. H. Tatsukawa *et al.*, *Cell Death Dis.* **7**, e2244 (2016).
11. L. A. Farrelly *et al.*, *Nature* **567**, 535 (2019).
12. M. Vermeulen *et al.*, *Cell* **131**, 58 (2007).
13. F. Jacob, *Science* **196**, 1161 (1977).

ACKNOWLEDGMENTS

The author is supported by Inserm, Sorbonne Université, Agence Nationale de la Recherche (ANR-16-CE16-0018 and ANR-19-CE16-0020); Laboratory of Excellence Bio-Psy (Investissements d'Avenir, ANR-11-IDEX-0004-02); and Fondation pour la Recherche Médicale.

10.1126/science.abb3533

SPINTRONICS

Spin pumping gathers speed

Coherent spin pumping from an antiferromagnet into a metal occurs at ~400 gigahertz

By **Axel Hoffmann**

The discovery of giant magnetoresistance in the mid-1980s demonstrated that magnetic structure can change electric resistivities substantially. Theoretical predictions and experimental demonstration of spin transfer torques in the 1990s demonstrated the inverse effect of injecting spin-polarized electric currents into ferromagnetic metals that could modify magnetic states (*1*). In general, injection of spin currents into magnetically ordered systems can excite magnetization dynamics (*2*), and magnetization dynamics can induce spin currents in adjacent materials through spin pumping (*3*). Coherent spin pumping effects have now been observed with antiferromagnetically ordered materials, as reported on page 160 of this issue by Vaidya *et al.* (*4*) and by Li *et al.* (*5*). These results provide new opportunities for using spintronics phenomena at ultrafast time scales and considerably higher frequencies, exceeding by several orders of magnitude the limitations of ferromagnetic materials.

These findings add to the rich interplay between magnetic structures and their dynamics with electronic structures. These effects have revolutionized information technologies because they allow transient electrical signals to be stored as nonvolatile magnetic states. Thus, giant magnetoresistance was harnessed to create the sensitive magnetic field sensors that enabled tremendous advances in magnetic data storage, and injected spin-polarized electric currents into ferromagnetic metals were harnessed to switch states in nonvolatile magnetic memory devices.

Magnetization dynamics in magnetic heterostructures (for example, interfaces of magnetic materials with nonmagnetic metals) can exhibit an enormous variety of complex phenomena given the ubiquity of nonlocal effects. Namely, the time-dependent magnetization of a ferromagnet can pump angular momentum into adjacent materials. This spin pumping can generate spin accumulations and spin currents whose spatial and temporal distributions are governed by spin relaxation processes and can readily exceed the dimensions of contemporary electronic devices.

The resultant spin currents are typically detected indirectly through either their influence on the magnetization dynamics (where spin currents give rise to additional dissipation) or the conversion of spin currents into electric-charge currents. This latter phenomenon is known in the bulk of materials as the inverse spin Hall effect (*6*). Indeed, one of the earliest electric detections of spin Hall effects was through spin pumping (*7*). Spin pumping has been instrumental in detecting spin currents and quantifying spin Hall effects (*8*) and forms the basis for many contemporary energy-efficient spintronics applications (*9*).

For ferromagnetically ordered materials, the connection between magnetization dynamics and electric charge currents has already been extensively studied and has been incorporated into modern information technologies (*10*)—for example, in spin transfer torque magnetic random-access memory. For antiferromagnetic materials, the applied impact of similar spintronics effects is just starting to emerge (*11*), driven by the recent discovery of staggered (Néel) spin-orbit torques in metallic antiferromagnets that enable the electric manipulation of antiferromagnetic order (*12*).

In ferromagnets, individual magnetic moments (spins) are aligned parallel, resulting in a net magnetic moment, but in antiferromagnets, spins point in alternating directions so that the net magnetization vanishes. This alternating magnetic structure has a profound impact on magnetization dynamics. In ferromagnets, the dynamics is generally dominated by the crystalline anisotropies and applied magnetic fields, which results in fundamental excitation frequencies of the order of a few gigahertz and requires substantially higher energies for manipulating magnetization states at times <1 ns. By contrast, magnetization dynamics in antiferromagnets invariably involves strong exchange interactions because they require the relative canting between adjacent spins, which results in frequency dynamics closer to the terahertz regime and may enable much faster manipulation of magnetization.

Another distinction is that for the dynamics in ferromagnets, the magnetization always precesses with the same chirality, so

Department of Materials Science and Engineering, University of Illinois at Urbana-Champaign, Urbana, IL 61801, USA. Email: axelh@illinois.edu

itinerant magnetic excitations (magnons) in ferromagnets can only transport in one direction of angular momentum. By contrast, in antiferromagnets, because of the presence of opposite spins, magnetic excitations with opposite chiralities can transport angular momenta with opposite signs. Thus, in a way, spin transport by magnons in ferromagnets resembles charge transport in metals (with just one type of charge carrier, electrons), whereas spin transport in antiferromagnets resembles charge transport in semiconductors, where two complementary carriers (electrons and holes) can coexist.

The current work by Vaidya *et al.* demonstrates experimentally both of these aspects (see the figure). They observed coherent spin pumping for frequencies of up to 395 GHz, which is one to two orders of magnitude higher than corresponding typical measurements with ferromagnetic materials. Furthermore, using differently circular-polarized subterahertz radiation for the excitation of the dynamics in the antiferromagnetic manganese difluoride, Vaidya *et al.* demonstrated the preferential pumping of different directions of angular momentum into an adjacent conducting platinum layer. This finding underscores that antiferromagnets may be much more versatile than ferromagnets with respect to using magnetic excitations for information processing.

Similar results were also recently observed for a different antiferromagnet, chromium sesquioxide, by Li *et al.* (*5*). Their measurements were performed at only a single frequency of 240 GHz, which only allowed for the coherent excitation of magnon modes with a single chirality. However, in their measurements, incoherently excited magnons with opposite chirality from heating contributed to the spin pumping signals. Thus, they were able to distinguish coherent and incoherent contribution to the spin-current injection.

Given that the work from Vaidya *et al.* and Li *et al.* demonstrates unambiguously the connection between coherent magnetization dynamics in antiferromagnets and concomitant spin and charge currents, do reciprocal effects also exist? Namely, can direct-current electric charge currents, in analogy to similar effects in ferromagnets, modulate the dynamics of antiferromagnets, so that magnetic damping can be reduced or even result in autonomous, sustained oscillations at terahertz frequencies? This capability would provide new perspectives not only for using antiferromagnets in ultrafast and energy-efficient information technologies but also for integrating antiferromagnets into new terahertz applications, such as narrow-bandwidth tunable emitters and detectors. Thus, clear experimental demonstration of electrically driven coherent magnetization dynamics in antiferromagnets is the next milestone in the quest for practical applications of antiferromagnets. ■

Spin pumping with antiferromagnets

In an antiferromagnet (AF), terahertz irradiation excites magnetization dynamics at high frequencies because of additional exchange energy involved with the relative canting between the two spin directions.

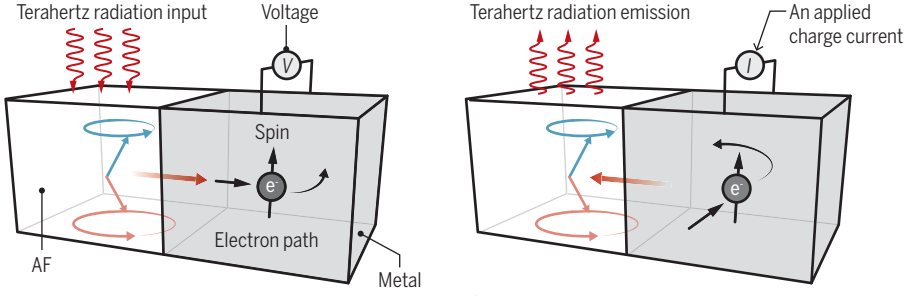

Spin pumping
Terahertz radiation pumps spin currents into adjacent metals, which get converted into charge currents and concomitant charge voltages through spin Hall effects.

Spin torque driven magnetization dynamics
Charge currents are converted to spin current through spin Hall effects. Injection into antiferromagents can excite magnetization dynamics that can drive terahertz emission.

REFERENCES AND NOTES

1. D. C. Ralph, M. D. Stiles, *J. Magn. Magn. Mater.* **320**, 1190 (2008).
2. S. I. Kiselev *et al.*, *Nature* **425**, 380 (2003).
3. Y. Tserkovnyak *et al.*, *Rev. Mod. Phys.* **77**, 1375 (2005).
4. P. Vaidya *et al.*, *Science* **368**, 160 (2020).
5. J. Li *et al.*, *Nature* **578**, 70 (2020).
6. A. Hoffmann, *IEEE Trans. Magn.* **49**, 5172 (2013).
7. E. Saitoh, M. Ueda, H. Miyajima, G. Tatara, *Appl. Phys. Lett.* **88**, 182509 (2006).
8. O. Mosendz *et al.*, *Phys. Rev. Lett.* **104**, 046601 (2010).
9. A. Hoffmann, S. D. Bader, *Phys. Rev. Appl.* **4**, 047001 (2015).
10. A. D. Kent, D. C. Worledge, *Nat. Nanotechnol.* **10**, 187 (2015).
11. J. Železný, P. Wadley, K. Olejník, A. Hoffmann, H. Ohno, *Nat. Phys.* **14**, 220 (2018).
12. P. Wadley *et al.*, *Science* **351**, 587 (2016).

10.1126/science.aba8388

PALEONTOLOGY

Rafting on a wide and wild ocean

During the Oligocene, now-extinct monkeys crossed the treacherous ocean from Africa to South America

By **Marc Godinot**

Scientists first met with skepticism the notion that small mammals crossed large oceanic barriers to populate faraway lands. However, progress in phylogenetics during the 1980s forced researchers to admit that the excellent North American fossil record showed no relatives of South American caviomorph rodents or platyrrhine (New World) monkeys, and that their closest relatives lived on the Afro-Arabian landmass during the Eocene epoch (56 to 34 million years ago). Therefore, to reach South America, these animals would have had to cross the South Atlantic Ocean—which probably was more than 1500 to 2000 km wide during this period. On page 194 of this issue, Seiffert *et al.* (*1*) report on fossils, from Santa Rosa in Amazonian Perú, that provide evidence of a third mammalian lineage of African origin that briefly appeared in South America in the early Oligocene (35 to 32 million years ago): a now-extinct parapithecid anthropoid monkey (genus: *Ucayalipithecus*).

Crossing an ocean on a raft is an exceptional feat, especially for small mammals, some of which lack the capacity to endure seasonal food shortages. Such a crossing also necessitates the accessibility of big vegetation-containing rafts (produced by tropical storms), favorable oceanic currents, a drop in sea level, and, possibly, island stopovers on emerged parts of the mid-Atlantic ridge (see the figure). Indeed, only two mammalian groups crossed the Atlantic Ocean during a time period of more than 50 million years, from the Eocene to the present. Scientists have wondered whether the crossings were one and the same event for both groups.

For several decades, fossil evidence has suggested that rodents were present in the

Ecole Pratique des Hautes Etudes, Museum National d'Histoire Naturelle, Centre National de la Recherche Scientifique, and Paris 6 University, Paris, France.
Email: marc.godinot@mnhn.fr

GRAPHIC: C. BICKEL/*SCIENCE*

South American land mammal age, which preceded the mammal age, during which primates appeared. However, the discovery of primates (*Perupithecus* and at least one other form) much earlier in the Santa Rosa fauna appeared to bring the two events closer together in time (*2*).

Although the dispersing genera are not yet identified, new discoveries are revealing closer representatives of both groups on the South American and African continents. Caviomorph rodents of late Middle Eocene age (*3*) demonstrate a dispersal from one continent to the other at least ~41 million years ago. As for primates, not only was *Perupithecus* recognized to be relatively similar to some late Eocene African relatives, but Seiffert *et al*. show that their *Ucayalipithecus* fossil is extremely close to similar well-dated fossils from African relatives. This similarity provides a relatively narrow time window for the dispersal of the *Ucayalipithecus* primate or its ancestor (35 to 32 million years ago).

The morphology of the newly discovered *Ucayalipithecus* fossil leaves no doubt that it is a parapithecid, a distinct family, unique among primates, that until now was known to have existed only in Egypt, Libya, and Tanzania. Thus, it is likely that the parapithecid and the ancestor of the other Santa Rosa primates came from the same dispersal event. Hence, paleontologists now have convincing evidence for two distinct dispersals, one for rodents and one for primates, each separated by 10 million years or more.

These dispersals raise many intriguing issues for further research. Concerning primate dispersals out of Africa, there is a strong contrast between the two sides of the continent. Dispersals to Madagascar crossed much shorter distances; however, because of unfavorable currents, such crossings were also rare. Yet 2 years ago, scientists showed that, on the eastern side of Africa, two different lemur lineages crossed over to Madagascar (*4*). So why did two types of anthropoids cross over on one side and two types of lemurs on the other? A possible explanation is size. During the Eocene in Africa, anthropoids were small and some strepsirrhine primates were large, whereas later, during the Oligocene, anthropoids became larger. A large size is a serious obstacle to surviving several days of rafting. However, there were also some small strepsirrhines in the Eocene that might have been carried along westward.

Rafting route

A *Ucayalipithecus* monkey or its ancestor sailed from West Africa to South America on the south equatorial paleocurrent (SEC). Recent data (*11*) suggest that teiid lizards crossed over from South America on the north equatorial countercurrent (NECC), eventually arriving in Eocene Europe. Continental positions are from the Oligocene.

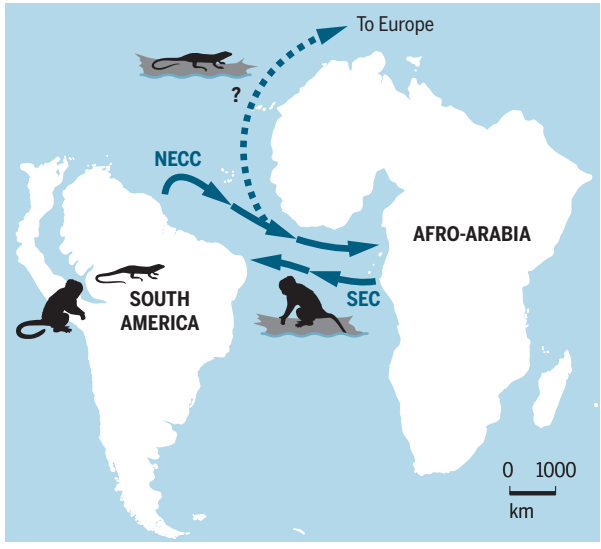

South American rain forests, like this one in Amazonian Perú, are among the most diverse tropical forests on Earth. Some of its components came from Africa during the Tertiary period.

If several dispersals of mammals took place, other animals and plants should follow the same patterns—for example, the trees that gave rise to the natural rafts. Plant dispersals are tracked through dated phylogenetic analyses. Molecular phylogenies of a woody plant family (*5*) and of gecko lizards (*6*) provide hypotheses of such dispersals. When the fossil record indicates the absence of a family in North America, the case for dispersal becomes stronger, as for amphisbaenids, a group of fossorial lizards (*7*). When fossils provide the primary evidence, the scenario becomes even more convincing, as for the primate reported here, rodents, and probably also birds with weak flight capabilities (*8*).

After crossing an ocean, species face serious challenges in order to survive and flourish in their new environment. As Seiffert *et al*. note, these early anthropoids must have been remarkably adaptable to harsh conditions to have survived the crossing. Furthermore, they succeeded in invading a new territory; the environment was not empty, and the early anthropoids settled more than 4000 km away from their landing area. Yet, despite this impressive performance, parapithecids did not manage to survive for long and diversify. This is even more surprising considering that parapithecids were specialized for hard-object feeding, and one of the present-day subfamilies of South American monkeys, the Pitheciinae (sakis and ouakaris), is also adapted to feeding on hard fruits and seeds. Were these resources already present at the time of crossing over, or were there changes in the composition of South American tropical forests?

These forests were established by the Paleocene (66 to 56 million years ago) and were not disturbed by warming episodes. In contrast, they experienced high diversification rates during these episodes (*9*). An exciting research avenue concerns the composition of these forests, in which rodents and primates play an important role in seed dispersal (*10*). A better record of fossil fruits and seeds in South America should provide critical information on both forest composition and plant dispersal—two important aspects of these tropical forests, which are the most diverse on Earth. ■

REFERENCES AND NOTES

1. E. R. Seiffert *et al.*, *Science* **368**, 194 (2020).
2. M. Bond *et al.*, *Nature* **520**, 538 (2015).
3. P.-O. Antoine *et al.*, *Proc. R. Soc. London Ser. B* **279**, 1319 (2012).
4. G. F. Gunnell *et al.*, *Nat. Commun.* **9**, 3193 (2018).
5. L. Bardon *et al.*, *Bot. J. Linn. Soc.* **171**, 19 (2013).
6. T. Gamble *et al.*, *J. Evol. Biol.* **24**, 231 (2011).
7. N. Vidal, A. Azvolinsky, C. Cruaud, S. B. Hedges, *Biol. Lett.* **4**, 115 (2008).
8. G. Mayr, H. Alvarenga, C. Mourer-Chauviré, *Naturwissenschaften* **98**, 961 (2011).
9. C. Jaramillo, A. Cárdenas, *Annu. Rev. Earth Planet. Sci.* **41**, 741 (2013).
10. P.-M. Forget *et al.*, in *Seed Dispersal*, A. J. Dennis *et al.*, Eds. (CAB International, 2007), pp. 5–36.
11. M. L. Augé, S. Brizuela, *Palaeobio. Palaeoenv.* 10.1007/s12549-019-00414-2 (2020).

10.1126/science.abb4107

CREDITS: (GRAPHIC) A. KITTERMAN/*SCIENCE*; (PHOTO) CYRIL RUOSO/MINDEN PICTURES

POLICY FORUM

BIOSECURITY

Embrace experimentation in biosecurity governance

We must rethink and test assumptions about relationships among biological research, security, and society

By **Sam Weiss Evans[1,2,3], Jacob Beal[4], Kavita Berger[5], Diederik A. Bleijs[6], Alessia Cagnetti[7], Francesca Ceroni[8,9], Gerald L. Epstein[10], Natàlia Garcia-Reyero[11], David R. Gillum[12], Graeme Harkess[13], Nathan J. Hillson[14], Petra A. M. Hogervorst[6], Jacob L. Jordan[15], Geneviève Lacroix[16], Rebecca Moritz[17], Seán S. ÓhÉigeartaigh[3], Megan J. Palmer[18], Mark W. J. van Passel[6]**

As biological research and its applications rapidly evolve, new attempts at the governance of biology are emerging, challenging traditional assumptions about how science works and who is responsible for governing. However, these governance approaches often are not evaluated, analyzed, or compared. This hinders the building of a cumulative base of experience and opportunities for learning. Consider "biosecurity governance," a term with no internationally agreed definition, here defined as the processes that influence behavior to prevent or deter misuse of biological science and technology. Changes in technical, social, and political environments, coupled with the emergence of natural diseases such as coronavirus disease 2019 (COVID-19), are testing existing governance processes. This has led some communities to look beyond existing biosecurity models, policies, and procedures. But without systematic analysis and learning across them, it is hard to know what works. We suggest that activities focused on rethinking biosecurity governance present opportunities to "experiment" with new sets of assumptions about the relationship among biology, security, and society, leading to the development, assessment, and iteration of governance hypotheses.

Traditional international biosecurity efforts have focused largely on risk management (i.e., addressing accidental and deliberate risks from pathogens and toxins) and dual-use research (i.e., potential malicious exploitation of knowledge, skills, and technology). These efforts assume that we already know what to worry about (lists of known pathogens and toxins) and how to govern it (access control), even if organizations implementing biosecurity recognize the shortcomings and limitations of these assumptions (*1*).

In the past decade, however, our ability to manipulate living organisms and entire genomes has advanced rapidly through the development of tools such as CRISPR, modern sequencing techniques, and genome synthesis and assembly approaches. This has allowed us to generate microbes, cell types, animals, plants, materials, and tools (e.g., gene drives), all of which have elicited security concerns. Moreover, concern about state and non-state actor weaponization of biology continues (*2*–*4*). The following examples show how new approaches to governance, although innovative, are currently sporadic and often ad hoc responses to particular security deficiencies.

After heated debate about two experiments involving the identification of specific mutations in H5N1 avian influenza that enable spread between mammals, the U.S. government developed policies on review and oversight of dual-use research of concern (DURC), requesting federal funding agencies and institutions to review, modify, and/or oversee certain research. Under the assumption that such oversight would be implemented only if minimally invasive, the policies restricted oversight to a subset of work on a subset of known pathogens and experimentally derived traits. Recognizing that these policies still focus on known pathogens and do not address risks from modification of respiratory pathogens, the United States developed an additional policy focused instead on post-experiment attributes of an organism in 2017. This Potential Pandemic Pathogen Care and Oversight policy was also the first to consider under which conditions such research is ethical. Regular and systematic review of these policies is essential (*5*) but currently ad hoc.

A decade ago, the U.S. Federal Bureau of Investigation (FBI) Biological Countermeasures Unit decided that countering potential biosecurity events required staying abreast of advances in biology and engaging closely with the life science research community, including universities, companies, and the emerging do-it-yourself (DIY) community labs. This meant building internal scientific expertise and community liaison capacity, both of which were contrary to the public's image of the FBI and how it operates (*6*). Moreover, these efforts called on scientists to take responsibility for identifying and addressing potential security concerns.

The American Biological Safety Association (ABSA) International observed that biosafety professionals have been increasingly asked to assess security in addition to safety aspects of research, but do not know how to assess security concerns, and, perhaps more important, how to think about malicious intent and intentional release. ABSA concluded that further training would improve security and promote common biosecurity practices throughout the scientific community through educational opportunities and development of a global biosecurity credential (*7*).

We do not have perfect knowledge of the ways that biology might be used by malicious actors, or of the best ways to prevent such uses. No a priori reason exists to believe that our original assumptions and hypotheses are optimal. The consequences of getting assumptions wrong, such as a pandemic caused by a laboratory-derived pathogen, are among the strongest arguments for testing a wide range of assumptions in ways that can provide signals of effectiveness prior to catastrophic events.

An experimental approach focuses attention on the need to be systematic and open about analyzing the limitations of existing systems and promoting actions that address or work around them. It also means developing better methods to collect data

[1]Program on Science, Technology, and Society, Harvard University, Cambridge, MA, USA. [2]Program on Emerging Technology, Massachusetts Institute of Technology, Cambridge, MA, USA. [3]Centre for the Study of Existential Risk, University of Cambridge, Cambridge, UK. [4]Raytheon BBN Technologies, Cambridge, MA, USA. [5]Gryphon Scientific, Takoma Park, MD, USA. [6]Netherlands Biosecurity Office, National Institute for Public Health and the Environment, Bilthoven, Netherlands. [7]Polo d'Innovazione Genomica Genetica e Biologia (PoloGGB), Terni, Italy. [8]Department of Chemical Engineering, Imperial College London, London, UK. [9]Imperial College Centre for Synthetic Biology, London, UK. [10]Center for the Study of Weapons of Mass Destruction, National Defense University, Washington, DC, USA. [11]Engineer Research and Development Center, U.S. Army, Vicksburg, MS, USA. [12]Arizona State University, Tempe, AZ, USA. [13]Pirbright Institute, Pirbright, UK. [14]Joint Genome Institute, U.S. Department of Energy, Berkeley, CA, USA. [15]Nuclear Threat Initiative, Washington, DC, USA. [16]Centre for Biosecurity, Public Health Agency of Canada, Ottawa, Canada. [17]University of Wisconsin, Madison, WI, USA. [18]Center for International Security and Cooperation, Stanford University, Stanford, CA, USA. Email: samuel_evans@harvard.edu

such hypotheses held up, and if not, what might need changing. This lesson might involve, for example, structured feedback from community labs about FBI engagement, and routinized sharing across field offices of standard procedures for developing community relationships. Working with social scientists who can help to identify assumptions and develop alternatives that might better align with the goals of governance could be helpful in designing and documenting these experiments in governance (*14*).

Developing a capacity to quickly identify difficult or unanticipated cases allows for governing processes to adapt and account for them. To the extent possible, sharing case studies—including both failures and "near misses"—in a timely fashion could aid other biosecurity processes greatly. iGEM developed this capacity and quickly put it to work when a 2016 student team claimed to be developing a gene drive. After working closely with the team and experts to understand exactly what was and was not accomplished, iGEM became one of the first places to produce a policy on gene drives. It then wrote up its lessons learned and shared them with the wider biosecurity community.

Learning involves connecting with communities that have tried similar experiments and could build on earlier results. These groups range from networks of community biolabs to international efforts such as the Global Health Security Agenda's action package on biosafety and biosecurity. Two examples of connecting communities are the leadership programs through the Johns Hopkins Center for Health Security (Emerging Leaders in Biosecurity Initiative) and Stanford University [Synthetic Biology Leadership Excellence Accelerator Program (LEAP)], both of which provide opportunities for policy experts and/or scientists to learn about biosecurity concerns and approaches for addressing those concerns within their networks. Additionally, specific fora such as the Biological and Toxin Weapons Convention Meeting of Experts, or non-state venues such as the ABSA International Biosecurity Symposium, provide opportunities for stakeholders to engage in biosecurity governance. Developing communication across communities means addressing barriers to communication, such as industrial considerations of competition sensitivity, governmental controls (e.g., export restriction, classification), and differing terminology.

Taking a structured approach to experimental design, periodically reassessing, and cooperating may seem like simple steps to take, but our collective experience suggests that biosecurity efforts over the past two decades—from promoting self-governance to requiring oversight of pathogen research—have largely not taken these steps. They require thinking beyond the current crisis, testing design choices (e.g., the use of lists), and being willing and able to rethink basic assumptions, such as the idea that both science and security are things that can be governed in isolation from other aspects of society.

An immediate step to expand and revise these lessons is for philanthropies, governments, and others to fund a review of existing biosecurity governance experiments, with the aim of determining how they are being implemented in practice. The findings from such a review could be integrated into policy redesign and could inform networks of biosecurity practitioners. Such a review also would focus on industries and regions of the world that have little to no current biosecurity governance in place. The industrial and commercial development of biology represents a substantial amount of biological research and innovation. Industrial organizations have considerable influence on state governance decisions, and in addition they are trying out biosecurity governance themselves through efforts such as sequence screening in the International Gene Synthesis Consortium, which might benefit from a more experimental design. For many regions of the world without biosecurity governance, getting basic oversight capacity in place is already a major challenge.

The biosecurity community should establish and strengthen shared resources to help groups wishing to establish new governance systems for their communities, such as the Analytical Approach for the Development of a National Biosafety and Biosecurity System, published by the Public Health Agency of Canada. It also should strengthen resources for cooperation and learning across regions of the world, such as the International Network on Biotechnology run by the United Nations Interregional Crime and Justice Research Institute.

Publicly discussing specific instances of biosecurity concern that our governance systems do not cover can itself be an information hazard, but the processes of biosecurity governance may be less of a hazard to discuss. Institutions have many reasons beyond security (such as reputational and intellectual property risks) to not share information, and we encourage the exploration of options to discuss these more sensitive issues. A particularly important challenge is enabling the safe migration of useful lessons between more restricted environments (e.g., classified facilities, industrial operations) and less restricted environments (e.g., the DIY community). Sharing an evidence base that describes what has and has not worked is a necessary aspect of developing biosecurity governance that simultaneously reduces risk and promotes scientific progress (*15*).

At present, no capability for systematic learning about the effectiveness and limitations of current biosecurity governance exists. If we can come to understand governance as an experimental space, we will be able to make more than sporadic movement past reactive approaches, and thus protect our economic vitality, academic freedom, and the health and security of our states, people, and environment. ■

REFERENCES AND NOTES

1. D. DiEuliis, V. Rao, E. A. Billings, C. B. Meyer, K. Berger, *Health Secur.* **17**, 83 (2019).
2. C. McLeish, D. Feakes, *Sci. Public Policy* **35**, 5 (2008).
3. L. Stampnitzky, *Disciplining Terror: How Experts Invented "Terrorism"* (Cambridge Univ. Press, 2013).
4. *National Security Strategy of the United States* (The White House, 2017).
5. Institute of Medicine and National Research Council, *Globalization, Biosecurity, and the Future of the Life Sciences* (National Academies Press, 2006).
6. S. Tocchetti, S. A. Aguiton, *Sci. Technol. Human Values* **40**, 825 (2015).
7. R. L. Moritz, K. M. Berger, B. R. Owen, D. R. Gillum, *Science* **367**, 856 (2020).
8. M. J. Palmer, F. Fukuyama, D. A. Relman, *Science* **350**, 1471 (2015).
9. F. Daviter, in *Learning in Public Policy: Analysis, Modes and Outcomes*, C. A. Dunlop, C. M. Radaelli, P. Trein, Eds. (Palgrave Macmillan, 2018), pp. 145–165.
10. I. van de Poel, D. C. Mehos, L. Asveld, in *New Perspectives on Technology in Society: Experimentation Beyond the Laboratory*, I. van de Poel, L. Asveld, D. C. Mehos, Eds. (Routledge, 2018), pp. 1–15.
11. P. Millett *et al.*, *Appl. Biosaf.* **24**, 64 (2019).
12. B. Rappert, *Front. Public Health* **2**, 74 (2014).
13. N. Hafer *et al.*, *Sci. Progress* (February 2009); www.scienceprogress.org/wp-content/uploads/2009/02/how_scientists_view_law_enforcement.pdf.
14. A. S. Balmer *et al.*, *Sci. Technol. Stud.* **28**, 3 (2015).
15. National Academies of Sciences, Engineering, and Medicine, *Governance of Dual Use Research in the Life Sciences: Advancing Global Consensus on Research Oversight: Proceedings of a Workshop* (National Academies Press, 2018).

ACKNOWLEDGMENTS

The views expressed in the paper are those of the authors and not of any institutions with which they may be affiliated. This document does not contain technology or technical data controlled under either U.S. International Traffic in Arms Regulation or U.S. Export Administration Regulations. We thank participants of the Novel Practices in Biosecurity Governance workshop organized by S.W.E. at the University of Cambridge in July 2019 through the Biosecurity Research Initiative at St. Catharine's (BioRISC) and the Centre for the Study of Existential Risk (CSER). The workshop was supported with funding from the Hauser-Raspe Workshop Series. S.W.E. was supported by a Schmidt Futures grant and the Templeton World Charity Foundation. J.L.J. and M.J.P. were supported by the Open Philanthropy Project. N.G.-R. was supported by the Future Innovation Fund. D.R.G. is the 2020 president of ABSA. S.W.E. and M.J.P. are on iGEM's Safety and Security Committee and LEAP. M.W.J.v.P. recently stepped down as Chair of Action Package 3 for the Global Health Security Agenda (GHSA). K.B. serves as deputy chair of the GHSA Consortium. G.H. sits on the Biosafety Strategic Leadership Group. N.J.H. runs the Joint Genome Institute extended screening for synthetic biology funding distribution.

10.1126/science.aba2932

immunoSEQ®

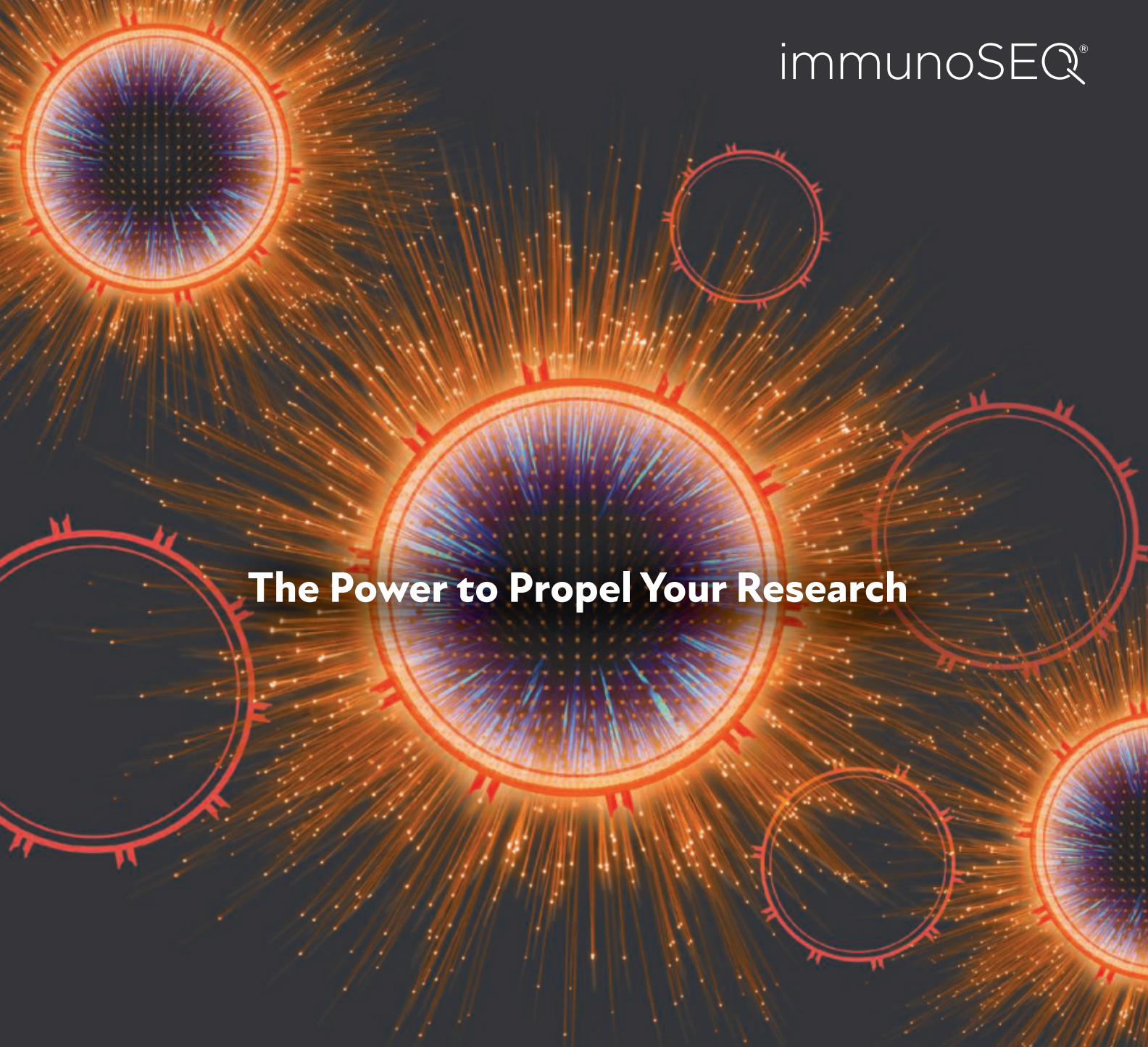

The Power to Propel Your Research

Illuminate the properties and dynamics of the immune repertoire with the quantitative power of the immunoSEQ assay. In our lab or yours, our proven solution elucidates the breadth and depth of T- and B-cell receptors to help you interpret the vast immune system with clarity. Adaptive Biotechnologies champions your research so you can accelerate your path to discovery.

Set your research in motion at AdaptiveBiotech.com

Adaptive biotechnologies®

For Research Use Only.
Not for use in diagnostic procedures.

ANIMAL BEHAVIOR

Considering nonhuman culture

Animals have much to teach us about communication, mate preference, and social hierarchy

By **Mary Ellen Hannibal**

Becoming Wild: How Animal Cultures Raise Families, Create Beauty, and Achieve Peace
Carl Safina
Henry Holt, 2020. 384 pp.

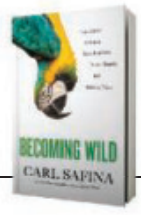

Nonhuman culture has been hugely underestimated, to the detriment of both *Homo sapiens* and the creatures with whom we share Earth, argues Carl Safina in his new book, *Becoming Wild*. Framing culture as a process of learned behaviors that help shape modes of living, Safina's bracing and enlightening book focuses on three distinct dimensions of nonhuman life: In sperm whales, Safina finds layered communication strategies for organizing and maintaining family and clan. In macaws and other visually stunning animals, he finds that beauty is an enduring cultural attribute. And in Uganda's Budongo Forest, Safina focuses on the nuances of chimpanzee behaviors by which social structure is established and enforced.

As he did in *Beyond Words*, in this book Safina wants to decenter the human (*1*). He considers the persistent influence of Aristotle's scala naturae, which ordered the universe into a ladder with God at the top, *Homo sapiens* next, and animals and plants below, with each layer having priority over those under it. We may balk at such an antiquated conception of life, but how many of us regularly consider the individuality and subjectivity of the nonhuman life around us?

Readers follow along as Shane Gero, cruising off the coast of the small Caribbean island Dominica, drops a hydrophone into the deep waters. The immensity of sea and sky are suddenly populated with evidence of a booming unseen. Gero's equipment detects sonar clicks made by sperm whales miles away, allowing him to eavesdrop on a complex, multilevel communication network. Gero, a marine biologist, uses bioacoustics to classify different call types among the whales, who use unique calls to recognize each other, keep themselves segregated by clan, and make movement decisions. Clicking may be instinctive and inherited, but the finer characteristics of the sounds are learned. The fact that these whales learn from each other is evidence that their lives are more than competition, predation, survival, and selection—they include social learning and culture.

Safina is a marine biologist, and his writing on the watery depths and its denizens is sublime. Traveling with Gero at a fast clip, Safina writes, "We're at what's called sea level, as though an ocean is solely surficial…In reality we are skimming the thick, wide, densely inhabited world beneath us. The vast majority of the life on Earth flows through the universe below."

Sperm whales, we learn, have the only "cultural groupings that exist at transoceanic scale. Everywhere sperm whales have been studied…researchers see attraction within clans, repulsion between." These whales thus evince a sense of self, identifying themselves as individuals among other individuals that belong to distinct groups. Such fascinating realizations have practical impacts.

Sperm whales rely on complex communication strategies to organize and maintain family and clan.

For hundreds of years, whales have been hunted to near or outright extinction. Their decimation continues today. Taking out individual whales has reverberating impacts, both in the ocean ecosystem at large and among the family and clan groups that these individual whales help to cohere.

Safina ponders beauty in the animal kingdom while exploring the Tambopata Macaw Project, an endeavor to understand the ecology of macaws and other parrots in order to help conserve them in the lowlands of southeastern Peru. He is beguiled by the dozen and a half species of "spectacularly huge, spectacularly hued" birds. These charms also make them very attractive to the exotic pet trade, which is one of the reasons for the birds' vast decline. (Macaw populations are also being decimated today as a result of habitat loss and fragmentation.)

The extravagance of macaws begs one of the longest-standing questions in evolutionary biology: Why and how would natural selection result in the seeming superfluousness of such great beauty? Here, Safina references the work of ornithologist Richard Prum, who has recently argued that Darwin was right in asserting that beautiful males are thus because females like them that way (*2*).

"And what of the beautiful macaws who have expanded my soul?" Safina asks. Noting that beauty is a "realm of diversity," he wonders what will happen if human impacts continue to simplify that diversity: "What are the implications for the continued evolution of beauty—or for the survival of the beautiful?"

Chimps, we learn in the book's final section, share not only most of our DNA but also a lot of our behaviors. And while these include degrees of altruism and empathy, in general, it is not a pretty picture. Safina recounts the example of a male chimp that beat and eventually murdered a female, evidently because she refused to follow him around when he demanded that she do so. "Violence from *inside* the community; that's what's unusual about chimps—and about us," he writes.

Some of Safina's assertions may require tweaks and adjustments as more data come in—the study of cognition, both animal and human, is still in its infancy—but in stretching his own mind, he challenges us to be more acutely aware of species whose social lives have much to teach us. ■

The reviewer is the author of *Citizen Scientist: Searching for Heroes and Hope in an Age of Extinction* (The Experiment, 2016). Email: maryellenhannibal@gmail.com

PHOTO: CARL SAFINA

REFERENCES AND NOTES

1. C. Safina, *Beyond Words: What Animals Think and Feel* (Henry Holt, 2015).
2. R. O. Prum, *The Evolution of Beauty: How Darwin's Forgotten Theory of Mate Choice Shapes the Animal World—and Us* (Doubleday, 2017).

10.1126/science.aba6489

GemPharmatech
www.gempharmatech.com

GemPharmatech Co., Ltd. (GPT), currently operating both in China and United States, is a leading international company focusing on mouse model development, production and services. We are dedicated to support the biomedical research and pharmaceutical R&D. GPT provides one-stop solutions related to mouse model.

Knock-Out All Project (KOAP) Mice Resources:
aiming to generate cKO/KO mouse strains for over 20,000 protein-coding genes in three years

ACE2, ALKBH1, C3AR1, CGAS, DNM1L, FNDC5, GPNMB, GPX4, IFNAR1, METTL3, NAT10, NSUN2, OPA1, SENP1, TET3, TLR2, TMEM173, VDR, etc.

Search your ideal models via signal pathways:
http://pathway.gempharmatech.com:8082/pathway

Immuno-Deficiency Mice and Derivatives:
severe immuno-deficiency mice displaying excellent engraftment of human tissue

NCG, NCG-B2M-KO, NCG-hIL15, NCG-X (No irradiation required), HuPBMC-NCG, HuHSC-NCG, etc.

Humanized I/O Mice Resources:
single, double, and triple knock-in models covering almost all published human immune checkpoint targets
Bispecific Antibody Evaluation: BALB/c-hCD3e
Humanized Immune Checkpoint: PD1, PDL1, CTLA4, 4-1BB, TIGIT, TIM3, LAG3, SIGLEC9, SIGLEC15, OX40, CD47/SIRPα, CD73, VISTA, CSF1R, etc.

GemPharmatech

5,000+
Annual Capacity of Mouse Model Generation

10,000+
In-house Animal Models

140,000+
Total Cages in SPF Facility

AAALAC-Accredited Facility

Support disease studies with right animal models

Web：www.gempharmatech.com
Tel：+86 (025) 5864-1508 China +1 (857) 600-6638 USA
E-mail：globalservice@gempharmatech.com

Social isolation can affect mental health, putting vulnerable people at greater risk.

PHOTO: ISTOCK.COM/IZUSEK

英文杂志首发qq群 1067583220

Edited by **Jennifer Sills**

Protecting older adults during social distancing

As the coronavirus disease 2019 (COVID-19) pandemic progresses, social distancing has emerged as an effective measure to restrain the spread of infections. Many people are now confining themselves to indoor spaces and communicating with their loved ones only through the use of electronic tools. This may have a detrimental effect on mental health, especially for adults over the age of 65, who may be less comfortable with virtual solutions (*1*). We must work to prevent social distancing from becoming social isolation among this vulnerable group.

Social isolation in seniors has been linked to increased depression and suicidality as well as to increased pro-inflammatory and decreased anti-viral immune responses (*2*–*4*). These effects may further increase the susceptibility of this population to COVID-19. Health care systems and communities must consider the mental health burden of social distancing for the elderly and find ways to keep them engaged and motivated. Mainstream media, such as television and radio, can play an important role by including content focused on the elderly and encouraging seniors to express their views through live calls. Data indicate that the elderly view television as a medium to cope with depressive symptoms and might benefit from such engagement (*5*). Volunteers can maintain regular phone contact with the homebound elderly population, providing friendship and fostering a mentoring relationship, as it has been shown that adults over 60 years of age find their life more meaningful when they have the opportunity to give advice (*6*). Finally, existing mental health support hotlines could add outgoing calls during which mental health professionals could reach out to the elderly and screen for symptoms of anxiety and depression. These measures could improve older adults' compliance with social distancing and help reduce the impact of COVID-19 on their mental health.

Ali Jawaid
Brain Research Institute, University of Zurich, Zurich, Switzerland. Email: jawaid@hifo.uzh.ch

REFERENCES AND NOTES

1. B. Knowles, V. L. Hanson, *Comm. ACM* **61**, 72 (2018).
2. S. W. Cole *et al.*, *Proc. Natl. Acad. Sci. U.S.A.* **112**, 15142 (2015).
3. Z. I. Santini *et al.*, *Lancet Pub. Health* **5**, e62 (2020).
4. K. Gerst-Emerson, J. Jayawardhana, *Am. J. Pub. Health* **105**, 1013 (2015).
5. G. T. Nguyen *et al. Gerontologist* **48**, 300 (2009).
6. M. H. Schafer, L. Upenieks. *Soc. Psych. Quart.* **79**, 22 (2016).

10.1126/science.abb7885

Aggregated mobility data could help fight COVID-19

As the coronavirus disease 2019 (COVID-19) epidemic worsens, understanding the effectiveness of public messaging and large-scale social distancing interventions is critical. The research and public health response communities can and should use population mobility data collected by private companies, with appropriate legal, organizational, and computational safeguards in place. When aggregated, these data can help refine interventions by providing near real-time information about changes in patterns of human movement.

Research groups and nonprofit humanitarian agencies have refined data use agreements to stipulate clear guidelines that ensure responsible data practices (*1*). New tools for specifying different levels of privacy for different users and providing privacy-preserving results, such as the OpenDP platform (*2*), will effectively manage data access, and aggregation steps have been carefully reviewed on a legal and methodological basis to ensure that the analyses follow ethical guidelines for human participants (*3*). To monitor social distancing interventions, for example, rather than showing individual travel or behavior patterns, information from multiple devices is aggregated in space and time, so that the data reflect an approximation of population-level mobility (*4*).

The estimates of aggregate flows of people are incredibly valuable. A map that examines the impact of social distancing messaging or policies on population mobility patterns, for example, will help county officials understand what kinds of messaging or policies are most effective. Comparing the public response to interventions, in terms of the rate of movement over an entire county from one day to the next, measured against a

baseline from normal times, can provide insight into the degree to which recommendations on social distancing are being followed. We will need these estimates, not only now but also when we need to resume life again without risking a major resurgence.

The protection of personal privacy must be paramount. Consent-based data sharing models and data protection laws provide for the legal grounds to use personal data during emergencies, but we do not advocate the use of individual data (*5*, *6*). The measures proposed do not need to run afoul of data protection goals, as a recent statement by the Chair of the European Data Protection Board in the context of the COVID-19 outbreak clarifies (*7*).

There are already precedents in Asia and Europe (*8*). Deutsche Telekom has shared aggregated data with Germany to help measure social distancing, in compliance with EU laws (*9*). The more such analyses are initiated and concluded openly, and in accordance with the law, the greater will be the public trust and our ability to produce reliable analytic insights. Associated risks should be thoughtfully addressed and weighed against the benefits of the data, which could help reduce the death toll in vulnerable populations.

Caroline O. Buckee[1]*, Satchit Balsari[2], Jennifer Chan[3,4], Mercè Crosas[5], Francesca Dominici[6], Urs Gasser[7], Yonatan H. Grad[1], Bryan Grenfell[8], M. Elizabeth Halloran[9,10], Moritz U. G. Kraemer[11,12], Marc Lipsitch[1], C. Jessica E. Metcalf[8], Lauren Ancel Meyers[13], T. Alex Perkins[14], Mauricio Santillana[15,12], Samuel V. Scarpino[16], Cecile Viboud[17], Amy Wesolowski[18], Andrew Schroeder[19]

[1]Center for Communicable Disease Dynamics, Harvard T.H. Chan School of Public Health, Boston, MA 02115 USA. [2]Emergency Medicine, Beth Israel Deaconess Medical Center, Harvard Medical School, Boston, MA 02115, USA. [3]Emergency Medicine, Feinberg School of Medicine, Northwestern University, Chicago, IL 60611. [4]NetHope, Inc., Fairfax, VA 22030, USA. [5]Institute for Quantitative Social Science, Harvard University, Boston, MA 02138, USA. [6]Harvard Data Science Initiative, Harvard University, Boston, MA 02138, USA. [7]Berkman Klein Center for Internet and Society, Harvard University Harvard Law School, Boston, MA 02138, USA. [8]Princeton University, Princeton, NJ 08540, USA. [9]Center for Inference and Dynamics of Infectious Diseases, Fred Hutchinson Cancer Research Center, Seattle, WA 98109, USA. [10]University of Washington, Seattle, WA 98195, USA. [11]Department of Zoology, University of Oxford, Oxford OX1 3SZ, UK. [12]Boston Children's Hospital, Boston, MA 02115, USA. [13]The University of Texas at Austin, Austin, TX 78702, USA. [14]Department of Biological Sciences and Eck Institute for Global Health, University of Notre Dame, Notre Dame, IN 46556, USA. [15]Department of Pediatrics, Harvard Medical School, Boston, MA 02115, USA. [16]Network Science Institute, Northeastern University, Boston, MA 02115, USA. [17]Fogarty International Center, National Institutes of Health, Bethesda, MD 20892, USA. [18]Department of Epidemiology, Johns Hopkins Bloomberg School of Public Health, Baltimore, MD 21205, USA. [19]Direct Relief, Santa Barbara, CA 93117, USA.
*Corresponding author.
Email: cbuckee@hsph.harvard.edu

Disinfectants used to combat the spread of COVID-19 will end up in the environment.

PHOTO: NARAYAN MAHARJAN/NURPHOTO/GETTY IMAGES

REFERENCES AND NOTES

1. F. Greenwood *et al.*, "The signal code: A human rights approach to information during crisis" (Signal Program on Human Security and Technology, Harvard Humanitarian Initiative, 2015); https://hhi.harvard.edu/sites/default/files/publications/signalcode_final.pdf.
2. Harvard University Privacy Tools and Privacy Insights Project, OpenDP (http://opendp.io).
3. Y. de Montjoye *et al.*, *Sci. Data* **5**, 180286 (2018).
4. P. Maas *et al.*, "Facebook disaster maps: Aggregate insights for crisis response & recovery," Facebook (2019); https://research.fb.com/wp-content/uploads/2019/04/iscram19_camera_ready.pdf.
5. California Consumer Privacy Act (2020); https://oag.ca.gov/privacy/ccpa.
6. B. Puckett, S. J. McMenemy, "Maintaining employees' privacy during a public health crisis," *National Law Review* (2020); www.natlawreview.com/article/maintaining-employees-privacy-during-public-health-crisis.
7. "Statement of the EDPB Chair on the processing of personal data in the context of the COVID-19 outbreak" (2020); https://edpb.europa.eu/sites/edpb/files/files/news/edpb_covid-19_20200316_press_statement_en.pdf.
8. S. Lai *et al.*, "Assessing spread risk of Wuhan novel coronavirus within and beyond China," medRxiv 2020.02.04.20020479 (2020); https://doi.org/10.1101/2020.02.04.20020479.
9. E. Pollina, D. Busvine, "European mobile operators share data for coronavirus fight," *Reuters* (2020).

COMPETING INTERESTS

S.V.S. is a member of the Scientific Advisory Board of BioFire Diagnostic's Trend Surveillance System, which includes paid consulting work.

Published online 23 March 2020
10.1126/science.abb8021

Disinfection threatens aquatic ecosystems

In an effort to contain the spread of coronavirus disease 2019 (COVID-19), China has been applying chlorine disinfectants to both indoor and outdoor spaces. To minimize opportunities for the severe acute respiratory syndrome–coronavirus 2 (SARS-CoV-2)—the virus that causes COVID-19—to thrive, China has dispensed more than 5000 tons of disinfectants in Wuhan City alone (*1*). These chemicals can get into sewage systems and pollute drinking water resources (*1*). Both the direct runoff and indirect sewage effluents will eventually end up in lakes and rivers, putting aquatic ecosystems at risk (*2*).

Chlorine disinfectants threaten aquatic plants and wildlife in two ways. First, chlorine can directly harm organisms by destroying their cell walls or damaging their proteins by oxidation (*2*). Second, the chemicals in the disinfectants can bond with other materials to form harmful compounds. In surface water, dissolved organic matter is extremely high (*3*), which could allow the synthesis of disinfection by-products, such as trihalomethanes or haloacetic acids (*2*). These by-products have been shown to be very toxic to aquatic organisms (*4*). In addition, disinfectants could combine with nitrogen, forming chloramine or N-nitrosodimethylamine (*5*), both of which have been identified as carcinogens (*6*).

As COVID-19 spreads across the globe, the increased use of disinfectants could lead to worldwide secondary disasters in aquatic ecosystems. We appeal to the governments of China and other affected countries to conduct aquatic ecological integrity assessments (*7*) during and after the pandemic. This could save biodiversity and protect humans from future health threats stemming from polluted water.

Hong Zhang[1,4]*, Wenzhong Tang[1,4], Yushun Chen[2,4], Wei Yin[3]

[1]State Key Laboratory of Environmental Aquatic Chemistry, Research Center for Eco-Environmental Sciences, Chinese Academy of Sciences, Beijing 100085, China. [2]State Key Laboratory of Freshwater Ecology and Biotechnology, Institute of Hydrobiology, Chinese Academy of Sciences, Wuhan, Hubei 430072, China. [3]Changjiang Water Resources Protection Institute, Wuhan, Hubei 430051, China. [4]University of Chinese Academy of Sciences, Beijing 100049, China.
*Corresponding author.
Email: hongzhang@rcees.ac.cn

REFERENCES AND NOTES

1. China Ministry of Ecology and Environment, "Will viruses and disinfection affect water quality? The Ministry of Ecology and Environment responded" (2020); www.mee.gov.cn/ywgz/ssthjbh/dbssthjgl/202003/t20200311_768408.shtml [in Chinese].
2. D. L. Sedlak, U. von Gunten, *Science* **331**, 42 (2011).
3. J. A. Leenheer, in *Environmental Chemistry of Lakes and Reservoirs*, L. A. Baker, Ed. (American Chemical Society, 1994), pp. 195–221.
4. J. Liu, X. Zhang, *Water Res.* **65**, 64 (2014).
5. E. Bei *et al.*, *Water Res.* **98**, 168 (2016).
6. S. Krytopoulos, *Br. J. Cancer* **40**, 666 (1979).
7. J. R. Karr, *Environ. Toxicol. Chem.* **12**, 1521 (1993).

10.1126/science.abb8905

TECHNICAL COMMENT ABSTRACTS

Comment on "Late Upper Paleolithic occupation at Cooper's Ferry, Idaho, USA, ~16,000 years ago"

Sturt W. Manning

Davis *et al*. (Research Articles, 30 August 2019, p. 891) report human occupation at Cooper's Ferry, Idaho, USA, ~16,000 years ago, well before Greenland Interstadial 1 (GI-1). Critical review suggests that this early date is not supported by the evidence. Human occupation might have begun in the mid-16th millennium before the present, but it would have been more likely after ~15,000 years ago, coeval with GI-1.

Full text: dx.doi.org/10.1126/science.aaz4695

Response to Comment on "Late Upper Paleolithic occupation at Cooper's Ferry, Idaho, USA, ~16,000 years ago"

L. G. Davis, L. Becerra-Valdivia, D. B. Madsen, T. Higham

Manning builds an inappropriate Bayesian age model to assert that the initial occupation at Cooper's Ferry began only ~15,935 ± 75 to 15,130 ± 20 cal yr B.P., suggesting that our estimation of ~16,560 to 15,280 cal yr B.P. is unsupported. However, this analysis both ignores evidence of human occupation from the earliest undated cultural deposits and reflects a misapplication of Bayesian age-modeling techniques. Consequently, his results are unreliable.

Full text: dx.doi.org/10.1126/science.aaz6626

ERRATA

Erratum for the Report: "An sp-hybridized molecular carbon allotrope, cyclo[18]carbon" by K. Kaiser *et al*., *Science* **367**, eabb5604 (2020). Published online 13 March 2020; 10.1126/science.abb5604

Erratum for the Report: "A room-temperature single-photon source based on strongly interacting Rydberg atoms" by F. Ripka *et al*., *Science* **367**, eabb4382 (2020). Published online 6 March 2020; 10.1126/science.abb4382

Erratum for the Review: "What would it take for renewably powered electrosynthesis to displace petrochemical processes?" by P. De Luna *et al*., *Science* **367**, eabb0992 (2020). Published online 6 March 2020; 10.1126/science.abb0992

Erratum for the Report: "Synthesis and characterization of the pentazolate anion *cyclo*-N_5^- in $(N_5)_6(H_3O)_3(NH_4)_4Cl$" by C. Zhang *et al*., *Science* **367**, eabb2965 (2020). Published online 21 February 2020; 10.1126/science.abb2965

Erratum for the Report: "Fluorination of arylboronic esters enabled by bismuth redox catalysis" by O. Planas *et al*., *Science* **367**, eabb2416 (2020). Published online 14 February 2020; 10.1126/science.abb2416

NEW!

Open-Design Upright Microscope

- NEW: Optional motorized or fixed XY stage, or motorized translator
- Open-design microscope with motorized focus
- Quickly configurable based on experimental needs
- Optimized *In vivo* and *In vitro* experimentation on one setup
- Uses standard Olympus objectives
- OCC or DIC transmitted light (LED)
- Epi-fluorescent imaging

BOB™

The Sutter BOB – designed to eliminate the conventional microscope frame – is a versatile, open-design upright microscope platform ideal for slice electrophysiology, widefield fluorescent imaging, two-photon imaging, photostimulation and new techniques just being developed!

SUTTER INSTRUMENT

PHONE: +1.415.883.0128
FAX: +1.415.883.0572
EMAIL: INFO@SUTTER.COM
WWW.SUTTER.COM

The Best Antibody Discovery Technology Is Now at Your Fingertips

Trianni Mouse Antibodies are a Match for Humans

The Trianni Mouse™ platform is a transgenic antibody discovery platform offering the entire human variable gene diversity in a single organism.

The V(D)J gene segments in The Trianni Mouse are chimeric, but the variable domains of **antibodies made by the mouse are entirely human.** The result is human antibody leads generated from antibody genes optimized for function in the mouse.

To learn more about this innovative platform, visit **Trianni.com.**

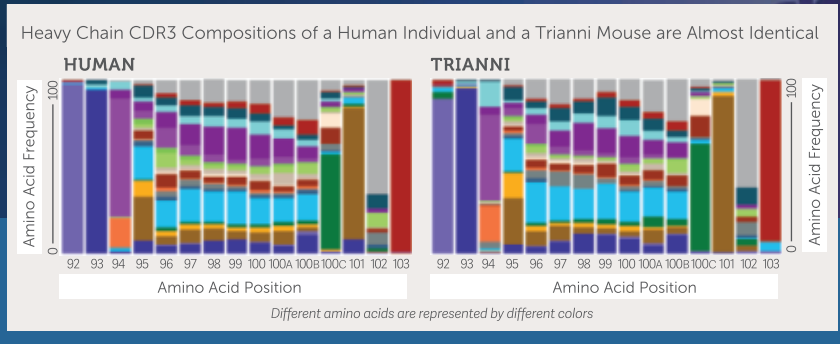
Heavy Chain CDR3 Compositions of a Human Individual and a Trianni Mouse are Almost Identical
HUMAN
TRIANNI
Amino Acid Frequency
0
100
92 93 94 95 96 97 98 99 100 100A 100B 100C 101 102 103
Amino Acid Position
Different amino acids are represented by different colors

TRIANNI

Exceptional Human Antibody Discovery Technology

Science Webinars

AAAS

Science Webinars help you keep pace with emerging scientific fields!

Stay informed about scientific breakthroughs and discoveries.
Gain insights into current research from top scientists.
Take the opportunity to ask questions during live broadcasts.
Get alerts about upcoming free webinars.

Sign up at: webinar.sciencemag.org/stayinformed

they visualized dynamic activities during embryonic organ formation, including neurotransmission and cell division in the brain, autophagy in the retina, viral gene delivery, and placental drug transfer. They also tracked diverging fates of human and mouse neural crest cells in interspecies chimeras. —BAP

Science, this issue p. 181

SOLAR CELLS

Engineering perovskites with anions

The bandgap of the perovskite top layer in tandem silicon solar cells must be tuned to ~1.7 electron volts. Usually, the cation composition is varied because the bromine-rich anion compositions with wide bandgaps are structurally unstable. Kim *et al.* show that by using phenethylammonium as a two-dimensional additive, along with iodine and thiocyanate, bromine-rich perovskite films can be stabilized. A tandem silicon cell delivered >26% certified power conversion efficiency, and a perovskite device maintained 80% of its initial power conversion efficiency of >20% after 1000 hours under illumination. —PDS

Science, this issue p. 155

TROPICAL FORESTS

Forest dynamics and demography

Tropical forest succession has been viewed mostly by considering trees in categories of early-, mid-, and late-successional species, corresponding to a fast–slow continuum of life history strategies. Rüger *et al.* now show that the fast–slow continuum does not capture the demographic strategy of the long-lived pioneer species, an important component of many tropical forests (see the Perspective by Bugmann). They developed a forest model that allows for objective predictions of tropical forest dynamics and validated the model's predictions against independent data. These findings should advance our understanding of tropical forest dynamics and facilitate sustainable tropical forest management. —AMS

Science, this issue p. 165; see also p. 128

T CELLS

The skinny on T cell fatty acid uptake

When T cells take up residence in a tissue, adaptation to that tissue is key for their survival. Frizzell *et al.* studied metabolic adaptation of tissue-resident memory T (TRM) cells at three different sites: skin, liver, and small intestine. They found that TRM cells in each kind of tissue rely on distinct members of the fatty acid–binding protein (FABP) family of proteins for uptake of fatty acids. By transferring liver-resident TRM cells into naïve mice, they found that FABP expression of these TRM cells was reprogrammed by the tissue they ended up seeding in the recipient mice. This study reinforces the idea that immune cells are integral components of the tissues in which they reside. —AB

Sci. Immunol. **5**, eaay9283 (2020).

BIOENGINEERING

Acellular advantage

Cell therapy for cardiac remodeling after myocardial infarction is therapeutic in part owing to paracrine effects. Capitalizing on this feature of heart tissue regeneration, K. Huang *et al.* created acellular cardiac patches from decellularized myocardium and encapsulated factors secreted from human cardiac stromal cells. Patches retained potency after cryopreservation and improved cardiac function, reduced infarct size, and increased angiogenesis when applied to rat and pig hearts after myocardial infarction. —CC

Sci. Transl. Med. **12**, eaat9683 (2020).

IN OTHER JOURNALS

Edited by **Caroline Ash** *and* **Jesse Smith**

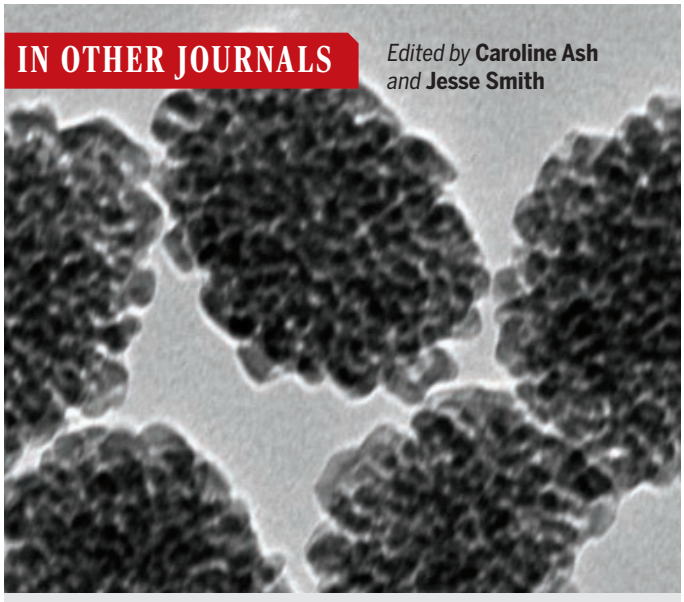

CREDIT: B. LI *ET AL.*, *CHEM. MATER.* 10.1021/ACS.CHEMMATER.0C00573 (2020)

NANOMATERIAL

A hot way to change shape

Heating cycles are used to transform nanomaterials, but this can often cause shape deformation or particle aggregation. Li *et al.* show that the addition of strong capping ligands—in this case, polyacrylic acid—can stabilize shapes or help to control final properties during the calcination of β-FeOOH ellipsoidal particles. When heated in air at temperatures of ~350°C, the particles transformed into porous α-Fe_2O_3 of similar shape and size, which then could be reduced to form magnetic Fe_3O_4 particles. The authors also demonstrated that the strong ligand technique worked with β-FeOOH nanorods, Prussian blue nanocubes, cobalt hydroxide nanoplates, and $Ni(OH)_2$ nanoplates. —MSL

Chem. Mater. 10.1021/acs.chemmater.0c00573 (2020).

Porous ellipsoidal α-Fe_2O_3 nanoparticles made by high-temperature calcination of β-FeOOH in the presence of polyacrylic acid

OLFACTION

Mammalian smell sensation

Olfactory receptor (OR) genes are the largest gene repertoire in the mammalian genome, representing 2 to 5% of all protein coding among species. Vertebrate OR genes were thought to have intronless coding regions, but Barnes *et al.* have found that this is not always the case. They inspected every OR locus in the human and mouse reference genomes, taking great care to ensure consistency of their annotation within and between species. For each OR gene, the structural features, as well as protein conservation, were considered to determine protein-coding potential and to define the coding sequence. Thirteen human and 41 mouse OR genes contained an intact coding sequence split across two exons, several of which were previously considered to be pseudogenes. —PRS

BMC Genomics **21**, 196 (2020).

NANOPORE MATERIALS

Anion gating of hydrophobic nanopores

Hydrophobic nanopores can control ion currents when subjecting them to external stimuli to induce

selective wetting. Polster *et al.* created hydrophobic–hydrophilic junctions in single nanopores (10 to 140 nanometers in effective diameter) in silicon nitride membranes. Part of the channel was lined with a hydrophilic, positively charged polyelectrolyte, and the rest with a perfluorinated silane. These nanopores had a negative voltage bias threshold for transporting chloride anions, but bromide and iodide were transported at positive bias as well. Simulations suggested that these more polarizable anions shed solvent water more readily and accumulate on the hydrophobic walls to induce wetting. —PDS

ACS Nano 10.1021/acsnano.9b09777 (2020).

NEUROSCIENCE

Individual brain networks

A better understanding of how networks connect in the brain is important for the personalized treatment of neurological conditions such as Parkinson's disease and psychiatric illnesses such as Tourette's syndrome. Circuits regulating sensorimotor, cognitive, and limbic processes link the brain's cortex to subcortical structures such as the thalamus. Greene *et al.* used functional magnetic resonance imaging to map the connectivity of subcortical structures, revealing variability among individuals. Somatomotor networks showed less interindividual variation, whereas cognitive control networks showed more. Integrative zones included motor, visual, or cognitive control networks. Thus, a consensus map of where pathways are located may not be precise or helpful for a given individual, reflecting the imperfect success of transcranial magnetic stimulation and deep-brain stimulation in the treatment of depression or essential tremor. —PJH

Neuron **105**, 742 (2020).

AUTISM

Tau reduction prevents autism

Autism is a highly prevalent neurodevelopmental disorder associated with impaired sociality and communication and repetitive behaviors. So far, available treatments offer little benefit. Tai *et al.* established a link between the neurodegeneration-associated protein tau and autism spectrum disorders (ASDs). They found that genetic methods for reducing tau in two distinct mouse models of autism alleviated symptoms ranging from epilepsy to overactive signaling pathways. Even partial (~50%) reduction of tau ameliorated autistic behaviors. Tau directly interacted with and inhibited the phosphatase activity of PTEN, a negative phosphatidylinositol 3-kinase (PI3K) regulator, which likely underlies the beneficial effects of tau reduction. Thus, tau regulation of PTEN, and thus the downstream PI3K–Akt–mammalian target of rapamycin pathway, may link multiple ASDs and potentially provide a target for therapeutic interventions. —SMH

Neuron 10.1016/j.neuron.2020.01.038 (2020).

EDUCATION

At the center of engagement and learning

Moving toward more student-centric STEM education results in an increase in student–student interactions. Do these increased peer interactions lead to learning gains? Williams *et al*. used network analysis—specifically, centrality, a measurement of how "central" a particular student is within the classroom network—to examine student interactions in an introductory physics classroom using modeling instruction. Students' centrality was found to predict future academic performance more than prior grade point average, suggesting that student engagement is connected to academic performance. However, this relationship did not emerge until the second half of the semester, suggesting that the relationship between engagement and academic performance, although important, is nuanced. Qualitative methods are recommended as a follow-up to further investigate how students themselves perceive their engagement in learning communities. —MMc

Phys. Rev. Phys. Educ. Res. **15**, 020150 (2019).

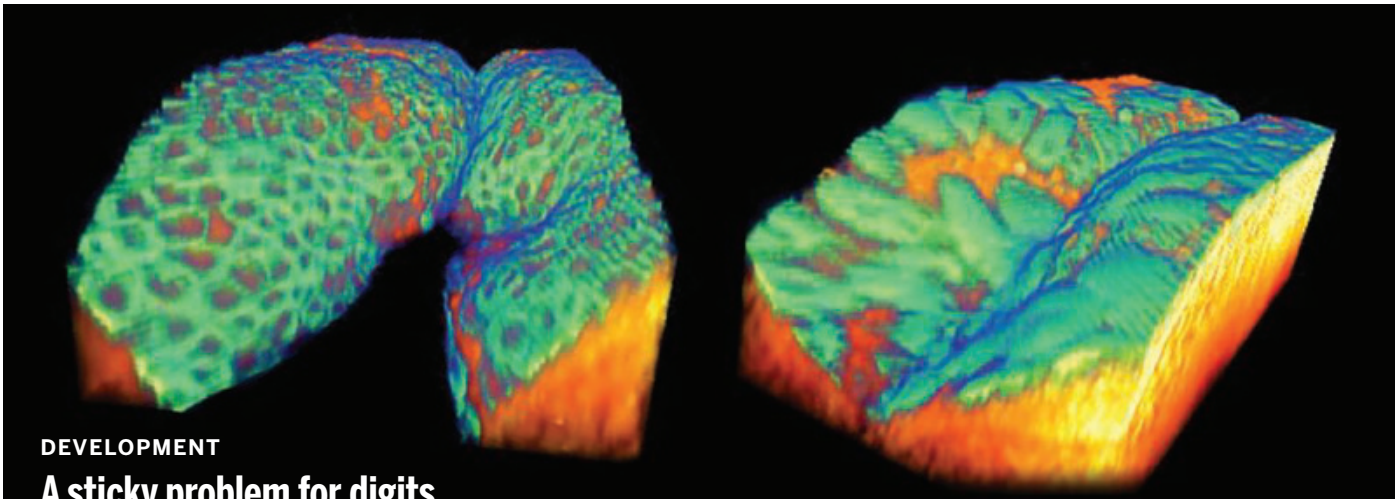

DEVELOPMENT

A sticky problem for digits

Cell death during development is important for finger and toe separation, but additional developmental programs are also required for proper digitation. Kashgari *et al.* show that, after the death of the mesenchyme cells from which digits form, a structure called the interdigital epithelial tongue invaginates into the mesenchyme, allowing the digits to bifurcate. In normal digit formation, the outermost layer of the embryonic epidermis, the periderm, prevents digit adhesion. However, after the digits separate, they sometimes fuse back together, causing a condition known as syndactyly. This occurs when the transcription factor grainyhead-like 3 (GRHL3) is lacking, which results in the usually nonsticky periderm becoming sticky. —BAP

Dev. Cell. **52**, 764 (2020).

3D reconstructions of two adjacent digits of a mouse showing, on the left, normal digit separation and, on the right, digit fusion in mutant mouse embryos

IMAGES: G. KASHGARI *ET AL*., *DEV. CELL.* **52**, 764 (2020)

Science Webinars

AAAS

Science Webinars help you keep pace with emerging scientific fields!

Stay informed about scientific breakthroughs and discoveries.

Gain insights into current research from top scientists.

Take the opportunity to ask questions during live broadcasts.

Get alerts about upcoming free webinars.

Sign up at: webinar.sciencemag.org/stayinformed

RESEARCH ARTICLE SUMMARY

NEUROSCIENCE

Widespread receptor-driven modulation in peripheral olfactory coding

Lu Xu*, Wenze Li*, Venkatakaushik Voleti, Dong-Jing Zou, Elizabeth M. C. Hillman†, Stuart Firestein†

INTRODUCTION: The mammalian nose is arguably the best chemical sensor on the planet, able to detect and discriminate among a large and diverse repertoire of mostly small, organic molecules. It accomplishes this, at least in part, through a large family of G protein–coupled receptors (GPCRs) expressed in specialized olfactory sensory neurons (OSNs) arrayed over an epithelium deep within the nasal cavity. Each neuron expresses only one of the ~1000 receptor genes. It is thought that the specific activation of subsets of these receptors by a particular odor translates into a code that can be read by higher brain centers to create a perception. However, we rarely encounter pure odors. Our daily life is a stream of encounters with rich blends of odors, from garbage to cologne. Even a simple cup of coffee has >800 volatile components. To study how the olfactory system encodes this much more complex information, we explored how neurons within the peripheral olfactory epithelium of a mouse's nose responded to a series of odor mixtures. Our analysis was enabled by a new high-speed three-dimensional (3D) imaging method called SCAPE (Swept Confocally Aligned Planar Excitation) microscopy, which allows the responses of thousands of single neurons within the intact olfactory epithelium to be monitored in parallel during delivery of repeated odor combinations.

RATIONALE: Previous studies using single, monomolecular odors suggested that the diverse expression of receptors in OSNs could provide unambiguous representations of individual odors. However, it is unclear how the brain might be able to decode signals when multiple odor components within a blend generate overlapping patterns. Moreover, when smelling a mixture of odors, it is common to perceive one odor dominating another. Psychophysical tests have revealed both suppressive and enhancing effects of particular odors within a blend. However, it has long been assumed that such odor-coding interactions occur at higher processing levels within the brain. Here, we studied whether combinatorial effects of odors affect neural representations at the peripheral sensory level.

RESULTS: Using SCAPE microscopy to image calcium-sensitive fluorescent proteins in OSNs, we were able to simultaneously monitor the activity of cells within a large volume of the intact mouse olfactory epithelium with single-cell resolution. Analyzing the responses of thousands of single neurons to blends of up to three odors, we discovered a series of surprising interactions that distorted the representation of the odor mixture compared with a simple combinatorial sum of responses to individual odors. Among the eight chemically distinct odors tested, we observed that the presence of one odor could either enhance or suppress the response of a neuron to another odor, even if the modulating odor by itself did not elicit a response from the neuron. This means that an odorless molecule could alter the perception of another odor, and that a neuron's response to an odor blend can be much larger or smaller than its response to components of the blend. Overall, we observed clear evidence of agonism, antagonism, partial agonism, and enhancement occurring at the receptor level, suggesting a richer repertoire of receptor modulation mechanisms than previously thought. Finally, we note that enhancement of responses may be evidence of an allosteric modulatory site, a rare finding in class A GPCRs that bind small molecules.

ON OUR WEBSITE

Read the full article at http://dx.doi.org/10.1126/science.aaz5390

CONCLUSION: Although inhibition and enhancement are well established in sensory systems, they are only a feature of higher circuit processing. Here, we observed complex receptor modulation at the level of peripheral olfactory sensory receptors. We propose that these peripheral modulatory interactions are crucial for discriminating complex blends of odors with overlapping activation patterns because they prevent the saturation of receptors and allow each new component to alter the overall activation pattern, rendering it distinctive. This result suggests that higher brain regions may rely on pattern recognition rather than on reading an additive combinatorial code to build a perception. This work also demonstrates an exciting and versatile new paradigm for high-throughput characterization of single-cell responses in intact systems. ■

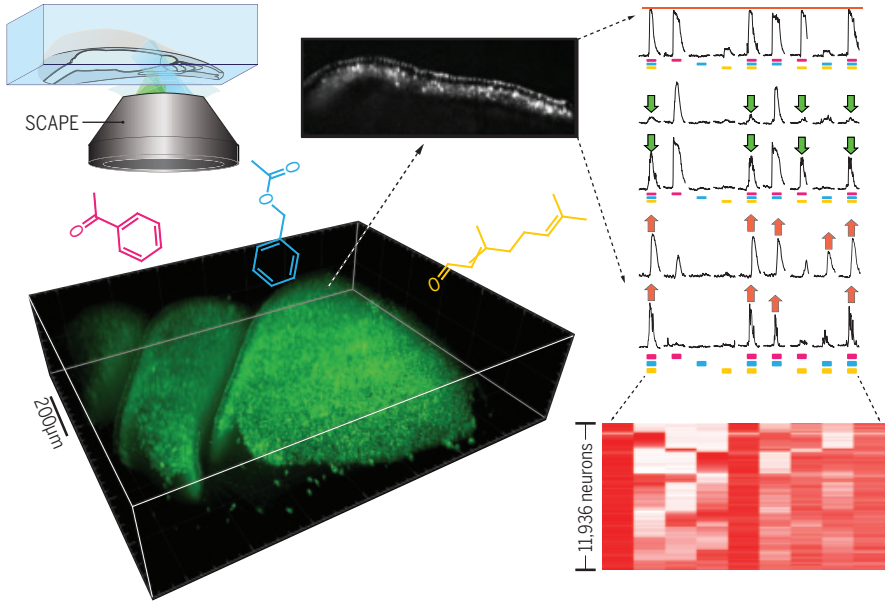

Large-scale single-cell recording of OSNs reveals receptor-driven modulation effects. Volumetric imaging of GCaMP in intact olfactory epithelium using high-speed SCAPE microscopy enables analysis of responses to mixtures of different odor molecules. Single-neuron response time courses show that odor mixtures can enhance (red) or suppress (green) responses compared with individual odors. Heatmap shows assessment of >10,000 individual neurons across five mice.

The list of author affiliations is available in the full article online.
*These authors contributed equally to this work.
†Corresponding author. Email: sjf24@columbi a.edu (S.F.); elizabeth.hillman@columbia.edu (E.M.C.H.)
Cite this article as L. Xu *et al.*, *Science* **368**, eaaz5390 (2020). DOI: 10.1126/science.aaz5390

RESEARCH ARTICLES

SOLAR CELLS

Efficient, stable silicon tandem cells enabled by anion-engineered wide-bandgap perovskites

Daehan Kim[1]*, Hee Joon Jung[2]*, Ik Jae Park[3]*, Bryon W. Larson[4], Sean P. Dunfield[4,5], Chuanxiao Xiao[4], Jekyung Kim[1], Jinhui Tong[4], Passarut Boonmongkolras[1], Su Geun Ji[3], Fei Zhang[4], Seong Ryul Pae[1], Minkyu Kim[1], Seok Beom Kang[6], Vinayak Dravid[2], Joseph J. Berry[4,7,8], Jin Young Kim[3]†, Kai Zhu[4]†, Dong Hoe Kim[4,6]†, Byungha Shin[1]†

Maximizing the power conversion efficiency (PCE) of perovskite/silicon tandem solar cells that can exceed the Shockley-Queisser single-cell limit requires a high-performing, stable perovskite top cell with a wide bandgap. We developed a stable perovskite solar cell with a bandgap of ~1.7 electron volts that retained more than 80% of its initial PCE of 20.7% after 1000 hours of continuous illumination. Anion engineering of phenethylammonium-based two-dimensional (2D) additives was critical for controlling the structural and electrical properties of the 2D passivation layers based on a lead iodide framework. The high PCE of 26.7% of a monolithic two-terminal wide-bandgap perovskite/silicon tandem solar cell was made possible by the ideal combination of spectral responses of the top and bottom cells.

Perovskite photovoltaic (PV) technology has advanced substantially, with the present record efficiency for single-junction devices reaching >25% (*1*–*4*). One of the most promising strategies for commercializing these devices is to apply a perovskite top cell in tandem with a Si bottom cell to reach ultrahigh efficiency beyond the Shockley-Queisser limit for single-junction devices (*5*). Since the report of a two-terminal (2T) perovskite/Si tandem solar cell by Mailoa *et al.* (*6*), several groups have reported encouraging results (*7*–*10*). Most of the studies on perovskite/Si tandem solar cells have perovskite absorbers with the conventional bandgap of 1.5 to 1.6 eV, but the ideal bandgap for the tandem configuration is ~1.67 to 1.75 eV for the top cell and 1.12 eV for the bottom cell, which, fortuitously, is the Si bandgap (*11*). Although some of the reported perovskite/Si tandem devices have used a wide-bandgap perovskite (near 1.7 eV), the power conversion efficiencies (PCEs) reported have been ≤25% (*8*).

The bandgap of perovskites can be tuned by (partial) replacement of iodine anions with bromine or chlorine. However, the replacement of I with Br by more than ~20%, which is necessary to enlarge the bandgap to ~1.7 eV, leads to stability issues under illumination through phase separation that forms I-rich and Br-rich structures (*12*). One approach to stabilize the perovskite is to create a two-dimensional (2D) phase in which sheets of $[PbX_6]^{-2}$ octahedra are separated by an excess number of long-chain (or aromatic) molecules that act as a passivation agent (*13*–*17*). Common long-chain or aromatic molecule–based 2D additives include n-butylammonium iodide (n-BAI) and phenethylammonium iodide (PEAI) (*13*, *15*). For example, Wang *et al.* have used n-BAI as a 2D additive and demonstrated an extended lifetime of up to 1000 hours under illumination (*13*). Kim *et al.* have developed a wide-bandgap perovskite with PEAI as a 2D additive and demonstrated successful integration into perovskite/Cu(In,Ga)Se_2 tandem solar cells (*17*). Formation of passivation layers induced by these 2D additives improved efficiency, particularly the open-circuit voltage (V_{OC}); however, excessive incorporation of 2D-forming molecules often reduced the fill factor (FF) because of their electrically insulating nature. Thus, the concentration of the added 2D molecules has been limited to ~1 mol % in the precursor solutions.

Most of the recent studies have focused on the cation components of the 2D additives rather than focusing on the anions. We developed a 2D-3D mixed wide-bandgap (1.68 eV) perovskite using a mixture of thiocyanate (SCN) with the more-conventional choice, iodine. Through a careful application of atomic-resolution transmission electron microscopy (TEM), we demonstrated that electrical and charge transport properties as well as the physical location of 2D passivation layers can be controlled with anion engineering of the 2D additives. Moreover, we can use this approach to extend light stability and to improve device performance. For a perovskite device, we achieved a PCE of 20.7% that retained >80% of its initial efficiency after 1000 hours of continuous illumination in working conditions. For a monolithic 2T perovskite/Si tandem solar cell, the champion 2T tandem device achieved a PCE of 26.7%.

Anion engineering of wide-bandgap solar cells

The wide-bandgap (1.68 eV) perovskite used in this study was $(FA_{0.65}MA_{0.2}Cs_{0.15})Pb(I_{0.8}Br_{0.2})_3$. An additional 2 mol % of $Pb(SCN)_2$ was added to the perovskite precursor solution to accelerate the 3D perovskite grain growth (*17*). To form a 2D phase, PEA-based additives had an anion component mixture of I and SCN with various ratios of SCN/(SCN + I), ranging from 0 to 100%. Solar cells were fabricated with an indium tin oxide (ITO)/poly(triaryl amine) (PTAA)/perovskite/C_{60}/bathocuproine (BCP)/Ag device structure (fig. S1). Representative current density-voltage (*J-V*) curves of devices with three different SCN/(SCN+I) ratios—0, 75, and 100% (Fig. 1A)—show that the highest V_{OC} was from the pure PEAI and the highest J_{SC} was from the pure PEASCN, but the highest performance was from the mixed anion sample.

We further investigated the influence of the anion composition in the 2D additives on the PV parameters using a series of samples with different ratios of SCN to (SCN + I). In all of the samples, the concentration of the 2D additives added to the precursor solutions was fixed at 2 mol %, which was determined by the device optimization (fig. S2). Increasing SCN/(SCN + I) decreased V_{OC} but improved J_{SC} and FF (Fig. 1B). The variation of V_{OC} was not caused by slight changes in the optical bandgap of the different perovskite films (fig. S3). A compromise between the PV parameters produced the highest efficiency with the additives of 75% SCN, in other words, $PEA(I_{0.25}SCN_{0.75})$. Thus, SCN promoted the J_{SC} and FF of the devices, but iodine seemed essential in defect passivation that led to higher V_{OC}.

The *J-V* curve of the champion cell with the $PEA(I_{0.25}SCN_{0.75})$ additive (Fig. 1C) led to a 20.7% PCE and a stabilized power output (SPO) >20%. The external quantum efficiency (EQE) shown in fig. S4A from the same device showed a minimal mismatch with the J_{SC} from the *J-V* scan (<4%) and negligible *J-V* hysteresis between the different scan directions (fig. S4B). For a long-term stability test of the devices under continuous illumination in an N_2-filled environment (*18*), samples without any encapsulation were subjected to *J-V* measurements every 30 min (Fig. 1D). Compared with

[1]Department of Materials Science and Engineering, Korea Advanced Institute of Science and Technology (KAIST), Daejeon 34141, Republic of Korea. [2]Department of Materials Science and Engineering, Northwestern University, Evanston, IL 60208, USA. [3]Department of Materials Science and Engineering, Seoul National University, Seoul 08826, Republic of Korea. [4]National Renewable Energy Laboratory, Golden, CO 80401, USA. [5]Materials Science and Engineering Program, University of Colorado Boulder, Boulder, CO 80309, USA. [6]Department of Nanotechnology and Advanced Materials Engineering, Sejong University, Seoul 05006, Republic of Korea. [7]Department of Physics, University of Colorado Boulder, Boulder, CO 80309, USA. [8]Renewable and Sustainable Energy Institute, University of Colorado Boulder, Boulder, CO 80309, USA.
*These authors contributed equally to this work.
†Corresponding author. Email: jykim.mse@snu.ac.kr (J.Y.K.); kai.zhu@nrel.gov (K.Z.); donghoe.k@sejong.ac.kr (D.H.K.); byungha@kaist.ac.kr (B.S.)

the samples with pure PEAI and PEASCN additives, the mixed anion additive that led to the champion device exhibited much-improved stability—80% of the initial efficiency was maintained even after 1000 hours of continuous illumination (*J-V* curves acquired during the stability tests are shown in fig. S5). A greatly extended light stability of a wide-bandgap perovskite (~1.67 eV) has recently been demonstrated by McGehee *et al.* (*19*) that uses a triple-halide alloy (mixture of Cl, Br, and I). The extended stability in that case has been attributed to markedly improved structural and optoelectronic properties (enhanced carrier lifetime and mobility and reduced defect density) of the perovskite. We also observed improved structural and optoelectronic properties via the optimized anion-engineered 2D additive, as discussed later in this work.

Structural characterization

We explored the roles of different PEA-based additives on the device operation through extensive structural analysis. The films were examined by scanning electron microscopy (SEM) (Fig. 2, A to C). The average grain size was larger for the SCN-based PEA source than that of the pure PEAI additive, which confirmed the previous reports on the enhanced grain growth promoted by SCN molecules (*17*, *20*). However, compared with the perovskite film with only $Pb(SCN)_2$ (fig. S6B), PEA apparently suppressed grain growth, which limited the average grain size to less than ~500 nm. Consistent with the SEM results, x-ray diffraction (XRD) (Fig. 2D) revealed that films with the PEASCN additive were more crystalline than a film with the PEAI additive, as determined by the full width at half maximum of the XRD peaks (fig. S7). The PbI_2 phase peak was observed in all of the films and was strongest for the pure PEAI film. In addition to the well-defined grains of the 3D perovskite, patches of a new phase with a bright SEM image contrast (indicating a more insulating nature than the darker 3D perovskite grains) were observed. Most of these patches were preferentially located at grain boundaries instead of residing directly over grains.

To probe the chemical and structural properties of the new phase coexisting with the 3D perovskite host, we performed cross-sectional TEM studies including atomic-resolution scanning TEM (STEM) images. Figure 2, E and F, presents bright-field and high-resolution TEM images of the $PEA(I_{0.25}SCN_{0.75})$ sample that show the layered structure (2D phase) located at the grain boundary. The interplanar d-spacing of the 2D phase of 7.1 Å measured from the high-resolution image (Fig. 2G) was also confirmed by selected-area diffraction in fig. S8B. High-angle annular dark-field (HAADF) and annular bright-field (ABF) STEM images (Fig. 2, H and I) helped identify the atomic configuration of the 2D phase. HAADF can be interpreted as Z-contrast imaging, which renders a heavier element brighter with no contrast reversals (*21*, *22*), and ABF phase-contrast imaging visualizes weak-phase objects of low-Z atoms such as hydrogen and oxygen (*23*). As the dark contrast of light atoms in the ABF was not pronounced enough to be well resolved, the contrast of the ABF was reversed to yield a reverse ABF (RABF), in which light atoms now appeared bright on the dark background.

The measured d-spacing values of the 2D phase were 2.3 and 7.1 Å along the in-plane and out-of-plane directions, respectively. Notably, these values are near the planar spacings of PbI_2 (110) and (001), respectively, with just 1 and 1.7% expansion compared with the (110) and (001) planar spacing of pure PbI_2 (JCPDS-73-1750, Trigonal $P\bar{3}m1$, a = 4.5570 Å and c = 6.9790 Å). This result suggested that the 2D phase was primarily PbI_2. Direct comparisons of the atomic-scale structures of pure PbI_2 and those of our 2D phase are presented in fig. S9. A subtle distinction between our 2D phase and the pure PbI_2 is the observation of interlayer atomic or molecular dopants in the RABF image (and also in the HAADF image, although the contrast is more diffuse) of our 2D phase, whereas such contrast was absent in the pure PbI_2. These data suggest that the interlayer dopants were likely SCN or Cs, and the incorporation of the interlayer dopants must be at least partially responsible for the lattice expansion.

To further confirm the structural origin of our 2D phase, we performed STEM simulations of PbI_2 and PEA_2PbI_4 (fig. S10), which illustrated much better matching of the real high-resolution STEM images with the simulations of PbI_2 compared with PEA_2PbI_4. Energy-dispersive spectroscopy analysis of a surface 2D phase (fig. S11) revealed that the 2D phase

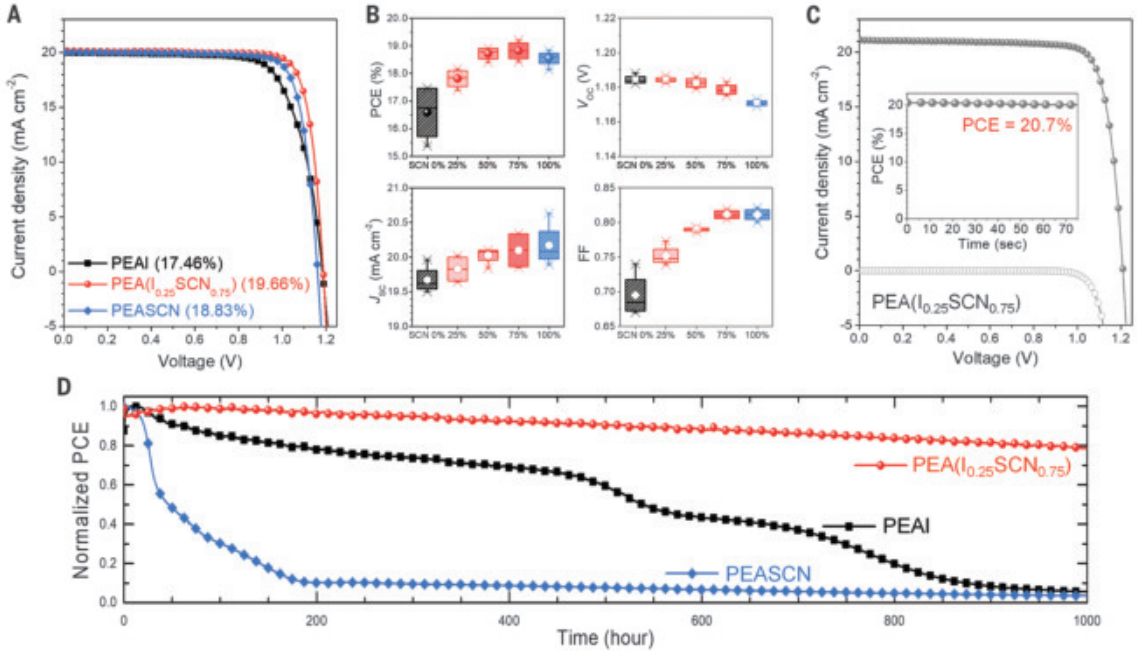

Fig. 1. Device performance and stability under illumination of perovskite solar cells with different 2D additives. (**A**) Representative *J-V* curves of perovskite solar cells with different incorporated additives. Precursor solutions consisted of a mixture of FAI, MABr, PbI_2, $PbBr_2$, and CsI to form a stoichiometric 3D perovskite + Pb $(SCN)_2$ + $PEA(I_{(1-x)}SCN_x)$, where x = 0, 0.75, or 1. (**B**) Statistics of PV parameters with various ratios of SCN to (SCN + I) in the 2D additives (x = 0, 0.25, 0.5, 0.75, or 1). (**C**) *J-V* curve of the champion wide-bandgap perovskite solar cell [$PEA(I_{0.25}SCN_{0.75})$]. (**D**) Long-term stability (PCE normalized over the initial efficiency) of perovskite devices under light illumination without encapsulation.

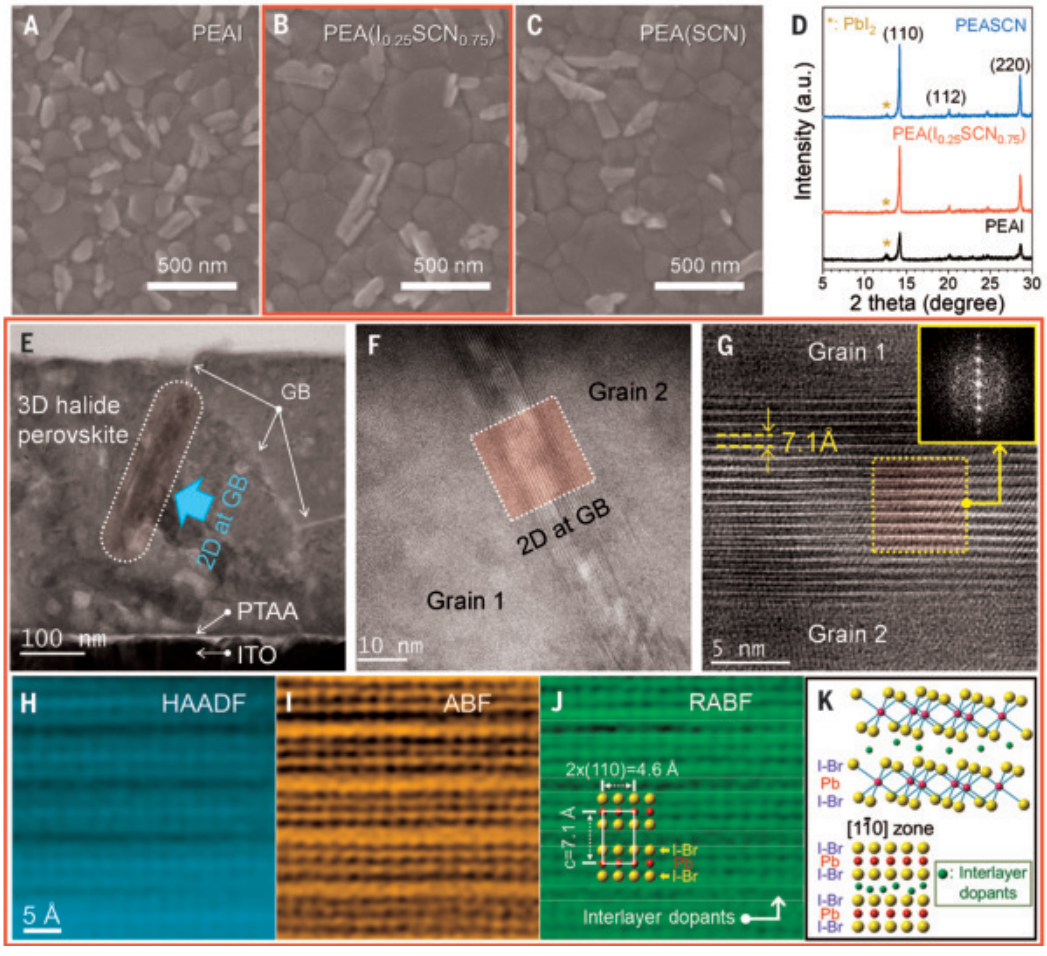

Fig. 2. Structural properties of perovskite films. (**A** to **D**) Plan-view SEM images [(A) to (C)] and XRD patterns (D) of perovskite films formed with different 2D additives. a.u., arbitrary unit. (**E** to **G**) TEM images from PEA($I_{0.25}SCN_{0.75}$) showing the 2D phase at the grain boundary (GB) of the 3D perovskite host. The inset of (G) shows a fast Fourier transform pattern. (**H** to **K**) Atomic-scale STEM images [(H) to (J)] and the schematic (K) of the atomic structure of the 2D phase (PbI_2 with interlayer dopants). Results from the PEA($I_{0.25}SCN_{0.75}$) sample, (B) and (E to K), are marked by red boxes.

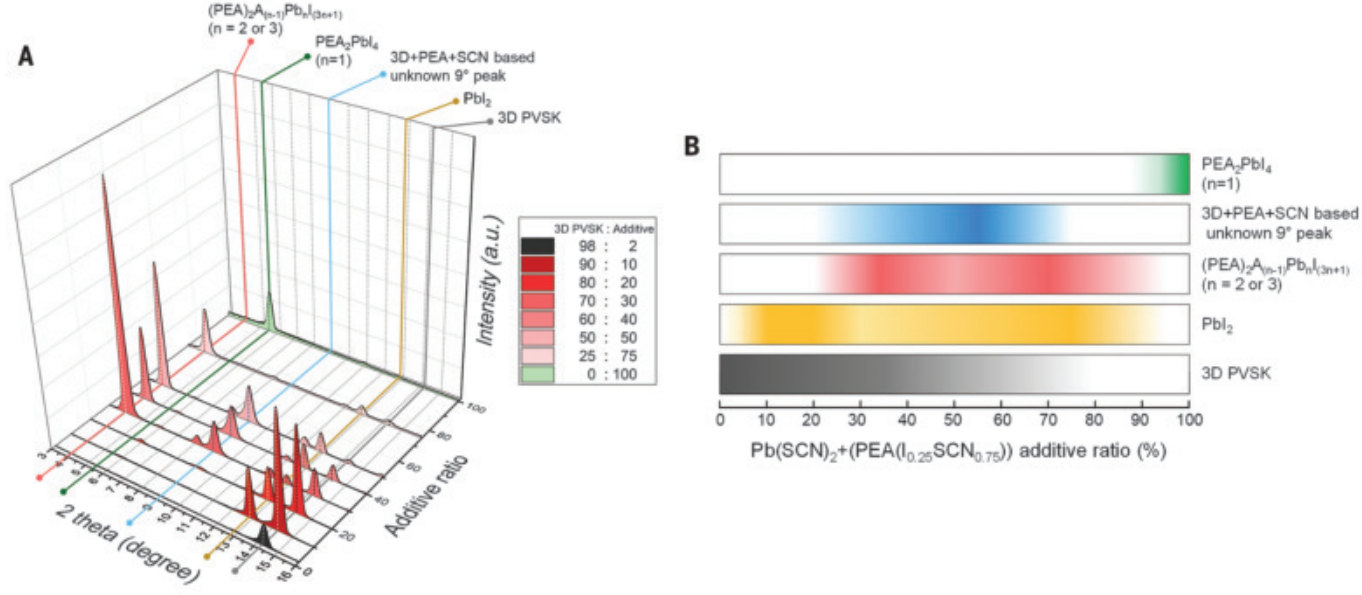

Fig. 3. Series of XRD of films formed with varying ratios of 2D additive to 3D perovskite precursor chemicals. (**A**) XRD patterns with differing ratios (mole %) of 2D additives, i.e., $Pb(SCN)_2$ + PEA($I_{0.25}SCN_{0.75}$), to 3D perovskite precursors. (**B**) Color-coded visualization of different phases formed. The intensity of the color represents the strength of the corresponding XRD peak. The white background in each row represents the absence of the phase.

contained Pb, I, Br, N, and Cs, which confirms that it is PbI_2-based with the inclusion of SCN, Br, and Cs. The sample with only the $Pb(SCN)_2$ additive without PEA appeared to have only surface 2D phases, whereas the $PEA(I_{0.25}SCN_{0.75})$ sample had a 2D phase both on the surface and at grain boundaries (figs. S11 and S12). Previous studies have shown segregation of PEA molecules at grain boundaries of perovskites and their passivation effect (*24*). The large size of PEA is only readily hosted at grain boundaries. For the grain boundary with 2D phase present, the space between the grain and the 2D phase is where we expect PEA molecules to reside. Thus, we speculate that PEA not only acted as a passivation agent itself, but that it also assisted the passivation of grain boundaries by preferentially placing the PbI_2-based 2D phase.

Previous studies have identified 2D passivation layers derived from PEAI (or BAI) as PEA_2PbI_4 (or BA_2PbI_4), a low-dimensional perovskite, $A_2A'_{(n-1)}B_nX_{(3n+1)}$, with $n = 1$ (*13*). An obvious difference between these reports and our work is the inclusion of SCN in the anion component of the 2D additives. To elucidate reaction pathways under our precursor chemistry, we carried out a series of XRD measurements on perovskite films formed by precursor solutions where 3D perovskite chemicals (FAI, MABr, CsI, $PbBr_2$, and PbI_2) were mixed with 2D additives [$Pb(SCN)_2$ and $PEA(I_{0.25}SCN_{0.75})$] (Fig. 3). We investigated a wide range of the relative concentrations of 2D additives to the 3D perovskite chemicals—from 2 mol %, which was the condition used to yield films for photovoltaic devices, to 100 mol %.

As anticipated, in the film produced with only the 2D additive chemicals (100 mol %), only the PEA_2PbI_4 phase was present. But, when 3D perovskite precursor chemicals were added (25% was the minimum mole % of the 3D perovskite chemicals in our study), the PEA_2PbI_4 phase was suppressed and new phases—an unidentified 9° peak, low-dimensional perovskite $(PEA)_2A_{(n-1)}Pb_nI_{(3n+1)}$ ($n = 2$ or 3), PbI_2, and 3D perovskite—began to form. Upon reducing the relative concentration of the 2D additives to below 20%, all of these phases, except PbI_2 and 3D perovskite, disappeared. Notably, upon reducing the ratio of the 2D additives from 30 to 20%, the low-dimensional perovskite peak disappeared while the PbI_2 peak intensified, which suggests that as these two phases compete for Pb and I, PbI_2 dominates over the low-dimensional phase. Preferential formation of PbI_2 over the other secondary phases, which was more pronounced with the reducing concentration of the 2D additives, agreed well with the TEM results presented in Fig. 2.

Similar XRD measurements were performed on perovskite films with pure PEAI or PEASCN (fig. S13). A similar trend was observed in terms of the appearance and disappearance of different phases with the 2D additive ratio. However, PEA_2PbI_4 was absent with the full PEASCN (it formed only when PEAI was present in the precursor solutions), which indicates the difficulty of forming a PEA-based 2D phase with SCN anions. Also, at the same mole % of the 2D additives, the relative intensity of the PbI_2 was larger with the increasing ratio of I to SCN in the PEA source (fig. S14). We believe that the more-facile formation of PbI_2 with an increasing ratio of I to SCN accounted for the trend of the V_{OC} change in the devices shown in Fig. 1B. As revealed by TEM, PbI_2-based 2D layers exist at grain boundaries. These layers could become thicker, cover wider areas of grain boundaries, or do both of these things with the increasing ratio of I to SCN. This process led to more-effective passivation and a larger V_{OC}. Both PEA molecules and the PbI_2-based 2D phase at the grain boundaries, the formation of which we speculate is catalyzed by the presence of PEA, should contribute to passivation. The positive role of PbI_2 residing at grain boundaries—that is improving *V*oc—has been well-documented in the literature (*25*). However, the insulating nature of PbI_2, especially when present in large quantities, would likely decrease FF, as observed in our device results (*26*).

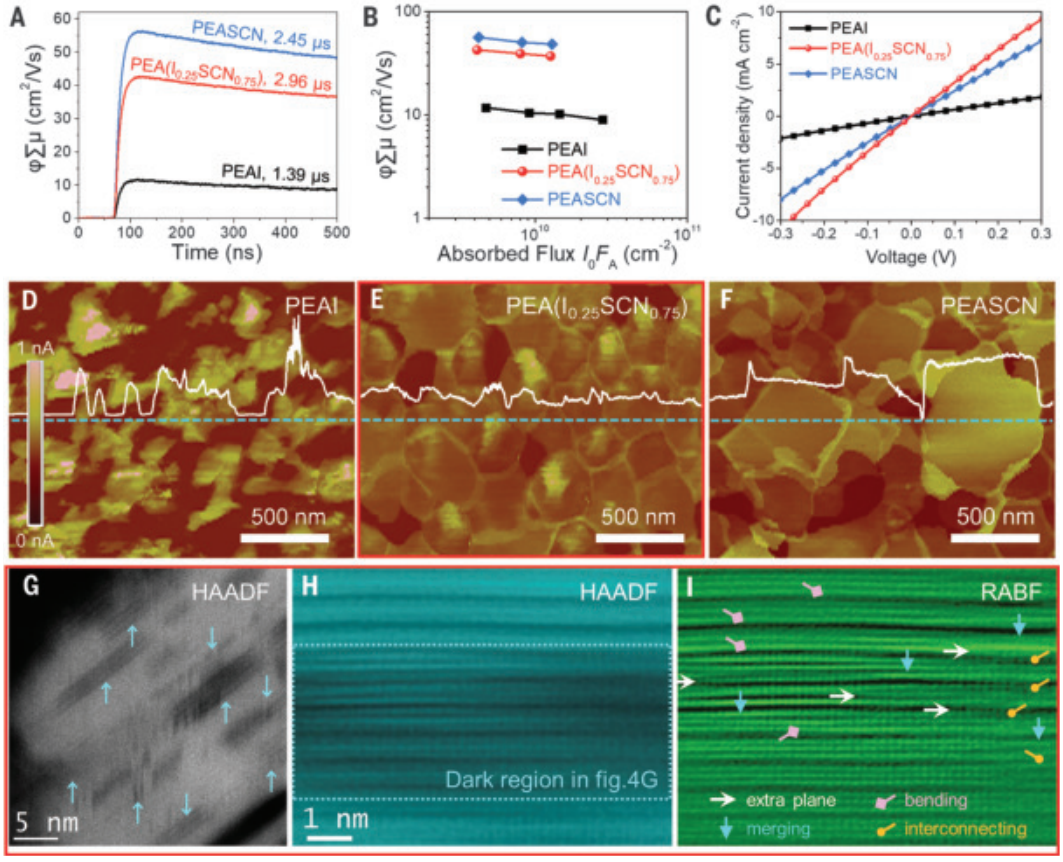

Fig. 4. Electrical properties of perovskite films and the observation of planar defects in 2D passivation layers. (**A**) Photoconductivity transient of perovskite films measured by time-resolved microwave conductivity. (**B**) Excitation intensity dependence of the photoconductivity in the absorbed flux (I_0F_A) range from 4.0×10^9 to 3.0×10^{10} cm^{-2}. (**C**) Vertical *J-V* curve of ITO/perovskite/Au. (**D** to **F**) C-AFM maps. (**G**) HAADF image revealing the formation of regions with defects (dark contrast indicated by arrows) within the 2D phase in the $PEA(I_{0.25}SCN_{0.75})$ film. (**H** and **I**) Atomically resolved HAADF and RABF images of the 2D phase. Planar defects such as insertion of extra planes (edge dislocation-like) and the merging or splitting and bending of layers are indicated. Different types of defects are marked by arrows in different colors in (I).

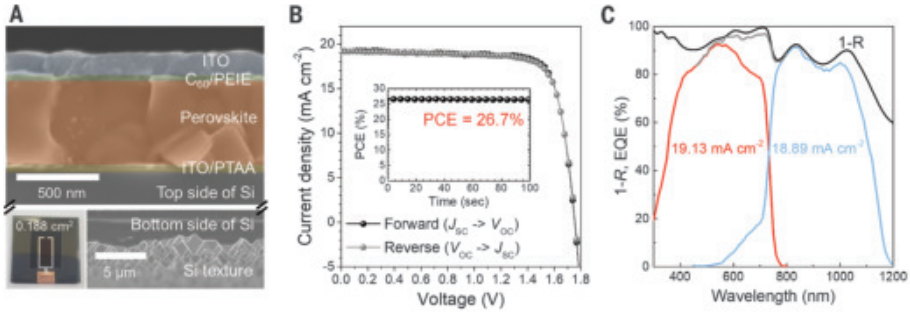

Fig. 5. Structure and photovoltaic performance for the 2T perovskite/Si tandem device. (**A**) Cross-sectional SEM image showing the full device structure of our 2T perovskite/Si tandem device. The inset shows a photograph of a tandem solar cell. (**B**) *J-V* curve of the champion perovskite/Si 2T tandem device with stabilized power output shown in the inset. (**C**) EQE and 1–*R* spectrum of the tandem device. Gray line is the sum of both EQEs from the top and bottom cells.

Charge transport

To understand the impact on device performances with the different additives, we examined the electrical and charge transport properties of the perovskite films by time-resolved microwave conductivity (TRMC), conductive–atomic force microscopy (C-AFM), and vertical *J-V* measurements. In TRMC, the transient change in the density of mobile charge carriers photogenerated by a 5-ns pump-laser pulse was monitored through attenuation of an ~9-GHz frequency microwave probe, which yielded information about free carrier mobility and lifetime (*27*–*29*). Figure 4A compares mobility transients measured at an absorbed photon flux of ~1×10^{10} cm^{-2} using 640-nm laser excitation. By fitting the decay rate of the mobility yield product ($\varphi\sum\mu$)—where φ is the carrier generation yield (usually near unity for high-quality perovskites) (*28*) and μ is the mobility for carriers—we determined the carrier lifetime, as indicated by the numerical values in Fig. 4A. All samples containing a PEA source had long lifetimes in the microsecond regime. The PEA($I_{0.25}SCN_{0.75}$) sample, in particular, had the longest lifetime (approaching 3 μs). The PEA($I_{0.25}SCN_{0.75}$) and PEASCN samples exhibited a high mobility product value (>40 cm^2 V^{-1} s^{-1}), whereas the PEAI sample exhibited a relatively small value of ~10 cm^2 V^{-1} s^{-1}. These mobility values were well maintained over a wide range of the excitation intensity (Fig. 4B).

To identify the factors affecting the various FFs of the samples with different ratios of anions in the PEA source (Fig. 1B), we investigated the electrical conductivity of different perovskite films by vertical dark *J-V* measurements using a structure consisting of ITO/perovskite/Au (Fig. 4C). When SCN was present, electrical conductivity was higher, which yielded a higher FF. We also performed C-AFM measurements to examine the spatial distribution of the current paths through the thickness of the perovskite films. Samples for the C-AFM measurements were ITO/PTAA/perovskite, and current mapping was constructed by a Pt-Ir-coated tip at the sample bias of +1 V. For PEA($I_{0.25}SCN_{0.75}$) (Fig. 4E) and PEASCN (Fig. 4F), the preferential current flow was through the grain boundaries with a relatively uniform contribution to the current through intragrain regions. The PEA($I_{0.25}SCN_{0.75}$) sample exhibited slightly less grain-to-grain fluctuation than the PEASCN. In contrast, the PEAI sample (Fig. 4D) had a nonuniform current distribution, and many dead areas were visible. Dead regions in PEASCN and PEA($I_{0.25}SCN_{0.75}$) samples were much fewer in number relative to those in the PEAI sample.

In imaging studies (Fig. 4, G to I), a feature was commonly found in the 2D phase, located at the grain boundaries of the film with PEA($I_{0.25}SCN_{0.75}$) additives. Darker contrast in HAADF was observed in many regions within the 2D phase (blue arrows in Fig. 4G). Atomically resolved STEM images focusing on one of these dark regions (Fig. 4, H and I) revealed anomalies in the stacking of the 2D layers. Examples include (i) the insertion of an extra half-plane (i.e., edge dislocation), (ii) the merging or splitting of adjacent layers within a stack of PbI_2 (consisting of layers of I only, Pb only, and, again, I only), (iii) the bending of layers, and (iv) the interconnection between layers of PbI_2. We speculate that the formation of these unusual planar defects stemmed from chemical inhomogeneity caused by local evaporation of SCN molecules, which are very volatile, during heat treatment (*20*). These planar defects could facilitate charge-conduction paths across 2D layers that would otherwise be difficult to achieve (*30*), and the defects both enhance charge collection (improving J_{SC}) and reduce the overall series resistance of the perovskite film (improving FF).

2T tandem solar cells

We used our wide-bandgap perovskite to fabricate 2T monolithic perovskite/Si tandem solar cells. The Si bottom cell was textured only on the backside. On top of the Si bottom cell, the following stacking of layers was prepared: ITO as the recombination layer, PTAA, wide-bandgap perovskite, C_{60}, and polyethylenimine (PEIE) as not only an electron transport layer but also a buffer layer to minimize sputter damage during the subsequent ITO deposition (Fig. 5A). Further details about the tandem cell fabrication are provided in supplementary materials. The active area of the 2T tandem cell was 0.188 cm^2, as defined by the aperture. The champion 2T tandem device achieved 26.7% PCE with a J_{SC} of 19.2 mA cm^{-2}, V_{OC} of 1.756 V, and FF of 0.792 with negligible hysteresis and a stabilized power output value >26.5% (Fig. 5B). Ideal spectral matching between the 1.68-eV perovskite and the 1.12-eV Si led to a J_{SC} > 19 mA cm^{-2}. To verify our in-house measurement, a 2T tandem device of the same design with an active area of 1.001 cm^2 was certified with an efficiency of 26.2%. The official report is included in the supplementary materials (fig. S16).

In Fig. 5C, the EQE of the tandem device and the 1–*R* (reflectance) spectrum are presented. The current densities through the top and the bottom cell were consistent with the J_{SC} from the *J-V* curve. The separate contributions of the top perovskite and the bottom Si cells to the total V_{OC} of the tandem device were determined by Si cell measurement with light filtered by the perovskite top cell (*31*). The *J-V* curves of the light-filtered Si cell, as well as the unfiltered Si cell, are shown in fig. S15. The light-filtered Si cell has a 9.4% PCE with a V_{OC} of 0.62 V. Comparing the total V_{OC} of the 2T tandem device and the V_{OC} from the light-filtered Si bottom cell, we found that the gain in V_{OC} from the perovskite top cell was 1.132 V, or 64% of the total V_{OC}. This large contribution from the perovskite top cell exceeds that of other reported 2T perovskite/Si tandem cells with identified relative contributions of each cell (table S1). The high performance of our wide-bandgap perovskite cell validates the use of perovskites to potentially reach >30% PCE for Si-based tandems once the Si bottom cell is further optimized.

REFERENCES AND NOTES

1. National Renewable Energy Laboratory, "Best Research-Cell Efficiency Chart" (2019); www.nrel.gov/pv/cell-efficiency.html.
2. J. Tong *et al.*, *Science* **364**, 475–479 (2019).
3. D. Kim *et al.*, *J. Phys. Chem. C* **120**, 21330–21335 (2016).
4. S. R. Pae *et al.*, *ACS Appl. Mater. Interfaces* **10**, 534–540 (2018).
5. Y. Rong *et al.*, *Science* **361**, eaat8235 (2018).
6. J. P. Mailoa *et al.*, *Appl. Phys. Lett.* **106**, 121105 (2015).
7. F. Sahli *et al.*, *Nat. Mater.* **17**, 820–826 (2018).
8. B. Chen *et al.*, *Joule* **3**, 177–190 (2019).
9. H. Shen *et al.*, *Sci. Adv.* **4**, eaau9711 (2018).
10. M. Jošt *et al.*, *Energy Environ. Sci.* **11**, 3511–3523 (2018).
11. T. Leijtens, K. A. Bush, R. Prasanna, M. D. McGehee, *Nat. Energy* **3**, 828–838 (2018).
12. E. T. Hoke *et al.*, *Chem. Sci.* **6**, 613–617 (2015).
13. Z. Wang *et al.*, *Nat. Energy* **2**, 17135 (2017).
14. Y. Liu *et al.*, *Sci. Adv.* **5**, eaaw2543 (2019).

the two sublattice magnetization are proportional to $\vec{M}_1 \times \dot{\vec{M}}_1$ and $\vec{M}_2 \times \dot{\vec{M}}_2$, respectively, if we view $\vec{M}_1$ and $\vec{M}_2$ as two independent ferromagnets. As illustrated in Fig. 1 (upper right inset), the two sublattices rotate in the same angular direction with a 180° phase difference; thus, $\vec{M}_1 \approx -\vec{M}_2$ and $\dot{\vec{M}}_1 \approx -\dot{\vec{M}}_2$. Consequently, contributions from the two sublattices add up, yielding a total pumped spin current proportional to $\vec{L} \times \dot{\vec{L}} + \vec{M} \times \dot{\vec{M}}$. Because $H_E \gg H_A$ in MnF_2, we have $|\vec{L}| \gg |\vec{M}|$, and $\vec{M}$ can be approximately expressed in terms of $\vec{L}$ as $\vec{M} \approx \left[\frac{H}{H_E}\vec{L} \times (\hat{z} \times \vec{L}) - \frac{1}{\gamma\mu_0 H_E}\dot{\vec{L}} \times \vec{L}\right]$ (*33*), from which one can tell that $\vec{L} \times \dot{\vec{L}}$ is much larger than $\vec{M} \times \dot{\vec{M}}$. That is to say, it is the Néel vector $\vec{L}$, rather than the vanishingly small magnetization $\vec{M}$, that generates the most essential part of coherent spin pumping. Furthermore, it was predicted in (*19*) that the polarization of the driving ac field determines the direction of the pumped spin current. Dynamical modes with opposite chirality coexist in a colinear AF system at zero field and can be selectively excited by an ac field with matching polarization. In other words, spins are pumped with opposite polarizations depending on whether the right- or left-handed mode is excited (by a right- or left-handed circularly polarized stimulus). A magnetic field breaks the degeneracy between the opposite chirality modes. Consequently, only the correct combination of the irradiation frequency and handedness excites a particular AF mode. Therefore, depending on the handedness of the circular polarization and the frequency of irradiation at a given magnetic field, opposite spin currents would be generated in the adjacent nonmagnetic material and transform into opposite ISHE electric signals.

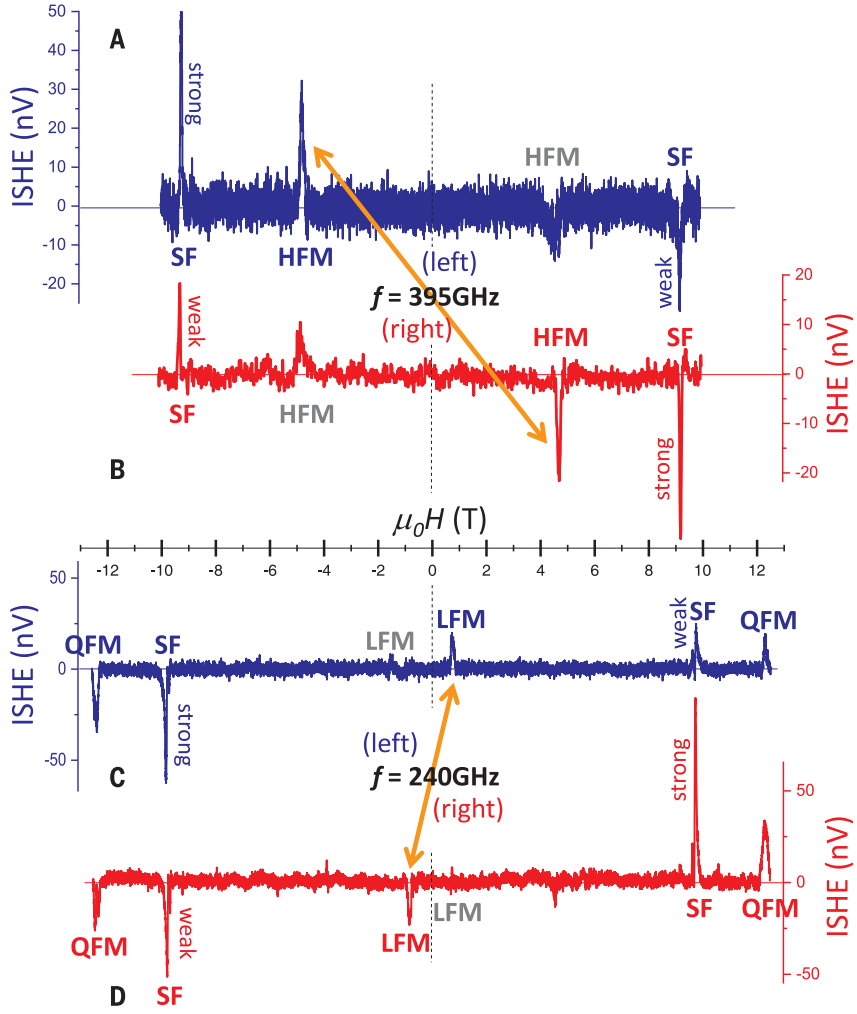

Fig. 2. Inverse spin Hall effect in MnF_2/Pt. ISHE signal obtained in MnF_2/Pt for sample 3 at f = 395 GHz (**A**) left- and (**B**) right-handed circularly polarized microwaves and for sample 2 at f = 240 GHz microwaves with both (**C**) left- and (**D**) right-handed circular polarization. A monotonous signal background has been subtracted from all spectra (*26*). Three distinct features are observed at 240 GHz: The LFM at $\mu_0 H = \pm 0.8$ T, the SF transition resonance at $\mu_0 H = \pm 9.73$ T, and the QFM resonance at $\mu_0 H = \pm 12.37$ T. Only the HFM and the SF resonances are observable for 395 GHz at $\mu_0 H = \pm 4.70$ and ± 9.15 T, respectively, within the available field range.

In the following text, we discuss the measurements of the electrical signals observed by sweeping the magnetic field while irradiating MnF_2/Pt samples with circularly polarized subterahertz microwaves of frequency f. The measured ISHE spectra in samples 3 and 2 are shown in Fig. 2, A and B (f = 395 GHz), and Fig. 2, C and D (f = 240 GHz), respectively. Figure S2 shows the power dependence data for f = 395 GHz. For f = 240 GHz, clear voltage signals were observed associated with the spectra for the LFM, the SF mode, and the QFM. All signals reversed sign when the applied magnetic field reversed direction, which is consistent with the time-reversal symmetry. However, the signal magnitudes differed for opposite handedness of the microwave stimuli, suggesting that chiral AF modes were selectively excited according to the circular polarization. This contrasting magnitude becomes more pronounced in Fig. 2, C and D, where the LFM appears only at a positive (negative) field ($\mu_0|H| = 0.80$T) for the left-handed (right-handed) irradiation. This is indeed the expected behavior of a circularly polarized AF mode in the presence of an external magnetic field. For positive (negative) fields, the LFM mode's chirality is left-handed (right-handed), as it has a spin angular momentum parallel to the magnetic field, whereas the opposite is true for the HFM. There is also a noticeable difference in the strength of the SF signals when only the magnetic field or only the circular polarization is reversed. On the other hand, the magnitude of the QFM resonance remains nearly constant, which we will discuss further in the following text.

Coherent spin pumping versus incoherent spin Seebeck effect

A central question arises from these observations: Do the voltage signals originate from coherent spin pumping at the MnF_2/Pt interface or the incoherent spin Seebeck effect (*34*, *35*) induced by a temperature gradient resulting from microwave heating? In ferromagnets, this is a challenging question because only the right-handed mode exists; therefore, both coherent and incoherent contributions have the same spin polarization that electrical measurements alone cannot distinguish (*36*). In this setting, one would need to perform control experiments, such as changing the layer-stacking order or conducting thermal transport measurements. The situation is fundamentally different in antiferromagnets. The coexistence of both chiral modes in AF systems allows us to distinguish between coherent and incoherent contributions from the electrical measurements alone. The high-frequency (395 GHz) data for sample 3 in Fig. 2, A and B (see analogous data for sample 2 in fig. S1 and

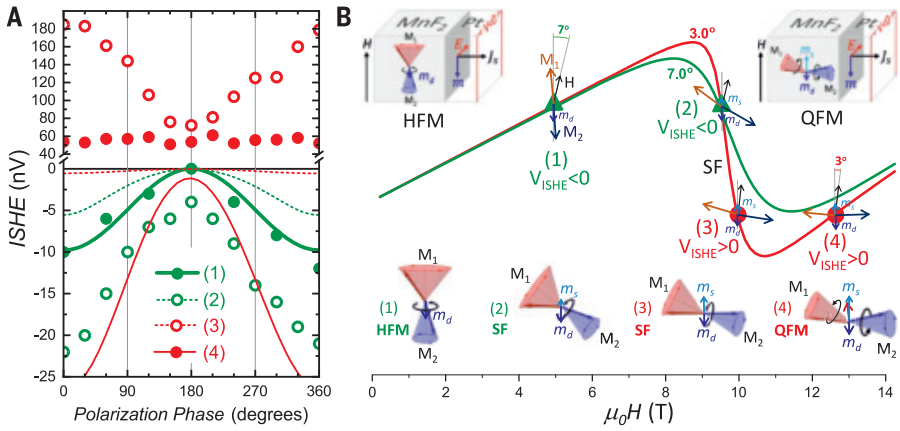

Fig. 4. Evolution of spin dynamics across the SF transition. (**A**) ISHE signals of the 395-GHz HFM (point 1), 395-GHz SF (point 2), 240-GHz SF (point 3), and 240-GHz QFM (point 4). Experimental data (dots) and numerical simulation based on coherent spin pumping (curves) agree quantitatively for point 1 and qualitatively for point 2; points 3 and 4 cannot be captured by coherent spin pumping. We used a larger microwave power in the 240-GHz resonances—hence the larger magnitude of the signals for points 3 and 4. (**B**) Illustration of the orientations of the sublattice magnetizations $\vec{M}_1$ and $\vec{M}_2$ and the applied field H_0 (with H_A along the vertical *z* axis) for four resonances (1 and 2 for 395 GHz and 3 and 4 for 240 GHz) representative of the change in AF dynamics in transiting from the HFM into the QFM through the SF region. The upper sketches represent the orientation and spin polarization of the pumped spin current and the induced ISHE electric field with respect to the measuring circuit in the sample. The lower insets illustrate the precessional cones of $\vec{M}_1$ and $\vec{M}_2$ for each of the resonances.

surprising, as they partially retain the features (especially the chirality) of the HFM, whereas the ground state undergoes a gradual evolution from the colinear configuration into the SF configuration. However, the sign of the 395-GHz SF resonance is opposite that of the 240-GHz resonance and requires a more detailed analysis.

In Fig. 4A, we directly compare the phase-modulation pattern for four particular resonances under positive magnetic fields; Fig. 4B relates them to four representative points on the upper-frequency branch and illustrates their physical meaning. In the low-field regime, as described by point 1, the nonequilibrium (dynamical) spin angular momentum m_d carried by the HFM opposes the magnetic field. In the high-field regime, once the sublattice magnetizations have flopped into a direction perpendicular to the applied magnetic field, as depicted by point 4, a finite (static) magnetization m_s along the magnetic field is induced in the ground state because the Zeeman interaction cants both sublattices toward the applied field. The QFM refers to a right-handed rotation of the induced magnetization m_s, similar to a ferromagnet (*21*), which is why it is named QFM; the sublattice magnetizations are still strongly antiferromagnetically connected by the predominant exchange interaction. Correspondingly, the nonequilibrium spin angular momentum m_d induced upon excitation is negative with respect to the magnetic field; its sign follows that of the HFM. However, the measured ISHE signal arising from the QFM does not follow this rule, indicating that the spin current may not be originating from coherent spin pumping at point 4. As a theoretical check, we numerically calculated the dc coherent spin pumping for all points given by the following expression (*19*)

$$\frac{e}{\hbar}\vec{I}_s = G_r(\vec{n}\times\dot{\vec{n}} + \vec{m}\times\dot{\vec{m}}) - G_i\dot{\vec{m}} \qquad (5)$$

where $G_r = g_r e^2/h$ is the mixing conductance extracted from Eq. 4. Note that the last term averages to zero on a magnetization precession cycle and thus does not contribute to dc spin pumping. The corresponding calculated ISHE voltages generated by the pumped spins are shown in Fig. 4A (lines). Theory can quantitatively account for the behavior of the HFM (point 1 in Fig. 4A); however, it fails to explain the SF and the QFM signals. For the upper-frequency branch, the theory predicts the same polarization modulation and sign for all ISHE signals arising from coherent spin pumping, with varying magnitudes for the different points. Figure S6 shows the calculated trajectories of the sublattice magnetizations corresponding to points 1 to 4 in Fig. 4; sublattice magnetization with overall projection along the applied field displays a larger precession angle than its opposite, resulting in a dynamical net moment against the applied field in all cases (i.e., negative ISHE voltage). Experimentally, the 395-GHz SF signal exhibits the expected sign and polarization modulation but is substantially larger than expected from theory. The 240-GHz SF has the expected polarization modulation but not the sign. Finally, as mentioned above, the QFM exhibits neither the modulation nor the sign predicted by theory, confirming that coherent spin pumping is unlikely to be the mechanism behind the system response after the SF transition.

A possible explanation of the independence of the QFM signal on the microwave polarization is that the QFM signal arises from a combined effect of magnetic proximity and thermal spin-current generation. Specifically, it is possible that the ground-state magnetization polarizes the conduction electrons in the Pt so that most spins are parallel to the magnetization and, hence, to the applied magnetic field. At the QFM resonance, microwave heating leads to a temperature gradient in the thickness direction, which in turn generates a spin-polarized current in the Pt that converts into an ISHE voltage.

In the unusual regime of the SF transition, the spin dynamics gradually loses the HFM characteristic while acquiring the QFM behavior. In Fig. 4B, point 2 (point 3) marks the 395-GHz (240-GHz) SF resonance, where the sign of ISHE follows that of the HFM (QFM) at point 1 (point 4). This strongly suggests that there must be a turning point between points 2 and 3 at which the spin current starts to be dominated by the ground-state magnetization rather than the nonequilibrium spin angular momentum in MnF_2. However, the exact location of this critical point and how the eigenmodes evolve in the vicinity of this point can only be determined numerically in the presence of a finite misalignment angle. In fig. S5, we calculated the net equilibrium magnetization as a function of field, qualitatively verifying the above behavior.

By comparing Fig. 2 and Fig. 4 for the 240-GHz resonance, we further notice that the SF signal (point 3) is stronger than the QFM signal (point 4) even though the ground-state magnetization, and hence the proximity effect, is apparently smaller at point 3, as the QFM behavior there is not fully developed. A possible reason is that within the narrow window of SF transition, the ground state becomes highly unstable, which appreciably enlarges the dynamical susceptibility $\chi(\omega)$. Under fixed microwave power, the heat production rate is proportional to $|\chi(\omega)|^2$. Therefore, it is natural to expect a markedly larger heating effect at point 3 than at point 4. The subtle behavior in the vicinity of SF transition calls for further systematic measurements with additional microwave frequencies.

Outlook

The demonstration of the coherent spin-pumping effect in MnF_2/Pt opens the door to advancements in controlling and understanding spin-transfer torques in AF-based systems that may lead to energy-efficient and

fault-tolerant spintronic devices operating at terahertz frequencies. Further exploration of spin pumping in AF-based systems will enable a thorough understanding of the relation between the structural symmetries of antiferromagnets, the characteristics of their spin dynamics, and the polarization of the associated terahertz signals, which will aid the design of next-generation spintronic applications in which antiferromagnets are active players.

REFERENCES AND NOTES

1. L. Néel, *Ann. Phys.* **11**, 232–279 (1936).
2. P. Wadley *et al.*, *Science* **351**, 587–590 (2016).
3. D. Kriegner *et al.*, *Nat. Commun.* **7**, 11623 (2016).
4. R. Cheng, D. Xiao, A. Brataas, *Phys. Rev. Lett.* **116**, 207603 (2016).
5. R. Khymyn, I. Lisenkov, V. Tiberkevich, B. A. Ivanov, A. Slavin, *Sci. Rep.* **7**, 43705 (2017).
6. R. Khymyn, I. Lisenkov, V. S. Tiberkevich, A. N. Slavin, B. A. Ivanov, *Phys. Rev. B* **93**, 224421 (2016).
7. R. Kleiner, *Science* **318**, 1254–1255 (2007).
8. J. Nogués, I. K. Schuller, *J. Magn. Magn. Mater.* **192**, 203–232 (1999).
9. B. G. Park *et al.*, *Nat. Mater.* **10**, 347–351 (2011).
10. Y. Y. Wang *et al.*, *Phys. Rev. Lett.* **109**, 137201 (2012).
11. X. Marti *et al.*, *Nat. Mater.* **13**, 367–374 (2014).
12. I. Fina *et al.*, *Nat. Commun.* **5**, 4671 (2014).
13. S. Y. Bodnar *et al.*, *Nat. Commun.* **9**, 348 (2018).
14. M. Meinert, D. Graulich, T. Matalla-Wagner, *Phys. Rev. Appl.* **9**, 064040 (2018).
15. J. Železný *et al.*, *Phys. Rev. Lett.* **113**, 157201 (2014).
16. R. Lebrun *et al.*, *Nature* **561**, 222–225 (2018).
17. A. S. Núñez, R. Duine, P. Haney, A. MacDonald, *Phys. Rev. B* **73**, 214426 (2006).
18. H. V. Gomonay, V. M. Loktev, *Phys. Rev. B* **81**, 144427 (2010).
19. R. Cheng, J. Xiao, Q. Niu, A. Brataas, *Phys. Rev. Lett.* **113**, 057601 (2014).
20. P. Ross *et al.*, *J. Appl. Phys.* **118**, 233907 (2015).
21. C. Kittel, *Phys. Rev.* **82**, 565 (1951).
22. T. Nagamiya, K. Yosida, R. Kubo, *Adv. Phys.* **4**, 1–112 (1955).
23. There is an additional zero-energy mode (spin-superfluid mode) after the SF transition. This mode becomes visible only at low frequencies when the field is applied away from the easy anisotropy axis, but this mode is not accessible within our range of frequencies and will not be further discussed in this work.
24. J. Kotthaus, V. Jaccarino, *Phys. Rev. Lett.* **28**, 1649–1652 (1972).
25. M. Hagiwara *et al.*, *Int. J. Infrared Millim. Waves* **20**, 617–622 (1999).
26. A detailed discussion is presented in supplementary text section S1: "Spectroscopy and ISHE Measurements."
27. I. S. Jacobs, *J. Appl. Phys.* **32**, S61–S62 (1961).
28. Y. Tserkovnyak, A. Brataas, G. E. Bauer, *Phys. Rev. Lett.* **88**, 117601 (2002).
29. A. Brataas, Y. Tserkovnyak, G. E. Bauer, B. I. Halperin, *Phys. Rev. B* **66**, 060404 (2002).
30. Y. Tserkovnyak, A. Brataas, G. E. Bauer, *Phys. Rev. B* **66**, 224403 (2002).
31. E. Saitoh, M. Ueda, H. Miyajima, G. Tatara, *Appl. Phys. Lett.* **88**, 182509 (2006).
32. Ø. Johansen, A. Brataas, *Phys. Rev. B* **95**, 220408 (2017).
33. R. Cheng, thesis, The University of Texas at Austin (2014).
34. S. M. Rezende, R. L. Rodríguez-Suárez, A. Azevedo, *Phys. Rev. B* **93**, 014425 (2016).
35. S. M. Wu *et al.*, *Phys. Rev. Lett.* **116**, 097204 (2016).
36. W. Lin, C. L. Chien, arXiv:1804.01392 [cond-mat.mtrl-sci] (28 Mar 2018).
37. The presence of the sample prevents the achievement of perfect circular polarization, which results in a small residual ISHE signal that varies with the size of the sample.
38. L. Liu, R. A. Buhrman, D. C. Ralph, arXiv:1111.3702 [cond-mat.mes-hall] (16 Nov 2011).
39. W. Zhang *et al.*, *Appl. Phys. Lett.* **103**, 242414 (2013).
40. P. Vaidya, Sub-Terahertz Spin Pumping from an Insulating Antiferromagnet, Version 1.0, Harvard Dataverse (2020); https://doi.org/10.7910/DVN/RFCH1Q.

ACKNOWLEDGMENTS

We thank A. Ramirez of the Materials Advancement Portal at UC Santa Cruz (https://materials.soe.ucsc.edu/home) for providing the MnF_2 single crystal. **Funding:** P.V., R.C., D.L., and E.d.B. acknowledge support from the Air Force Office of Scientific Research under grant FA9550-19-1-0307. A.B. acknowledges support from the European Research Council via Advanced Grant 669442 "Insulatronics" and the Research Council of Norway via project 262633 "QuSpin." The work at UC Santa Cruz was supported in part by the University of California Multicampus Research Programs and Initiatives grant MRP-17-454963. A portion of this work was performed at the National High Magnetic Field Laboratory, which is supported by the National Science Foundation Cooperative Agreement DMR-1644779 and the state of Florida. **Author contributions:** P.V., S.A.M., J.v.T., D.L., and E.d.B, conceived and designed the experiments. P.V. and J.v.T performed the high-frequency experiments. S.A.M. performed the materials characterization experiments. S.A.M. and D.L. provided the samples. P.V. and E.d.B analyzed the data and performed numerical simulations. Y.L. and R.C. computed the dynamical response of the system and the corresponding spin pumping. A.B. suggested the experimental detection. Both R.C. and A.B. assisted with the theoretical interpretations of the results. All authors contributed to discussions and manuscript writing. **Competing interests:** The authors declare no competing interests. **Data and materials availability:** All data in the main text and the supplementary materials, along with the code used to analyze the data and generate the fitted plots, are available at the Harvard Dataverse (*40*).

SUPPLEMENTARY MATERIALS

science.sciencemag.org/content/368/6487/160/suppl/DC1
Materials and Methods
Supplementary Text
Figs. S1 to S7
References (*41*, *42*)
Movies S1 to S4

9 September 2019; accepted 12 March 2020
10.1126/science.aaz4247

REPORTS

TROPICAL FORESTS

Demographic trade-offs predict tropical forest dynamics

Nadja Rüger[1,2,3]*, Richard Condit[4,5], Daisy H. Dent[3,6], Saara J. DeWalt[7], Stephen P. Hubbell[3,8], Jeremy W. Lichstein[9], Omar R. Lopez[3,10], Christian Wirth[1,11,12], Caroline E. Farrior[13]

Understanding tropical forest dynamics and planning for their sustainable management require efficient, yet accurate, predictions of the joint dynamics of hundreds of tree species. With increasing information on tropical tree life histories, our predictive understanding is no longer limited by species data but by the ability of existing models to make use of it. Using a demographic forest model, we show that the basal area and compositional changes during forest succession in a neotropical forest can be accurately predicted by representing tropical tree diversity (hundreds of species) with only five functional groups spanning two essential trade-offs—the growth-survival and stature-recruitment trade-offs. This data-driven modeling framework substantially improves our ability to predict consequences of anthropogenic impacts on tropical forests.

Tropical forests are highly dynamic. Only about 50% of the world's tropical forests are undisturbed old-growth forests (*1*). The remaining half comprises forests regenerating after previous land use, timber or fuelwood extraction, or natural disturbances. Even unmanaged old-growth forests are a dynamic mosaic of patches recovering from single or multiple treefall gaps (*2*). Thus, understanding how forest structure and composition of the diverse tree flora change during recovery from disturbance is fundamental to predicting carbon dynamics, as well as to planning sustainable forest management (*3*). Despite the importance of regenerating tropical forests for the global carbon cycle and timber industry, our mechanistic understanding and ability to forecast compositional changes of these forests remain severely limited (*4*).

Conceptually, tropical forest succession has been viewed mostly through a one-dimensional lens distinguishing species along a fast-slow life-history continuum, or growth-survival trade-off (*4*–*6*). "Fast" species are light-demanding and grow quickly, but survive poorly, and dominate early successional stages, whereas "slow" species are shade-tolerant and grow slowly, but survive well, and reach dominance in later successional stages. However, several studies suggest that tropical tree communities are also structured along a second major trade-off axis that is orthogonal to the growth-survival trade-off: the stature-recruitment trade-off (*7*, *8*). The stature-recruitment trade-off distinguishes long-lived pioneers (LLPs) from short-lived breeders (SLBs). LLPs grow fast and live long, and hence attain a large stature, but exhibit low recruitment. SLBs grow and survive poorly, and hence remain short-statured, but produce large numbers of offspring (*8*). However, we are lacking a systematic assessment of how important these trade-offs are for tropical forest dynamics.

To evaluate the importance of the growth-survival and stature-recruitment trade-offs for tropical forest dynamics, we parameterized the

perfect plasticity approximation (PPA) model (*9*, *10*) with demographic trade-offs derived from forest inventory data. The PPA model simulates the dynamics of a potentially large number of species based on a small set of demographic rates (growth, survival, and recruitment) and accounts for height-structured competition for light by distinguishing up to four canopy layers (*11*). Canopy gaps are filled by the tallest trees from lower canopy layers, without regard for their horizontal position [perfect plasticity assumption (*9*)].

Our study site is the tropical moist forest at Barro Colorado Island (BCI), Panama, where recruitment, growth, and survival of individual trees have been monitored in a 50-ha plot for more than 30 years (*2*, *11*, *12*). To account for the dependence of these demographic rates on light availability, we assigned all monitored individuals of 282 tree and shrub species to one of four canopy layers on the basis of their size and the size of their neighbors (*11*, *13*) and estimated model parameters (annual diameter growth and survival rates) for each species in each canopy layer (*8*). Additionally, we calculated species recruitment rates per unit of basal area. A dimension reduction of model parameters [weighted principal components analysis (PCA) (*14*)] reveals the two demographic trade-offs, that is, the growth-survival trade-off and the stature-recruitment trade-off, which together explain 65% of demographic variation among the 282 species (Fig. 1).

Our goal here is to explore whether this low-dimensional demographic trade-off space can capture tropical forest dynamics, and if so, how much demographic diversity is necessary to accurately predict changes in basal area (a proxy for carbon storage in aboveground biomass) over time. We used species' positions in the trade-off space to estimate model parameters for all 282 species (*11*), thus smoothing across observed relationships between demographic rates. We simulated forest dynamics under four scenarios that differed in the number of trade-offs (one versus two) and level of demographic diversity [number of simulated species or plant functional types (PFTs); Table 1 and Fig. 2A]. We tested model performance for the 50-ha old-growth plot at BCI (also used to derive demographic rates) and for a chronosequence of nearby secondary forests that share a similar topography and soil and a majority of tree species (*15*).

To compare the observed dynamics of the 50-ha old-growth plot in BCI with model predictions, we initialized the model with inventory data from 1985 and simulated forest dynamics until 2010. When only the growth-survival trade-off was included, basal area was predicted to decline because of a decline in the number of trees >20 cm in diameter, especially of fast species (Fig. 2B and fig. S1). Including the stature-recruitment trade-off improved the match between predicted and observed basal area and aboveground biomass (AGB; Fig. 2B and figs. S2 and S3) for different PFTs and size classes (figs. S4 and S5). However, when all species were simulated individually (scenario 4), the number of large trees (>60 cm in diameter) and basal area were incorrectly predicted to increase (fig. S1). This was attributable to the greater influence of measurement errors due to small sample sizes when parameterizing the model for 282 species (*11*), although most species-level predictions were reliable (fig. S6). Maximum diameters were accurately predicted by all scenarios, except for scenario 2, where observed maximum diameters >150 cm were not reproduced (fig. S7). This test shows that the model scenarios that included both trade-offs were able to reproduce the structure and stability of the forest over the time span that was used to derive demographic rates.

Next, we tested the ability of the model to predict successional changes in secondary forests. We used the same model parameterization scenarios, initialized the model with data from 40-year-old secondary forest, and compared predictions of forest dynamics with observations from a chronosequence of 60-, 90-, and 120-year-old secondary forests (two 1-ha plots in each age class). As in old-growth forest, predictions of secondary succession were most accurate when forest diversity was represented by five PFTs spanning both demographic trade-offs. When only the growth-survival trade-off was included, the increase of basal area (Fig. 2C) and AGB (fig. S2) during succession was underestimated because the number of large trees (>60 cm in diameter) was underestimated (fig. S8). By contrast, when both trade-offs were included, observed successional changes in basal area, AGB, and abundance for different PFTs and size classes were accurately reproduced (Fig. 2C and figs. S2 and S8 to S10). However, when all species were simulated individually (scenario 4), the number of large trees (>60 cm in diameter) and basal area of fast species and LLPs were overestimated. The observed peak in basal area in the 90-year-old secondary forest is likely caused by remnant trees in the study plots and disappears when larger spatial scales are considered (*16*). The diameter distribution after 400 years of simulation closely matched the observed diameter distribution only when both demographic trade-offs were included (Fig. 3A).

In addition to the above simulations, we also ran simulations with alternative initial conditions to explore the robustness of our results. The alternative initial conditions [bare ground and 20-year-old forest; (*11*)] did not qualitatively affect our results. For all initial conditions, the five-PFT scenario spanning both demographic trade-offs yielded predictions that best matched observations (fig. S11). Together, the old-growth and secondary forest simulations suggest a close match between the five-PFT scenario and the available data. However, even with this multidecadal dataset, we have only a limited capacity to rigorously test a forest dynamics model. For example, we used chronosequence data to

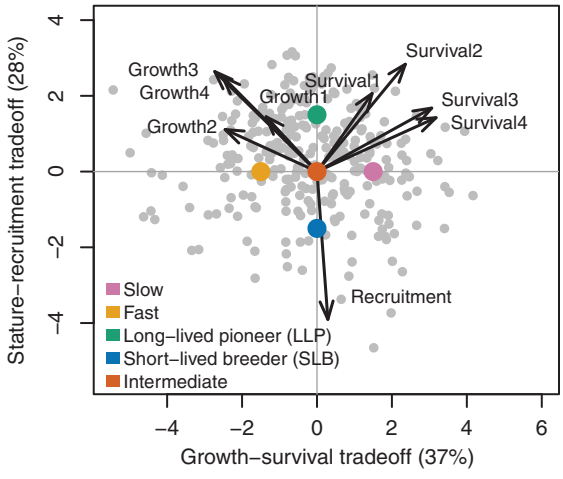

Fig. 1. Demographic trade-offs for 282 tree species at BCI, Panama. Arrows show loadings of a weighted PCA on annual diameter growth and survival rates of individuals ≥1 cm in diameter in four canopy layers (where Growth1 indicates growth in full sun and Growth4 indicates growth of individuals that are shaded by three canopy layers) and the number of sapling recruits per unit of basal area. Colored dots are locations in demographic space of plant functional types (PFTs) that were used in model scenarios 1 and 3.

[1]German Centre for Integrative Biodiversity Research (iDiv) Halle-Jena-Leipzig, Deutscher Platz 5e, 04103 Leipzig, Germany. [2]Department of Economics, University of Leipzig, Grimmaische Straße 12, 04109 Leipzig, Germany. [3]Smithsonian Tropical Research Institute, Apartado 0843-03092, Balboa, Ancón, Panama. [4]Field Museum of Natural History, 1400 S. Lake Shore Dr., Chicago, IL 60605, USA. [5]Morton Arboretum, 4100 Illinois Rte. 53, Lisle, IL 60532, USA. [6]Biological and Environmental Sciences, University of Stirling, Stirling FK9 4LA, UK. [7]Department of Biological Sciences, Clemson University, Clemson, SC 29634, USA. [8]Department of Ecology and Evolutionary Biology, University of California, Los Angeles, CA 90095, USA. [9]Department of Biology, University of Florida, Gainesville, FL 32611, USA. [10]Instituto de Investigaciones Científicas y Servicios de Alta Tecnología (INDICASAT), Edificio 209, Clayton, Panama. [11]Systematic Botany and Functional Biodiversity, Institute of Biology, University of Leipzig, Johannisallee 21-23, 04103 Leipzig, Germany. [12]Max Planck Institute for Biogeochemistry, Hans-Knöll Str. 10, 07745 Jena, Germany. [13]Department of Integrative Biology, University of Texas at Austin, Austin, TX 78712, USA.
***Corresponding author. Email: nadja.rueger@idiv.de**

BROWN DWARFS

A measurement of the wind speed on a brown dwarf

Katelyn. N. Allers[1]*†, Johanna M. Vos[2]†, Beth A. Biller[3,4]†, Peter. K. G. Williams[5,6]†

Zonal (latitudinal) winds dominate the bulk flow of planetary atmospheres. For gas giant planets such as Jupiter, the motion of clouds can be compared with radio emissions from the magnetosphere, which is connected to the planet's interior, to determine the wind speed. In principle, this technique can be applied to brown dwarfs and/or directly imaged exoplanets if periods can be determined for both the infrared and radio emissions. We apply this method to measure the wind speeds on the brown dwarf 2MASS J10475385+2124234. The difference between the radio period of 1.751 to 1.765 hours and infrared period of 1.741 ± 0.007 hours implies a strong wind (+650 ± 310 meters per second) proceeding eastward. This could be due to atmospheric jet streams and/or low frictional drag at the bottom of the atmosphere.

Gas giant exoplanets and brown dwarfs (objects with masses of 13 to 72 times that of Jupiter) rotate on time scales of hours to days (*1*–*4*). If there are any inhomogeneous features at the top of their atmospheres, such as clouds, the rotational modulation causes quasi-periodic variability in their brightness. Photometric searches for periodic brightness modulations can therefore probe the rotational properties of these objects. Quasi-periodic near- and mid-infrared (IR) variability is common in isolated brown dwarfs of spectral types L and T (*2*, *5*).

Within the Solar System, it is possible to observe the effects of rapid rotation on the atmospheric physics of the giant planets. Zonal winds—latitudinal flows resulting from rapid rotation and convection—dominate the bulk atmospheric flow of Jupiter (*6*). Models of the atmospheric dynamics of brown dwarfs and exoplanets incorporate the effects of rotation and zonal winds (*7*–*9*). These studies have shown that wind speeds and flow patterns are determined by the efficiency with which the atmosphere can radiatively cool and the coupling between the atmosphere and interior of the planet, among other atmospheric conditions.

Wind speeds have been measured for some hot, gas giant exoplanets using Doppler shifts in transit spectroscopy (*10*). This technique requires a tidally locked planet (for which the rotation period and orbital period are equal) as well as high-speed winds (several kilometers per second) driven by heat redistribution from the highly irradiated day side to the night side of the planet (*10*). These conditions are not typical for planetary-mass objects, particularly those with wide separations from their parent star or free-floating objects that are not gravitationally bound to a star.

Photometric variability studies of brown dwarfs and free-floating, planetary-mass objects have inferred the presence of zonal winds (*11*, *12*). Changes in the rotational brightness modulation of a highly variable brown dwarf over several months could be due to wind speeds of 45 m s^{-1} (*11*). Quasi-periodic variability data for two brown dwarfs have been modeled as originating from beating, planetary-scale, atmospheric wave pairs with differential wind velocities of several hundred meters per second (*12*).

We describe an alternative technique for measuring wind speeds (v_{wind}) on exoplanets and brown dwarfs. Observations of Jupiter are typically interpreted using a coordinate system determined from Jupiter's radio emission, known as System III, whose rotation period is 9 hours 55 min 30 s (*13*). This radio periodicity corresponds to the rotation rate of Jupiter's magnetosphere. Because the Jovian magnetic field originates >7000 km below its visible surface (*14*), the radio period is determined by the rotation of the interior of the planet, which is expected to rotate as a rigid body (*15*). An alternative coordinate system derived for Jupiter's surface is known as System I, which has a period of 9 hours 50 min 30 s, measured from the rotation of its atmospheric features in optical and infrared light from 10°N to 10°S. The 5-min difference between the radio System III period ($T_{interior}$) and optical–infrared (IR) System I period ($T_{atmosphere}$) corresponds to a velocity difference at the radius of Jupiter's visible surface (R = 71,492 km) of

$$v_{wind} = 2\pi R\left(\frac{1}{T_{atmosphere}} - \frac{1}{T_{interior}}\right) = +106\ \mathrm{ms}^{-1} \quad (1)$$

which agrees with the measured wind speed observed in Jupiter's equatorial region (*16*).

Radio observations of brown dwarfs have been used to measure the rotational modulation of their magnetic field (*17*), in some cases with period uncertainties as low as 0.11 min. Radio emission from brown dwarfs originates from the same mechanism (electron-cyclotron maser instability, ECMI) as Jupiter's radio emission, as shown by observations (*18*) and models (*19*). For brown dwarfs of spectral types L and T, the magnetic field is expected to originate well below the visible surface (*20*). Therefore, we expect the radio period of brown dwarfs and exoplanets to represent their interior period of rotation, as it does for Jupiter.

If global maps of Jupiter were degraded to unresolved photometric measurements (akin to those available for brown dwarfs), they would have variability amplitudes as large as 20% (*21*), which is similar to those seen in the most highly variable brown dwarfs (*3*). Optical–IR photometric monitoring of brown dwarfs can determine rotational periods with precisions <1 min from the ground (*22*) or from space (*2*). Wind speed measurements of brown dwarfs and planetary-mass objects should therefore be possible by measuring radio and IR periods using current facilities.

We applied this method to observations of two brown dwarfs: 2MASS J10475385+2124234 (hereafter 2MASS J1047+21) and WISE J112254.73+255021.5 (hereafter WISE J1122+25). No infrared period was detected for WISE J1122+25 (*23*), so we focus our discussion on 2MASS J1047+21.

2MASS J1047+21 is a brown dwarf of spectral type T6.5 which is 10.6 pc away (*24*). On the basis of its luminosity and evolutionary models for typical brown dwarf ages of 0.5 to 10 billion years, 2MASS J1047+21 has an estimated mass of 16 to 68 times that of Jupiter and an estimated temperature of 880 ± 76 K (*24*), which is cooler than other brown dwarfs with detected radio emission. Circularly polarized bursts of radio emission have been detected from 2MASS J1047+21, consistent with ECMI and indicating a rotation period of 1.77 ± 0.04 hours (*25*) and a magnetic field strength of 5.6 kG (*26*).

We used the Infrared Array Camera on the Spitzer Space Telescope to search for photometric variability of 2MASS J1047+21 at 4.5 μm (*23*). Observations were conducted on 7 April 2017 for 7 hours and on 15 April 2018 for 14 hours. We detect sinusoidal variability in both epochs with an amplitude of 0.5% (Fig. 1), indicating that a single, long-lived atmospheric feature is likely responsible for the variability. We used two approaches to determine the IR period: a sinusoidal model fitted using a Markov Chain Monte Carlo (MCMC) algorithm (Fig. 1), and an analysis of the Lomb-Scargle periodogram (Fig. 2A) using bootstrap and Monte Carlo techniques for uncertainty determination (Fig. 2, B and C). The resulting periods and uncertainties agree with each other (*23*). We adopt an IR period of 1.741 ± 0.007 hours.

We also observed 2MASS J1047+21 at 4–8 GHz with the Karl G. Jansky Very Large Array (VLA)

[1]Department of Physics and Astronomy, Bucknell University, Lewisburg, PA 17837-2029, USA. [2]Department of Astrophysics, American Museum of Natural History, New York, NY 10024-5102, USA. [3]Scottish Universities Physics Alliance, Institute for Astronomy, University of Edinburgh, Edinburgh EH9 3HJ, UK. [4]Centre for Exoplanet Science, University of Edinburgh, Edinburgh EH9 3FD, UK. [5]Center for Astrophysics, Harvard Smithsonian, Cambridge, MA 02138-1516, USA. [6]American Astronomical Society, Washington, DC 20006-1681, USA.
*Corresponding author. Email: katelynallers@gmail.com
†These authors contributed equally to this work.

and their pulse widths. This approach yields a period range of 1.751 to 1.765 hours. Folding the radio data by different periods (Fig. 4) shows that pulses align in phase for periods in the range 1.751 to 1.765 hours but are not well aligned for periods outside that range.

For an IR period of $T_{\mathrm{atmosphere}}$ = 1.741 ± 0.007 hours, a uniformly distributed radio period of T_{interior} = 1.751 to 1.765 hours, and a radius of 67,200 km (*24*), Eq. 1 gives a wind speed for 2MASS J1047+21 of 650 ± 310 m s^{-1}. This assumes that the IR variability originates in the equatorial region, but Eq. 1 can be adapted to other latitudes by scaling by the cosine of the latitude. The inclination of 2MASS J1047+21's rotation is unknown, but all other radio-bursting brown dwarfs with known inclinations are viewed nearly equator-on (*18*). Photometric variability most commonly originates at equatorial to mid-latitudes of less than 35° (*21*, *27*). Thus, latitudinal or viewing-angle effects would likely change the result by less than the uncertainty. The measured wind speed is that of the (unknown) atmospheric inhomogeneity that dominates the photometric variability. If this atmospheric feature occurs between bands of zonal wind having alternating wind direction, our measured wind speed would underestimate the true zonal wind speeds. Some of Jupiter's atmospheric features are

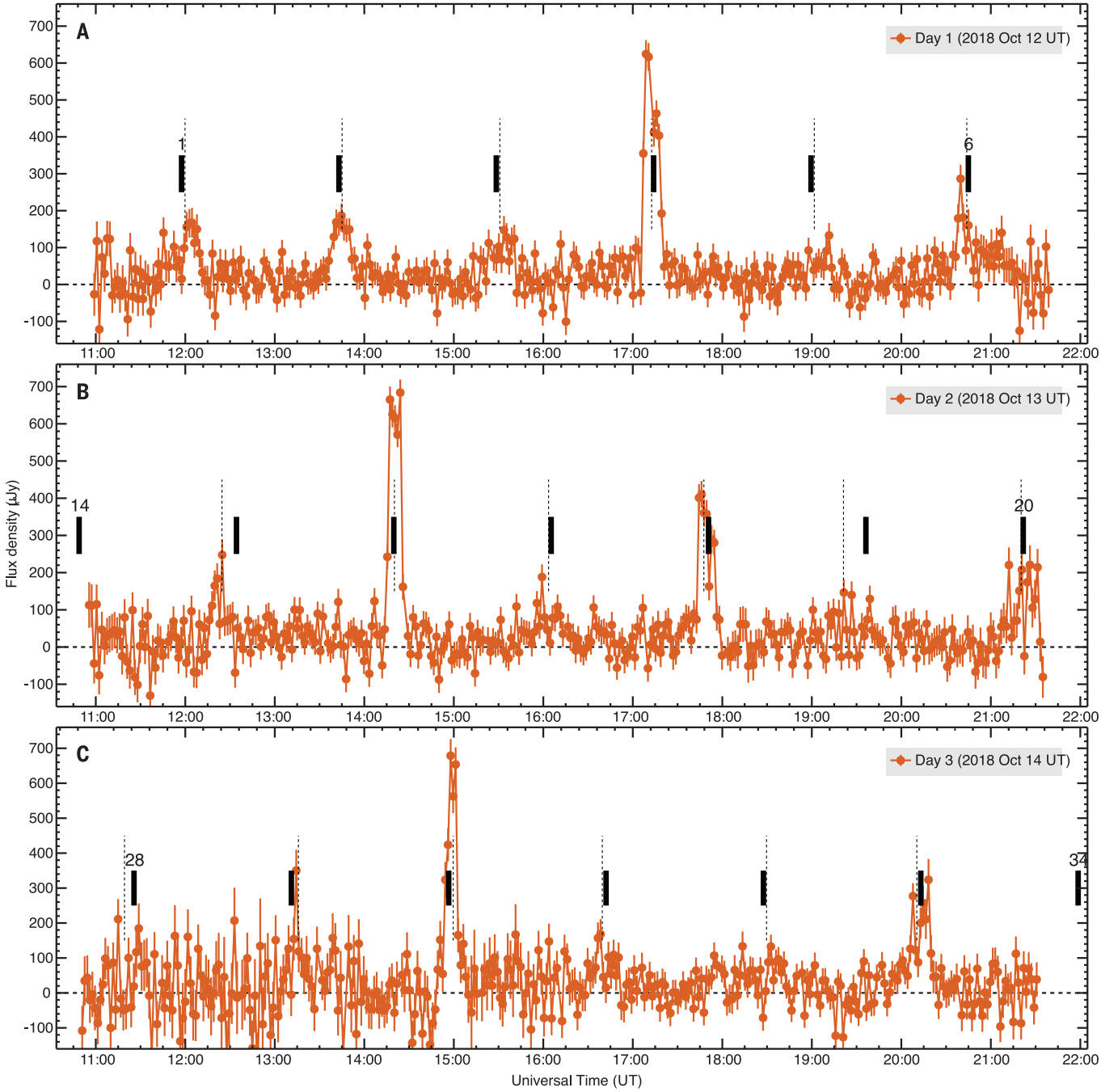

Fig. 3. Radio light curve of 2MASS J1047+21 from VLA observations. (**A** to **C**) Left-circularly polarized radio flux in microjanskys (points) on three consecutive nights of observations, each lasting about 10 hours. 1σ uncertainties are plotted as vertical lines for each data point. Radio pulses of varying intensity are evident. Thin vertical dashed lines indicate pulse TOAs (*23*). Thick vertical solid lines indicate TOAs from the best-fitting period derived from these data, labeled with the number of rotations since the start of the observation. The data cover about 18 rotations out of 34 that occurred in this period.

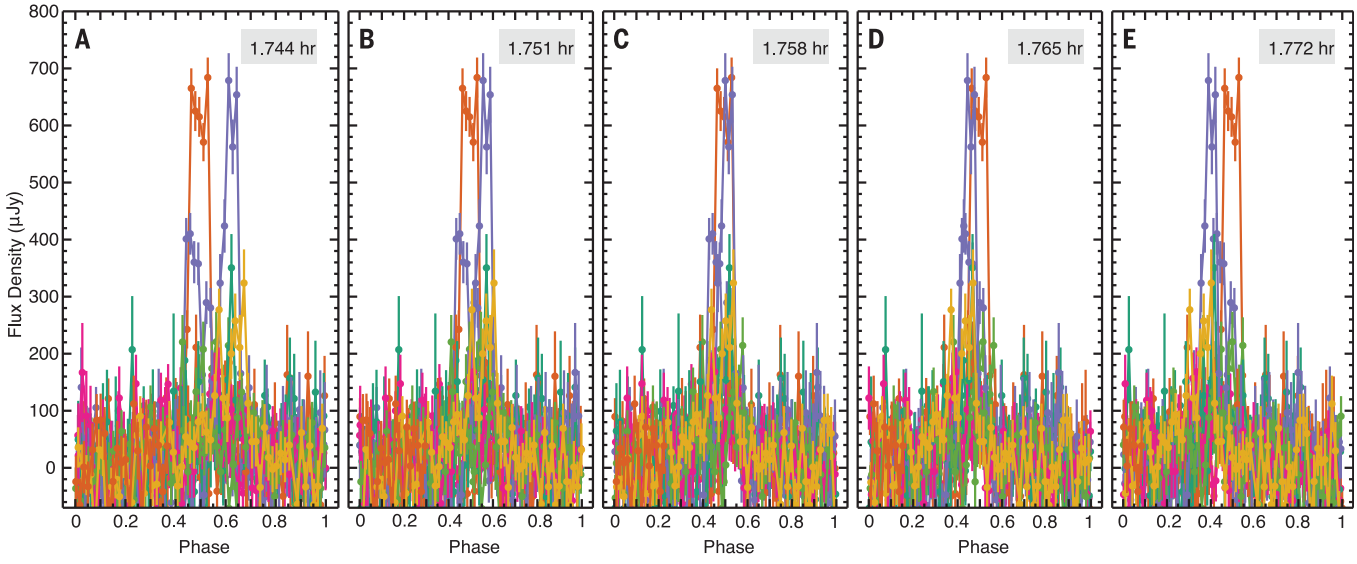

Fig. 4. Alignment of pulses for possible periods of the radio data. (**A** to **E**) The data (points) from Fig. 3 are folded by periods that differ by 0.007 hours for comparison of the phase (fraction of a rotation period) of radio pulses. Each color (arbitrarily) indicates the data from a separate rotation. 1σ uncertainties are plotted as vertical lines for each data point. (C) The radio pulses folded at the period preferred by our analysis (*23*). At this period, the pulses from all of our observed rotations are aligned at a phase of around 0.5. The pulses are aligned at a phase of around 0.5 for periods of 1.751 to 1.765 hours (B to D), whereas the phases of the pulses are not aligned for periods outside of this range (A and E).

transported by processes other than wind (*28*), but the effect of these processes would fall within the uncertainties of our wind speed measurement for 2MASS J1047+21.

We detect a positive (eastward) wind speed at >98% confidence (2.1σ). As with Jupiter, the IR period of 2MASS J1047+21 is shorter than its radio period, indicating an atmosphere that is rotating faster than the interior. The wind speed on 2MASS J1047+21 is higher than on the gas giant planets in the Solar System (*16*, *29*). Analytic theory predicts that larger atmospheric heat fluxes lead to higher wind speeds (*7*). Three-dimensional numerical simulations show that zonal winds of hundreds of meters per second can occur when strong convective forcing and/or weak damping (either radiative or frictional) promote the formation of atmospheric jet streams (*9*).

Our method for determining the wind speed can in principle also be applied to exoplanets, which have rotation rates and periodic variability similar to those of brown dwarfs (*1*, *4*). Exoplanets with masses similar to Jupiter's have magnetic field strengths of around 100 G (*30*), which is weaker than the kilogauss fields of brown dwarfs (*26*). Because the frequency at which ECMI emission is detected is proportional to the magnetic field strength, we expect exoplanets to emit at lower radio frequencies.

REFERENCES AND NOTES

1. I. A. G. Snellen *et al.*, *Nature* **509**, 63–65 (2014).
2. S. A. Metchev *et al.*, *Astrophys. J.* **799**, 154 (2015).
3. B. A. Biller *et al.*, *Astron. J.* **155**, 95 (2018).
4. Y. Zhou *et al.*, *Astron. J.* **157**, 128 (2019).
5. J. Radigan, D. Lafrenie're, R. Jayawardhana, E. Artigau, *Astrophys. J.* **793**, 75 (2014).
6. Y. Kaspi *et al.*, *Nature* **555**, 223–226 (2018).
7. A. P. Showman, Y. Kaspi, *Astrophys. J.* **776**, 85 (2013).
8. G. Lee, C. Helling, I. Dobbs-Dixon, D. Juncher, *Astron. Astrophys.* **580**, A12 (2015).
9. A. P. Showman, X. Tan, X. Zhang, *Astrophys. J.* **883**, 4 (2019).
10. T. Louden, P. J. Wheatley, *Astrophys. J.* **814**, L24 (2015).
11. J. Radigan *et al.*, *Astrophys. J.* **750**, 105 (2012).
12. D. Apai *et al.*, *Science* **357**, 683–687 (2017).
13. P. K. Seidelmann *et al.*, *Celestial Mech. Dyn. Astron.* **98**, 155–180 (2007).
14. C. A. Jones, *Icarus* **241**, 148–159 (2014).
15. T. Guillot *et al.*, *Nature* **555**, 227–230 (2018).
16. J. Tollefson *et al.*, *Icarus* **296**, 163–178 (2017).
17. E. Berger *et al.*, *Astrophys. J.* **695**, 310–316 (2009).
18. G. Hallinan *et al.*, *Astrophys. J.* **684**, 644–653 (2008).
19. J. D. Nichols *et al.*, *Astrophys. J.* **760**, 59 (2012).
20. M. M. Kao *et al.*, *Astrophys. J.* **818**, 24 (2016).
21. H. Ge *et al.*, *Astron. J.* **157**, 89 (2019).
22. M. Gillon *et al.*, *Astron. Astrophys.* **555**, L5 (2013).
23. Materials and methods are available as supplementary materials.
24. J. C. Filippazzo *et al.*, *Astrophys. J.* **810**, 158 (2015).
25. P. K. G. Williams, E. Berger, *Astrophys. J.* **808**, 189 (2015).
26. M. M. Kao, G. Hallinan, J. S. Pineda, D. Stevenson, A. Burgasser, *Astrophys. J.* **237** (suppl.), 25 (2018).
27. J. M. Vos, K. N. Allers, B. A. Biller, *Astrophys. J.* **842**, 78 (2017).
28. D. S. Choi, A. P. Showman, A. R. Vasavada, A. A. Simon-Miller, *Icarus* **223**, 832–843 (2013).
29. E. García-Melendo, S. Pérez-Hoyos, A. Sánchez-Lavega, R. Hueso, *Icarus* **215**, 62–74 (2011).
30. P. W. Cauley, E. L. Shkolnik, J. Llama, A. F. Lanza, *Nature Astronomy* **3**, 1128–1134 (2019).
31. P. K. G. Williams, K. N. Allers, J. M. Vos, B. A. Biller, Dynamic spectrum of 2MASSW J1047539+212423 observed by the Karl G. Jansky Very Large Array, as a Numpy save file, Zenodo (2020).

ACKNOWLEDGMENTS

This study was based on observations made with the Spitzer Space Telescope, which is operated by the Jet Propulsion Laboratory, California Institute of Technology, under a contract with NASA. The National Radio Astronomy Observatory is a facility of the National Science Foundation operated under cooperative agreement by Associated Universities, Inc. This work benefited from the Exoplanet Summer Program in the Other Worlds Laboratory (OWL) at the University of California, Santa Cruz, funded by the Heising-Simons Foundation. We acknowledge S. Beiler, E. Berger, M. Kao, L. Lanwermeyer, M. Marley, S. Metchev, B. Pantoja, D. Powell, E. Shkolnik, A. Showman, X. Tan, J. Tolman, and X. Zhang for useful conversations. We also thank the anonymous reviewers, whose thoughtful comments improved this manuscript. **Funding:** Support for Program numbers 14188 and 14686 was provided by NASA through a grant from the Space Telescope Science Institute, which is operated by the Association of Universities for Research in Astronomy, Incorporated, under NASA contract NAS 5-26555. J.M.V. acknowledges funding support from the National Science Foundation under award AST-1614527 and Spitzer Cycle 14 Caltech/JPL Research Support Agreement 1627378. **Author contributions:** K.N.A. planned and proposed the Spitzer Space Telescope observations, conducted an independent check of the data reduction, calculated the wind speeds, and wrote the manuscript. J.M.V. led the reduction and analysis of the Spitzer data, including the MCMC modeling, production of Figs. 1 and figs. S1 to S5, and associated text. B.A.B. performed the Lomb-Scargle analysis, produced Fig. 2 and fig. S6, and wrote part of the manuscript. P.K.G.W. planned, proposed, and reduced the VLA data, conducted the radio pulse time-of-arrival (TOA) analysis, produced Figs. 3 and 4, and wrote the corresponding text. **Competing interests:** We declare no competing interests. **Data and materials availability:** The VLA data are available via the NRAO Science Data Archive http://archive-new.nrao.edu/ under Project Code 18A-427. The Spitzer data are available via the Spitzer Heritage Archive http://sha.ipac.caltech.edu using Program IDs 13031 and 13231. The light curve data and code used for analysis and figure production are available at https://github.com/johannavos/BDwindspeeds/ and archived at https://doi.org/10.5281/zenodo.3700897. The VLA dynamic spectrum (an intermediate data product) is archived at Zenodo (*31*).

SUPPLEMENTARY MATERIALS

science.sciencemag.org/content/368/6487/169/suppl/DC1
Materials and Methods
Supplementary Text
Tables S1 to S3
Figs. S1 to S6
References (*32*–*58*)

26 September 2019; accepted 12 March 2020
10.1126/science.aaz2856

MESOSCOPIC PHYSICS

Fractional statistics in anyon collisions

H. Bartolomei[1]*, M. Kumar[1]*†, R. Bisognin[1], A. Marguerite[1]‡, J.-M. Berroir[1], E. Bocquillon[1], B. Plaçais[1], A. Cavanna[2], Q. Dong[2], U. Gennser[2], Y. Jin[2], G. Fève[1]§

Two-dimensional systems can host exotic particles called anyons whose quantum statistics are neither bosonic nor fermionic. For example, the elementary excitations of the fractional quantum Hall effect at filling factor $\nu = 1/m$ (where m is an odd integer) have been predicted to obey Abelian fractional statistics, with a phase ϕ associated with the exchange of two particles equal to π/m. However, despite numerous experimental attempts, clear signatures of fractional statistics have remained elusive. We experimentally demonstrate Abelian fractional statistics at filling factor $\nu = 1/3$ by measuring the current correlations resulting from the collision between anyons at a beamsplitter. By analyzing their dependence on the anyon current impinging on the splitter and comparing with recent theoretical models, we extract $\phi = \pi/3$, in agreement with predictions.

In three-dimensional space, elementary excitations fall into two categories depending on the phase ϕ accumulated by the many-body wave function while exchanging two particles. This phase governs the statistics of an ensemble of particles: Bosonic particles, for which $\phi = 0$, tend to bunch together, whereas fermions ($\phi = \pi$) antibunch and follow Pauli's exclusion principle. In two-dimensional systems, other values of ϕ can be realized (*1*, *2*), defining types of elementary excitations called anyons (*3*) that obey fractional or anyonic statistics with intermediate levels of bunching or exclusion. The fractional quantum Hall effect (*4*, *5*), obtained by applying a strong magnetic field perpendicular to a two-dimensional electron gas, is one of the physical systems predicted to host anyons. For a filling factor ν of the first Landau level belonging to the Laughlin series (*5*)—that is, $\nu = 1/m$, where m is an odd integer—the exchange phase is predicted to be given by $\phi = \pi/m$ (*6*, *7*) interpolating between the bosonic and fermionic limits.

Direct experimental evidence of fractional statistics has remained elusive. To date, most efforts have focused on the implementation of single-particle interferometers (*8*, *9*), where the output current is expected to be directly sensitive to the exchange phase ϕ. However, despite many experimental attempts (*10*–*15*), clear signatures are still lacking because the observed modulations of the current result not only from the variation of the exchange phase but also from Coulomb blockade and Aharonov-Bohm interference (*16*). In the case of non-Abelian anyons (*17*), where the exchange of quasiparticles is described by topological unitary transformations, recent heat conduction measurements showed evidence of a non-Abelian state (*18*, *19*), although these results give only indirect evidence of the underlying quantum statistics.

Here, we measured the fluctuations or noise of the electrical current generated by the collision of anyons on a beamsplitter (*20*), thereby demonstrating that the elementary excitations of the fractional quantum Hall effect at filling factor $\nu = 1/3$ obey fractional statistics with $\phi = \pi/3$. The measurement of the current noise generated by a single scatterer of fractional quasiparticles (*21*, *22*) has already shown that they carry a fractional charge $e^* = e/3$. Shortly after these seminal works, it was theoretically predicted (*20*, *23*–*26*) that in conductors comprising several scatterers, noise measurements would exhibit two-particle interference effects where exchange statistics play a central role, and would thus be sensitive to the exchange phase ϕ. In this context, current-current correlation measurements in collider geometries are of particular interest, as they have been extensively used to probe the quantum statistics of particles colliding on a beamsplitter. In a seminal two-particle collision experiment, Hong *et al.* (*27*) demonstrated that photons tend to bunch together in the same splitter output, as expected from their bosonic statistics. In contrast, collision experiments implemented in quantum conductors (*28*–*30*) have shown a suppression of the cross-correlations between the output current fluctuations caused by the antibunching of electrons, as expected from their fermionic statistics. This behavior can also be understood as a consequence of the Pauli exclusion principle that forbids two fermions from occupying the same quantum state at the splitter output. This exclusion principle can be generalized to fractional statistics (*31*, *32*) by introducing an exclusion quasiprobability p (*20*) interpolating between the fermionic and bosonic limits. In a classical description of a two-particle collision (Fig. 1A) (*33*), p accounts for the effects of quantum statistics on the probability K of finding two quasiparticles in the same output arm of the beamsplitter: $K = T(1 - T)(1 - p)$, where T is the single-particle backscattering probability (Fig. 1A). The fermionic case is $p = 1$, leading to perfect antibunching, $K = 0$. Contrary to fermions, the bunching of bosons enhances K, meaning that $1 - p > 1$ and $p < 0$.

To implement collision experiments in quantum conductors, it is necessary to combine a beamsplitter for quasiparticles, a way to guide them ballistically, and two sources to emit them. The two first ingredients can be easily implemented in two-dimensional electron gases in the quantum Hall regime. Quantum point contacts (QPCs) can be used as tunable beamsplitters and, at high magnetic field, charge transport is guided along the chiral edge channels. By combining these elements, single-particle (*34*) and two-particle (*35*) electronic interferometers have been realized, and fermionic antibunching resulting from the collision between two indistinguishable electrons has been observed (*30*). Investigating the anyonic case requires replacing the conventional electron sources (such as biased ohmic contacts) by sources of fractional anyonic quasiparticles. As suggested in (*20*) and as sketched in Fig. 1B, this implies using three QPCs. Two input QPCs labeled QPC1 and QPC2 are biased by dc voltages V_1 and V_2 and tuned in the weak backscattering regime to generate diluted beams of fractional quasiparticles. Indeed, it is known that in the fractional quantum Hall regime, the partitioning of a dc electrical current I^0 with a small backscattering probability $T \ll 1$ occurs through the random transfer of quasiparticles of fractional charge $q = e^*$ (*24*). As experimentally observed, the proportionality of the current noise (*21*, *22*) with the input current I^0, the transmission T, and the fractional charge e^* shows that this random transfer follows a Poissonian law. QPC1 and QPC2 can thus be used as Poissonian sources of anyons, which then collide on a third quantum point contact labeled cQPC; cQPC is used as a beamsplitter in the collision experiment. The fractional statistics of the colliding quasiparticles can be revealed by measuring the cross-correlations between the electrical currents at the output of the beamsplitter.

The sample (Fig. 1C) is a two-dimensional electron gas (GaAs/AlGaAs). The magnetic field is set to $B = 13$ T, corresponding to a filling factor $\nu = 1/3$ for a charge density $n_s = 1.09 \times 10^{15}$ m^{-2}. At this field and at very low electronic temperature $T_{el} = 30$ mK, ballistic charge transport occurs along the edges of the sample without backscattering (*33*). As discussed above, the two quasiparticle sources comprise two quantum point contacts with transmissions T_1 and T_2 (T_1, $T_2 \ll 1$). We apply the voltages V_1

[1]Laboratoire de Physique de l'Ecole Normale Supérieure, ENS, Université PSL, CNRS, Sorbonne Université, Université de Paris, F-75005 Paris, France. [2]Centre de Nanosciences et de Nanotechnologies (C2N), CNRS, Université Paris-Saclay, Palaiseau, France.
*These authors contributed equally to this work.
†Present address: Low Temperature Laboratory, Department of Applied Physics, Aalto University, Espoo, Finland.
‡Present address: Department of Condensed Matter Physics, Weizmann Institute of Science, Rehovot, Israel.
§Corresponding author. Email: gwendal.feve@ens.fr

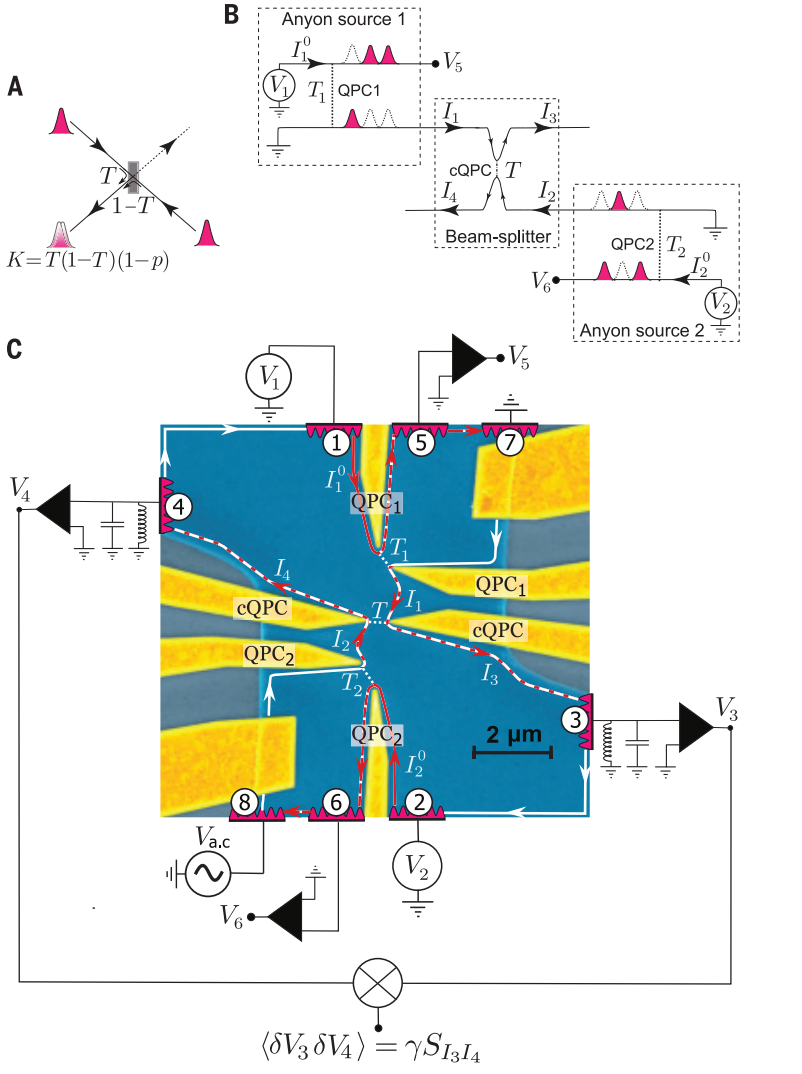

Fig. 1. Sample and principle of the experiment. (**A**) Exclusion quasiprobability p: The probability K to have two anyons exiting in the same output edge channel is modified by the factor $(1 - p)$. (**B**) Principle of the experiment: The voltage V generates the currents I^0 toward QPC1 and QPC2. These two QPCs, tuned in the weak-backscattering regime $T_1, T_2 \ll 1$, act as random Poissonian sources of anyons that collide on cQPC. (**C**) False-colored scanning electron microscope (SEM) image of the sample. The electron gas is shown in blue and the gates in gold. Edge currents are shown as red lines (red dashed lines after partitioning).

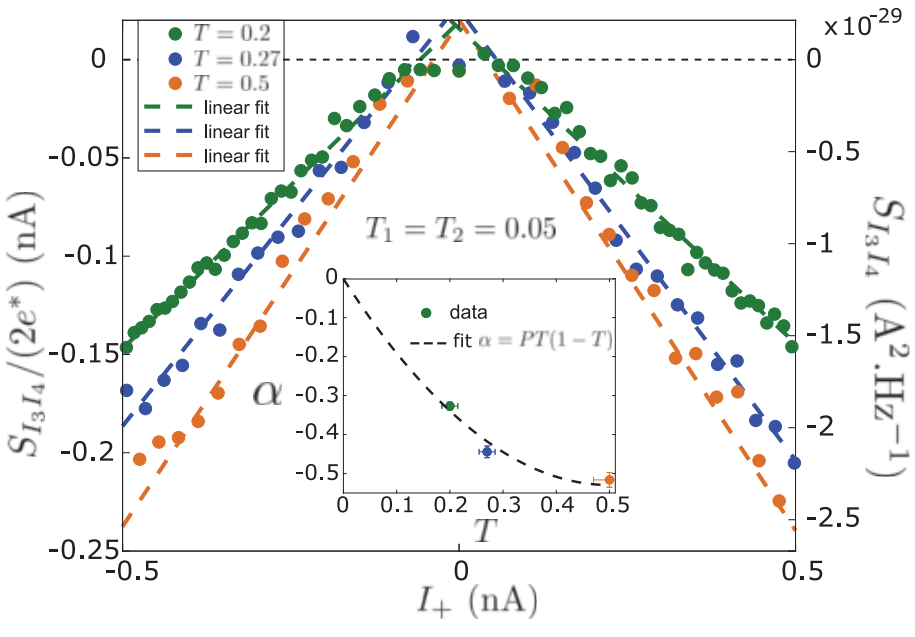

Fig. 2. Fano factor in anyon collision. $S_{I_3I_4}$ for $T_1 = T_2 = 0.05$ is shown as a function of I_+ and for various transmissions T of the central QPC. The dashed lines are linear fits of $S_{I_3I_4}/2e^*$. Inset: Slope α extracted from the linear fits as a function of the central QPC transmission T. The horizontal error bars correspond to the standard deviation of T. The vertical error bars are given by the uncertainties of the linear fits.The dashed line is a fit to $\alpha = PT(1 - T)$ with $P = -2.1 \pm 0.1$.

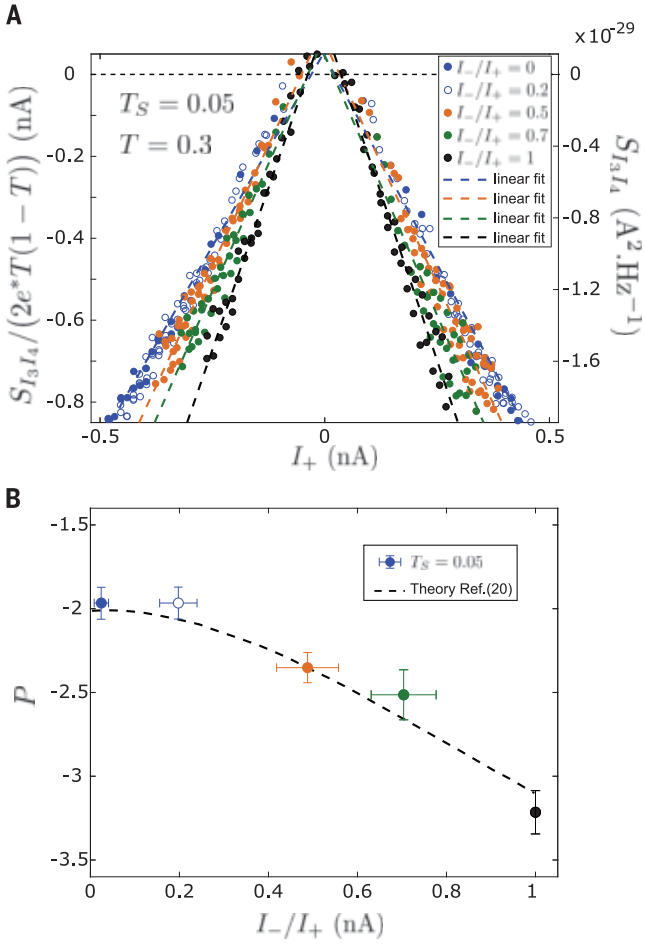

Fig. 4. Experimental test of the quantum mechanical description of an anyon collision. (**A**) $S_{I_3I_4}$ as a function of I_+ for various values of the ratio I_-/I_+. The dashed lines are linear fits of $S_{I_3I_4}$. (**B**) Generalized Fano factor P extracted from the slope of the linear fits in (A), plotted as a function of the ratio I_-/I_+. The colors correspond to the ratios I_-/I_+ plotted in (A). The horizontal error bars correspond to the standard deviation of the ratio I_-/I_+ of the data. The vertical error bars are given by the uncertainties of the linear fits. The dashed line is the prediction extracted from (*20*) for the quantum description of anyon collisions with $\phi = \pi/3$.

transmissions T of the beamsplitter: $T = 0.2$, $T = 0.27$, and $T = 0.5$ (*37*) (Fig. 2). In the three cases, for $I_+ \geq 50$ pA, negative cross-correlations varying linearly with the current I_+ were observed. We extracted the slope α of the variation of $S_{I_3I_4}/2e^*$ by a linear fit (dashed lines) of the experimental data. The three extracted values of α are plotted in the inset of Fig. 2 as a function of the beamsplitter transmission T. The observed T dependence agrees with the binomial law $T(1-T)$ (dashed line) extending Eq. 7 for transmissions beyond the weak-backscattering regime (*32*). The generalized Fano factor can be extracted from the fit of α with the dependence $\alpha = PT(1-T)$, giving $P = -2.1 \pm 0.1$ and demonstrating the fractional statistics at $\nu = 1/3$ with the predicted exchange phase $\phi = \pi/3$. In striking contrast, we observed $P \approx 0$ at filling factor $\nu = 2$ (fig. S5), corresponding to the expected fermionic behavior for an integer filling factor.

The fermionic behavior can be restored at $\nu = 1/3$ by increasing the transmissions of the input QPCs T_1 and T_2, thereby deviating from the weak-backscattering regime suitable for the emission of anyons. For $T_S = 1$ (black points in Fig. 3A), we observed fermionic behavior: $S_{I_3I_4} = 0$ for all values of I_+. For intermediate values of T_S, the current-voltage characteristics of the input QPCs were strongly nonlinear (Fig. 3B). T_S decreased when I_+ increased, eventually restoring the weak-backscattering limit at large bias. The measurements of $S_{I_3I_4}$ for $T_S = 0.14$ and $T_S = 0.2$ (for $I_+ = 0$) plotted in Fig. 3A reflect this evolution. At low current I_+, fermionic behavior was observed: $S_{I_3I_4} = 0$. At higher current, where the weak-backscattering limit is restored, the linear evolution of the cross-correlations with I_+ was recovered, with a generalized Fano factor almost constant. P slightly increased from $P = -2.00 \pm 0.15$ for $T_S = 0.04$ to $P = -1.94 \pm 0.12$ for $T_S = 0.14$, and to $P = -1.73 \pm 0.10$ for $T_S = 0.2$. As expected, the domain where the fermionic behavior was observed ($S_{I_3I_4} = 0$) increased when the transmission T_S increased; it varied from $|I_+| \leq 200$ pA at $T_S = 0.14$ to $|I_+| \leq 400$ pA at $T_S = 0.2$. These data confirm that $P = -2$ is observed only in the regime of anyon emission and that regular fermionic behavior $P \approx 0$ takes place away from the weak-backscattering limit.

Finally, we checked in more detail the agreement between our measurements and the quantum description of anyon collisions (*20*) by investigating the dependence of the Fano factor P on the ratio I_-/I_+. Contrary to the previous experiments where $I_- = 0$ was imposed by $V_1 = V_2$ and $T_1 = T_2$, we instead modified the ratio I_-/I_+ by varying the values of the input voltages $V_1 \neq V_2$. Figure 4A presents the evolution of $S_{I_3I_4}$ as a function of the total current I_+ for four different values of the ratio I_-/I_+ and $T_S = 0.05$. We observed in the four cases a linear evolution with I_+, with a slope P that decreases when I_-/I_+ increases. The different values of P extracted from a linear fit of the data (dashed lines in Fig. 4A) are plotted in Fig. 4B. For $I_-/I_+ \leq 0.2$, P is constant with $P \approx -2$. P then decreases linearly toward $P \approx -3$ for $I_-/I_+ \approx 1$. These experimental results can be compared with the calculation of (*20*) (dashed line). The excellent agreement between our experimental results and the calculations further supports the quantum description of anyons with $\phi = \pi/3$.

Our measurement of the Fano factor $P = -2$ demonstrates the anyonic statistics of the charge carriers with an exchange phase $\phi = \pi/3$ in accordance with the predictions for the Laughlin state $\nu = 1/3$. Interestingly, the prediction $P = -2$ for $\phi = \pi/3$ is valid when edge reconstruction effects can be neglected. Although neutral modes have been observed even at $\nu = 1/3$ (*38*), the agreement with the prediction for a simple edge structure suggests that their effect can be neglected in our experiment (*33*). Collision experiments similar to ours could be used to characterize the elementary excitations of other fractional quantum Hall phases with different fractional statistics or even more exotic cases where non-Abelian statistics (*17*) are predicted. Additionally, combining collision experiments with the triggered emission of fractional quasiparticles (*39*, *40*) would allow one to perform on-demand braiding of single anyons in a quantum conductor.

REFERENCES AND NOTES

1. J. Leinaas, J. Myrheim, *Nuovo Cim. Soc. Ital. Fis. B* **37**, 1–23 (1977).
2. F. Wilczek, *Phys. Rev. Lett.* **48**, 1144–1146 (1982).
3. F. Wilczek, *Phys. Rev. Lett.* **49**, 957–959 (1982).
4. D. C. Tsui, H. L. Stormer, A. C. Gossard, *Phys. Rev. Lett.* **48**, 1559–1562 (1982).
5. R. B. Laughlin, *Phys. Rev. Lett.* **50**, 1395–1398 (1983).
6. B. I. Halperin, *Phys. Rev. Lett.* **52**, 1583–1586 (1984).
7. D. Arovas, J. R. Schrieffer, F. Wilczek, *Phys. Rev. Lett.* **53**, 722–723 (1984).
8. C. de C. Chamon, D. E. Freed, S. A. Kivelson, S. L. Sondhi, X. G. Wen, *Phys. Rev. B* **55**, 2331–2343 (1997).
9. K. T. Law, D. E. Feldman, Y. Gefen, *Phys. Rev. B* **74**, 045319 (2006).
10. F. E. Camino, W. Zhou, V. J. Goldman, *Phys. Rev. Lett.* **98**, 076805 (2007).
11. N. Ofek *et al.*, *Proc. Natl. Acad. Sci. U.S.A.* **107**, 5276–5281 (2010).
12. D. T. McClure, W. Chang, C. M. Marcus, L. N. Pfeiffer, K. W. West, *Phys. Rev. Lett.* **108**, 256804 (2012).
13. R. L. Willett, C. Nayak, K. Shtengel, L. N. Pfeiffer, K. W. West, *Phys. Rev. Lett.* **111**, 186401 (2013).
14. J. Nakamura *et al.*, *Nat. Phys.* **15**, 563–569 (2019).
15. R. L. Willett, K. Shtengel, C. Nayak, L. N. Pfeiffer, Y. J. Chung, M. L. Peabody, K. W. Baldwin, K. W. West, arXiv 1905.10248 [cond-mat.mes-hall] (24 May 2019).
16. B. I. Halperin, A. Stern, I. Neder, B. Rosenow, *Phys. Rev. B* **83**, 155440 (2011).
17. G. Moore, N. Read, *Nucl. Phys. B* **360**, 362–396 (1991).
18. M. Banerjee *et al.*, *Nature* **559**, 205–210 (2018).
19. Y. Kasahara *et al.*, *Nature* **559**, 227–231 (2018).

is fundamentally limited by a resistance-capacitance (*RC*) time constant (*9*).

Geometric diodes are an alternative paradigm that takes advantage of noncentrosymmetric structures to induce current flow preferentially in one direction (*5*, *10*, *11*). A geometric diode (Fig. 1C) can be created by using a sawtooth geometry in which electrons undergo quasi-specular reflection at the boundaries of the structure, directing electrons through a constriction in the forward direction. In the reverse direction, electrons are reflected backward, blocking current. To function, the physical dimensions of a geometric diode must be comparable to the mean free path (MFP) of the majority carrier, allowing the devices to operate in the ballistic or quasi-ballistic regime, in which surface reflections dominate over other charge-carrier scattering mechanisms (*11*). These structures are theoretically limited not by *RC* time constants but by the inherent ballistic motion and flight time of charge carriers. Potential advantages include near zero-bias turn-on and ac operation into the terahertz regime (*9*, *12*), unlocking applications that include high-speed signal processing or data transfer (*13*, *14*) and long-wavelength energy harvesting (*15*, *16*).

Four-terminal ballistic rectifiers operating at cryogenic temperatures (*17*) and room temperature (*18*) and quantum ratchets operating at cryogenic temperatures (*3*) have been reported with two-dimensional electron gases. Rectifying devices have also been fabricated with graphene (*6*, *19*), but two-terminal geometric diodes with large dc asymmetry (>5) at room temperature have yet to be realized. We demonstrate NW-based three-dimensional (3D) ballistic geometric diodes that exhibit dc asymmetries as high as 10^3 at room temperature and that ratchet electrons at ac frequencies exceeding 40 GHz. The two-terminal geometric diodes are composed of silicon (Si) NWs in which the diameter is modulated to produce a tapered, noncentrosymmetric sawtooth with cylindrical symmetry (Fig. 2A). Key geometric parameters include the outer wire diameter (*D*), constriction diameter (*d*), ratchet length (*L*), ratchet angle (θ), and constriction angle (φ). These single-crystal Si structures are fabricated by a bottom-up vapor-liquid-solid (VLS) growth process (*20*) using Au catalyst nanoparticles that dictate *D*.

To modulate diameter, the dopant precursor flow rate was rapidly varied during VLS growth to vary dopant concentration along the NW axis to yield abrupt and radially uniform profiles (*21*), as shown by scanning transmission electron microscopy elemental analysis for n-type NWs doped with phosphorus (fig. S1). Wet-chemical etching of the NWs yielded a diameter profile that is dependent on the encoded dopant profile (*22*, *23*). For example, Fig. 2B displays scanning electron microscopy (SEM) images of two n-type NW segments that were etched under the same conditions but yielded different values of θ and *d* with the same *D* and *L*. The dopant and diameter profiles for the two segments (Fig. 2C) demonstrate that larger θ and lower *d* were synthetically encoded by using lower doping levels within the tapered region.

Thus, through control of catalyst diameter, etch conditions, and doping level, the fabrication process yielded direct structural tunability of the geometric parameters. The constriction angle φ is, however, limited from a more ideal

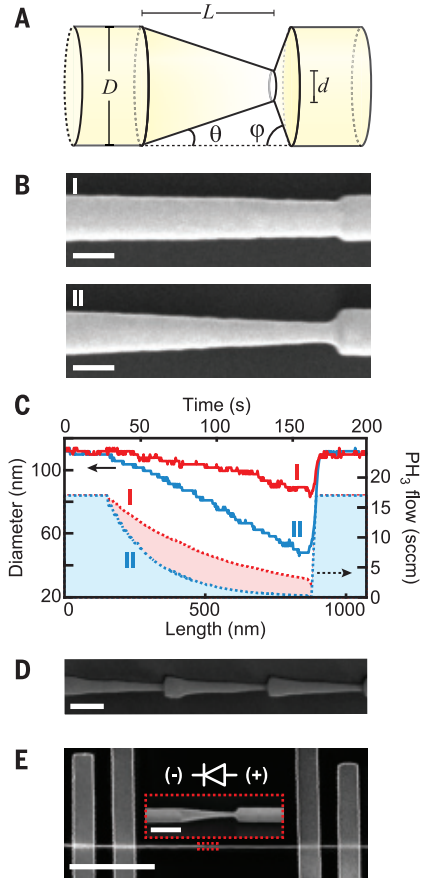

Fig. 2. Designing Si NW ratchets. (**A**) Design and geometric parameters for a two-terminal NW geometric diode with 3D morphology. (**B**) SEM images of two NW geometric diodes. Scale bars, 100 nm. (**C**) Diameter profiles (solid lines) and phosphine (PH_3) dopant precursor flow profiles (dashed lines) for the two geometric diodes, I (red) and II (blue), shown in (B). sccm, standard cubic centimeters per minute. (**D**) SEM image of a NW with three geometric diodes encoded in series. Scale bar, 200 nm. (**E**) SEM image of a single-NW device with two Ti/Pd electrical contacts on either side of the geometric diode. Scale bar, 5 μm. (Inset) Higher-magnification SEM image of the red boxed region and circuit-diagram representation of the geometric diode, showing the anode (+) and cathode (−). Scale bar, 250 nm.

value of 90° by the wet-etch process, yielding typical values of 30° to 60°. In addition, the bottom-up process allowed multiple geometric diodes to be encoded in series within a single NW (Fig. 2D). All ratchet geometries described herein used dopant profiles that produced nominally intrinsic Si at the constriction and had features on a scale comparable to the electron MFP in Si at room temperature, which we estimate to be ~10 to ~30 nm or more (see supplementary text section of the supplementary materials).

To probe the geometric diode behavior, n-type single-NW devices were fabricated (*20*), as shown by the representative SEM images in Fig. 2E. Four electrical contacts were defined per NW to ensure Ohmic contacts (fig. S2), and, except where noted, measurements were performed under vacuum directly after fabrication. The dc current-voltage (*I-V*) curves were collected using the polarity indicated in Fig. 2E, and room-temperature results for four NWs with θ ranging from 0° to 13° are shown in Fig. 3A. The NW with θ = 0° showed a linear *I-V* response, whereas NWs with θ > 0° showed increasingly nonlinear and diode-like *I-V* responses. The dc asymmetry of the devices progressively increased from unity to >10 for $|V_{app}| = 1$ V (Fig. 3A, inset). Results for >100 measured devices showed that the dc asymmetry exhibited the polarity indicated in the diode schematic in Fig. 2E with 100% yield. Moreover, devices with prolonged air exposure, for which native oxide had formed on the surface (fig. S3), yielded values > 10^3, as shown by the *I-V* curve and dc asymmetry data in Fig. 3B.

We modeled the diodes to understand the geometric dependence of the behavior. Finite-element (FE) electrostatic simulations (fig. S4), which have been shown to accurately describe NW p-n junctions (*20*, *24*), demonstrated that the degenerately doped n-type segments adjacent to the sawtooth geometry caused all potentials to drop across the sawtooth region and served as electron reservoirs that could inject electrons into the sawtooth region. However, the FE simulations did not reproduce the diode response of the devices because they did not account for the quasi-ballistic nature of electrons. Thus, we developed a simple analytical model (*20*, *25*) to qualitatively capture these effects by describing the trajectories of single electrons within the sawtooth region (Fig. 3C, inset) assuming ballistic trajectories without phase coherence effects (see supplementary text) (*11*). The model integrates over trajectories that originate with a narrow angular distribution (accounting for the field-driven transport) within one MFP of the constriction, considering both direct transmission through the constriction and multiple specular reflections from the NW surface. It permits the calculation of transmission

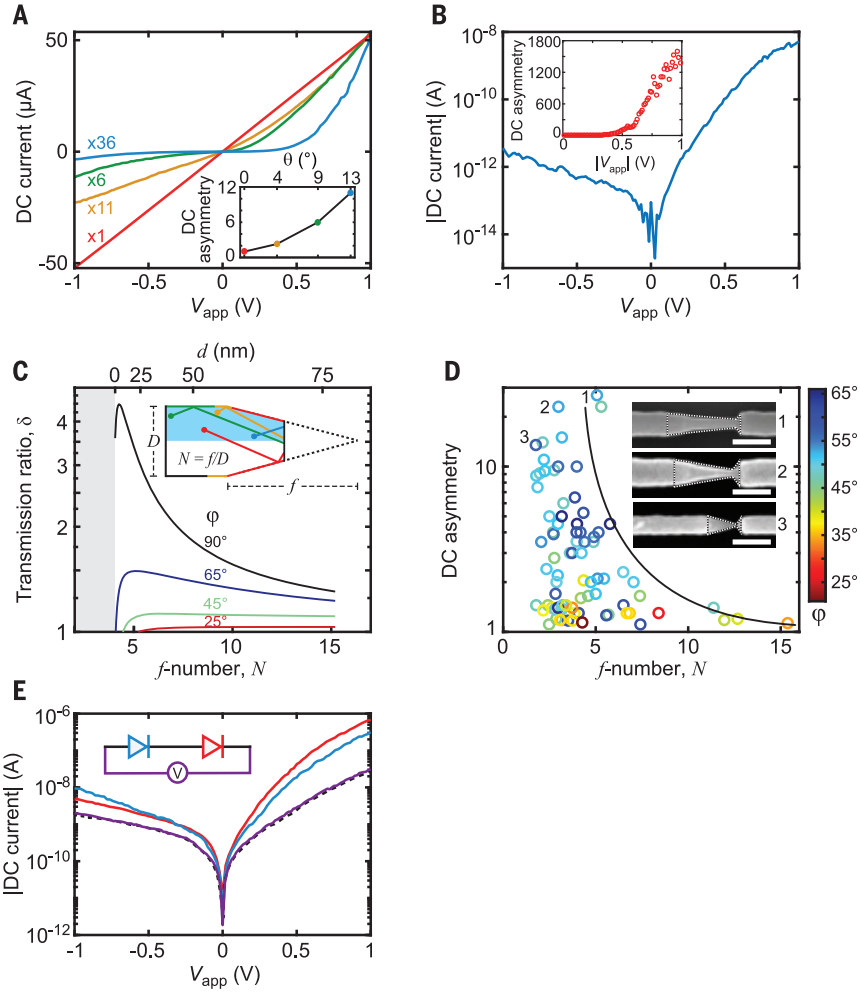

Fig. 3. Two-terminal geometric diodes. (**A**) *I-V* curves measured from four separate single-NW devices with θ of 0° (red), 4° (orange), 9° (green), and 13° (blue). Current values for each device are scaled by the factors indicated. (Inset) The dc asymmetry at $|V_{app}|$ = 1 V as a function of θ. (**B**) Semi-logarithmic *I-V* curve for a device with stable native oxide. (Inset) The dc asymmetry as a function of $|V_{app}|$. (**C**) δ calculated as a function of *N* (lower axis) with *D* = 100 nm and *L* = 400 nm, assuming φ of 90° (black), 65° (blue), 45° (green), and 25° (red), where MFP is 0.3*D*. The *d* corresponding to values of *N* are shown on the upper axis. (Inset) Schematic illustration of the analytical model showing example trajectories of electrons originating within a set MFP of the constriction that successfully pass through the constriction. Colored trajectories denote qualitatively different pathways that involve either direct transmission (blue) or specular reflection (green, orange, and red) from the corresponding color-coded segments of the NW surface. The geometric parameters *f* and *D* that define *N* are also shown. (**D**) Experimental values of dc asymmetry at $|V_{app}|$ = 1 V collected from 81 single-NW devices plotted as a function of *N*. Data points are color-coded according to the constriction angle φ. The black line is a guide to the eye. (Inset) SEM images of three high-asymmetry devices, labeled 1 to 3, overlaid with a diagram of their geometry. Scale bars, 200 nm. (**E**) Semi-logarithmic *I-V* curves for two diodes encoded in series within a single NW, showing the *I-V* response across both diodes (purple) and response of the individual diodes (red and blue). Dashed line represents the predicted response of the series-connected diodes based on the responses of individual diodes.

coefficients for passage through the constriction (*11*, *17*), and we use the ratio (δ) of transmission coefficients in forward and reverse bias for qualitative comparison to the dc asymmetry measured by experiment (see supplementary text).

Figure 3C displays δ for different values of φ at a fixed *L* as a function of *f*-number (*N*) with $N = f/D$, where *f* is the effective focal length of the ratchet (Fig. 3C, inset) and $N = (2\tan(\theta))^{-1}$. For relatively large values of φ and *N* values above ~5, the model predicted that as *N* decreased, δ increased. For *N* below ~5, however, δ approached unity because *d* approached zero. The model also showed that δ depended strongly on the initial angular distribution, and substantially higher values could be achieved by varying this distribution (fig. S5). Moreover, for a fixed *N*, decreasing φ caused δ to decrease, because a smaller φ corresponded to an increasingly symmetric sawtooth structure.

Figure 3D displays experimental results correlating measured geometric structures with the *I-V* behavior. Champion devices for each value of *N* exhibited a trend of increasing dc asymmetry with decreasing *N*, in qualitative agreement with the trends for δ. As expected, there was no correlation between *N* and φ; however, lower values of φ precluded a high dc asymmetry, in agreement with the trends for δ from the model. Images of three select devices (labeled 1 to 3), each with a dc asymmetry > 10 (Fig. 3D, inset) show the various geometries that produced high asymmetry values.

Because MFP substantially increases at lower temperatures (*8*, *26*), we measured temperature-dependent *I-V* characteristics between 350 and 77 K (fig. S6). As temperature decreased, the dc asymmetry increased from 3.5 at 350 K to ~500 at 77 K, which is consistent with an increase in MFP. In addition, p-type NW devices were fabricated and exhibited a reversal of diode polarity, as expected because the majority carriers changed from electrons to holes (fig. S7). The low-temperature and p-type data thus further verified the quasi-ballistic mechanism of operation.

The champion room-temperature dc asymmetry (Fig. 3B), achieved with a stable surface oxide on n-type NWs after extended exposure to ambient conditions, yielded a value of ~1600 at $|V_{app}|$ = 1 V with φ = 46° and *N* = 5.4. The higher asymmetry with surface oxide can be attributed to a smaller effective constriction and band bending that screened surface defects and improved specular reflection. Alternate surface passivation strategies, including aluminum oxide and thermal oxide, yielded similar results (fig. S8).

The bottom-up fabrication process also facilitated the series connection of multiple subunits within a single NW, as illustrated by the SEM image of geometric diodes in series in Fig. 2D. To test this design, *I-V* curves for two geometric diodes encoded in a single NW, measured separately and in series, are shown in Fig. 3E. When measured in series, the device exhibited the expected combined response from the two individual diodes because the nonballistic, degenerate n-type segments between the diodes acted as an ohmic connection between the two. Analogously, separate NWs can be wired in parallel, exhibiting the expected current summation (fig. S9). Together the results indicate that a combination of surface treatments and series or parallel connections can be used to create tunable *I-V* characteristics.

The quasi-ballistic operation of the geometric diodes enables electron ratcheting at high ac frequencies, which manifests as rectification of an ac signal to produce a dc voltage (V_{dc}). The flight time of charge carriers through

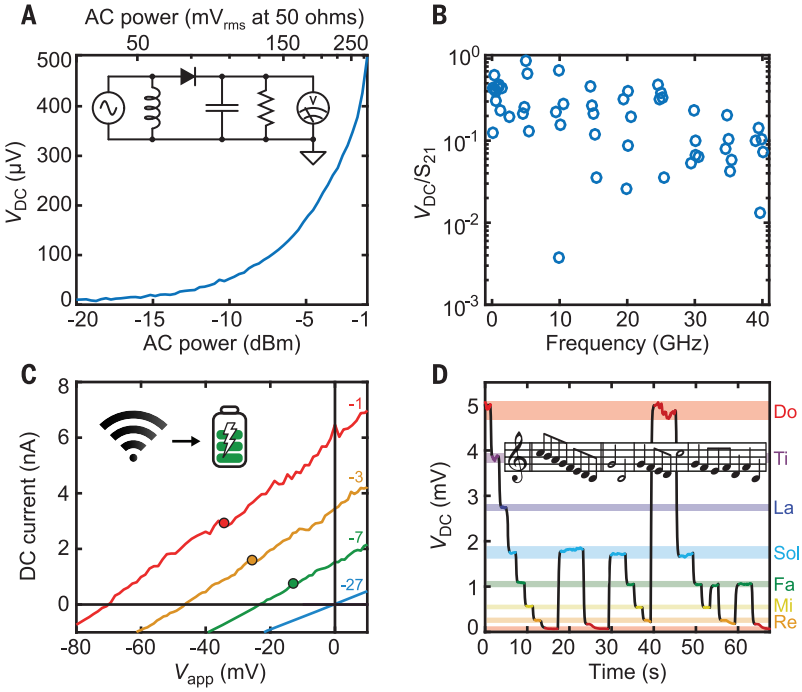

Fig. 4. High-frequency electron ratcheting. (**A**) V_{dc} as a function of applied ac power at 40 GHz, with power displayed in units of decibel-milliwatts (dBm) (lower axis) or voltage across a 50-ohm load (upper axis). (Inset) Circuit diagram of the measurement setup. (**B**) V_{dc} normalized to S_{21} as a function of frequency for a single NW device. (**C**) *I-V* response of a geometric diode with 5.2-GHz ac applied at powers of −27 (blue), −7 (green), −3 (orange), and −1 dBm (red). Circles denote the maximum power points for each diode. (Inset) Schematic illustration of energy harvesting at Wi-Fi frequencies. (**D**) Demodulation of a 20-GHz square-wave amplitude modulated signal, corresponding to musical notes, by the geometric diode. The V_{dc} response time is limited not by the diode but by the measurement unit and integrating capacitor. Color-coding corresponds to the solfège shown on the right-hand axis. (Inset) Musical notation corresponding to the input signal.

the quasi-ballistic region of the structure dictates the inherent response time, and for electrons at the Fermi velocity moving through the Si geometric diode, it is expected to exceed ~1 THz (see supplementary text). To test the frequency response of the diodes up to the instrumental limit of 40 GHz, the circuit shown diagrammatically in the inset of Fig. 4A was used to measure V_{dc} (*20*). Figure 4A shows the expected proportional increase of V_{dc} with power and verifies high-frequency electron ratcheting. Figure 4B shows V_{dc} as a function of frequency normalized by the separately measured transmitted power through a transmission line on the device chip (S_{21}) (*20*). This normalization partially accounted for frequency-dependent parasitic elements within the measurement system that alter the ac power applied to the device at each frequency (fig. S10). The quantity V_{dc}/S_{21} shows a relatively flat response from 100 MHz to 40 GHz, highlighting the broadband electron ratcheting effect in these diodes.

Because of their high-frequency response, the geometric diodes could be used for energy harvesting and signal processing applications. Figure 4C shows *I-V* curves of a geometric diode rectifying Wi-Fi signals (5.2 GHz) at varying powers. The *I-V* curves progressively shifted into quadrant II as ac power increased, corresponding to increasing power conversion and demonstrating the ability of the diodes to serve as long-wavelength energy harvesters in analogy to the operation of a solar cell (*27*). The geometric diodes could serve as the rectifying component of rectennas (*15*, *16*, *28*), harvesting background radiation for low-power consumption devices (*29*). Similarly, Fig. 4D shows the response of a geometric diode to a 20-GHz ac signal that was amplitude-modulated between −27 and −5 dBm to convey musical notes, producing clear V_{dc} levels for each signal amplitude. This example highlights the signal demodulation and processing capabilities of the geometric diodes. Together, Fig. 4, C and D, demonstrate that a single input signal could simultaneously provide data and be rectified into useable power (*30*). These demonstrations, combined with the ability to create parallel and series-connected custom diodes, highlight the potentially diverse application space for high-frequency electron ratchets operating at room temperature.

REFERENCES AND NOTES

1. P. M. Hoffmann, *Rep. Prog. Phys.* **79**, 032601 (2016).
2. B. Lau, O. Kedem, J. Schwabacher, D. Kwasnieski, E. A. Weiss, *Mater. Horiz.* **4**, 310–318 (2017).
3. H. Linke *et al.*, *Science* **286**, 2314–2317 (1999).
4. K. Loutherback, J. Puchalla, R. H. Austin, J. C. Sturm, *Phys. Rev. Lett.* **102**, 045301 (2009).
5. A. M. Song, *Appl. Phys. A Mater. Sci. Process.* **75**, 229–235 (2002).
6. Z. X. Zhu, S. Joshi, G. Moddel, *IEEE J. Sel. Top. Quantum Electron.* **20**, 3801409 (2014).
7. A. Lorke *et al.*, *Physica B* **249-251**, 312–316 (1998).
8. S. M. Sze, K. K. Ng, *Physics of Semiconductor Devices* (John Wiley & Sons, ed. 3, 2007).
9. D. M. Pozar, *Microwave Engineering* (Wiley, ed. 4, 2011).
10. V. I. Belinicher, B. I. Sturman, *Sov. Phys. Usp.* **23**, 199–223 (1980).
11. H. Linke, A. M. Song, in *Electron Transport in Quantum Dots*, J. P. Bird, Ed. (Springer, 2003), pp. 317–361.
12. M. Tonouchi, *Nat. Photonics* **1**, 97–105 (2007).
13. E. S. Kannan, I. Bisotto, J. C. Portal, T. J. Beck, L. Jalabert, *Appl. Phys. Lett.* **101**, 143504 (2012).
14. B. Clerckx *et al.*, *IEEE J. Sel. Areas Comm.* **37**, 4–33 (2019).
15. S. J. Byrnes, R. Blanchard, F. Capasso, *Proc. Natl. Acad. Sci. U.S.A.* **111**, 3927–3932 (2014).
16. X. Zhang *et al.*, *Nature* **566**, 368–372 (2019).
17. A. M. Song *et al.*, *Phys. Rev. Lett.* **80**, 3831–3834 (1998).
18. A. M. Song *et al.*, *Appl. Phys. Lett.* **79**, 1357–1359 (2001).
19. G. Auton *et al.*, *Nat. Commun.* **7**, 11670 (2016).
20. See materials and methods in the supplementary materials.
21. J. D. Christesen, C. W. Pinion, X. Zhang, J. R. McBride, J. F. Cahoon, *ACS Nano* **8**, 11790–11798 (2014).
22. J. D. Christesen, C. W. Pinion, E. M. Grumstrup, J. M. Papanikolas, J. F. Cahoon, *Nano Lett.* **13**, 6281–6286 (2013).
23. J. D. Christesen, C. W. Pinion, D. J. Hill, S. Kim, J. F. Cahoon, *J. Phys. Chem. Lett.* **7**, 685–692 (2016).
24. J. D. Christesen *et al.*, *Nano Lett.* **12**, 6024–6029 (2012).
25. P. Zhang, D. M. H. Hung, *J. Appl. Phys.* **115**, 204908 (2014).
26. S. S. Li, W. R. Thurber, *Solid-State Electron.* **20**, 609–616 (1977).
27. B. Lau, O. Kedem, M. Kodaimati, M. A. Ratner, E. A. Weiss, *Adv. Energy Mater.* **7**, 1701000 (2017).
28. Z. Zhu, S. Joshi, S. Grover, G. Moddel, in *Rectenna Solar Cells*, G. Moddel, S. Grover, Eds. (Springer, 2013), pp. 209–227.
29. X. Lu, P. Wang, D. Niyato, D. I. Kim, Z. Han, *IEEE Comm. Surv. and Tutor.* **17**, 757–789 (2015).
30. T. D. Ponnimbaduge Perera, D. N. K. Jayakody, S. K. Sharma, S. Chatzinotas, J. Li, *IEEE Comm. Surv. and Tutor.* **20**, 264–302 (2018).

ACKNOWLEDGMENTS

Funding: This work was primarily supported by a Packard Fellowship for Science and Engineering to J.F.C. This work made use of instrumentation at the Chapel Hill Analytical and Nanofabrication Laboratory (CHANL), a member of the North Carolina Research Triangle Nanotechnology Network (RTNN), which is supported by the NSF (ECCS-1542015) as part of the National Nanotechnology Coordinated Infrastructure (NNCI). **Author contributions:** J.P.C., J.D.C., D.J.H., S.C.W., and J.F.C. designed experiments. J.P.C., J.D.L., and T.S.T. fabricated devices. J.P.C., J.D.L., and C.J.M. measured devices. C.J.M., J.D.L., and M.A.B. assisted with electrical measurement design. J.D.L. constructed the analytical model. J.P.C., J.D.C., D.J.H., and T.S.T. synthesized NWs. J.R.M. performed TEM analysis. J.P.C. and J.F.C. wrote the manuscript with input from all authors. J.F.C. supervised all aspects of the project. **Competing interests:** None declared. **Data and materials availability:** All data needed to evaluate the conclusions in the paper are present in the paper or the supplementary materials.

SUPPLEMENTARY MATERIALS

science.sciencemag.org/content/368/6487/177/suppl/DC1
Materials and Methods
Supplementary Text
Figs. S1 to S11
References (*31*–*44*)

26 July 2019; resubmitted 21 January 2020
Accepted 17 March 2020
10.1126/science.aay8663

DEVELOPMENTAL BIOLOGY

Intravital imaging of mouse embryos

Qiang Huang[1,2]*†, Malkiel A. Cohen[3]*, Fernando C. Alsina[4], Garth Devlin[5], Aliesha Garrett[2], Jennifer McKey[6], Patrick Havlik[5], Nikolai Rakhilin[2], Ergang Wang[2], Kun Xiang[2], Parker Mathews[7], Lihua Wang[2], Cheryl Bock[8], Victor Ruthig[6], Yi Wang[2], Marcos Negrete[2], Chi Wut Wong[2], Preetish K. L. Murthy[2], Shupei Zhang[3], Andrea R. Daniel[9], David G. Kirsch[9,10], Yubin Kang[7], Blanche Capel[6], Aravind Asokan[5], Debra L. Silver[4], Rudolf Jaenisch[3,11]†, Xiling Shen[2]†

Embryonic development is a complex process that is unamenable to direct observation. In this study, we implanted a window to the mouse uterus to visualize the developing embryo from embryonic day 9.5 to birth. This removable intravital window allowed manipulation and high-resolution imaging. In live mouse embryos, we observed transient neurotransmission and early vascularization of neural crest cell (NCC)–derived perivascular cells in the brain, autophagy in the retina, viral gene delivery, and chemical diffusion through the placenta. We combined the imaging window with in utero electroporation to label and track cell division and movement within embryos and observed that clusters of mouse NCC-derived cells expanded in interspecies chimeras, whereas adjacent human donor NCC-derived cells shrank. This technique can be combined with various tissue manipulation and microscopy methods to study the processes of development at unprecedented spatiotemporal resolution.

Different methods are used to study embryonic development in mice, a common mammalian research model (*1*). However, each has its limitations. Histology on fixed embryos does not capture developmental dynamics. Ultrasound or magnetic resonance imaging has limited resolution and does not take advantage of transgenic strains with fluorescent reporters (*2*, *3*). The peri-implantation to early organogenesis stages can be imaged by means of optical coherence microscopy or light sheet fluorescence microscopy after removal of the mouse embryo from the uterus and culture in medium for 24 to 48 hours (*4*–*6*). However, despite efforts to mimic the intrauterine environment (*7*), culturing embryos past embryonic day 9 (E9), when various organs form, remains difficult because of the inability to recapitulate the feto-placental nutritional exchange (*8*–*10*).

[1]Department of Pediatric Surgery, Second Affiliated Hospital of Xi'an Jiaotong University, Xi'an, Shaanxi, China. [2]Department of Biomedical Engineering, Pratt School of Engineering, Duke University, Durham, NC, USA. [3]Whitehead Institute for Biomedical Research, Cambridge, MA, USA. [4]Department of Molecular Genetics and Microbiology, School of Medicine, Duke University, Durham, NC, USA. [5]Department of Surgery, School of Medicine, Duke University, Durham, NC, USA. [6]Department of Cell Biology, School of Medicine, Duke University, Durham, NC, USA. [7]Division of Hematologic Malignancies and Cellular Therapy, Duke University Medical Center, Durham, NC, USA. [8]Duke Cancer Institute, School of Medicine, Duke University, Durham, NC, USA. [9]Department of Radiation Oncology, Duke University Medical Center, Durham, NC, USA. [10]Department of Pharmacology & Cancer Biology, Duke University Medical Center, Durham, NC, USA. [11]Department of Biology, Massachusetts Institute of Technology, Cambridge, MA, USA.
*These authors contributed equally to this work.
†Corresponding author. Email: drhuang@xjtu.edu.cn (Q.H.); jaenisch@wi.mit.edu (R.J.); xs37@duke.edu (X.S.)

Intravital imaging has been used to observe organs at high resolution but not whole embryos (*11*–*16*). We developed an implantable window for imaging the mouse embryo from E9.5 to birth. The window is circular, with a 10-mm inner diameter and 1.5-mm depth, and is covered with a glass coverslip that can be removed for manipulating the embryo (Fig. 1, A and B). The embryo becomes easily identifiable under a dissection microscope around E9.5, when the allantois fuses with the chorionic plate to form a labyrinthine layer that separates fetal and maternal blood vessels and provides a large surface area for gas and nutrient exchange (*17*). We developed a surgical procedure (supplementary materials, materials and methods) to implant the window and strip the decidua and uterine muscle, which impedes the view of the embryo from E9.5 to E12.5 (Fig. 1, C to E), without interfering with embryo survival as indicated by a beating heart (movie S1). To minimize motion from the dam's breathing, we sutured the uterine wall to the dam's abdominal muscle and the abdominal muscle to the window and designed a 3D-printed clip to stabilize the window (fig. S1A). If an embryo was to be tracked beyond E13.5 (when it tended to retract somewhat into the mother's abdominal cavity), its position was adjusted with a new window (fig. S1, B and C). The survival rate of embryos was 65.6% (21 of 32) after window implantation.

After E12.5, the decidua diminished, and the uterine wall became transparent (fig. S1D); therefore, there was no need to strip the decidua and uterine muscle (Fig. 1F). The window allowed observation of the embryo until birth; this view was reduced to partial after the embryo outgrew the window (typically by E15.5) (fig. S2A). We 3D-printed a larger, elliptical-shaped window to image the entire embryo at older stages, from E12.5 until birth (Fig. 1, G and H, and fig. S2B). The survival rates of embryos underneath the circular and elliptical windows were 81.9% (59 of 72) and 84.1% (37 of 44), respectively.

To test the effect of the window on the growth of the embryos, we implanted circular or elliptical windows at E11.5, E12.5, and E15.5 and weighed the embryos 3 days after implantation. Embryo weight was reduced by 28.2, 11.7, and 12.0%, respectively, relative to littermates that were not placed under a window (Fig. 1, I to K). Hematoxylin and eosin staining showed no structural abnormalities in the embryos underneath the window (fig. S2, C to E), and there were no differences in terms of complete blood components (fig. S2, F to H). Dams showed no notable signs of inflammation or anemia after window implantation (fig. S2I). All eight dams implanted with the circular windows gave birth vaginally to all pups (including the ones underneath the window), whereas only 2 of 7 dams with elliptical windows gave birth naturally, owing to the lack of abdominal contractions (fig. S2J and movie S2). The dam fed the pups normally (movie S3), and pups imaged embryonically underneath the windows were indistinguishable from their littermates and grew without noticeable abnormalities.

Transgenic mice with cell lineage–specific expression of fluorescent reporter proteins are commonly used to study development in live organisms (*4*). We used two types of microscopy—stereoscopic microscopy and two-photon microscopy—to observe embryos in *Wnt1-Cre-tdTomato* mice. In this transgenic strain, Wnt1-Cre is expressed in the dorsal neuroepithelium from E8.5, which leads to lineage labeling of neural crest cells (NCCs) and their descendants as well as the dorsal central nervous system (*18*–*20*). We crossed *Wnt1-Cre* mice with *ROSA26-CAG-tdTomato* mice to create the transgenic strain and placed the optical windows on dams at E11.5. The midbrain of F_1 embryos was clearly visible through the window and was imaged continuously for 6 hours with a stereoscopic microscope (Fig. 2, A and B, and movie S4).

Two-photon microscopy was then used to image the tdTomato-labeled cells in the midbrain from E10.5 to E11.0, with the decidua and uterine muscle stripped (Fig. 2C and fig. S3, A to E). We next implanted the window at E13.5. Using the vasculature on the surface of the uterus and in the embryonic brain as a roadmap, we were able to track the tdTomato$^+$ cells in the mouse embryonic brain for 24 hours (Fig. 2, D and E, and fig. S4, A to C). We further observed tdTomato$^+$ cells in a mesh-like, 200- to 300-μm-deep fluorescent layer in the E13.5 embryo (fig. S4D). To identify these cells, we fixed the whole embryos and stained for

various markers and discovered that these mesh-like cells overlapped with blood vessels marked by CD31$^+$ endothelial cells and had differentiated into platelet-derived growth factor receptor–β$^+$ (PDGFR-β$^+$) perivascular cells (fig. S4, E and F). Because previous reports showed that NCCs differentiate into perivascular cells in the thymus by E13.5 in mice (*21*), this observation indicated that NCCs also differentiate into perivascular cells to form vasculature in the brain as early as E13.5.

We then imaged embryos in transgenic mice that harbor the autophagy reporter *CAG-RFP-eGFP-LC3*, in which a CAG promoter drives

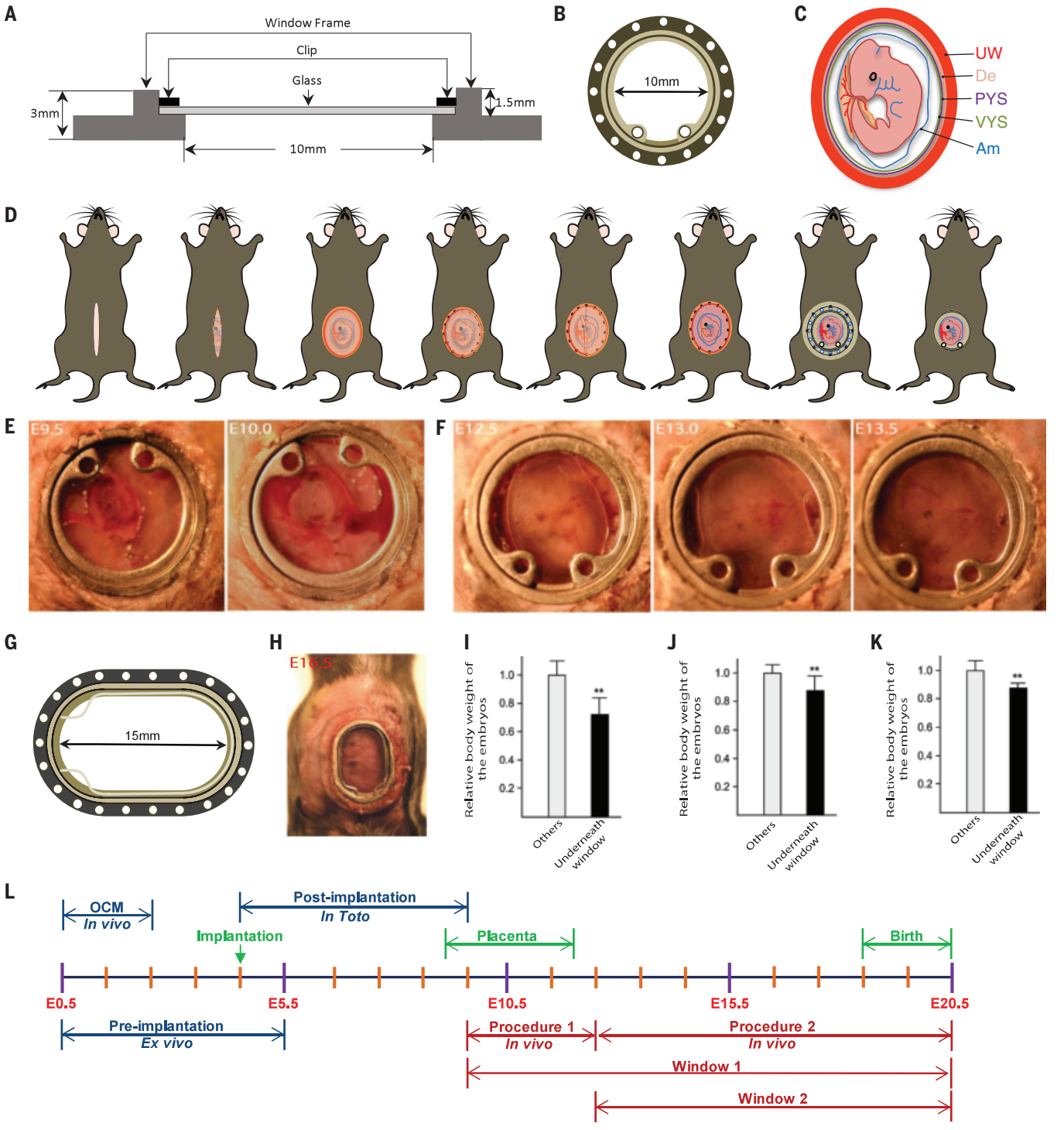

Fig. 1. Intravital imaging of mouse embryos. (**A** and **B**) Schematic illustration of (A) side view and (B) top view of the embryonic window. (**C**) Illustration of a mouse embryo at E9.5. UW, uterine muscle; De, decidua; PYS, parietal yolk sac; VYS, visceral yolk sac; Am, amnion. (**D**) Overview of the stripping surgical protocol. (**E**) Embryo growth from E9.5 to E10.0. (**F**) Embryo growth from E12.5 to E13.5. (**G** and **H**) An elliptical window used for imaging later stages. (G) Schematic illustration of the elliptical window. (H) View of the elliptical window at E16.5. (**I** to **K**) Embryo weights at (I) E14.5, 3 days after stripping surgery; (J) E15.5 and (K) E18.5, 3 days after nonstripping surgery. Data are mean ± SD; n = 3 dams, $^{**}P < 0.01$. (**L**) Timeline of embryo development and imaging procedures.

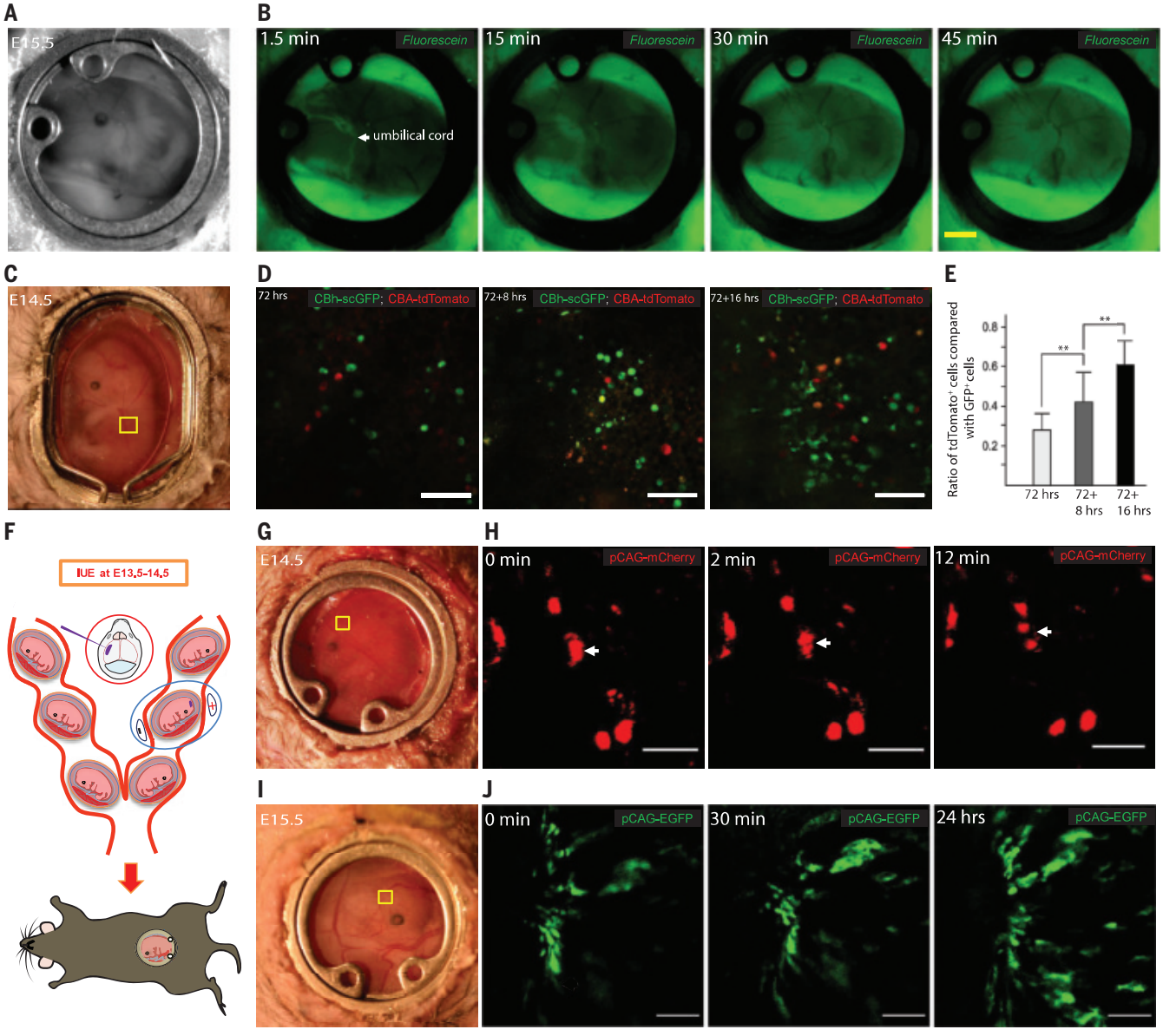

Fig. 3. Imaging chemical diffusion, embryonic AAV transduction, and cell movements after in utero electroporation. (**A**) View of an embryo at E15.5. (**B**) Diffusion of fluorescein into an embryo after dam retro-orbital injection. Scale bar, 2 mm. (**C**) Light-field view of an E14.5 embryo, 72 hours after AAV8g9-pTR-CBh-scGFP and AAV8g9-pTR-CBA-tdTomato co-injection. (**D**) GFP and tdTomato expression in the marked region in (C). Scale bar, 100 μm. (**E**) Ratio of tdTomato$^+$ and GFP$^+$ cells. Data are mean ± SD; n = 3 dams, $^{**}P < 0.01$. (**F**) Schematic of in utero electroporation. (**G**) Light-field view of an E14.5 embryo, 1 day after electroporation of pCAG-mCherry. (**H**) Movement of cells in the region marked in (G). Scale bar, 50 μm. (**I**) Light-field view of an E15.5 embryo, 1 day after electroporation of pCAG-EGFP. (**J**) Twenty four–hour imaging of the brain region marked in (I) showing cell migration. Scale bar, 100 μm.

through the dam's orbital vein and monitoring its passage through the umbilical cord and subsequent diffusion into the embryo. Fluorescein passed through the umbilical cord 1.5 min after injection and diffused into the whole embryo 30 min after injection (Fig. 3, A and B, and movie S6).

Adeno-associated viruses (AAVs) are used as vehicles for gene therapy (*30*, *31*), but the kinetics by which AAVs permeate the placenta and express exogenous genes in embryos have not been studied. We injected AAV serotypes 8 and 9 (AAV8 and AAV9) carrying a GFP reporter into the tail vein of dams at E11.5 and observed GFP expression in embryos at E14.5, 72 hours after injection (fig. S6, A and B). We confirmed similar GFP expression in the embryos from injected dams without the window (fig. S6C) and GFP expression in the placenta (fig. S6D). To assess the speed of viral transduction into the embryo, we injected a single-stranded AAV vector (ssAAV8-eGFP) and a self-complementary AAV vector (scAAV8-tdTomato) (*32*) into the tail vain of dams at E11.5. We started imaging the embryos at E14.5, 72 hours after injection. We initially detected more GFP signal than tdTomato signal, although the difference in expression diminished within 16 hours (Fig. 3, C to E). This experiment demonstrates the use of intravital imaging of AAV gene delivery and suggests that different AAV vectors have different transduction dynamics, an important consideration when targeting a specific embryonic stage.

In utero electroporation (IUE) can be used to introduce DNA into embryos to study

and hNCCs that were separate from any cluster diminished over time (fig. S8, G to M).

We have developed an intravital imaging window for manipulating and visualizing live mouse embryos in vivo from E9.5 until birth. The capability to image embryos in utero at high resolution opens new avenues for investigation, including brain formation, peripheral nerve development, placental development, birth defects, gene editing, immune system development, environmental effects, and interspecies chimera.

REFERENCES AND NOTES

1. A. K. Hadjantonakis, M. E. Dickinson, S. E. Fraser, V. E. Papaioannou, *Nat. Rev. Genet.* **4**, 613–625 (2003).
2. A. Di Cristofano, B. Pesce, C. Cordon-Cardo, P. P. Pandolfi, *Nat. Genet.* **19**, 348–355 (1998).
3. C. L. Gregg, J. T. Butcher, *Differentiation* **84**, 149–162 (2012).
4. P. Pantazis, W. Supatto, *Nat. Rev. Mol. Cell Biol.* **15**, 327–339 (2014).
5. K. McDole *et al.*, *Cell* **175**, 859–876.e33 (2018).
6. W. A. Muñoz, P. A. Trainor, *Methods Mol. Biol.* **1976**, 107–119 (2019).
7. M. N. Shahbazi, M. Zernicka-Goetz, *Nat. Cell Biol.* **20**, 878–887 (2018).
8. K. E. Brett, Z. M. Ferraro, J. Yockell-Lelievre, A. Gruslin, K. B. Adamo, *Int. J. Mol. Sci.* **15**, 16153–16185 (2014).
9. J. Cao *et al.*, *Nature* **566**, 496–502 (2019).
10. C. Stremmel *et al.*, *Nat. Commun.* **9**, 75 (2018).
11. A. Holtmaat *et al.*, *Nat. Protoc.* **4**, 1128–1144 (2009).
12. L. Ritsma *et al.*, *Sci. Transl. Med.* **4**, 158ra145 (2012).
13. N. Rakhilin *et al.*, *Nat. Commun.* **7**, 11800 (2016).
14. D. Entenberg *et al.*, *Nat. Methods* **15**, 73–80 (2018).
15. G. A. Pilz *et al.*, *Science* **359**, 658–662 (2018).
16. N. Rakhilin *et al.*, *Nat. Commun.* **10**, 5647 (2019).
17. J. Rinkenberger, Z. Werb, *Nat. Genet.* **25**, 248–250 (2000).
18. A. P. McMahon, A. L. Joyner, A. Bradley, J. A. McMahon, *Cell* **69**, 581–595 (1992).
19. Y. Chai *et al.*, *Development* **127**, 1671–1679 (2000).
20. X. Jiang, D. H. Rowitch, P. Soriano, A. P. McMahon, H. M. Sucov, *Development* **127**, 1607–1616 (2000).
21. K. Foster *et al.*, *J. Immunol.* **180**, 3183–3189 (2008).
22. F. Lin, Z. V. Wang, J. A. Hill, *Autophagy* **10**, 691–693 (2014).
23. T. Kaizuka *et al.*, *Mol. Cell* **64**, 835–849 (2016).
24. R. Gómez-Sintes *et al.*, *Cells* **6**, 37 (2017).
25. H. Tian *et al.*, *Nature* **478**, 255–259 (2011).
26. M. Yuryev *et al.*, *Front. Cell. Neurosci.* **9**, 500 (2016).
27. N. J. Michelson, J. R. Eles, A. L. Vazquez, K. A. Ludwig, T. D. Y. Kozai, *J. Neurosci. Res.* **97**, 620–638 (2019).
28. H. S. Leong *et al.*, *Nat. Protoc.* **5**, 1406–1417 (2010).
29. P. Wick *et al.*, *Environ. Health Perspect.* **118**, 432–436 (2010).
30. D. B. Cox, R. J. Platt, F. Zhang, *Nat. Med.* **21**, 121–131 (2015).
31. C. E. Nelson *et al.*, *Nat. Med.* **25**, 427–432 (2019).
32. A. K. Gruenert *et al.*, *PLOS ONE* **11**, e0152589 (2016).
33. M. dal Maschio *et al.*, *Nat. Commun.* **3**, 960 (2012).
34. J. Wu *et al.*, *Nature* **540**, 51–59 (2016).
35. F. Soldner, R. Jaenisch, *Cell* **175**, 615–632 (2018).
36. M. A. Cohen *et al.*, *Proc. Natl. Acad. Sci. U.S.A.* **113**, 1570–1575 (2016).
37. R. Jaenisch, *Nature* **318**, 181–183 (1985).
38. M. A. Cohen, S. Markoulaki, R. Jaenisch, *Stem Cell Rep.* **10**, 1445–1452 (2018).

ACKNOWLEDGMENTS

We thank L. Cameron (Duke University) and M. Itano (University of North Carolina) for assistance with two-photon microscopy, and the Innovation Co-Lab at Duke University. This work was supported by NSFC81670468, 2017KJXX-43, 2018SF-208, China Scholarship Council (to Q.H.); by NIH R35GM122465 and DK119795 (to X.S.); by the Emerald Foundation, the Leo Foundation, and Melanoma Research Foundation (to R.J. and M.A.C.); by NIH R37HD045022, 1R01-NS088538, and 5R01-MH104610 (to R.J.); by NIH NS083897, NS098176, NS110388 and MH119813 (to D.L.S.); and by NIH R35 CA197616 (to D.G.K.). **Author contributions:** Q.H. and X.S. designed the experiments. Q.H. performed the experiments with assistance from A.G., N.R., E.W., K.X., P.M., L.W., C.B., V.R., Y.W., M.N., C.W.W., P.K.L.M., A.R.D., D.G.K., and Y.K.; M.A.C., S.Z., and R.J. designed and performed the chimeras experiments. F.C.A. and D.L.S. designed and performed the in utero electroporation experiments. G.D., P.H., and A.A. designed and generated the AAV vectors. J.M. and B.C. assisted with embryo imaging and handling. **Competing interests:** The authors declare no competing interests. **Data and materials availability:** All data are available in the main text or the supplementary materials.

SUPPLEMENTARY MATERIALS

science.sciencemag.org/content/368/6487/181/suppl/DC1
Materials and Methods
Figs. S1 to S8
References (*39*–*46*)
Movies S1 to S9

29 October 2019; accepted 16 March 2020
10.1126/science.aba0210

IMMUNOLOGY

Dendritic cell–derived hepcidin sequesters iron from the microbiota to promote mucosal healing

Nicholas J. Bessman[1,2,3], Jacques R. R. Mathieu[4,5]*, Cyril Renassia[4,5]*, Lei Zhou[1,2,3], Thomas C. Fung[1,2,3], Keith C. Fernandez[1,2,3], Christine Austin[6], Jesper B. Moeller[1,2,3,7], Sara Zumerle[4,5]†, Sabine Louis[4,5], Sophie Vaulont[4,5], Nadim J. Ajami[8], Harry Sokol[9], Gregory G. Putzel[1], Tara Arvedson[10], Robbyn E. Sockolow[11], Samira Lakhal-Littleton[12], Suzanne M. Cloonan[13,14], Manish Arora[6], Carole Peyssonnaux[4,5]‡, Gregory F. Sonnenberg[1,2,3]‡

Bleeding and altered iron distribution occur in multiple gastrointestinal diseases, but the importance and regulation of these changes remain unclear. We found that hepcidin, the master regulator of systemic iron homeostasis, is required for tissue repair in the mouse intestine after experimental damage. This effect was independent of hepatocyte-derived hepcidin or systemic iron levels. Rather, we identified conventional dendritic cells (cDCs) as a source of hepcidin that is induced by microbial stimulation in mice, prominent in the inflamed intestine of humans, and essential for tissue repair. cDC-derived hepcidin acted on ferroportin-expressing phagocytes to promote local iron sequestration, which regulated the microbiota and consequently facilitated intestinal repair. Collectively, these results identify a pathway whereby cDC-derived hepcidin promotes mucosal healing in the intestine through means of nutritional immunity.

Inflammatory bowel disease (IBD), colorectal cancer, and gastrointestinal infections cause tissue inflammation that drives bleeding, malabsorption, and diarrhea (*1*–*3*). As a result, patients frequently exhibit anemia that is difficult to treat, and bleeding introduces a new source of iron to the intestine (*4*, *5*). Hepcidin, the master regulator of systemic iron homeostasis, is produced as a peptide hormone from the liver and promotes degradation of the cellular iron efflux transporter ferroportin (*4*, *6*–*10*). Ferroportin is expressed on red pulp macrophages and the basolateral surface of duodenal enterocytes, where it facilitates iron recycling from senescent red blood cells and import of dietary iron, respectively (*4*, *6*–*10*). Despite these advances, it remains unclear whether hepcidin has a role in gastrointestinal health or disease.

To address this, we exposed wild-type ($Hamp^{+/+}$) and hepcidin-deficient ($Hamp^{-/-}$) mice to a model of intestinal tissue damage, inflammation, and repair by administering dextran sodium sulfate (DSS) in their drinking water. During DSS administration, $Hamp^{+/+}$ and $Hamp^{-/-}$ mice exhibited similar weight loss (Fig. 1A), indicative of comparable inflammation and tissue damage. However, upon removal of DSS, $Hamp^{-/-}$ mice exhibited persistent weight loss, continued disruption of

[1]Jill Roberts Institute for Research in Inflammatory Bowel Disease (JRI), Weill Cornell Medicine, Cornell University, New York, NY, USA. [2]Joan and Sanford I. Weill Department of Medicine, Division of Gastroenterology and Hepatology, Weill Cornell Medicine, Cornell University, New York, NY, USA. [3]Department of Microbiology and Immunology, Weill Cornell Medicine, Cornell University, New York, NY, USA. [4]Université de Paris, INSERM U1016, Institut Cochin, CNRS UMR8104, 75014 Paris, France. [5]Laboratory of Excellence GR-Ex, Paris, France. [6]Department of Environmental Medicine and Public Health, Icahn School of Medicine at Mount Sinai, New York, NY 10029, USA. [7]Department of Molecular Medicine, University of Southern Denmark, Odense, Denmark. [8]MD Anderson Cancer Center, Houston, TX, USA. [9]Sorbonne Université, Inserm, Centre de Recherche Saint-Antoine, CRSA, AP-HP, Hôpital Saint Antoine, Service de Gastroenterologie, F-75012 Paris, France. [10]Department of Oncology Research, Amgen Inc., Thousand Oaks, CA, USA. [11]Department of Pediatrics, Division of Gastroenterology and Nutrition, Weill Cornell Medicine, Cornell University, New York, NY, USA. [12]Department of Physiology, Anatomy and Genetics, University of Oxford, Oxford OX1 3PT, UK. [13]Division of Pulmonary and Critical Care Medicine, Weill Cornell Medicine, Cornell University, New York, NY, USA. [14]Trinity College Dublin, Dublin, Ireland.
*These authors contributed equally to this work. †Present address: Department of Medicine, University of Padova and VIMM Veneto Institute of Molecular Medicine, Padova, Italy.
‡**Corresponding author. Email: gfsonnenberg@med.cornell.edu (G.F.S.); carole.peyssonnaux@inserm.fr (C.P.)**

We deleted hepcidin in cDCs by crossing CD11c^{Cre} mice with *Hamp*$^{F/F}$ mice. *Hamp*$^{\Delta CD11c}$ mice exhibited a selective loss of hepcidin expression in cDCs (Fig. 3A and fig. S4A). DC development and systemic iron in *Hamp*$^{\Delta CD11c}$ mice were comparable to controls (fig. S4, B to D). Furthermore, lymphocyte, myeloid, and granulocyte responses were similar in *Hamp*$^{\Delta CD11c}$ mice and controls during naïve conditions and after administration of DSS (figs. S4, E and F, and S5, A to C). Global transcriptional profiling also revealed minimal changes in cDC subsets from *Hamp*$^{\Delta CD11c}$ mice relative to controls (fig. S6). Thus, cDC-derived hepcidin does not affect immune responses in these contexts.

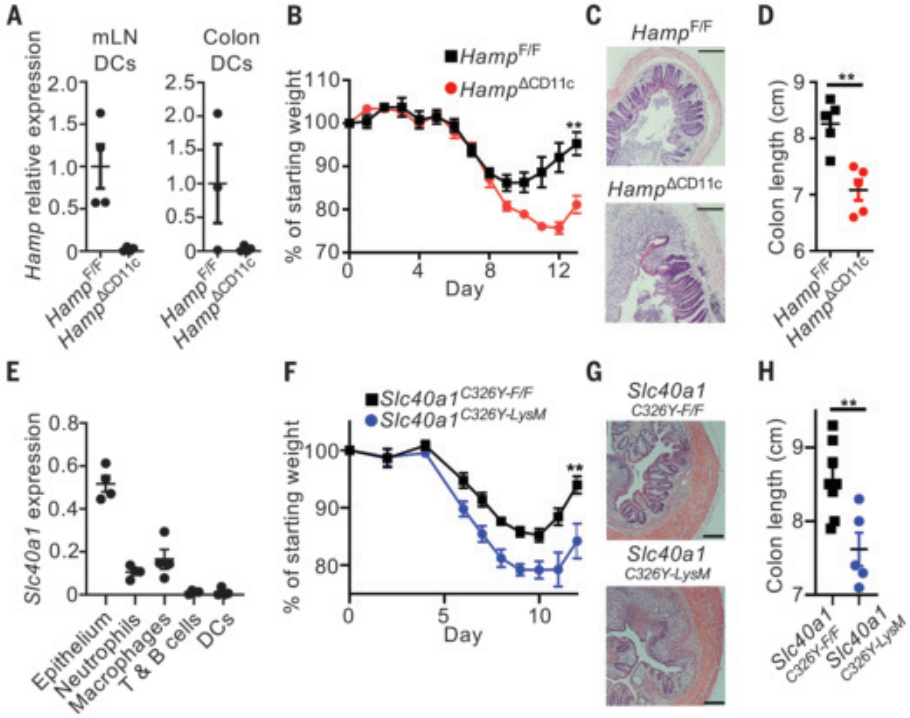

Fig. 3. Dendritic cell–derived hepcidin acts on ferroportin-expressing phagocytes to facilitate mucosal healing. (**A**) Hepcidin expression was determined by qPCR in mice exposed to DSS for 7 days. (**B** to **D**) Mice were given DSS for 8 days, and recovery was monitored by weight change (B), H&E staining of the distal colon (C), and colon shortening (D). (**E**) Sort-purified cells from the naïve mouse colon were analyzed for Slc40a1 expression by qPCR. (**F** to **H**) Mice were given DSS for 7 days, and recovery was monitored by weight change (F), H&E staining of the distal colon (G), and colon shortening (H). Data in (D) and (H) were analyzed by unpaired two-tailed Student *t* test. In (B) and (F), weights at killing, normalized to starting weight, were analyzed by unpaired two-tailed Student *t* test. Data in (A) to (D) are representative of at least two independent experiments with $n = 3$ to 5 per group; data in (F) and (H) are pooled from, and data in (G) are representative of, three independent experiments with $n = 1$ to 3 per group. Data are means ± SEM. $^{**}P < 0.01$. Scale bars, 200 μm.

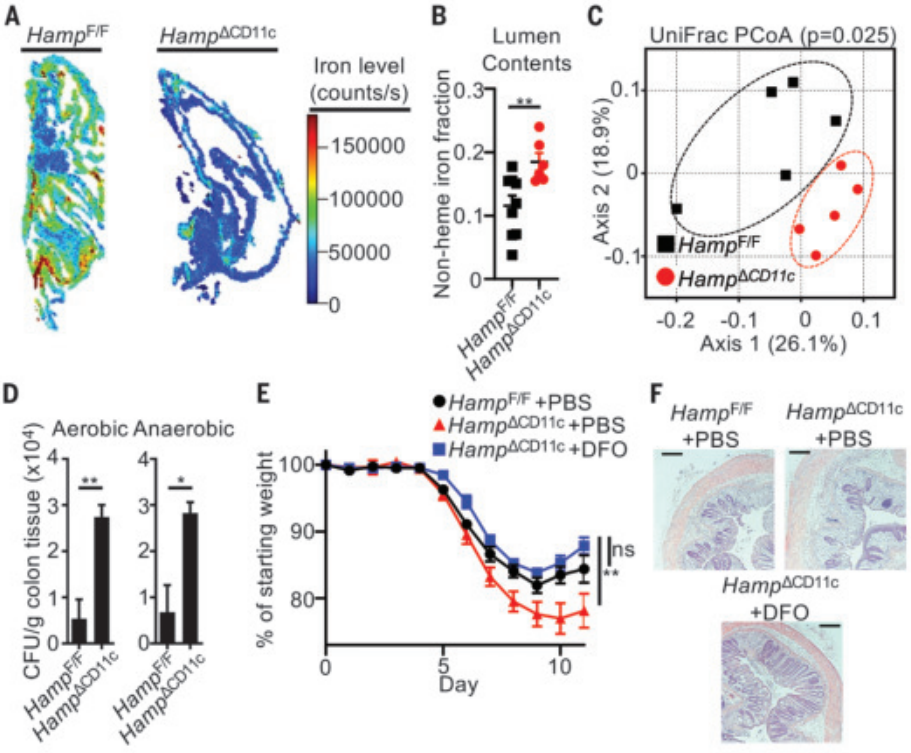

Fig. 4. Dendritic cell–derived hepcidin sequesters iron to shape the intestinal microbiota. (**A** and **B**) Mice were exposed to DSS for 7 days. Whole cecal tissues were analyzed for iron levels by quantitative mass spectrometry imaging (A), and iron levels were quantified in colon lumen contents (B). (**C**) Fecal microbiota were analyzed by 16*S* rRNA gene sequencing and principal coordinates analysis. (**D**) Mice were exposed to DSS for 7 days, and bacterial colony-forming units (CFU) were quantified from colon tissue homogenates. (**E** and **F**) Mice were given DSS in drinking water for 7 days and treated daily with either phosphate-buffered saline (PBS) vehicle or DFO from day 0 through day 11. DSS-induced disease and recovery were monitored by weight loss (E) and H&E staining of the distal colon (F). In (A), two independent experiments with $n = 1$ to 5 per group were performed; representative data are shown. Data in (B) and (E) are pooled from two independent experiments, each with $n = 3$ to 5 per group. Data in (C) and (D) are representative of two independent experiments with $n = 5$ per group. In (B) and (D), groups were compared by unpaired two-tailed Student *t* test. In (C), *P* value was determined using a permutational multivariate ANOVA test. In (E), weights at killing, normalized to starting weight, were analyzed by one-way ANOVA using Tukey multiple comparisons. In (F), representative data are shown from two independent experiments with $n = 3$ to 5 per group. Data are means ± SEM. Scale bars, 200 μm. $^{*}P < 0.05$, $^{**}P < 0.01$.

By contrast, *Hamp*$^{\Delta CD11c}$ mice exhibited significantly reduced body weight after removal of DSS, abnormal colon tissue architecture, and shortened colons relative to controls (Fig. 3, B to D). *Zbtb46*^{Cre}-mediated deletion of hepcidin in cDCs resulted in a similar impairment of tissue repair relative to controls (fig. S7). Thus, cDC-derived hepcidin is essential for mucosal healing.

We next profiled the colonic expression of ferroportin (*Slc40a1*) and observed high expression in epithelium, neutrophils, and macrophages (Fig. 3E). To determine whether these are the targets of hepcidin that facilitate mucosal healing, we used mice in which a hepcidin-resistant ferroportin variant, *Slc40a1*^{C326Y}, is expressed from the endogenous locus after Cre-mediated recombination (fig. S8A) (*16*). The expression of *Slc40a1*^{C326Y} in DCs or intestinal epithelial cells had no impact on mucosal healing (fig. S8, B to E). By contrast, *Slc40a1*^{C326Y} expression in macrophages and neutrophils via LysM^{Cre} resulted in significantly reduced body weight, abnormal colonic tissue architecture, and shortened colons relative to controls and after removal of DSS (Fig. 3, F to H). Consistent with posttranslational regulation of ferroportin, DC-derived hepcidin did not have an impact on *Slc40a1* or *Hmox1* mRNA levels in macrophages (fig. S8F). Thus, ferroportin-expressing macrophages and/or neutrophils are a critical target for hepcidin-mediated mucosal healing.

To test whether this intestinal hepcidin-ferroportin axis regulates local iron distribution in the gut, we used quantitative mass spectrometry imaging. Strikingly, iron levels within the cecal tissue of DSS-treated *Hamp*$^{\Delta CD11c}$ mice were decreased relative to controls (Fig. 4A and fig. S9, A and B). Consistent with this, non-heme iron levels were increased in the luminal content of *Hamp*$^{\Delta CD11c}$ mice relative to controls after DSS-induced damage, but not in naïve mice (Fig. 4B and fig. S9, C and D). This likely involves conversion of heme-bound iron from erythrocytes into non–heme-bound iron via heme oxygenase 1 in phagocytes (*17*), which would then efflux to extracellular space through ferroportin unless regulated by hepcidin. Iron sequestration is a key component of nutritional immunity (*4*, *18*, *19*), so we examined whether cDC-derived hepcidin alters the microbiota. *Hamp*$^{\Delta CD11c}$ mice exhibited a significant shift in microbiota composition relative to littermate controls (Fig. 4C). Fecal microbiota transplantation (FMT) from *Hamp*$^{\Delta CD11c}$ mice to wild-type germ-free recipients was sufficient to transfer impaired mucosal healing relative to controls (fig. S10). *Catenibacterium* and *Bifidobacterium* were significantly different genera in *Hamp*$^{\Delta CD11c}$ mice relative to controls (fig. S11A). Notably, *Bifidobacterium* species support epithelial barrier function, and dietary iron supplementation can suppress *Bifidobacterium* species and exacerbate inflammation (*20*). We found that *Bifidobacterium* species expanded with restricted dietary iron, and that oral administration of *Bifidobacterium* species increased expression of intestinal tight junctions in wild-type mice and enhanced mucosal healing in *Hamp*$^{\Delta CD11c}$ mice (fig. S11, B to E). *Bifidobacterium* only partially restored normal mucosal healing, and the pathways by which DC-derived hepcidin promotes colonization with this microbe remain unclear. In addition, *Hamp*$^{\Delta CD11c}$ mice also exhibited significantly increased levels of tissue-infiltrating bacteria relative to controls after DSS exposure, and antibiotic treatment eliminated DSS-induced phenotypes (Fig. 4D and fig. S12). To determine whether excess extracellular iron impairs healing in *Hamp*$^{\Delta CD11c}$ mice, we administered deferoxamine (DFO), which sequesters extracellular iron from bacteria by chelation (*21*). DFO treatment in DSS-exposed *Hamp*$^{\Delta CD11c}$ mice was sufficient to completely restore mucosal healing (Fig. 4, E and F).

Our results outline a model in which cDCs produce hepcidin in response to microbiota-derived signals, and subsequently limit iron release from intestinal phagocytes to prevent tissue infiltration by the microbiota and thus promote mucosal healing (fig. S13). This contrasts with liver-derived hepcidin, which acts as an endocrine hormone, is induced by inflammatory cytokines, and has the potential to protect against systemic infection (*7*, *22*, *23*). It will be important to interrogate whether DC-derived hepcidin has the potential for a direct impact on the immune response (although this was not observed in our models) or on systemic iron homeostasis in other contexts. Furthermore, our results indicate that hepcidin mimetics could be a beneficial therapeutic strategy in the context of FMT or gastrointestinal diseases where mucosal healing is an emerging therapeutic goal.

REFERENCES AND NOTES

1. M. Karin, T. Lawrence, V. Nizet, *Cell* **124**, 823–835 (2006).
2. A. Kaser, S. Zeissig, R. S. Blumberg, *Annu. Rev. Immunol.* **28**, 573–621 (2010).
3. B. Khor, A. Gardet, R. J. Xavier, *Nature* **474**, 307–317 (2011).
4. M. U. Muckenthaler, S. Rivella, M. W. Hentze, B. Galy, *Cell* **168**, 344–361 (2017).
5. G. Weiss, L. T. Goodnough, *N. Engl. J. Med.* **352**, 1011–1023 (2005).
6. A. Donovan *et al*., *Cell Metab.* **1**, 191–200 (2005).
7. H. Drakesmith, E. Nemeth, T. Ganz, *Cell Metab.* **22**, 777–787 (2015).
8. E. Fung *et al*., *Mol. Pharmacol.* **83**, 681–690 (2013).
9. T. Ganz, E. Nemeth, *Annu. Rev. Med.* **62**, 347–360 (2011).
10. E. Nemeth *et al*., *Science* **306**, 2090–2093 (2004).
11. S. R. Pasricha, K. McHugh, H. Drakesmith, *Annu. Rev. Nutr.* **36**, 417–434 (2016).
12. N. K. Shanmugam, E. Trebicka, L. L. Fu, H. N. Shi, B. J. Cherayil, *J. Immunol.* **193**, 1398–1407 (2014).
13. S. Zumerle *et al*., *Blood* **123**, 3646–3650 (2014).
14. C. Peyssonnaux *et al*., *Blood* **107**, 3727–3732 (2006).
15. B. J. Sasu *et al*., *Blood* **115**, 3616–3624 (2010).
16. S. Lakhal-Littleton *et al*., *eLife* **5**, e19804 (2016).
17. H. Kayama *et al*., *Proc. Natl. Acad. Sci. U.S.A.* **115**, 8418–8423 (2018).
18. C. A. Lopez, E. P. Skaar, *Cell Host Microbe* **23**, 737–748 (2018).
19. H. Drakesmith, A. M. Prentice, *Science* **338**, 768–772 (2012).
20. A. Sarkar, S. Mandal, *Microbiol. Res.* **192**, 159–171 (2016).
21. R. C. Hider, A. V. Hoffbrand, *N. Engl. J. Med.* **379**, 2140–2150 (2018).
22. C. Casu, E. Nemeth, S. Rivella, *Blood* **131**, 1790–1794 (2018).
23. K. Michels, E. Nemeth, T. Ganz, B. Mehrad, *PLOS Pathog.* **11**, e1004998 (2015).

ACKNOWLEDGMENTS

We thank members of the Sonnenberg laboratory for discussions and critical reading of the manuscript, the Epigenomics Core of Weill Cornell Medicine, and S. Mozumder and K. Kim for technical assistance. **Funding:** Research in the Sonnenberg laboratory is supported by NIH fellowship F32AI124517 (N.J.B.); Crohn's and Colitis Foundation fellowship 608975 (L.Z.); and NIH grants R01AI143842, R01AI123368, R01AI145989, R21CA249274, and U01AI095608, the NIAID Mucosal Immunology Studies Team (MIST), the Searle Scholars Program, an American Asthma Foundation Scholar Award, an Investigators in the Pathogenesis of Infectious Disease Award from the Burroughs Wellcome Fund, a Wade F. B. Thompson/Cancer Research Institute (CRI) CLIP Investigator grant, the Meyer Cancer Center Collaborative Research Initiative, Linda and Glenn Greenberg, and JRI (G.F.S.). G.F.S. is a CRI Lloyd J. Old STAR. Funding support also included the European Research Council (FP7/2011-2015 #261296); the "Fondation pour la Recherche Médicale" (DEq. 20160334903); the Laboratory of Excellence GR-Ex (ANR-11-LABX-0051); a labex GR-Ex fellowship (J.R.R.M. and S.L.); the French National Research Agency (ANR-11-IDEX-0005-02); the "Fondation ARC pour la recherche sur le cancer" (S.Z.); NIH grants PP30ES023515 and 1U2CES030859 (C.A. and M.A.); NIH grant R00HL125899 (S.M.C.); NICHD grant R00HD087523 (C.A.); and Science Foundation Ireland grant FRL4862 (S.M.C.). The JRI IBD Live Cell Bank is supported by the JRI, Jill Roberts Center for IBD, Cure for IBD, the Rosanne H. Silbermann Foundation, and Weill Cornell Medicine Division of Pediatric Gastroenterology and Nutrition. **Author contributions:** N.J.B. and G.F.S. conceived the project; N.J.B., L.Z., T.C.F., K.C.F., J.B.M., J.R.R.M., C.R., S.L., and S.Z. performed experiments and analyzed data; S.V. and S.L.-L. provided mouse models and expertise; H.S. performed pathological analyses; T.A. provided tools and expertise; C.P. provided mouse models and designed and supervised experiments; N.J.A. and G.G.P. analyzed sequencing data; C.A. and M.A. performed and analyzed iron imaging; R.E.S. provided essential advice and guidance; S.M.C. provided guidance and iron measurements; and N.J.B. and G.F.S. wrote the manuscript with input from all the authors. **Competing interests:** G.F.S. holds stock and is a member of an advisory board for Celsius Therapeutics Inc. T.A. is an employee of Amgen Inc. H.S. is a co-founder of Exeliom Biosciences and has received unrestricted study grants from Danone, Biocodex, and Enterome; board membership, consultancy, or lecture fees from Carenity, Abbvie, Astellas, Danone, Ferring, Mayoly Spindler, MSD, Novartis, Roche, Tillots, Enterome, Maat, BiomX, Biose, Novartis, and Takeda. The other authors declare no competing interests. **Data and materials availability:** All data necessary to understand and evaluate the conclusions of this paper are provided in the manuscript and supplementary materials. Microarray and 16*S* rRNA sequencing data are available from the GEO database with accession numbers GSE143869 and GSE139371. Floxed mice are available with a material transfer agreement with INSERM.

SUPPLEMENTARY MATERIALS

science.sciencemag.org/content/368/6487/186/suppl/DC1
Materials and Methods
Figs. S1 to S13
References (*24*–*30*)

9 July 2018; resubmitted 22 August 2019
Accepted 11 February 2020
10.1126/science.aau6481

QUANTUM GASES

Bose polarons near quantum criticality

Zoe Z. Yan, Yiqi Ni, Carsten Robens, Martin W. Zwierlein*

The emergence of quasiparticles in interacting matter represents one of the cornerstones of modern physics. However, in the vicinity of a quantum critical point, the existence of quasiparticles comes under question. Here, we created Bose polarons near quantum criticality by immersing atomic impurities in a Bose-Einstein condensate (BEC) with near-resonant interactions. Using radiofrequency spectroscopy, we probed the energy, spectral width, and short-range correlations of the impurities as a function of temperature. Far below the superfluid critical temperature, the impurities formed well-defined quasiparticles. Their inverse lifetime, given by their spectral width, increased linearly with temperature at the so-called Planckian scale, consistent with quantum critical behavior. Close to the BEC critical temperature, the spectral width exceeded the impurity's binding energy, signaling a breakdown of the quasiparticle picture.

A great success of quantum many-body physics is the description of a large variety of strongly interacting systems by a collection of weakly interacting quasiparticles (*1*). A paradigmatic example of such a quasiparticle is an electron propagating through an ionic crystal. As anticipated by Landau (*2*), Pekar found that the electron can create its own bound state by polarizing its environment (*3*, *4*); the electron dressed by lattice distortions forms a quasiparticle, which he named the polaron. The polaron concept (*5*, *6*) finds wide application across condensed matter physics in phenomena ranging from colossal magnetoresistance, to charge transport in organic semiconductors, to high-temperature superconductivity (*7*). However, near quantum phase transitions, where different phases of matter compete, the quasiparticle concept may break down (*8*). In such a quantum critical regime, where the temperature (T) sets the only energy scale, all relaxation times become as short as allowed by quantum mechanics, i.e., on the order of the Planckian time scale $\hbar/k_B T$, where $\hbar$ is Planck's constant and k_B is Boltzmann's constant. The ensuing breakdown of well-defined quasiparticles appears to be at work in the "strange metal" regime of cuprate superconductors, where resistivity is found to scale linearly with temperature and at the Planckian scale (*9*, *10*).

Ultracold quantum gases provide an ideal testing ground to study the fate of quasiparticles near quantum critical points. Species composition and densities, interaction strengths, and confining geometries can be precisely controlled (*11*). Quantum gases close to Feshbach resonances have been shown to be controlled by quantum critical points at zero temperature, separating the vacuum of a given species from the phase at finite density (*8*, *12*–*16*). These points control the behavior of the gas in the quantum-critical region at nonzero temperature (*8*). The immersion of dilute impurities into a gas of another species with resonant mutual interactions thus places the mixture in direct vicinity of the quantum critical point separating the impurity vacuum from the phase at finite impurity density (*13*). In addition, the impurities can serve as a sensor of quantum and classical critical behavior of the host gas itself (*17*). The dressing of resonant impurities into quasiparticles in a cold-atom environment was first observed in the case of the Fermi polaron (*18*–*24*), an atomic impurity embedded in a Fermi sea (*25*–*28*). Impurities dressed by a Bose-Einstein condensate (BEC) have been posited to form the paradigmatic Bose polarons originally considered by Pekar (*29*–*31*). Predicting the Bose polaron's fate upon entering the regime of strong impurity-boson interactions has proven a challenge even at zero temperature, yielding diverging results on its properties from the ground-state energy to the effective mass (*31*–*40*). The complexity of describing the strongly coupled Bose polaron increases further at nonzero temperatures (*41*, *42*). Even for weak interactions, the decay rate of polarons has been predicted to be strongly enhanced with increasing temperature, achieving its maximal value near the BEC transition temperature of the host gas (*41*). Near resonance, in the quantum critical regime of the boson-impurity mixture, the very existence of a well-defined quasiparticle is in question (*8*, *13*, *15*, *16*). Experimentally, evidence of Bose polaronic phenomena was observed in the expansion (*43*) and trapping (*44*) of fermions immersed in a BEC, through the phononic Lamb shift (*45*), and in the dynamics of impurities (*46*). The continuum of excited states of impurities was probed in radiofrequency (rf) injection spectroscopy (*16*) on Bose-Fermi mixtures (*47*, *48*) and in a two-state mixture of bosons (*49*), yielding evidence for polaronic energy shifts of such excitations.

MIT–Harvard Center for Ultracold Atoms, Research Laboratory of Electronics, and Department of Physics, Massachusetts Institute of Technology, Cambridge, MA 02139, USA.
*Corresponding author. Email: zwierlein@mit.edu

Here, we created and studied the strongly coupled Bose polaron in equilibrium by immersing fermionic impurities into a Bose gas near an interspecies Feshbach resonance and explored the impurity's evolution in the quantum critical regime of the Bose-Fermi mixture, including the onset of quantum degeneracy of the bosonic bath. The experiment started with an ultracold gas of fermionic ^{40}K atoms immersed in a BEC of ^{23}Na (*43*) at a temperature $T \approx 130$ nK. Both species were trapped in an optical dipole trap as ellipsoidal atom clouds in their respective hyperfine ground states: $|F = 1, m_F = 1\rangle$ for ^{23}Na and $|9/2, -9/2\rangle \equiv |\downarrow\rangle$ for ^{40}K. Peak boson and fermion densities were $n_{Na} = 6 \times 10^{13}$ cm^{-3} and $n_K = 2 \times 10^{11}$ cm^{-3}, respectively, corresponding to an impurity concentration of 0.3%. The BEC was weakly interacting, with an interboson scattering length of $a_{BB} = 52a_0$ (*50*). To create strongly coupled Bose polarons in their attractive ground state, we ramped the magnetic field close to an interspecies Feshbach resonance (*43*, *16*), where impurities in the $|\downarrow\rangle$ state were strongly attracted to the sodium atoms with a peak interaction strength of $(k_n a)^{-1} = -0.3$. Here, $k_n = (6\pi^2 n_{Na})^{1/3} = (1300a_0)^{-1}$ is the inverse interboson distance, a is the interspecies scattering length, and a_0 is the Bohr radius. For these near-resonant interactions, the thermal equilibration time set by two-body collisions was near its unitarity-limited value of $\frac{\hbar}{E_n} \approx 4\,\mu$s, three orders of magnitude faster than the lifetime of the gas mixture in this regime, limited by three-body losses to ~4 ms. Here, $E_n = \hbar^2 k_n^2/4m_r$ is the degeneracy energy scale and $m_r = m_K m_{Na}/(m_K + m_{Na})$ is the reduced mass of the impurity-boson scattering problem. By preparing the strongly interacting system within 2 ms, we could study Bose polarons in equilibrium before losses became dominant. At the chosen magnetic field, impurities in the $|\downarrow\rangle$ state were strongly interacting with the condensate, whereas they were noninteracting in the hyperfine state $|9/2,-7/2\rangle \equiv |\uparrow\rangle$. This provided us with the ideal conditions to perform rf ejection spectroscopy, whereby an rf pulse transfers impurities from the interacting $|\downarrow\rangle$ state into the noninteracting $|\uparrow\rangle$ state. We used an rf pulse of Gaussian envelope with a full-width-half-maximum resolution of 6 kHz and measured the fraction of impurities $I(\omega)$ transferred into the $|\uparrow\rangle$ state.

Figure 1 displays the locally resolved rf spectrum of strongly coupled Bose polarons. As shown in Fig. 1D, the rf transfer $I(\omega)$ is strongly spatially dependent, and its maximum is shifted furthest from the bare atomic resonance for impurities deep inside the BEC (Fig. 1B). Here, the rf photon must supply a large additional amount of energy to transfer the bound impurity into the noninteracting state. The central peak shift in Fig. 1C corresponds to an energy shift of $h \cdot 32$ kHz $= 0.82\,E_n$, indicating

an impurity energy that is unitarity limited, given by the degeneracy energy scale E_n. For comparison, the mean-field energy experienced by bosons in the BEC is only $\approx h\cdot 0.8$ kHz. In addition to the strong shift, we also observed long tails at higher frequencies in the rf transfer, a telltale sign of contact interactions (*51*–*53*).

Interpreting the spatially resolved spectrum under the assumption of the local density approximation (*16*, *54*) gives access to the rf spectrum of the impurity as a function of the condensate's local chemical potential $\mu(z) = \mu_0 - V_{Na}(z)$. Here, $\mu_0 = 4\pi\hbar^2 a_{BB} n_{Na}/m_{Na}$ is the condensate's chemical potential at its peak density, and $V_{Na}(z)$ is the radially centered trapping potential along the axial direction. Figure 2A shows the rf spectrum as a function of $\beta\mu(z)$, the chemical potential normalized by $\beta = 1/k_B T$. The interaction parameter $(k_n a)^{-1}$ also varies with the local density $n_{Na}(z)$ as indicated. A strong shift of the rf transfer for positive chemical potentials is clearly visible. Figure 2B shows a selection of spectra, indicating the temperature T normalized by the local critical temperature $T_C(z) = 3.31\frac{\hbar^2}{k_B m_{Na}}[n_{Na}(z)]^{2/3}$ for a homogeneous gas. The absolute frequency of the spectral peak continuously decreases with higher reduced temperatures (left panel). However, when normalized by the degeneracy energy scale E_n, the spectral peak frequency in fact increases, indicating a more strongly bound impurity with increasing temperatures up to the critical temperature T_C (right panel). This finding is summarized in Fig. 3A, where the peak frequency shift ω_p is interpreted as the ground-state energy $E_p = -\hbar\omega_p$ of the Bose polaron (*16*). Stronger binding of the impurity to the bosonic bath with increasing temperature has been predicted (*42*). Additionally, a broadening of the spectral function underlying the rf spectrum may contribute to the observed shift (*24*). Above T_C, the peak energy shift suddenly jumps to zero, despite the near-unitarity–limited interactions. This behavior is expected when the temperature exceeds the energy difference between the attractive and repulsive branches of the resonantly interacting impurity, which occurs near the onset of quantum degeneracy (*55*, *56*). A similar jump in binding energy was recently observed for an impurity resonantly interacting with a nearly degenerate Fermi gas (*24*). At weaker attractive interaction, we observed that the Bose polaron is less strongly bound to the bath, as expected (*32*, *57*) (see Fig. 3A).

In the strongly interacting regime where $|k_n a| \gg 1$, our measurements probed a regime where the binding energy is much larger than the condensate's local mean-field energy. In this regime, a universal description for the Bose polaron at low temperatures emerges from a lowest order T-matrix and an equivalent variational approach (*16*, *32*, *57*): here, the impurity acquires an energy shift that is the sum of the individual and uncorrelated shifts from each host boson:

$$E_p \equiv -\frac{\hbar^2\kappa^2}{2m_r} = -\frac{2\pi\hbar^2 n_{Na}}{m_r} f(i\kappa) \qquad (1)$$

where $f(i\kappa) = -\frac{a}{1-\kappa a}$ is the two-body scattering amplitude evaluated at imaginary momentum $i\kappa$, as appropriate for a bound state. The equation implicitly gives E_p, whose natural energy scale is confirmed as the degeneracy energy scale E_n for an effective particle of reduced

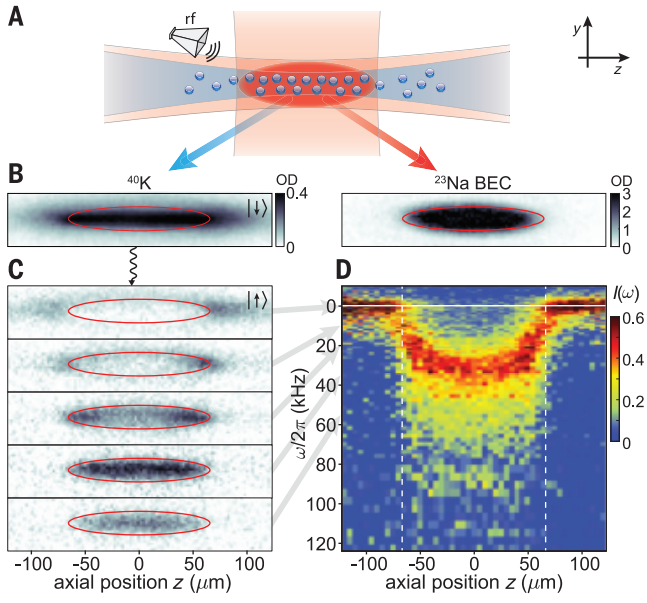

Fig. 1. Locally resolved rf ejection spectroscopy of strongly coupled Bose polarons. Shown are the data for a peak interaction strength of $(k_n a)^{-1} = -0.3$. (**A**) Illustration of impurities (blue) immersed in a BEC (red), both trapped in a dual-color optical dipole trap. (**B**) In situ column densities shown as optical densities (ODs) of ^{40}K impurities in the strongly interacting spin state $|\downarrow\rangle$ (left) immersed in a ^{23}Na BEC (right), where the red ellipses mark the BEC's Thomas-Fermi boundary. (**C**) Impurities transferred into the noninteracting $|\uparrow\rangle$ state at various rf frequencies, as indicated by the gray arrows between (C) and (D). (**D**) Local rf transfer $I(\omega)$ of the impurity column density as a function of axial position. The dashed vertical lines mark the condensate's axial Thomas-Fermi radius, and the solid horizontal line at $\omega/2\pi = 0$ kHz denotes the bare atomic transition.

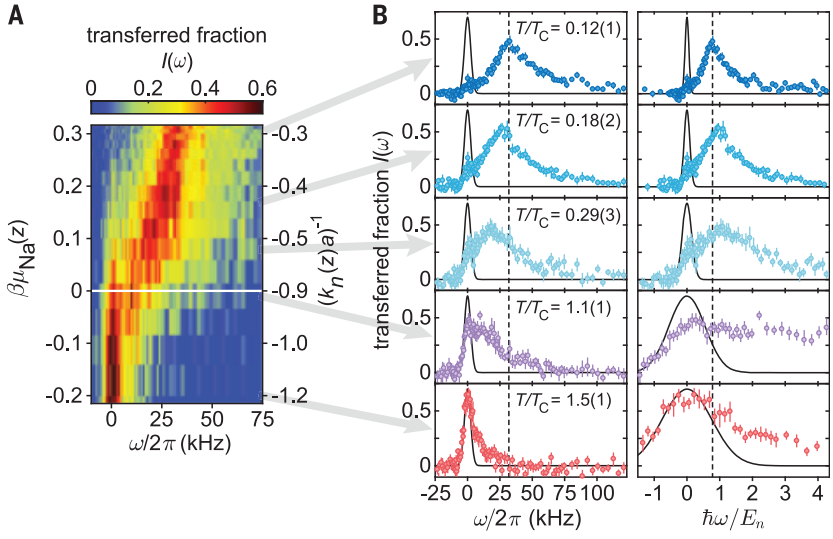

Fig. 2. Radiofrequency ejection spectra of Bose polarons at various reduced temperatures T/T_C. The peak interaction strength is $(k_n a)^{-1} = -0.3$. (**A**) Color density map of the rf transfer $I(\omega)$ as a function of the normalized local chemical potential $\beta\mu(z)$ and the local interaction strength $(k_n a)^{-1}$. The solid white line marks the BEC phase transition at $\beta\mu = 0$. (**B**) Fraction of impurities transferred into the noninteracting state $|\uparrow\rangle$ as a function of rf frequency (left) and of normalized frequency, $\hbar\omega/E_n$ (right) (*16*). The dashed black line marks the peak transfer location of the impurities at the lowest T/T_C. The solid black lines show the rf spectrum of bare ^{40}K atoms, indicating the spectral resolution. Error bars reflect 1σ statistical uncertainty (*16*).

mass m_r and density n_{Na}. In this scenario, E_p/E_n is a universal function of $(k_n a)^{-1}$ only. For weak attractive impurity-boson interactions $[(k_n a)^{-1} \ll -1]$, one finds the mean-field result $E_p = 2\pi\hbar^2 n_{Na} a/m_r$, whereas on the molecular side of the Feshbach resonance in the limit $(k_n a)^{-1} \gg 1$, the polaron energy becomes equal to the energy of a two-body molecule of size a, $E_p = -\frac{\hbar^2}{2m_r a^2}$. On resonance, the approach yields $E_p/E_n = -0.71$, which is similar to the result for the unitary Fermi polaron, $E_p/E_n = -0.61$ (*25*, *58*). The Bose polaron is more strongly bound than its fermionic counterpart owing to the lack of constraints imposed by Pauli exclusion (*16*). The polaron energies according to the T-matrix approach for $T = 0$ are indicated as open diamonds in Fig. 3A. A linear extrapolation to zero temperature of our strong-coupling binding energy data appears to agree well with this theory. Alternatively, assuming the increase in binding strength with temperature results from coupling to the BEC's finite temperature phonon bath, one may attempt a T^4 fit to the data (*41*). Both the linear and quartic extrapolations exclude a simple mean-field prediction that yields $E_p/E_n = -1.4$ for $(k_n a)^{-1} = -0.3$.

The binding energy alone does not reveal whether the impurities in the bosonic bath form well-defined quasiparticles. This requires knowledge of the impurities' spectral width, a measure of the quasiparticle's decay rate (*18*, *24*, *59*, *60*). Generally, the width of an rf spectrum corresponds to the rate at which the coherent evolution of an atomic spin is interrupted during the rf pulse. For quasiparticles, it is momentum-changing collisions with host bosons that cause such decoherence, the same process that limits the quasiparticle's lifetime. The rf spectral width thus directly measures the inverse lifetime of the quasiparticles (*18*, *24*, *59*, *60*). Figure 3B shows that the strong-coupling impurity's spectral width follows a linear dependence with temperature, and quite substantially at the Planckian scale: half-width at half-maximum $(\Gamma) = 8.1(5)\, k_B T/\hbar$. Observing decay rates at this scale is consistent with quantum critical behavior (*8*). The observed linear trend suggests a well-defined quasiparticle with vanishing spectral width in the limit of zero temperature. However, near T_C, the rf spectral width increases substantially beyond the measured binding energy E_p, signaling a breakdown of the quasiparticle picture. We attribute both the linear temperature dependence at the Planck scale $k_B T/\hbar$ and the quasiparticle breakdown to the proximity of the Bose-Fermi mixture's quantum multicritical points (*13*, *16*): the impurity gas is close to the quantum phase transition between the vacuum of impurities, $n_K = 0$, and the phase at nonzero impurity density, $n_K > 0$; interactions are tuned near the resonant point $(k_n a)^{-1} \to 0$; and the host boson gas traverses its own quantum critical regime near the onset of quantum degeneracy at $\mu_B \to 0$. Here, because only one relevant energy scale remains $[k_B T \approx k_B T_C \approx 0.55 E_n$ (*61*)], the spectral width also scales as $E_n/\hbar$ and no quasiparticles are predicted to persist (*8*, *12*). In this regime, the impurities have the shortest mean-free path possible with contact interactions, i.e., one interboson distance. For all temperatures $T < T_C$, the scattering rate at the Planckian scale naturally emerges, assuming polarons scatter with thermal excitations of the saturated Bose gas, at density $n_{th} \sim 1/\lambda_B^3$. Given a unitarity-limited scattering cross section $\sigma \sim \lambda_{rel}^2$ and the most probable relative scattering speed $v_{rel} \propto \sqrt{\frac{k_B T}{m_r}}$, we derive a rate $\Gamma = n_{th}\sigma v_{rel} \sim (m_B/m_r)^{3/2} k_B T/\hbar$ (*16*). Here, $\lambda_{B/rel}$ are the thermal de Broglie wavelengths at the boson and the reduced mass, respectively. At weaker interaction strengths

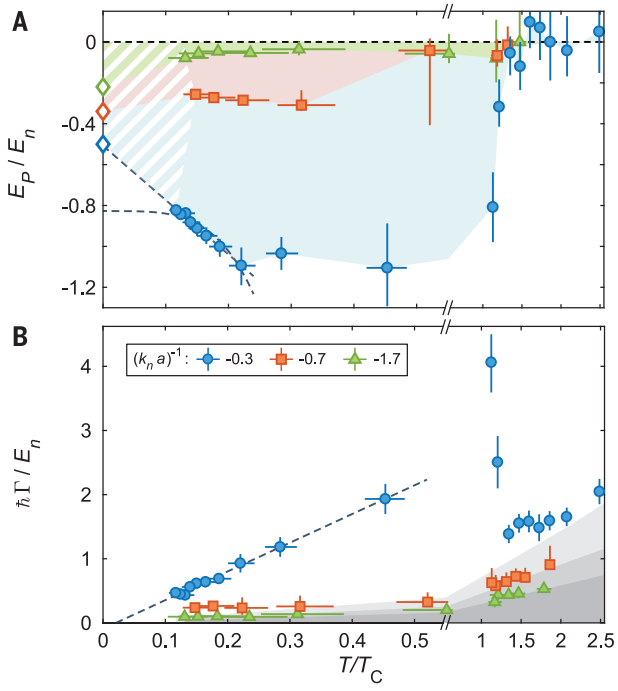

Fig. 3. Evolution of the Bose polaron as a function of the local reduced temperature T/T_C. Shown are the data for various peak interaction strengths $(k_n a)^{-1}$ (*16*). (**A**) Energy of the Bose polaron. The shaded areas are a guide to the eye, and the blue dashed lines represent linear and quartic extrapolations to zero temperature. The prediction of the lowest-order T-matrix calculation (*16*) is represented by open diamonds at $T = 0$. (**B**) The inverse lifetime of the Bose polaron, represented by the half-width at half-maximum (Γ) of the local rf spectra (*16*). The gray shaded areas indicate the spectral resolutions of the corresponding rf pulses. The dashed line is a linear fit to the data below T_C.

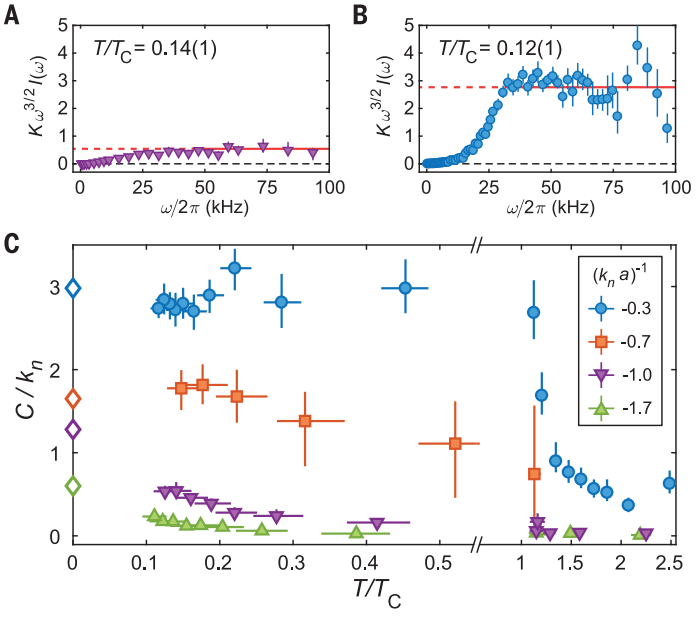

Fig. 4. Contact of the Bose polaron. The low-temperature rf transfer for (**A**) $(k_n a)^{-1} = -1$ and (**B**) $(k_n a)^{-1} = -0.3$ multiplied by $K\omega^{3/2}$, with $K = \frac{8\sqrt{2\pi m_r}}{\Omega_R^2 \sigma \sqrt{\hbar}} \frac{1}{k_n}$, displays a plateau that yields the normalized contact C/k_n. The contact is obtained from fits in the frequency region indicated by the solid red line. (**C**) The contact, normalized by k_n, as a function of the reduced temperature at various interaction strengths. The open diamonds at $T = 0$ are the T-matrix predictions from Eq. 3.

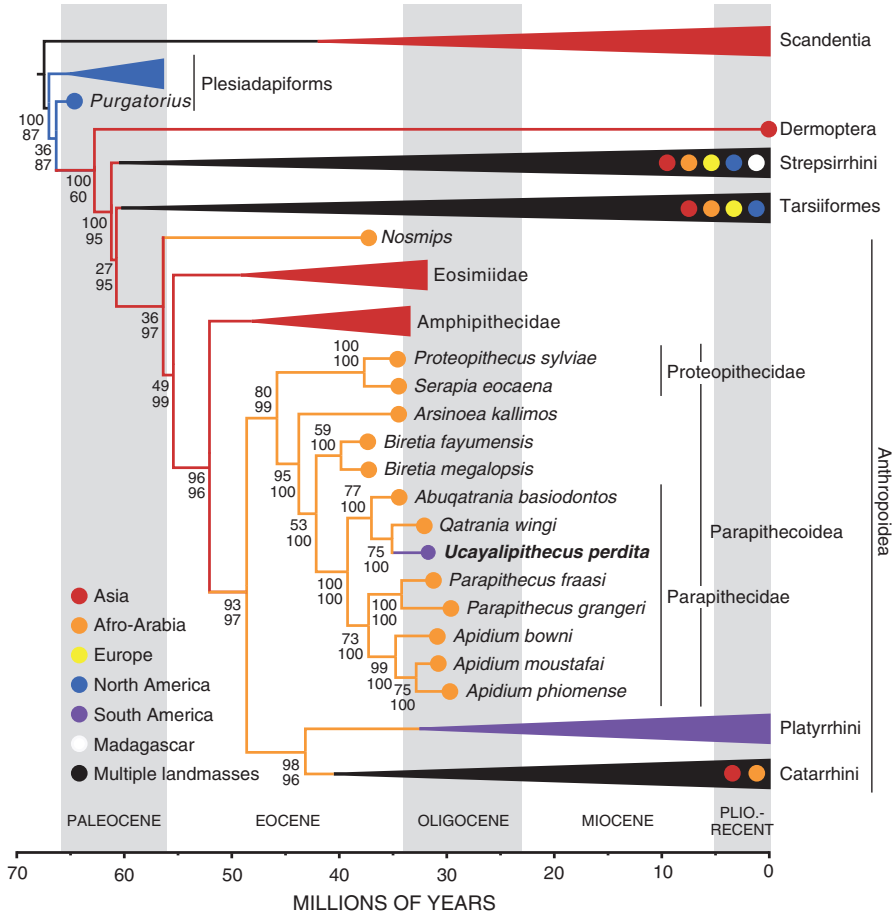

Fig. 2. Phylogenetic position and geographic origin of *Ucayalipithecus perdita*. "Allcompat" consensus tree derived from a Bayesian clock (or tip-dating) analysis of a combined molecular and morphological matrix in MrBayes 3.2.5, with major nonparapithecoid clades collapsed. Top number at each node is the posterior probability (×100) for each node on the basis of Bayesian clock analysis of the character matrix. Bottom number is the posterior probability of ancestral reconstructions of geography onto the allcompat tree (calculated in MrBayes). Multiple colored circles for a collapsed clade indicate that multiple geographic locations are present within that clade. Plio., Pliocene.

parapithecoids are stem anthropoids that have no relevance to either the phylogenetic or biogeographic origin of Platyrrhini (*14*, *21*). We tested an alternative hypothesis (which might be considered plausible based solely on biogeographic considerations) that *Ucayalipithecus* is not a parapithecid but rather a parapithecid-like stem platyrrhine by constraining *Ucayalipithecus* to form a clade with platyrrhines (including the bunodont late Oligocene stem platyrrhine *Branisella*) to the exclusion of parapithecids and estimating the ln marginal likelihoods of the primary and alternative hypotheses using stepping stone analyses of the morphological matrix in MrBayes. Comparison of estimated ln marginal likelihoods (constrained: −21,555.23; unconstrained: −21,524.55) yields a $2 \times \log_e$BF (BF, Bayes factor) test statistic of 61.36 and thus, based on the recommendations of (*22*), "very strong" evidence in favor of rejecting the alternative hypothesis that *Ucayalipithecus* is a stem platyrrhine. Bayesian ancestral reconstruction of continental geography onto the "allcompat" tree derived from the clock analysis unambiguously reconstructs an Afro-Arabian origin for the clade containing Parapithecoidea and crown Anthropoidea (PP = 0.97), as well as Parapithecoidea (PP = 0.99) and Parapithecidae (PP = 1.0), and therefore strongly supports independent dispersals of stem Platyrrhini and the *Ucayalipithecus* lineage from Afro-Arabia to South America.

We also tested the proposed upper Eocene age of the Santa Rosa locality in the clock analysis by placing a broad uniform prior on the tip age of *Ucayalipithecus*, from the beginning of the late Eocene to the end of the early Oligocene [37.8 to 28.1 million years ago (Ma)]. The resulting mean tip age for *Ucayalipithecus* was 31.7 Ma, about midway through the early Oligocene. A secondary clock analysis in which the single known tooth of *Perupithecus* was included, assigned the same broad age prior, and constrained to be a stem platyrrhine returned a mean tip age of 28.8 Ma for that taxon. Available evidence from the admittedly very limited sample of Santa Rosa anthropoids therefore supports a lower Oligocene, rather than an upper Eocene (*10*), age for the site. The divergence of *Ucayalipithecus* from its African sister taxon *Qatrania* is estimated to have occurred at 35.1 Ma (latest Eocene), suggesting that the transatlantic dispersal event that gave rise to the *Ucayalipithecus* lineage occurred between 35.1 and 31.7 Ma. Importantly, this interval includes the major eustatic drop in sea level that occurred in the earliest Oligocene (*23*), and our results leave open the possibility that dispersals of parapithecids and ancestral Platyrrhini to South America were broadly coincident with, and might have been facilitated by, this drop in sea level.

The discovery of a parapithecid stem anthropoid in the late Paleogene of Peruvian Amazonia is entirely unexpected and provides a notable example of how important paleontological information is for understanding the ephemeral forces that shaped modern biodiversity. Without these four tiny teeth recovered from an isolated outcrop deep in a remote part of the Amazon basin, it could not have been predicted that early stem platyrrhines of South America were living alongside, and competing for resources with, a phylogenetically independent anthropoid lineage. The fact that the Santa Rosa locality is more than 4000 km from the easternmost point of South America and far from any coastal area that could have served as the initial docking point for the ancestors of *Ucayalipithecus* after their transatlantic dispersal further suggests that parapithecids may have already been broadly distributed across equatorial South America by the time the fossils described here were deposited in Amazonian Perú. There is no reason to assume that platyrrhine competition with parapithecids in South America would have been trivial, as the arboreal (*24*) and largely frugivorous (*25*, *26*) parapithecoid relatives of *Ucayalipithecus* persisted in Africa alongside several other primate lineages for at least ~11.5 million years [from their first-appearance datum of ~37 Ma (*27*) to their last-appearance datum of 25.5 Ma (*28*)].

The recognition that both parapithecids and stem platyrrhines survived a transatlantic rafting event further reveals that these early anthropoid lineages were not only able to persist despite presumed water and food scarcity—thereby suggesting the existence of physiological adaptations that allowed them to successfully cope with a situation that mimicked strong seasonality (*3*)—but were able to immediately adjust their foraging behavior to the unfamiliar resources and phenological patterns that they encountered upon arrival in South America. This combined evidence from South American parapithecids and stem platyrrhines strongly suggests that early anthropoids must have been highly resilient to unpredictable environments and implies a degree of behavioral

flexibility that would have been an evolutionary advantage for Anthropoidea during the major environmental perturbations of the later Paleogene, including the global cooling event at the Eocene-Oligocene boundary.

REFERENCES AND NOTES

1. R. Hoffstetter, R. Lavocat, *C. R. Acad. Sci. (Paris)* **271**, 172–175 (1970).
2. J. G. Fleagle, *Primate Adaptation and Evolution* (Academic Press, ed. 3, 2013).
3. A. Houle, *Am. J. Phys. Anthropol.* **109**, 541–559 (1999).
4. J. G. Fleagle, C. C. Gilbert, in *Primate Biogeography: Progress and Prospects*, S. M. Lehman, J. G. Fleagle, Eds. (Springer, 2006), pp. 375–418.
5. M. F. Tejedor, thesis, Universidad Nacional de la Plata (2000).
6. M. Bond *et al.*, *Nature* **520**, 538–541 (2015).
7. P.-O. Antoine *et al.*, *Proc. Biol. Sci.* **279**, 1319–1326 (2012).
8. E. R. Seiffert *et al.*, *Hist. Biol.* **30**, 204–226 (2018).
9. K. E. Campbell Jr., *Nat. Hist. Mus. Los Angeles County Sci. Ser.* **40**, i–vi, 1–163 (2004).
10. M. Arnal, A. G. Kramarz, M. G. Vucetich, C. D. Frailey, K. E. Campbell Jr., *Pap. Palaeontol.* 10.1002/spp2.1264 (2019).
11. C. D. Frailey, K. E. Campbell Jr., *Nat. Hist. Mus. Los Angeles County Sci. Ser.* **40**, 71–130 (2004).
12. F. J. Goin, A. M. Candela, *Nat. Hist. Mus. Los Angeles County Sci. Ser.* **40**, 15–60 (2004).
13. E. L. Simons, R. F. Kay, *Nature* **304**, 624–626 (1983).
14. E. L. Simons, E. R. Seiffert, P. S. Chatrath, Y. Attia, *Folia Primatol.* **72**, 316–331 (2001).
15. K. C. Beard, P. M. C. Coster, *Am. J. Phys. Anthropol.* **159**, 714–721 (2016).
16. N. Egi, M. Takai, N. Shigehara, T. Tsubamoto, *Int. J. Primatol.* **25**, 211–236 (2004).
17. D. Silvestro *et al.*, *Syst. Biol.* **68**, 78–92 (2019).
18. G. F. Gunnell *et al.*, *Nat. Commun.* **9**, 3193 (2018).
19. F. Ronquist *et al.*, *Syst. Biol.* **61**, 539–542 (2012).
20. E. L. Simons, R. F. Kay, *Am. J. Primatol.* **15**, 337–347 (1988).
21. J. G. Fleagle, R. F. Kay, *J. Hum. Evol.* **16**, 483–532 (1987).
22. R. E. Kass, A. E. Raftery, *J. Am. Stat. Assoc.* **90**, 773–795 (1995).
23. K. G. Miller *et al.*, *Geol. Soc. Am. Bull.* **120**, 34–53 (2008).
24. J. G. Fleagle, E. L. Simons, *Am. J. Phys. Anthropol.* **97**, 235–289 (1995).
25. M. F. Teaford, M. C. Maas, E. L. Simons, *Am. J. Phys. Anthropol.* **101**, 527–543 (1996).
26. E. C. Kirk, E. L. Simons, *J. Hum. Evol.* **40**, 203–229 (2001).
27. E. R. Seiffert *et al.*, *Science* **310**, 300–304 (2005).
28. N. J. Stevens, E. R. Seiffert, E. M. Roberts, P. M. O'Connor, *Am. J. Phys. Anthropol.* **156** (suppl.), 296–297 (2015).
29. L. Marivaux *et al.*, *J. Hum. Evol.* **97**, 159–175 (2016).
30. J. I. Bloch *et al.*, *Nature* **533**, 243–246 (2016).
31. E. Seiffert *et al.*, A parapithecid stem anthropoid of African origin in the Paleogene of South America, Version 1, Dryad (2020); https://doi.org/10.5061/dryad.0vt4b8gtt.

ACKNOWLEDGMENTS

The Instituto Geológico, Minero, y Metalúrgico (INGEMMET), Lima, and particularly C. Chacaltana Budiel and L. Tejada Medina have facilitated and supported paleontological and geological work at the Santa Rosa locality since 1995. M. Vilca of INGEMMET and S. Hynek participated in fieldwork in 2016. Members of the Santa Rosa indigenous community assisted with fieldwork in 1998 and 2016. I. Mawhinney and M. Shazab helped to process the Santa Rosa matrix. T. Jashashvili scanned the *Ucayalipithecus* specimens. M.F.T. is a research associate at the Gothenburg Global Biodiversity Centre. **Funding:** J. Wigmore, W. Rhodes, and R. Seaver helped to fund the 1998 expedition that led to the recovery of the *Ucayalipithecus* partial upper molars. The Leakey Foundation, Gordon Getty, and A. Stenger supported fieldwork in 2016. Micro–computed tomography scanning was supported by the Keck School of Medicine of USC and the U.S. National Science Foundation (BCS-1231288). **Author contributions:** K.E.C. ran the Santa Rosa project. K.E.C. collected matrix from Santa Rosa in 1998. J.G.F., F.M.C., and K.E.C. collected matrix from Santa Rosa in 2016. M.F.T., N.M.N., and M.B. identified the upper molars of *Ucayalipithecus* in the collection from the 1998 field season. E.R.S. identified the lower molars of *Ucayalipithecus* in the collection from the 2016 field season. E.R.S., M.F.T., J.G.F., N.M.N., M.B., and K.E.C. analyzed the fossils. E.R.S. scored the taxa for phylogenetic analysis, ran the phylogenetic and biogeographic analyses, and created digital models. J.G.F., K.E.C., D.d.V., and E.R.S. picked the Santa Rosa matrix; D.d.V. created digital models. E.R.S. wrote the first draft and created the figures. All authors read and edited the paper. **Competing interests:** The authors declare no competing interests. **Data and materials availability:** Data used for the phylogenetic and biogeographic analyses are available for download on the Dryad Digital Repository (*31*). Digital surface models of the *Ucayalipithecus* specimens are available for download on MorphoSource (project 872). Fossils are deposited in the Colección Paleontológica del INGEMMET (CPI), Lima, Perú.

SUPPLEMENTARY MATERIALS

science.sciencemag.org/content/368/6487/194/suppl/DC1
Materials and Methods
Supplementary Text

5 November 2019; accepted 19 February 2020
10.1126/science.aba1135

NEUROSCIENCE

Dopaminylation of histone H3 in ventral tegmental area regulates cocaine seeking

Ashley E. Lepack[1], Craig T. Werner[2], Andrew F. Stewart[1], Sasha L. Fulton[1], Ping Zhong[3], Lorna A. Farrelly[1], Alexander C. W. Smith[1], Aarthi Ramakrishnan[1], Yang Lyu[1], Ryan M. Bastle[1], Jennifer A. Martin[2], Swarup Mitra[2], Richard M. O'Connor[1], Zi-Jun Wang[3], Henrik Molina[4], Gustavo Turecki[5], Li Shen[1], Zhen Yan[3], Erin S. Calipari[6], David M. Dietz[2], Paul J. Kenny[1], Ian Maze[1,7]*

Vulnerability to relapse during periods of attempted abstinence from cocaine use is hypothesized to result from the rewiring of brain reward circuitries, particularly ventral tegmental area (VTA) dopamine neurons. How cocaine exposures act on midbrain dopamine neurons to precipitate addiction-relevant changes in gene expression is unclear. We found that histone H3 glutamine 5 dopaminylation (H3Q5dop) plays a critical role in cocaine-induced transcriptional plasticity in the midbrain. Rats undergoing withdrawal from cocaine showed an accumulation of H3Q5dop in the VTA. By reducing H3Q5dop in the VTA during withdrawal, we reversed cocaine-mediated gene expression changes, attenuated dopamine release in the nucleus accumbens, and reduced cocaine-seeking behavior. These findings establish a neurotransmission-independent role for nuclear dopamine in relapse-related transcriptional plasticity in the VTA.

Cocaine increases dopamine neurotransmission from the ventral tegmental area (VTA) to reward-relevant brain regions. This action is central to its addictive properties. Non-neurotransmission roles for dopamine in cocaine dependency have not been considered. Our laboratory has recently described a role for serotonin (5-HT) in developing 5-HTergic neurons, whereby 5-HT located in the nucleus of these neurons was shown to covalently attach to histone proteins—specifically on H3 glutamine 5 (H3Q5)—to regulate gene expression through a process called serotonylation (*1*, *2*). We had hypothesized that this mechanism may generalize to other monoamines in brain, such as dopamine. If true, this process could potentially play a role in the addiction-relevant actions of drugs that stimulate dopaminergic transmission.

[1]Department of Neuroscience, Friedman Brain Institute, Icahn School of Medicine at Mount Sinai, New York, NY 10029, USA. [2]Department of Pharmacology and Toxicology, Program in Neuroscience, State University of New York at Buffalo, Buffalo, NY 14214, USA. [3]Department of Physiology and Biophysics, Jacobs School of Medicine and Biomedical Sciences, State University of New York at Buffalo, Buffalo, NY 14203, USA. [4]Proteomics Resource Center, The Rockefeller University, New York, NY 10065, USA. [5]Department of Psychiatry, McGill University, Montreal, QC H3A 1A1, Canada. [6]Department of Pharmacology, Center for Addiction Research, Vanderbilt University School of Medicine, Nashville, TN 37232, USA. [7]Department of Pharmacological Sciences, Icahn School of Medicine at Mount Sinai, New York, NY 10029, USA.
***Corresponding author. Email: ian.maze@mssm.edu**

Drug addictions are defined by pathological drug-seeking behavior that persists despite adverse consequences. Prolonged vulnerability to relapse is hypothesized to reflect the functional rewiring of brain reward circuitries (*3*, *4*). This is precipitated, at least in part, by drug-induced transcriptional plasticity in midbrain dopamine neurons (*5*, *6*). Histone mechanisms that control chromatin structures, and consequently gene expression, regulate addiction-relevant behaviors (*7*, *8*). Given that histone H3 can be modified by monoamines in response to fluctuations in intracellular availability, we assessed whether dopamine, like 5-HT, can be transferred to the H3 N-terminal tail. We performed targeted, peptide-based liquid chromatography–tandem mass spectrometry (LC-MS/MS) after in vitro transglutaminase 2 (TGM2) (*1*, *2*, *9*) enzymatic assays with dopamine. Peptide LC-MS/MS analyses (fig. S1, A to D) revealed Q5 as a reactive substrate for the dopaminyl mark [H3 glutamine 5 dopaminylation (H3Q5dop)]. Given that the serotonyl modification can exist both in isolation (H3Q5ser) and in combination with H3 lysine 4 trimethylation (H3K4me3Q5ser), we examined the effect of K4me3 on TGM2-mediated dopaminylation in vitro. Unmodified versus methylated mononucleosomes were subjected to TGM2 dopaminylation assays. Using an antibody against H3Q5dop, vide infra, we found that TGM2 equally dopaminylates unmodified and K4me3

substrates (fig. S2), which suggests that both modifications may occur in vivo.

To assess roles for H3 dopaminylation in the context of adult neuronal plasticity, we raised and fully validated single (H3Q5dop) and dual (H3K4me3Q5dop) modification-specific antibodies (fig. S3, A to J). We examined whether dopaminyl modifications in the adult brain are modulated by clinically relevant levels of drug exposure. We assessed the expression of these modifications in postmortem human brain tissues obtained from cocaine-dependent individuals compared with matched controls. We focused our investigations on the VTA, the origin of many of the dopaminergic projection neurons that compose the mesocorticolimbic dopamine system (*10*, *11*). H3Q5dop, but not H3K4me3Q5dop, was significantly reduced in its expression in the VTAs of cocaine users; H3K4me3, total H3, and Tgm2 were unchanged in their relative levels of expression (Fig. 1A and fig. S5A). However, nearly all of the cocaine users examined in this study displayed pronounced peripheral concentrations of cocaine metabolites at time of death, which may conflate the acute pharmacological actions of cocaine with long-term adaptive responses to the drug.

Therefore, we employed intravenous cocaine self-administration in rats, a well-established procedure to study drug abuse (*12*, *13*), to further explore potential contributions of H3Q5dop to addiction-relevant behaviors. Animals were trained to self-administer cocaine (or saline) under a fixed-ratio 5 schedule of reinforcement (see materials and methods for details). After training, independent cohorts of animals were allocated to two drug treatment groups (as were the respective saline controls): extended access (6-hour sessions) or restricted access (1-hour sessions) (Fig. 1B and fig. S4A). Animals with extended access to self-administration, but not those with restricted access, demonstrate a gradual escalation of intake across sessions (Fig. 1C and fig. S4A) (*12*, *14*, *15*). After 10 days of self-administration, VTA tissues were collected at three different time points: 0, 1, or 30 days. Global levels of H3Q5dop were significantly down-regulated in the VTAs of animals with extended access to cocaine at day 0 (Fig. 1D and fig. S5B), a time point that most appropriately mimics our human subject conditions, in that cocaine is still present at time of death. This reduction was transient, as H3Q5dop levels steadily increased over the course of the next 30 days (Fig. 1D and fig. S5B). By contrast, no changes in VTA H3Q5dop were observed in rats with restricted access to cocaine after 30 days of withdrawal (fig. S4B). Alterations in H3K4me3Q5dop, H3K4me3, total H3, or Tgm2 expression were not observed in animals with either extended or restricted access to cocaine compared with their controls (Fig. 1D, fig. S4B, and fig. S5, C to F). Finally, we assessed levels of the marks in VTA tissues at 30 days of withdrawal in animals receiving cocaine passively—either by being yoked to extended-access rats (fig. S4C and fig. S5G) or through experimenter-administered (intraperitoneal) injections (fig. S4D and fig. S5H)—and in animals trained to self-administer food under extended-access conditions (fig. S4E and fig. S5I). In all three cases, levels of H3Q5dop, along with expression of H3K4me3Q5dop, H3K4me3, total H3, and Tgm2, remained unaffected.

To explore the functional consequences of H3Q5dop during withdrawal, we delivered a virus vector into the VTA that expresses the H3 variant, H3.3—containing a glutamine-to-alanine substitution at position 5 on its N-terminal tail—which let us compare H3.3Q5A with H3.3 wild-type (WT) and empty vector controls (*1*). The H3.3Q5A vector expressed effectively in a nuclear-specific manner in adult neurons (Fig. 2A), leading to significant down-regulation of H3Q5dop (Fig. 2B). This reduced the expression of the mark in a dominant-negative fashion without our needing to manipulate the activity of Tgm2, an enzyme with diverse functions in the brain that are independent from its histone transamidase activity. H3K4me3Q5dop expression was unaffected by H3.3Q5A delivery. We explored the impact of attenuating H3Q5dop accumulation in the VTA on drug-induced transcriptional programs that may be responsible for cocaine seeking after prolonged withdrawal. After chronic cocaine versus saline self-administration, rats were infected, intra-VTA, with one of the three viruses, followed by a 30-day period of enforced abstinence (Fig. 2C). After withdrawal, infected

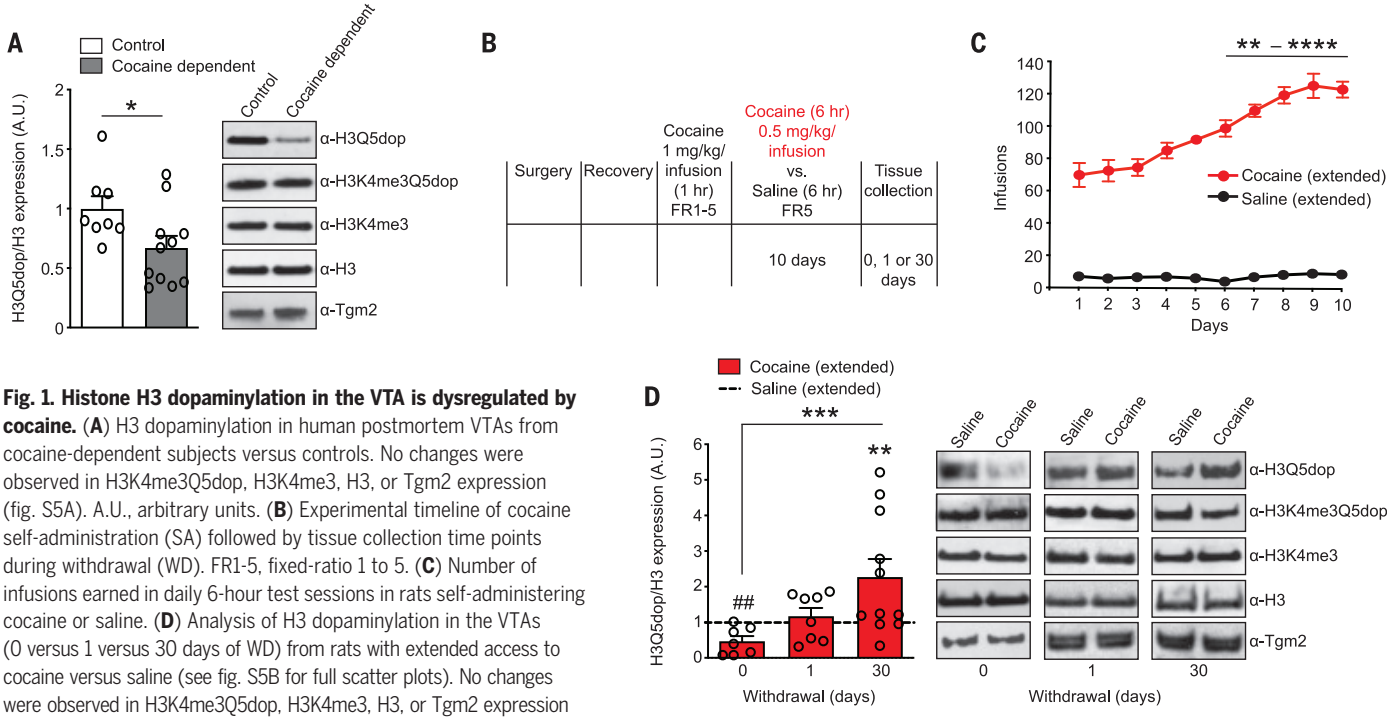

Fig. 1. Histone H3 dopaminylation in the VTA is dysregulated by cocaine. (**A**) H3 dopaminylation in human postmortem VTAs from cocaine-dependent subjects versus controls. No changes were observed in H3K4me3Q5dop, H3K4me3, H3, or Tgm2 expression (fig. S5A). A.U., arbitrary units. (**B**) Experimental timeline of cocaine self-administration (SA) followed by tissue collection time points during withdrawal (WD). FR1-5, fixed-ratio 1 to 5. (**C**) Number of infusions earned in daily 6-hour test sessions in rats self-administering cocaine or saline. (**D**) Analysis of H3 dopaminylation in the VTAs (0 versus 1 versus 30 days of WD) from rats with extended access to cocaine versus saline (see fig. S5B for full scatter plots). No changes were observed in H3K4me3Q5dop, H3K4me3, H3, or Tgm2 expression (fig. S5, C to E). Data presented as averages ± SEM. See supplementary materials for full figure legends with statistical comparisons.

VTA tissues were microdissected and processed for RNA sequencing (RNA-seq) (fig. S6, A and B). We first used a threshold-free rank-rank hypergeometric overlap test (RRHO) to assess the patterns and significance of the overlap (Fig. 2D) between differential (cocaine versus saline) gene expression profiles observed after infection with our viral control vectors (H3.3 WT versus empty). The effect of cocaine self-administration on gene expression significantly overlapped between the two groups, which indicates that viral H3.3 WT expression does not affect cocaine-mediated gene expression profiles (Fig. 2E, left panel). We then compared differential gene expression profiles after infection—with either empty (Fig. 2E, middle panel) or H3.3 WT viruses (Fig. 2E, right panel)—with H3.3Q5A-infected VTA after cocaine self-administration. In both cases, attenuating H3Q5dop expression resulted in significant reversals of cocaine-mediated gene expression. Pairwise comparisons were used to identify specific genes displaying dysregulated expression between cocaine versus saline animals (empty or H3.3 WT). Then, overlay assessments were performed to align these sets of genes with those that are also regulated in cocaine self-administering animals expressing H3.3Q5A versus empty [Fig. 2F and tables S1 and S2; 720 differentially expressed protein coding genes (PCGs) were found to overlap] or H3.3 WT (Fig. 2G and tables S3 and S4; 211 differentially expressed PCGs were found to overlap) viruses. Further evaluation of these overlapping PCGs found that ~95 to 87% were significantly rescued in their expression with

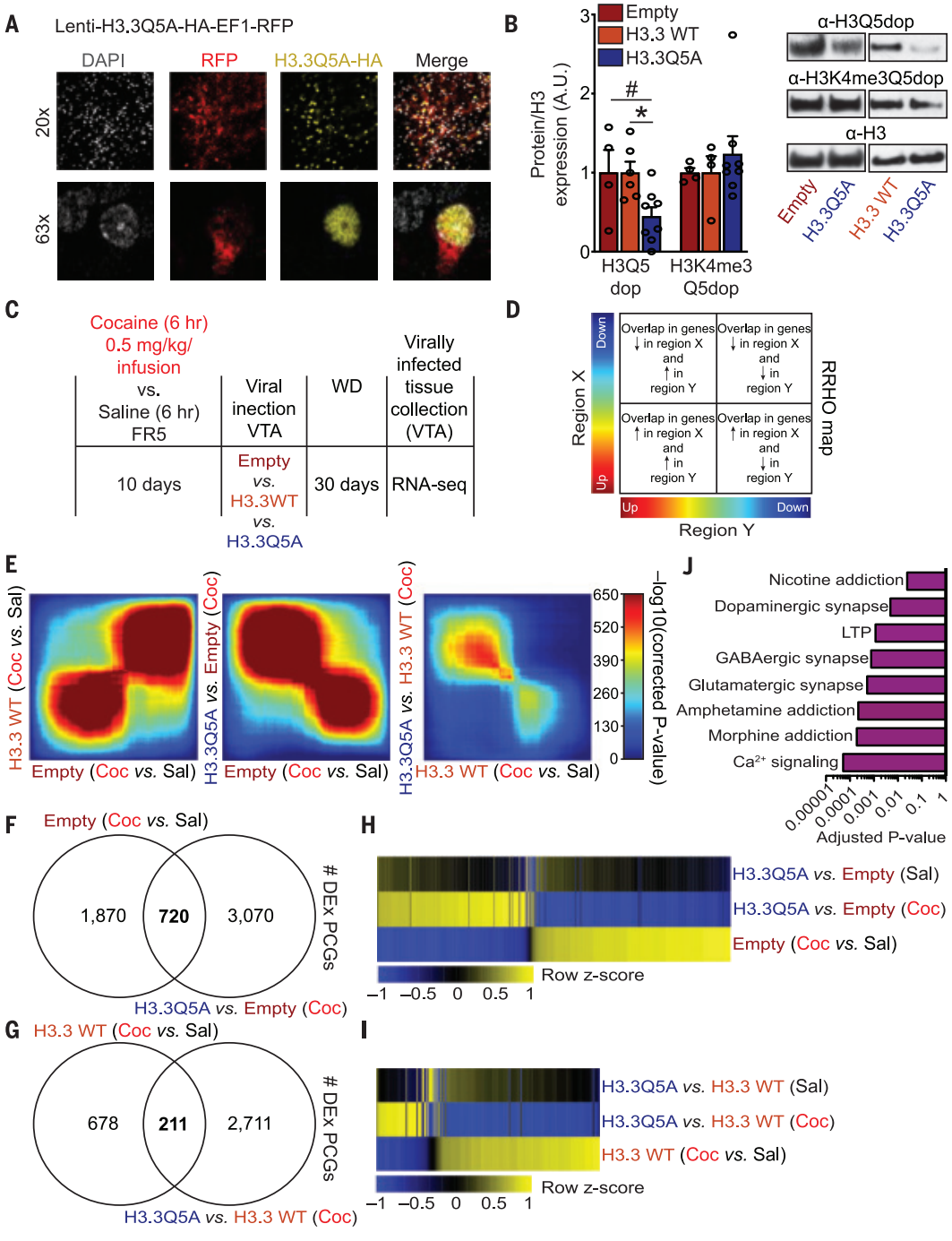

Fig. 2. H3Q5dop in the VTA contributes to cocaine-mediated gene expression. (**A**) VTA transduced with a lentivirus expressing H3.3Q5A-HA-EF1-RFP (red fluorescent protein) overlayed with a nuclear co-stain [4′,6-diamidino-2-phenylindole (DAPI)]. (**B**) H3 dopaminylation in VTAs infected with lentiviral vectors. (**C**) Experimental timeline of self-administration RNA-seq experiment after viral transduction. (**D**) RRHO map key describing the extent and directionality of overlap between differential gene expression. (**E**) RRHO comparing differential expression between cocaine-regulated genes. Each pixel represents the overlap between differential transcriptomes, with the significance of overlap of a hypergeometric test color-coded. Coc, cocaine; Sal, saline. (**F** and **G**) Overlap of differentially expressed (DEx) PCGs in VTA tissues comparing cocaine versus saline (empty) (F) or cocaine versus saline (H3.3 WT) (G) to H3.3Q5A versus empty or H3.3 WT (cocaine) animals, respectively. (**H** and **I**) Heat maps of overlapping genes obtained from RNA-seq data comparing cocaine versus saline (empty) and H3.3Q5A versus empty (cocaine) animals (H) or cocaine versus saline (H3.3 WT) and H3.3Q5A versus H3.3 WT (cocaine) animals (I) using normalized RNA expression values. (**J**) KEGG 2019 pathway enrichment analysis for the 211 overlapping PCGs displaying reversals in cocaine-mediated gene expression from (G) and (I). LTP, long-term potentiation. Data presented as averages ± SEM.

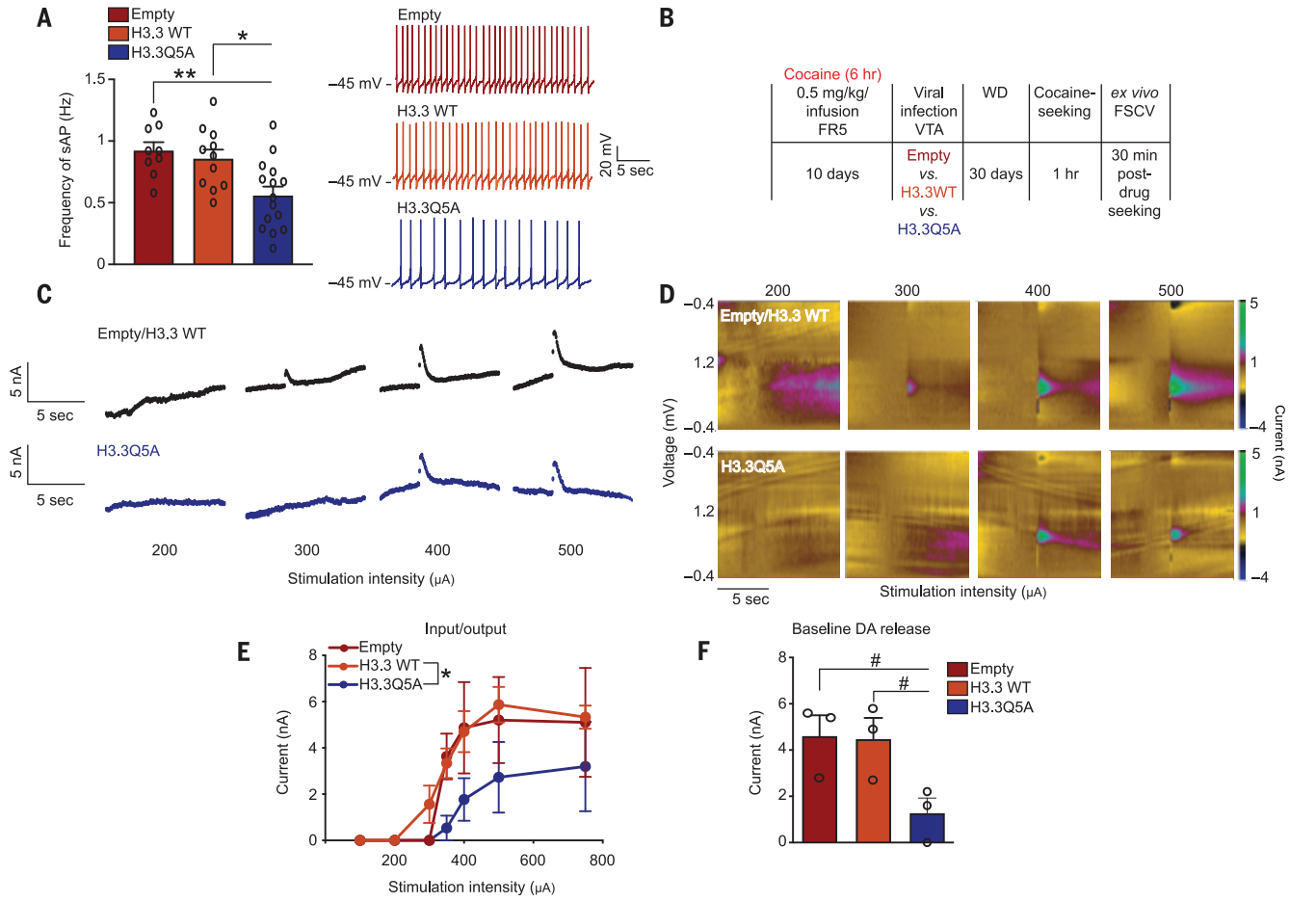

Fig. 3. Attenuating H3Q5dop expression in the VTA after extended access to cocaine reduces dopamine release in the ventral striatum. (**A**) Frequency of sAPs in VTA dopaminergic neurons from cocaine-naïve rats infected with empty vector, H3.3 WT, or H3.3Q5A. Representative sAP traces are provided. (**B**) Experimental timeline of cocaine SA FSCV experiments after viral transduction and 1 hour of cocaine seeking. (**C** to **E**) Current versus time traces (C) and color plots (D) demonstrating reduced dopamine release (evoked) in the NAc of H3.3Q5A versus empty and H3.3 WT (VTA) expressing animals. Quantified as input-output curves (E) (current versus stimulation intensity). (**F**) Baseline dopamine (DA) release into the NAc was similarly reduced by H3.3Q5A. Data presented as averages ± SEM.

H3.3Q5A delivery; H3.3Q5A expression in saline self-administering animals had little to no impact on the expression of overlapping genes (Fig. 2, H and I). Gene enrichment analysis [Human Kyoto Encyclopedia of Genes and Genomes (KEGG) 2019] indicated strong associations with pathways involved in the regulation of synaptic function and drug addiction (Fig. 2J and table S5). These findings suggest that H3Q5 dopaminylation plays an important role in cocaine-induced transcriptional plasticity in the VTA.

Next, we examined the effect of H3Q5dop on dopaminergic neuronal activity. Cocaine-naïve rats were injected intra-VTA with viruses expressing empty vector or H3.3 WT controls versus H3.3Q5A. We recorded spontaneous action potentials (sAPs) from infected dopaminergic neurons expressing hyperpolarization-activated currents (Fig. 3A). Attenuation of H3Q5dop significantly reduced the frequency of sAPs arising from dopaminergic neurons.

To more directly assess the impact that blocking H3Q5dop during cocaine withdrawal has on dopamine release into the nucleus accumbens (NAc), rats were allowed to self-administer cocaine under extended-access conditions and were infected intra-VTA with one of the three viruses. After 30 days of withdrawal and cue-induced cocaine seeking, ex vivo assessments of dopamine release using fast-scanning cyclic voltammetry (FSCV) were performed (Fig. 3B). Stimulation-induced dopamine release into the NAc was significantly attenuated (Fig. 3, C to F) in response to reductions in H3Q5dop accumulation.

To investigate what consequences modifying H3Q5dop levels has on relapse-relevant behaviors, we allowed an independent cohort of animals to self-administer cocaine under extended-access conditions followed by intra-VTA viral manipulations. After withdrawal, rats were returned to a drug-paired context, and cocaine seeking was assessed (Fig. 4A). Preventing H3Q5dop accumulation in animals with extended access significantly reduced their drug-seeking behavior (Fig. 4, B and C). Reducing H3Q5dop levels in the VTAs of a separate cohort of animals with restricted access did not affect their drug-seeking behavior (fig. S7, A to C). To ensure that such manipulations do not impair motivation to seek natural rewards, additional rats were trained to respond for food rewards under the same extended-access schedule of reinforcement, followed by viral manipulations, 30 days of ad libitum feeding, and subsequent reward seeking (fig. S8A). Food-seeking responses remained unaffected by manipulations of H3Q5dop (fig. S8, B and C). Given the fact that chronic cocaine use can elicit numerous additional behavioral abnormalities, we performed intra-VTA viral manipulations in cocaine-naïve rats, followed by assessments of psychomotor sensitization in response to repeated experimenter-administered cocaine.

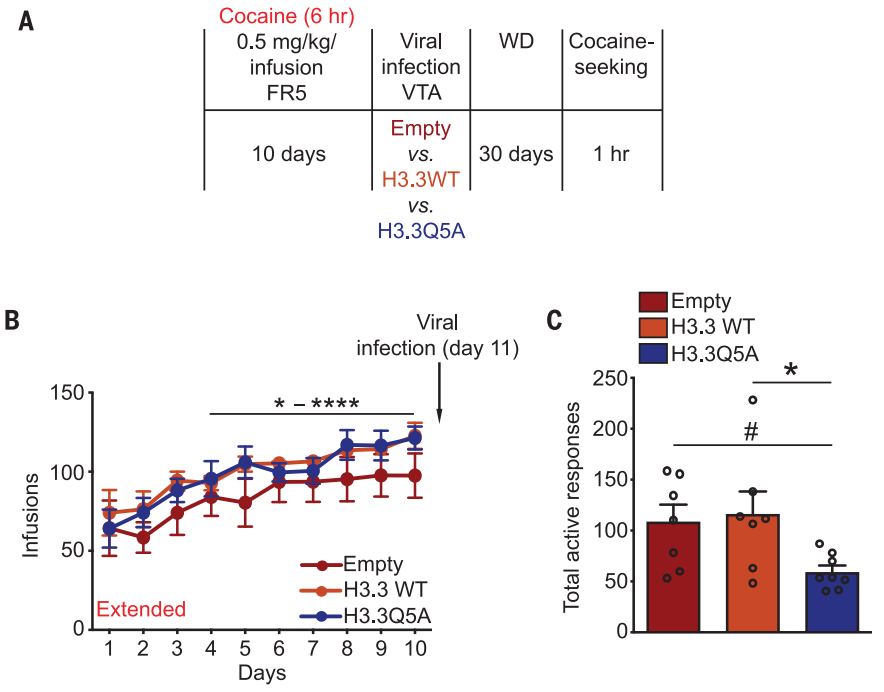

Fig. 4. Reducing H3Q5dop in the VTA attenuates cocaine seeking. (**A**) Experimental timeline of cocaine SA drug-seeking experiments after viral transduction. (**B** and **C**) After 10 days of extended access to cocaine, rats were infected intra-VTA with one of the three viral vectors (on day 11) (B), followed by 30 days of WD and 1 hour of cocaine seeking (C). Data presented as averages ± SEM.

Both control (H3.3 WT) and knockdown (H3.3Q5A) animals displayed similar levels of cocaine-induced locomotor sensitization (fig. S8, D and E).

We demonstrated that a previously uncharacterized chromatin modification, histone dopaminylation, is critically involved in regulating aberrant neuronal gene expression patterns in the VTA in response to cocaine consumption. The increased expression of H3Q5dop that follows prolonged withdrawal from extended, but not restricted, access to cocaine self-administration regulates relapse-like behaviors. It does so, in part, through the dysregulated transcription of addiction- and synaptic plasticity–related genes in the VTA, as well as through aberrant dopamine release dynamics in the NAc after cocaine withdrawal (fig. S9, model). Gaining a better understanding of the mechanistic roles for H3Q5dop in mediating permissive compared with repressive transcription, as well as the genes regulated through this mechanism, will greatly improve our knowledge of the molecular underpinnings of drug addiction.

REFERENCES AND NOTES

1. L. A. Farrelly *et al.*, *Nature* **567**, 535–539 (2019).
2. D. J. Walther *et al.*, *Cell* **115**, 851–862 (2003).
3. J. W. Grimm, B. T. Hope, R. A. Wise, Y. Shaham, *Nature* **412**, 141–142 (2001).
4. K. L. Conrad *et al.*, *Nature* **454**, 118–121 (2008).
5. C. L. Pickens *et al.*, *Trends Neurosci.* **34**, 411–420 (2011).
6. J. W. Grimm *et al.*, *J. Neurosci.* **23**, 742–747 (2003).
7. I. Maze, E. J. Nestler, *Ann. N. Y. Acad. Sci.* **1216**, 99–113 (2011).
8. H. D. Schmidt, J. F. McGinty, A. E. West, G. Sadri-Vakili, *Cold Spring Harb. Perspect. Med.* **3**, a012047 (2013).
9. R. Hummerich, J. O. Thumfart, P. Findeisen, D. Bartsch, P. Schloss, *FEBS Lett.* **586**, 3421–3428 (2012).
10. S. Cooper, A. J. Robison, M. S. Mazei-Robison, *Neurotherapeutics* **14**, 687–697 (2017).
11. R. A. Wheeler, R. M. Carelli, *Neuropharmacology* **56**, 149–159 (2009).
12. S. H. Ahmed, G. F. Koob, *Science* **282**, 298–300 (1998).
13. U. Shalev, J. W. Grimm, Y. Shaham, *Pharmacol. Rev.* **54**, 1–42 (2002).
14. H. M. Lesscher, L. J. Vanderschuren, *Rev. Neurosci.* **23**, 731–745 (2012).
15. V. Deroche-Gamonet, P. V. Piazza, *Neuropharmacology* **76**, 437–449 (2014).

ACKNOWLEDGMENTS

We would like to thank T. Muir and R. Thompson (Princeton Univ.) for generating dopaminylated peptides for use in antibody generation. We would also like to thank A. G. DiFeliceantonio (Virginia Tech) for providing supporting code for yoked cocaine experiments, K. Brennand and S. Powell (ISMMS) for providing hPSC-derived dopaminergic neurons for use in antibody control experiments, and A. Soshnev (Rockefeller Univ.) for help with illustrations. The NIDA Drug Supply Program generously gifted the cocaine used in these studies. **Funding:** This work was supported by grants from the National Institutes of Health [DP1 DA042078 (I.M.), R21 DA044767 (I.M.), P50 MH096890 (I.M.), R01 DA025983 (P.J.K.), R01 MH108842 (Z.Y.), R01 DA037257 (D.M.D.), R21 DA044486 (D.M.D.), F99 NS108543 (J.A.M.), R00 DA042111 (E.S.C.), and F31 DA045428 (A.E.L.)] as well as the MQ Mental Health Research Charity [MQ15FIP100011 (I.M.)], Alfred P. Sloan Foundation Fellowship in Neuroscience (I.M.), Brain Research Foundation's Fay/Frank Seed Grant Award (I.M.), Brain and Behavior Research Foundation (E.S.C. and A.C.W.S.), Whitehall Foundation (E.S.C.), and Edward Mallinckrodt, Jr. Foundation (E.S.C.). **Author contributions:** I.M. conceived of the project with input from A.E.L., D.M.D., and P.J.K. A.E.L., C.T.W., A.F.S., S.L.F., P.Z., L.A.F., A.C.W.S., Y.L., R.M.B., J.A.M., S.M., R.M.O., Z.-J.W., H.M., Z.Y., E.S.C., D.M.D., P.J.K., and I.M. designed the experiments and interpreted the data. A.R. and L.S. performed the sequencing-based bioinformatics with input from A.E.L. and I.M. G.T. provided human postmortem tissues. A.E.L., P.J.K., and I.M. wrote the manuscript. **Competing interests:** P.J.K. is a cofounder of Eolas Therapeutics, Inc. The remaining authors declare no competing interests, financial or otherwise. **Data and materials availability:** Data from RNA-seq experiments have been deposited in the National Center for Biotechnology Information Gene Expression Omnibus database under accession number GSE124055. We declare that the data supporting findings for this study are available within the article and supplementary materials. No restrictions on data availability apply.

SUPPLEMENTARY MATERIALS

science.sciencemag.org/content/368/6487/197/suppl/DC1
Materials and Methods
Extended Captions for Figs. 1 to 4
Figs. S1 to S9
Tables S1 to S5
References (*16*–*30*)

1 February 2019; accepted 14 February 2020
10.1126/science.aaw8806

RNA-Seq Library Prep Kit
The SEQuoia Complete Stranded RNA Library Prep Kit overcomes common challenges often experienced with traditional RNA-Seq library preparation kits. Using the kit, scientists can capture the complete transcriptome, including short [<200 base pairs (bp)] and long (>200 bp) RNAs, in a single library prep. This innovative approach is compatible with a broad range of sample inputs from a variety of sample types, including fresh-frozen, formalin-fixed paraffin-embedded, and liquid biopsy specimens, generating complementary DNA libraries suitable for strand-specific NGS on Illumina sequencers in less than 4 h. The kit includes access to the integrated SeqSense Analysis Solution and Toolkit software packages.
Bio-Rad Laboratories
For info: 800-424-6723
www.bio-rad.com/sequoia-complete

Circulating Cell-Free DNA Isolation Kit
AMS Biotechnology has expanded its range of cfPure Cell-Free DNA Purification Kits. These kits use silica-coated paramagnetic particles to purify circulating cell-free DNA (cfDNA) from <1 mL to >10 mL of serum or plasma. Its buffers were developed to ensure efficient recovery of 100 base pairs (bp)–500 bp DNA fragments in order to maximize recovery of cfDNA that can be used for a wide range of downstream applications, such as bisulfite sequencing, NGS, and quantitative PCR. The cfPure protocol is quick and easy, allowing users to process several samples in 1 h or less and making it ideal for biomarker screening. Designed for scalability, cfPure kits let you use just the number of beads and amount of reagent you need for your cfDNA extraction.
AMS Biotechnology
For info: 800-987-0985
www.amsbio.com/circulating-cell-free-dna.aspx

Next-Generation Sequencing Panel
Oxford Gene Technology introduces SureSeq CLL + CNV Panel—the company's latest high-quality, next-generation sequencing (NGS) offering for research into chronic lymphocytic leukemia (CLL). The panel fulfills the desire for reliable copy number variation (CNV) detection by NGS, including trisomy 12 and loss of heterozygosity (LOH) as well as somatic variants, even at low allele frequency. It has been tested to show excellent concordance with array data, can detect both small and large CNVs at 10% minor allele frequency (MAF), single-nucleotide variants, indels down to 1% MAF, and LOH at 5 megabases (Mb)–10 Mb. This comprehensive panel covers all the most up-to-date, evidence-based genes and genomic aberrations for CLL and will enable laboratories to simplify their laboratory workflow by replacing multiple assays with a single assay.
Oxford Gene Technology
For info: 914-467-5285
www.ogt.com/cll

RNA Sequencing and Data Analysis Services
Biogazelle offers HTPathwaySeq and HTTargetSeq, two novel, cost-effective, high-throughput RNA sequencing and data analysis services. HTPathwaySeq generates in-depth information on drug mode of action, highlights molecular similarities between compounds, and reveals potential compound-induced toxicities. It provides critical data for candidate prioritization for further drug development. HTTargetSeq supports development of RNA targeting oligonucleotides, such as short interfering RNAs and antisense oligonucleotides. HTTargetSeq addresses a key challenge in oligonucleotide drug development—accurate off-target gene identification—important for anticipation of safety issues as well as potential repurposing of off-target genes as novel therapeutic targets. Both HTPathwaySeq and HTTargetSeq are performed directly on cell lysates from 96-well culture plates. A typical experiment assesses 94 conditions plus internal controls in quadruplicate (384 samples). To facilitate data interpretation, results are shared through Savanna, Biogazelle's proprietary visualization app.
Biogazelle
For info: +32-9-245-96-43
services.biogazelle.com

Self-Delivering siRNA
Accell siRNA delivers short interfering RNA (siRNA) into difficult-to-transfect cells without additional reagents, virus, or instruments. Achieve guaranteed gene silencing in cells that have until now been beyond the reach of conventional RNA interference methods due to toxicity from transfection reagents, electroporation, or undesirable viral responses. Novel, patented siRNA modifications facilitate passive uptake, protection against nuclease degradation, specificity, and knockdown efficiency. Low toxicity enables extended-duration silencing from multiple doses—up to 30 days! Accell siRNA has proven performance in difficult-to-transfect cell types, such as immunological cells (Jurkat cells, primary T cells, lymphocytes, peripheral blood mononuclear cells, macrophages); neuronal cells (primary neurons, glioma cells, organotypic brain slices); primary cells (fibroblasts, cardiomyocytes, β-islet cells); and in vivo models [brain delivery, dermal (skin) delivery, periodontal model].
Horizon Discovery
For info: 800-235-9880
horizondiscovery.com

Custom Plasmid Construction
Ever design a great study only to have to spend a month or more making the constructs you need—a month that could have been better spent writing your next grant or collecting more data? System Biosciences' Syn2Clone Custom Construct Service is your opportunity to increase efficiency and get those other projects done. With Syn2Clone, you can simply select any of our backbone vectors—such as our lentivectors, PiggyBac constructs, minicircles, and more—and send us the sequence you want inserted. We will synthesize the DNA and insert it into your vector. It's fast (custom gene synthesis and subcloning in as little as two weeks), reliable, highly affordable, and guaranteed.
System Biosciences
For info: 888-266-5066
systembio.com/services/syn2clone-custom-constructs

Electronically submit your new product description or product literature information! Go to www.sciencemag.org/about/new-products-section for more information.

Newly offered instrumentation, apparatus, and laboratory materials of interest to researchers in all disciplines in academic, industrial, and governmental organizations are featured in this space. Emphasis is given to purpose, chief characteristics, and availability of products and materials. Endorsement by *Science* or AAAS of any products or materials mentioned is not implied. Additional information may be obtained from the manufacturer or supplier.

GEORGIA CANCER CENTER
AUGUSTA UNIVERSITY

The Georgia Cancer Center at Augusta University invites applications for the position of **Leader of the Cancer Immunology, Inflammation and Tolerance Program** from interested individuals with expertise in one of these areas. The Georgia Cancer Center has been undergoing an unprecedented expansion in its basic and population sciences programs as part of an initiative to achieve designation as an NCI Cancer Center. This leadership position will complement and build on research in the Program focused on the study of the tumor microenvironment, understanding the inflammatory and immunologic pathways that promote cancer growth and promote local immune tolerance, and developing immunological cancer treatment strategies. The Program supports a highly active program of clinical immunotherapy trials.

Applicants must have active extramural research funding from NCI and other similar sources, a strong track record of independent research and, preferably, the experience of working in an NCI designated Cancer Center. Successful applicants will join a collaborative Program that works closely to promote translational research with the clinical research oncologists. Candidates should have documented scholarly activities and achievements that qualify them for the rank of Full Professor and may qualify for and Endowed Chair.

A competitive salary and start-up package, commensurate with experience and academic qualifications is available. A summary of research interests, curriculum vitae and names of three references should be sent to Scott Dunlap at scdunlap@augusta.edu. Informal inquiries can be made to Dr. Esteban Celis at **ecelis@augusta.edu**. Applications will be reviewed until the positions are filled.

www.augusta.edu/cancer

Augusta University is an Equal Opportunity Affirmative Action, and Equal Access Employer. Augusta University has a strong interest in promoting diversity in its faculty and women and minority candidates are encouraged to apply.

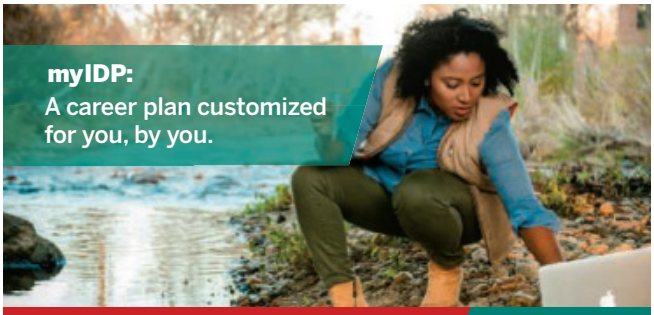

For your career in science, there's only one Science

Features in myIDP include:

- Exercises to help you examine your skills, interests, and values.
- A list of 20 scientific career paths with a prediction of which ones best fit your skills and interests.

myIDP Visit the website and start planning today!
myIDP.sciencecareers.org

ScienceCareers In partnership with:

FASEB Federation of American Societies for Experimental Biology
University of Massachusetts Medical School UMASS
UCSF University of California San Francisco
UIC
BURROUGHS WELLCOME FUND

RUTGERS
Cancer Institute of New Jersey
RUTGERS HEALTH

CO-DIRECTOR, CENTER OF EXCELLENCE FOR CANCER IMMUNOLOGY AND METABOLISM LEADERSHIP FACULTY POSITION

Rutgers Cancer Institute of New Jersey, a National Cancer Institute (NCI) Designated Comprehensive Cancer Center, seeks nominations or applications from leading scholars for the position of co-Director for the newly established Center of Excellence for Cancer Immunology and Metabolism. Working jointly with co-Director Dr. Eileen White, the Directors will be provided significant resources and additional faculty appointments that will build on existing strengths in both cancer metabolism and immunological research and its clinical translation.

The Center of Excellence for Cancer Immunology and Metabolism is a newly established center within the NCI-designated Rutgers Cancer Institute, designed to build on the strength of metabolism research to elaborate its role in regulating the immune response against cancer to develop novel approaches to cancer therapy.

Rutgers Cancer Institute is the consortium cancer center for Rutgers and Princeton Universities and the only NCI-designated Comprehensive Cancer Center in New Jersey. We are a leader in basic, clinical, prevention, and public health science, offering world-class quality cancer care providing the most advanced medicines and treatment options for patients in our network across the state. We are easily accessible to Manhattan, Newark Airport, and Philadelphia. Visit our website at www.cinj.org.

Qualified candidates must have a PhD, MD, or MD/PhD and outstanding academic credentials including a sustained record of peer reviewed funding and publications in cancer immunology and/or metabolism. Rank and tenure will be commensurate with experience. Academic appointment will be within the Rutgers Robert Wood Johnson Medical School. Initial inquiries will be treated as confidential.

To apply, please visit:
http://jobs.rutgers.edu/postings/112186

For further information, please contact: Larissa Varela, Rutgers Cancer Institute Faculty Recruitment & Affairs **(facultyaffairs@cinj.rutgers.edu).**

Rutgers, The State University of New Jersey, is an Equal Opportunity/ Affirmative Aon employer, and is compliant with the Americans with Disability Act (ADA). For more information please visit http://recruitment.rutgers.edu/ TheRUCommitment.htm. Women and minorities are encouraged to apply.

ScienceCareers online @sciencecareers.org

SPECIAL JOB FOCUS:

Biotechnology

Issue date: May 22
Book ads by May 7

Ads accepted until May 15 if space allows

Deliver your message to a global audience of targeted, qualified scientists.

129,566
subscribers in print every week

33,295
yearly unique active job seekers searching for biotechnology jobs

16,250
yearly applications submitted for biotechnology positions

What makes *Science* the best choice for recruiting?

- Read and respected by 400,000 readers around the globe
- Your ad dollars support AAAS and its programs, which strengthens the global scientific community.

Why choose this job focus for your advertisement?

- Relevant ads lead off the career section with a special biotechnology banner.

Expand your exposure by posting your print ad online:

- Additional marketing driving relevant job seekers to the job board.

To book your ad, contact:
advertise@sciencecareers.org

The Americas
202 326 6577
Europe
+44 (0) 1223 326527
Japan
+81 3 6459 4174
China/Korea/Singapore/ Taiwan
+86 131 4114 0012

Produced by the *Science*/AAAS Custom Publishing Office.

Science Careers
AAAS
SCIENCECAREERS.ORG

FOR RECRUITMENT IN SCIENCE, THERE'S ONLY ONE *SCIENCE*.

HIGH-LEVEL GLOBAL TALENTS RECRUITMENT

2020 Global Online Job Fair (www.edu.cn/cv)

April 09, 2020 Western China Doctoral Talents Recruitment

April 17, 2020 South Area of East China Doctoral Talents Recruitment

April 24, 2020 Specialty Session (Science & Engineering)

May 08, 2020 North Area of East China Doctoral Talents Recruitment

May 09, 2020 Hong Kong, Macao, Taiwan and the China Great Bay Area Doctoral Talents Recruitment

May 15, 2020 High-level Global Talents Recruitment

Qualification for Applicants

Global scholars, Doctor and Post-doctor

Key Disciplines

Life Sciences, Health Sciences and Physical Sciences

Participating Approach

Please send your CV to consultant@acabridge.edu.cn for 2020 Global Online Job Fair

Scan to check the sessions

EVEN SEPARATED BY MOUNTAINS AND RIVERS, WE HAVE OUR BLOOD TIGHTLY CONNECTED

The Coronavirus pandemic has forced many of us to consider different ways of working and communicating. Chinese universities and colleges are now holding online job fairs to help overseas scholars explore career options in China.

Fight with One Heart to Combat COVID-19

In these challenging times, Chinese universities and colleges have shot videos, sending greetings and wishes to their overseas compatriots. Please scan below QR code to receive messages of love and well wishes from high schools in your motherland.

By **Arpit Sharma**

Finding community during a pandemic

In early March, the first cases of COVID-19 were reported in my city, Boston. Suddenly, our university inundated us with emails encouraging good hygiene practices and social distancing. Then, a few days later, we were informed that all noncritical research should stop and that mandatory work-from-home policies would be implemented. Anxiety spread like wildfire. I had not expected my work life on campus to stop so suddenly. My lab mates and I think of our workspace as a home away from home, where we enjoy interacting at lab meetings and over coffee. I felt a pit in my stomach as I realized all that was over for now. I was afraid of feeling isolated.

QQ group:1067583220

What worried me even more was the extent of the isolation. Within a few days of learning that I'd be working at home for at least 6 weeks, I found out that a conference I was planning to attend in June was canceled. Not only was I going to miss my work environment, but I was also going to lose a great opportunity to meet researchers from around the world, share ideas, and present my work.

On the last day we were all in the lab together, my postdoc adviser mentioned he wanted to start an online seminar series. At first I felt relieved, thinking that virtual seminars would at least provide some respite from isolation. But I doubted they would measure up to the experience of in-person seminars.

"My sense of isolation has faded, and ... I feel more connected than ever."

Together with another lab head, my adviser spread the word that they were starting a Slack group, where researchers in our field—the science of aging—could have discussions and sign up to give seminars. The group quickly amassed roughly 600 members, and the speaker list filled up. That seemed promising, but I still wondered how many scientists would actually tune in to the seminars, which were slated to take place once every workday.

One week after our university closed, I settled into my makeshift work-from-home desk and logged on to my first virtual seminar. I was pleasantly surprised to see some familiar names online, some from as far away as Brazil and China. Midway through the talk, I noticed that more than 250 researchers were watching. As I took notes, jotting down intriguing experiments and impressive techniques, the unfamiliarity of the experience faded. I realized that despite being alone in my apartment, I was taking part in an event with researchers from around the world, some probably motivated by the same fear of isolation I had felt.

We have continued the daily seminars in the weeks since then, hearing from senior scientists, Ph.D. students, postdocs, and others in our field. After each seminar, we ask the speaker questions on Slack and take part in a group discussion about their research. I've found the talks helpful for learning about new lab techniques and identifying researchers whom I might be able to collaborate with in the future.

We've also used our Slack group to connect in more personal ways, such as by sharing updates on COVID-19 cases in our respective countries and commiserating about struggles that we're going through. I have been able to reconnect with colleagues whom I met at conferences years ago but had since lost touch with. My sense of isolation has faded, and—perhaps counterintuitively—I feel more connected than ever.

I began my work-at-home experience worried about losing the opportunity to connect with my colleagues. But I now realize that I am part of a global research community that can thrive online. I plan to continue my conversations with colleagues via our Slack group long after the pandemic is quelled. That will allow us to connect year-round, not just during our field's annual conference, and to include researchers for whom travel is difficult.

If you find yourself lonely working from home, I'd recommend starting your own online community with colleagues in your field. We're facing tough times and an uncertain future. But it's also an opportunity to rethink how we interact with one another, in ways that will benefit the scientific community in the long term. ■

Arpit Sharma is a postdoctoral scholar at the Harvard T. H. Chan School of Public Health in Boston. Do you have an interesting career story to share? Send it to SciCareerEditor@aaas.org.

ILLUSTRATION: ROBERT NEUBECKER

ScienceRobotics.org

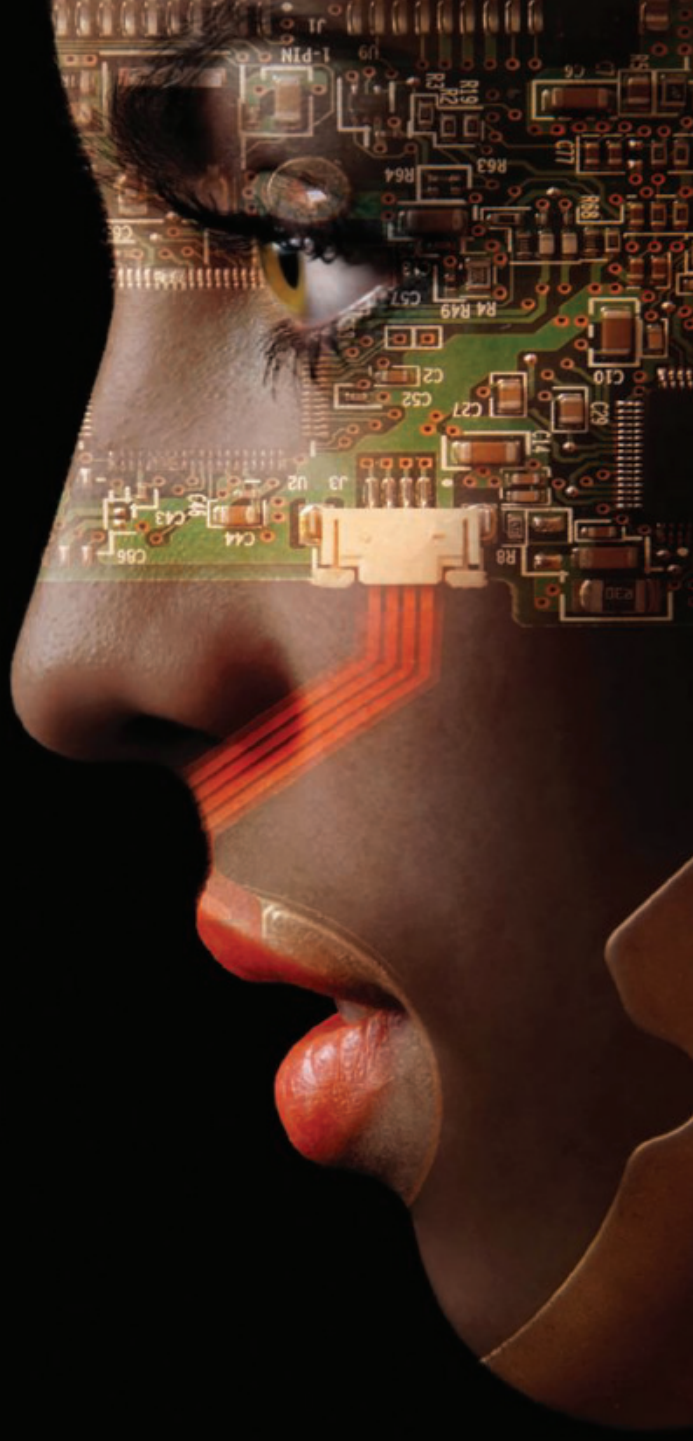

DOESN'T YOUR RESEARCH DESERVE THE BEST READERS?

Submit your research: **cts.ScienceMag.org**

Science Robotics
AAAS

Twitter: @SciRobotics
Facebook: @ScienceRobotics

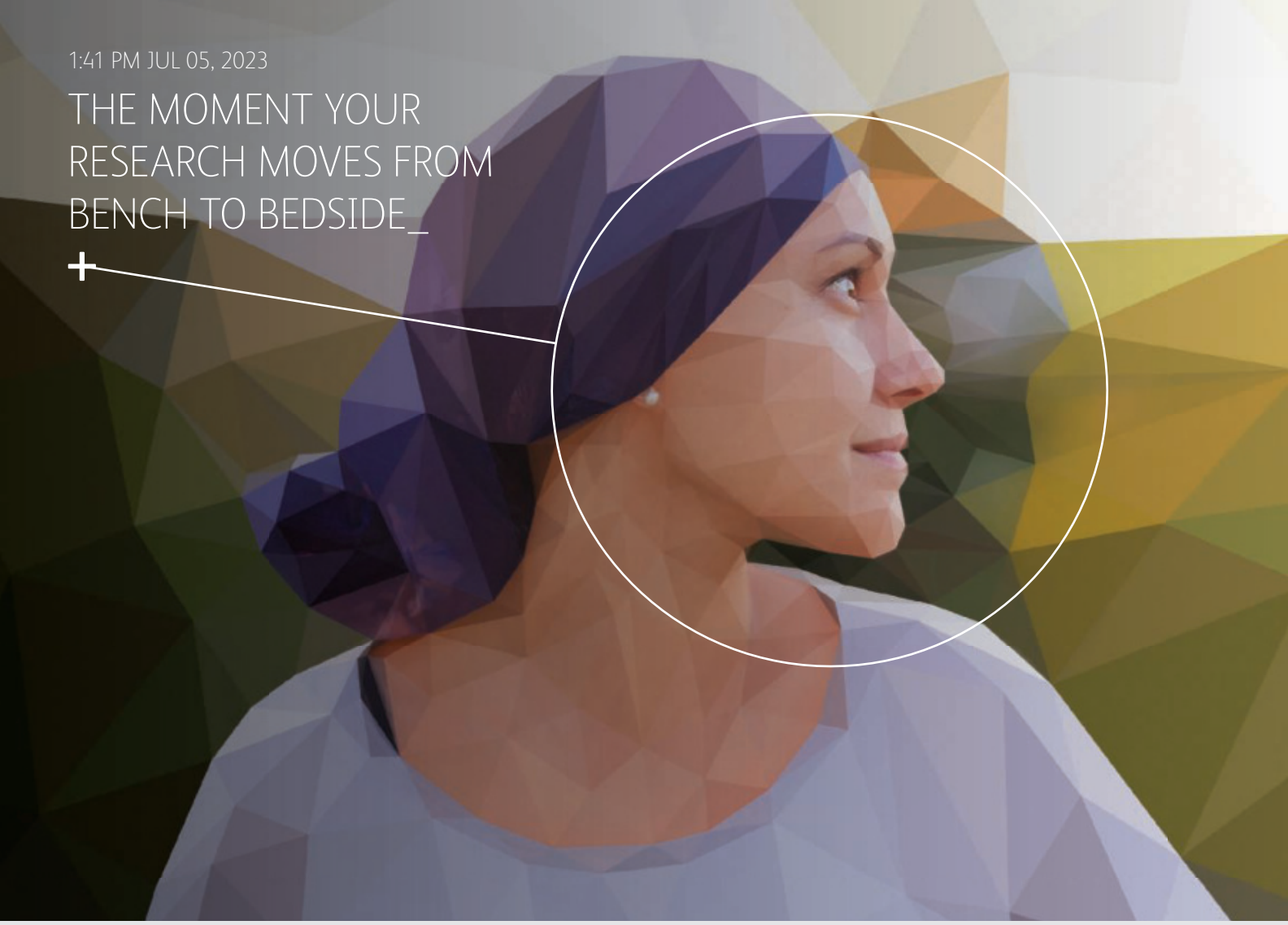

THE DIFFERENCE OF BREAKTHROUGH RESEARCH TO ENABLE MORE CURES

WITH BD AS YOUR PARTNER IN IMMUNO-ONCOLOGY FROM BENCH TO BEDSIDE. BD is your partner in immuno-oncology from discovery research to clinical applications, with a range of high-performance solutions designed to give you high-quality, reliable research data for even the most complex experiments. More solutions. More answers. More data you can trust. Discover more with BD at your side. **Discover the new BD.**

Learn more at **bd.com/Immuno-oncology**

BD

Advancing the world of health

For Research Use Only. Not for use in diagnostic or therapeutic procedures.
BD, San Jose, CA, 95131, U.S.

BD and the BD Logo are trademarks of Becton, Dickinson and Company or its affiliates. © 2019 BD. All rights reserved. (0619)